RL-971

Time Domain Characterization of Microwave Circuits

Kavita Goverdhanam

April 1999

RL-971 = RL-971

Time Domain Characterization of Microwave Circuits

by

Kavita Goverdhanam

A dissertation submitted in partial fulfillment
of the requirements for the degree of
Doctor of Philosophy
(Electrical Engineering)
in The University of Michigan
1999

Doctoral Committee:
- Professor Linda P.B. Katehi, Chair
- Professor John Volakis
- Professor Kamal Sarabandi
- Professor Andrew E. Yagle
- Dr. Rainee N. Simons
- Dr. James Harvey

To my wonderful Uday, sweet Supriya, jolly Sudhakaraa and inspiring parents, Smt. G. Shakuntala Rao and Shri. G. Ramakrishna Rao

ABSTRACT

Time Domain Characterization of Microwave Circuits

by

Kavita Goverdhanam

Chair: Linda P.B. Katehi

Advances in microwave and millimeter-wave circuit technology in parallel to the advances in computer technology have lead to the development of several sophisticated full-wave time and frequency domain techniques to solve Maxwell's equations in order to obtain the electromagnetic fields and propagation characteristics of these circuits. The goal of this research has been to solve Electromagnetic circuit problems in time domain using efficient numerical techniques. In doing so, the Finite Difference Time Domain (FDTD) based numerical methods have been studied.

The first part of this research focuses on using the FDTD technique to characterize novel microwave devices and circuits based on the Coplanar Stripline (CPS). CPS circuits have several applications in wireless communication because of advantages such as excellent propagation, small discontinuity parasitics, efficient use of the wafer area, capability to sustain back metalization, and simplified heat sinking and packaging. In this work, several CPS discontinuities have been characterized and based on these studies, novel CPS filters have been designed and characterized. In addition, minor variants of CPS are investigated

for potential applications in microwave circuit integration.

For the theoretical characterization of all the CPS circuits, the FDTD technique was used successfully - thus demonstrating the versatility of the FDTD technique in characterizing microwave circuits. However, despite it's versatility, simplicity and efficiency, the FDTD technique suffers from serious limitations due to the substantial computation resources required in modeling large-scale problems. The uniform-grid adaptation of this technique (the most widely used because of it's simplicity) is a dominant factor contributing to this limitation.

In view of the aforementioned disadvantages, the second part of this work focuses on developing an FDTD multigrid scheme using Haar wavelet based Multiresolution in Time Domain (MRTD). In particular, the Haar wavelet basis has been chosen because pulse bases which form the scaling function in the Haar system are the expansion functions in the conventional FDTD scheme. Thus, FDTD can be thought of as a particular case of MRTD based on Haar scaling functions alone. The general MRTD scheme using Haar scaling as well as wavelet functions has been developed here and applied to solve for the Electromagnetic fields in several 2D and 3D microwave circuits. The results obtained are compared with those computed using conventional FDTD technique in order to highlight the benefits of using the MRTD scheme. In the MRTD scheme, it is seen that the wavelet coefficients are significant only in areas with abrupt field variations and that the coefficients which are below a certain threshold level can be dropped without adverse effects. Thus, by combining the wavelet and scaling coefficients only in regions where the wavelet coefficients are significant, the dual benefit of enhanced field resolution and economy in memory can be realized. The selective enhancement of resolution in the desired sections of the computational domain translates to Multigrid capability. MRTD technique developed here combines all the advantages of the

conventional FDTD scheme with the additional benefits offered by Multiresolution Analysis, thus leading to a robust time domain tool that has the capability to resolve a number of problems that crop up during the characterization of complex electromagnetic circuits.

ACKNOWLEDGEMENTS

Several people have played a very significant role in the completion of my doctoral study at the University of Michigan. I would like to use this opportunity to express my gratitude to them.

First, I would like to thank my advisor, Professor Linda P. B. Katehi for her support, guidance and encouragement. She has been a constant source of inspiration. Her energy, drive, positive attitude, open mindedness and sincerity have made a lasting impression on me. I thank her for placing confidence in my abilities throughout this effort, but I am particularly thankful to her for her faith in me in the very beginning stages of my doctorate journey when I was struggling to find my place in the big scheme of things.

I would also like to thank the rest of members of my doctoral committee for their support, time and consideration. Their insight and suggestions have been invaluable. Special thanks are due to Dr. Rainee N. Simons for his constant guidance. I have benefited tremendously from the numerous discussions with him. I would also like to thank him for his numerous trips from Cleveland to Ann Arbor which facilitated very smooth discussions and exchange of ideas.

I have constantly benefited from interactions with Dr. Nihad Dib, Dr. Michael Krumpholz, Dr.Kazem Sabetfakhri and Dr. Emmanouil Tentzeris and I'd like to thank them for sharing their insight. I have also benefited from several discussions and conversations with Mr.

Konstantinos Sarris and would like to thank him for the same.

I would like to thank the Center for Parallel Computation for the excellent computing facilities. Special thanks are due to the support staff of DCO their prompt assistance whenever needed. I would also like to thank Prof. Rodney Johnson for his time and valuable suggestions regarding technical writing.

The support of Rad. Lab. staff and their constant willingness to help is greatly appreciated. I am also very greatful to all my colleagues at the Radiation Laboratory for making this department a very fun and jovial place to work. Special thanks to Dr. Rashaunda Henderson, Dr. Rhonda Drayton, Ms. Lee Harle, Ms. Katherine Herrick Mr. Stephane Legault, Mr. Mark Casciato and Mr. Eray Yasan for their thoughtfulness, friendship and fresh perspective.

Finally my deepest gratitude goes to my family - my parents, for always encouraging me to pursue my dreams, my bother Sudhakar and sister Supriya for always being proud of me, and my dear husband Uday for being so wonderfully caring, supportive and encouraging though out this effort - I couldn't have done this without my wonderful family.

TABLE OF CONTENTS

CHAPTERS

LIST OF TABLES

Table

LIST OF FIGURES

Figure

CHAPTER 1

Introduction

1.1 Background

In recent years, impressive advances have been made in microwave technology, spurred by the ever-increasing need for components suitable for application in the areas of mobile, personal and satellite communications, commercial radar systems and remote sensing, technologies to mention a few. Due to their significant and growing impact on the state of the art, new technologies and configurations continue to be a topic of great interest to the microwave engineering community. With the development of Microwave Integrated Circuits (MICs) and Monolithic Microwave Integrated Circuits (MMICs), bulky and expensive waveguide and coaxial components have been replaced with components that are small, lightweight, cost- effective, more reliable, reproducible and complex.

This evolving technology continues to exploit higher frequencies up to the millimeter and sub-millimeter wave ranges. This trend has necessitated the development of accurate full-wave techniques to solve Maxwell's equations in order to obtain the electromagnetic fields and propagation characteristics of these circuits. Given the complexity of the circuits, characterizing them accurately would require advanced computation resources. Fortunately, timely parallel advances in computer technology have made it feasible for several sophisticated full wave numerical techniques to characterize microwave circuits.

These techniques can be divided into frequency domain and time domain techniques. Among the frequency domain techniques the most common are the Method of Moments (MoM) [39], Finite Element method [40] and Finite Difference Method [41]. Among the time domain techniques, the Transmission Line Matrix (TLM) method [42] and the Finite Difference Time Domain (FDTD) Technique [43] are the most popular ones.

The choice of an appropriate numerical technique depends on the application and the problem under consideration. Issues such as these have been elaborately discussed in the literature [36]- [38]. In the present work, the FDTD technique [43] has been chosen to perform the characterization of the microwave circuits because of its efficiency, ease of implementation, and capability to qualitatively demonstrate electromagnetic field solutions in time domain. Time domain techniques have a definite advantage over frequency domain techniques when information over a broad frequency range is sought, because the result of the entire frequency range can be obtained with a single computation, followed by a Fourier transform to obtain the frequency response. These have been some of the motivating factors in choosing time domain characterization in general and the FDTD technique in particular to analyze the microwave circuits presented here. This technique has been used to successfully characterize the performance of a wide gamut of microwave circuits and antennas, and the abundant literature available stands proof to the versatility and robustness of the FDTD technique [70]- [73]. In the later part of this thesis, a new time domain technique which uses Multiresolution analysis (MRTD scheme), which implements an a variable grid FDTD is developed and applied successfully to characterize microwave circuits.

1.2 Objective

The objective of this work has been to solve Electromagnetic circuit problems in time domain using a technique that has the potential to address a number of problems that crop up during circuit characterization. To begin with, the FDTD technique was used as the tool to characterize microwave circuits. Using this technique, several novel microwave devices and circuits which are based on the Coplanar Stripline (CPS) were characterized successfully. Motivation for the interest in Coplanar Stripline circuits will be presented in the following section. While characterizing large/complex CPS circuits using the FDTD technique, the large memory requirement and computation time of the FDTD scheme often become a serious limitation in dictating the level of complexity that can be modeled with this technique. To address these problems, an FDTD multigrid scheme using Haar wavelet-based Multiresolution analysis (MRA) resulting in a Multiresolution Time Domain (MRTD) scheme has been developed. Details of the motivation for each of the aforementioned research efforts is discussed below.

1.3 Motivation

A study of the recent trends in microwave integrated circuits strongly indicates the extensive use of planar components in both hybrid MIC and MMIC circuits. As the name indicates, planar circuits comprise planar transmission structures such as microstrip lines, slotlines, coplanar waveguides and coplanar striplines. Although the microstrip line is very popular and has been extensively studied and very well characterized, uniplanar circuit structures such as CPW and CPS have also attracted a great deal of attention. This can be ascribed to several advantages that these lines have over the conventional microstrip line.

These include facilitating easy shunt and series mounting of active and passive devices; eliminating the need for wraparound and via holes, which introduce additional parasitics [2]-[3]; eliminating the need for back metalization; allowing the circuits to be integrated with solid-state devices on a single surface [1]; and allowing to be wafer probed at millimeter-wave frequencies [4]- [8].

While the dual structures CPS and CPW share all the aforementioned advantages, CPS has the additional advantage over CPW that it makes efficient use of wafer area, resulting in lower cost and larger density of circuit functions [13]. The CPS propagation parameters are independent of substrate thickness beyond a critical value, thereby simplifying heat sinking and packaging. The aforementioned advantages suggest that CPS is a strong candidate for planar circuit applications. While Microstrip and CPW lines have been extensively studied, characterized and used, the same cannot be said of CPS lines and circuits. Therefore, in this work, a number of CPS discontinuities have been characterized. Based on the results of these studies, a number of CPS circuits have been designed and characterized, thus demonstrating the potential of CPS based circuits.

In order to characterize the CPS discontinuities and circuits, the FDTD technique has been very successfully employed, demonstrating the efficacy of the approach. As mentioned previously, the FDTD technique was chosen to perform the analysis of the CPS circuits, due to its numerous advantages, including simplicity, efficiency and ease of implementation. However, despite these advantages, this technique suffers from serious limitations in modeling large-scale electromagnetic geometries with subwavelength details due to the substantial computation resources required.

The uniform-grid adaptation of this technique (the most widely used because of its simplicity) is a dominant factor contributing to this limitation. The orthogonality of the grid and uniform spacing of the grid points in the FD-TD scheme allow the first order spatial and temporal derivatives of Maxwell's equations to be approximated using central-difference operators. Thus in the conventional FD-TD scheme, the electromagnetic fields can be discretized based on a uniform lattice. However, it is often desired to have a refined mesh in localized regions such as edges, corners and other discontinuities where strong field variations occur. Using a uniform mesh in such situations results in the refinement of the mesh density in the entire computational domain. Such unnecessary high levels of refinement result in undesired increases in memory resources and computation time.

In order to circumvent these limitations, various nonuniform-grid FDTD schemes [52]–[56] have been developed allowing the use of a dense mesh wherever required and a coarse mesh elsewhere. In [49] a quasi-nonuniform FD-TD grid is developed that requires the reduction of the dense mesh cell to exactly one-third the size of the coarse mesh cell, thereby maintaining the central difference approximation. In [52] a non-uniform FDTD method is developed where the field in both the coarse and fine meshes is calculated using regular FD-TD discretized equations, and an interpolation in both space and time is utilized to calculate the tangential electric field on the coarse-fine mesh interface. In [55] and [56] a non-uniform scheme is developed, which, however, is not based on a central difference scheme, thereby increasing the numerical error in the fine grid from second order to first order.

It is clear that the aforementioned non-uniform schemes are fraught with limitations and/or additional complications that make them difficult to implement. The present research effort focuses on developing an FDTD multigrid using wavelet expansions. Time domain schemes which result from the use of wavelet expansions or Multiresolution Analysis are called Multiresolution Time Domain schemes.

Applications of orthonormal wavelet expansions in signal processing and numerical analysis are well known [74], [75]- [77]. In the last few years, it has been demonstrated that Multiresolution Analysis (MRA), which is the mathematical basis of wavelet expansions [59]- [60] can be successfully applied to Electromagnetics [61], [62]. In particular, the use of wavelets in the Method of Moments (MOM) for the solution of integral equations in frequency domain is well established [61], [57], [63]. However recent publications have demonstrated that the application of the method of moments directly to Maxwell's equations allows as well for the use of MRA in the time domain. In fact, it has been shown in [65] that Multiresolution time domain (MRTD) schemes based on Battle-Lemarie scaling functions exhibit highly linear dispersion characteristics and that the resulting MRTD scheme has savings of one or two orders of magnitude in time and memory in comparison to the conventional FDTD scheme. Part of the present research stems from these developments in MRA expansions in Electromagnetics.

In this thesis work, the Haar bases are chosen to develop the MRTD scheme. The reason for this choice is that pulse functions, which are the basis functions used for field expansions in the conventional FDTD scheme, are the scaling functions of the Haar bases. Thus, FDTD can be thought of as an incomplete scheme. A more complete scheme would be the MRTD scheme that uses the Haar scaling as well as wavelet functions for field expansions. Such a scheme encompasses the conventional FDTD scheme and combines all the advantages of the FDTD scheme with the other benefits that accrue by using Multiresolution, such as, linear dispersion, multigrid capability and significant economy in memory.

The potential for multigrid capability and economy in memory emerges from the fact that while scaling coefficients indicate the average values of the field, wavelet coefficients represent the derivatives or the variation of the field. Therefore, the wavelet coefficients are significant only in areas where a strong field variation occurs such as at edges, corners and other discontinuities. The coefficients in areas which have constant or smooth fields are negligible. The wavelet coefficients below a certain threshold level can be dropped and doing so does not adversely affect the condition numbering of the system [57].

The areas where both the scaling and wavelet functions are used correspond to a dense mesh with higher resolution levels while those areas where only the scaling are used corresponds to a coarse mesh with lower resolution. Thus by using the MRTD scheme, nonuniform gridding or Multigridding occurs naturally and in a mathematically correct manner without the need for any additional boundary conditions at the interface of the coarse and fine meshes.

1.4 Overview

The organization of this dissertation is as follows:

In chapter 2, an overview of the FDTD technique is presented. The procedure of discretizing the FDTD equations, the accuracy, stability and dispersion of this scheme, and the treatment of source term and boundary conditions has been reviewed.

In chapter 3, the FDTD scheme has been applied to characterize novel CPS circuits. To begin with, the motivation for investigating CPS circuits has been presented. This is followed by characterization of CPS discontinuities using FDTD scheme. Based on the study of these discontinuities, several CPS filters were designed. These filters and their characterization using FDTD technique are presented. The results obtained by characterizing CPS circuits using FDTD method are compared with measurements.

In chapter 4, variants of the Coplanar Stripline are investigated for potential applications in 3D microwave circuit integration. In particular, the Micro-coplanar Stripline (MCPS) has been proposed as a multilayer three dimensional transmission line for addressing the issues of size and complexity that arise with circuit integration. The FDTD scheme has been used to study the propagation characteristics of this line. In addition, this chapter also presents CPS based interconnects. Again, the FDTD scheme has been applied to characterize these interconnects. This chapter ends with a discussion of the computational aspects of characterizing the circuits in chapters 3 and 4 using the uniform grid FDTD scheme. The limitations of the FDTD technique are presented and the motivation for studying a non-uniform grid FDTD scheme is presented. the motivation for developing and efficient, non-

In chapter 5, a new time domain scheme, the Multiresolution Time Domain (MRTD) scheme, using Haar wavelet basis is presented. The motivation for using the Haar basis and the advantages of using MRTD schemes has been discussed. The Zero resolution 1D MRTD scheme and it's dispersion analysis has been presented. Also, the development of Zero resolution 2D MRTD scheme and it's applications to shielded structures has been presented.

Chapter 6, begins with the development of the zero resolution 3D MRTD scheme. The treatment of hard boundaries and open boundaries in the zero resolution MRTD schemes is presented. This scheme is applied to characterize simple microwave circuits. This is followed by a discussion of the limitations of using the zero resolution MRTD scheme where the scaling and wavelet schemes decouple. To overcome these limitation, higher resolution MRTD schemes is presented. Details of the implementation of first resolution 3D MRTD scheme are presented and followed by a discussion of the methodology of implementing higher resolution MRTD schemes of arbitrary resolution. The treatment of hard boundaries in the coupled MRTD schemes of first and higher resolution levels has been presented. Special attention is focused on the treatment of open boundaries using the Perfectly Matched Layer (PML) in the general MRTD scheme. Finally the MRTD scheme that is developed is validated by characterizing some 3D microwave circuits.

In Chapter7, the stability and dispersion analysis of Haar-based MRTD schemes is presented.

In chapter 8, the applications of MRTD schemes in the characterization of complex microwave circuits has been presented. It is shown that by using the MRTD scheme, the upper limit of the scaling field resolution is not dictated by the smallest geometrical detail as in the case of the conventional FDTD scheme. Instead it is shown that wavelets can be used to locally enhance field resolution in the desired section of the computational domain while maintaining a coarse grid elsewhere.

In chapter9, the significant accomplishments of this work have been summarized, followed by recommendations for future work.

CHAPTER 2

The Finite Difference Time Domain (FDTD) Scheme

2.1 FDTD Overview

The Finite Difference Time Domain (FDTD) scheme was introduced by Yee [43] and applied to electromagnetic scattering problems. In this method, the electric and magnetic fields in the computational domain of interest are calculated by using discretixed equations obtained from the first order derivatives of the differential form of Maxwell's equations. Thus, this scheme solves for both the electric and magnetic fields in time and space leading to a robust solution that is accurate for a very wide class of structures. Figure 2.1 shows the relative positions of the electric and magnetic field components in Yee's FDTD cell. As seen from the figure, in this scheme, the electric field, E and magnetic field H are interlaced in space such that every E component is surrounded by four circulating H components and every H component is surrounded by four circulating E components. Thus, the Yee algorithm simultaneously simulates the pointwise differential form and the macroscopic integral form of Maxwell's equations. Also, the E and H fields are interleaved in time by half a time step (the 'leap frog' arrangement). All the E field computations in the computational domain are computed for a particular time step using the H field data previously stored in the computer memory. This is followed by the computation of the H field components using the stored E field data. This cycle is continued until the time-stepping is concluded. This explicit 'leap frog' scheme avoids the problem involved with simultaneous equations and matrix inversion. The resulting finite-difference expressions for the time derivatives are 'central-difference' in nature and second order in accuracy. A thorough treatment of the FDTD technique has been presented in [47]. In the following sections, a brief overview of the scheme is presented.

2.2 3D FDTD Dicretized Equations

Consider Maxwell's curl equations shown below:

$$\mu\frac{\partial\overline{H}}{\partial t} = -\nabla \times \overline{E} - \rho\overline{H} \tag{2.1}$$

$$\epsilon\frac{\partial\overline{E}}{\partial t} = \nabla \times \overline{H} - \sigma\overline{E} \tag{2.2}$$

The vector equations 2.1 and 2.2 can be rewritten as the following six scalar equations:

$$\mu\frac{\partial H_x}{\partial t} = \frac{\partial E_y}{\partial z} - \frac{\partial E_z}{\partial y} - \rho H_x \tag{2.3}$$

$$\mu\frac{\partial H_y}{\partial t} = \frac{\partial E_z}{\partial x} - \frac{\partial E_x}{\partial z} - \rho H_y \tag{2.4}$$

$$\mu\frac{\partial H_z}{\partial t} = \frac{\partial E_x}{\partial y} - \frac{\partial E_y}{\partial x} - \rho H_z \tag{2.5}$$

$$\epsilon \frac{\partial E_x}{\partial t} = \frac{\partial H_z}{\partial y} - \frac{\partial H_y}{\partial z} - \sigma E_x \tag{2.6}$$

$$\epsilon \frac{\partial E_y}{\partial t} = \frac{\partial H_x}{\partial z} - \frac{\partial H_z}{\partial x} - \sigma E_y \tag{2.7}$$

$$\epsilon \frac{\partial E_z}{\partial t} = \frac{\partial H_y}{\partial x} - \frac{\partial H_x}{\partial y} - \sigma E_z \tag{2.8}$$

The following notation is used for a space point in a uniform rectangular lattice:

$$(l, m, n) = (l\Delta x, m\Delta y, n\Delta z) \tag{2.9}$$

In the above notation, Δx,Δy and Δz are the lattice space increments in the x, y and z directions respectively and l,m,n are integers. Any function f of space time evaluated at a discrete point in the grid and at a discrete point in time is denoted as follows:

$$f(l\Delta x, m\Delta y, n\Delta z, \lambda\Delta t) = {}_\lambda f_{l,m,n} \tag{2.10}$$

where Δt is the time increment assumed uniform over the interval of observation and λ is an integer.

To obtain the discrete approximations of the continuous partial differential Eqs.(2.3) - (2.8), central difference approximation is used for both the space and time first order-partial differentiation. The space partial derivative of f in the x-direction and the time derivative of f are approximated as follows:

$$\frac{\partial f}{\partial x}(l\Delta x, m\Delta y, n\Delta z, \lambda\Delta t) = \frac{{}_\lambda f_{l+1/2,m,n} - {}_\lambda f_{l-1/2,m,n}}{\Delta x} + O[(\Delta x)^2] \tag{2.11}$$

$$\frac{\partial f}{\partial t}(l\Delta x, m\Delta y, n\Delta z, \lambda\Delta t) = \frac{{}_{\lambda+1/2}f_{l,m,n} - {}_{\lambda-1/2}\, f_{l,m,n}}{\Delta t} + O[(\Delta t)^2] \tag{2.12}$$

Similarly, the expressions for $\frac{\partial f}{\partial y}$ and $\frac{\partial f}{\partial z}$ can be derived. From these, the discretized equations can be obtained as follows: Substituting for time and space derivatives in Eq.(2.3), we obtain the following equation:

$$\frac{{}_{\lambda+1/2}H^{x}_{l',m'-1/2,n'-1/2} - {}_{\lambda-1/2}\, H^{x}_{l',m'-1/2,n'-1/2}}{\Delta t} = \left(\frac{1}{\mu_{l',m',n'}}\right) \times$$
$$\left(\frac{{}_{\lambda}E^{y}_{l',m'-1/2,n'} - {}_{\lambda}\, E^{y}_{l',m'-1/2,n'-1}}{\Delta z} + \frac{{}_{\lambda}E^{z}_{l',m',n'-1/2} - {}_{\lambda}\, E^{z}_{l',m'-1,n'-1/2}}{\Delta y} - \rho_{l',m',n'}\, {}_{\lambda}H^{x}_{l',m'n'}\right) \tag{2.13}$$

Since H field is evaluated at time-steps $\lambda - 1/2$, we approximate the term ${}_{\lambda}H^{x}_{l',m'n'}$ on the right side of Eq.(2.13) as shown below:

$${}_{\lambda}H^{x}_{l',m'n'} = \frac{{}_{\lambda+1/2}H^{x}_{l',m'n'} + {}_{\lambda-1/2}H^{x}_{l',m'n'}}{2} \tag{2.14}$$

Using Eqs.(2.13) and (2.14) we obtain the following FDTD discretized equation corresponding to Eq.(2.3).

$${}_{\lambda+1/2}H^{x}_{l',m'-1/2,n'-1/2} = \left(\frac{1 - \frac{\rho_{l',m',n'}\Delta t}{2\mu_{l',m',n'}}}{1 + \frac{\rho_{l',m',n'}\Delta t}{2\mu_{l',m',n'}}}\right) {}_{\lambda-1/2}H^{x}_{l',m'-1/2,n'-1/2}$$
$$\left(\frac{\frac{\Delta t}{\mu_{l',m',n'}}}{1 + \frac{\rho_{l',m',n'}\Delta t}{2\mu_{l',m',n'}}}\right) \left(\frac{{}_{\lambda}E^{y}_{l',m'-1/2,n'} - {}_{\lambda}\, E^{y}_{l',m'-1/2,n'-1}}{\Delta z} - \frac{{}_{\lambda}E^{z}_{l',m',n'-1/2} - {}_{\lambda}\, E^{z}_{l',m'-1,n'-1/2}}{\Delta y}\right) \tag{2.15}$$

Similarly, the rest of the discretized Maxwell's equations in three dimensions corresponding to Eqs.(2.4) - (2.8) can be derived. These equations are shown below:

$$
\begin{gathered}
{}^{\lambda+1/2}H^{y}_{l'-1/2,m',n'-1/2} = \left(\frac{1-\frac{\rho_{l',m',n'}\Delta t}{2\mu_{l',m',n'}}}{1+\frac{\rho_{l',m',n'}\Delta t}{2\mu_{l',m',n'}}}\right) {}^{\lambda-1/2}H^{y}_{l'-1/2,m',n'-1/2} \\
\left(\frac{\frac{\Delta t}{\mu_{l',m',n'}}}{1+\frac{\rho_{l',m',n'}\Delta t}{2\mu_{l',m',n'}}}\right)\left(\frac{{}^{\lambda}E^{z}_{l',m',n'-1/2} - {}^{\lambda}E^{z}_{l'-1,m',n'-1/2}}{\Delta x} - \frac{{}^{\lambda}E^{x}_{l'-1/2,m',n'-1/2} - {}^{\lambda}E^{x}_{l'-1/2,m',n'-1}}{\Delta z}\right)
\end{gathered}
\tag{2.16}
$$

$$
\begin{gathered}
{}^{\lambda+1/2}H^{z}_{l'-1/2,m'-1/2,n'} = \left(\frac{1-\frac{\rho_{l',m',n'}\Delta t}{2\mu_{l',m',n'}}}{1+\frac{\rho_{l',m',n'}\Delta t}{2\mu_{l',m',n'}}}\right) {}^{\lambda-1/2}H^{z}_{l'-1/2,m'-1/2,n'} \\
\left(\frac{\frac{\Delta t}{\mu_{l',m',n'}}}{1+\frac{\rho_{l',m',n'}\Delta t}{2\mu_{l',m',n'}}}\right)\left(\frac{{}^{\lambda}E^{x}_{l'-1/2,m',n'} - {}^{\lambda}E^{x}_{l'-1/2,m'-1,n'}}{\Delta y} - \frac{{}^{\lambda}E^{y}_{l',m'-1/2,n'} - {}^{\lambda}E^{y}_{l'-1,m'-1/2,n'}}{\Delta x}\right)
\end{gathered}
\tag{2.17}
$$

$$
\begin{gathered}
{}^{\lambda}E^{x}_{l'-1/2,m',n'} = \left(\frac{1-\frac{\sigma_{l',m',n'}\Delta t}{2\epsilon_{l',m',n'}}}{1+\frac{\sigma_{l',m',n'}\Delta t}{2\epsilon_{l',m',n'}}}\right) {}^{\lambda-1}E^{x}_{l'-1/2,m',n'} + \left(\frac{\frac{\Delta t}{\epsilon_{l',m',n'}}}{1+\frac{\sigma_{l',m',n'}\Delta t}{2\epsilon_{l',m',n'}}}\right) \times \\
\left(\frac{{}^{\lambda-1/2}H^{z}_{l'-1/2,m'+1/2,n'} - {}^{\lambda-1/2}H^{z}_{l'-1/2,m'-1/2,n'}}{\Delta y} - \frac{{}^{\lambda-1/2}H^{y}_{l'-1/2,m',n'+1/2} - {}^{\lambda-1/2}H^{y}_{l'-1/2,m',n'-1/2}}{\Delta z}\right)
\end{gathered}
\tag{2.18}
$$

$$
\begin{gathered}
{}^{\lambda}E^{y}_{l',m'-1/2,n'} = \left(\frac{1-\frac{\sigma_{l',m',n'}\Delta t}{2\epsilon_{l',m',n'}}}{1+\frac{\sigma_{l',m',n'}\Delta t}{2\epsilon_{l',m',n'}}}\right) {}^{\lambda-1}E^{y}_{l',m'-1/2,n'} + \left(\frac{\frac{\Delta t}{\epsilon_{l',m',n'}}}{1+\frac{\sigma_{l',m',n'}\Delta t}{2\epsilon_{l',m',n'}}}\right) \times \\
\left(\frac{{}^{\lambda-1/2}H^{x}_{l',m'-1/2,n'+1/2} - {}^{\lambda-1/2}H^{x}_{l',m'-1/2,n'-1/2}}{\Delta z} - \frac{{}^{\lambda-1/2}H^{z}_{l'+1/2,m'-1/2,n'} - {}^{\lambda-1/2}H^{z}_{l'-1/2,m'-1/2,n'}}{\Delta x}\right)
\end{gathered}
\tag{2.19}
$$

$$
\begin{gathered}
{}^{\lambda}E^{z}_{l',m',n'-1/2} = \left(\frac{1-\frac{\sigma_{l',m',n'}\Delta t}{2\epsilon_{l',m',n'}}}{1+\frac{\sigma_{l',m',n'}\Delta t}{2\epsilon_{l',m',n'}}}\right) {}^{\lambda-1}E^{z}_{l',m',n'-1/2} + \left(\frac{\frac{\Delta t}{\epsilon_{l',m',n'}}}{1+\frac{\sigma_{l',m',n'}\Delta t}{2\epsilon_{l',m',n'}}}\right) \times \\
\left(\frac{{}^{\lambda-1/2}H^{y}_{l'+1/2,m',n'-1/2} - {}^{\lambda-1/2}H^{y}_{l'-1/2,m',n'-1/2}}{\Delta x} - \frac{{}^{\lambda-1/2}H^{x}_{l',m'+1/2,n'-1/2} - {}^{\lambda-1/2}H^{x}_{l',m'-1/2,n'-1/2}}{\Delta y}\right)
\end{gathered}
\tag{2.20}
$$

In the equations above, $\rho_{l',m',n'}$ and $\sigma_{l',m',n'}$ are the electric and magnetic loss coefficients for the (l',m',n') cell. $\overline{E}$ and $\overline{H}$ fields are alternately calculated using the discretized equations, resulting in a centered differences for the time derivatives as well. While the Yee algorithm described above can be interpreted as a direct approximation of the pointwise derivatives of Maxwell's time dependent Curl equations, it can also be shown that the same equations can be obtained by using the contour integral representation based on Ampere's Law and Faraday's Law in integral form. This offers a better understanding of the physics behind the scheme and has been very useful in modeling the electromagnetic fields in problems with fine geometrical features such as wires, slots and curved surfaces [47].

2.3 Reduction of 3D FDTD to 2.5D, 2D and 1D Schemes

For analyzing guided-wave structures using FDTD technique, computation requirements can be reduced by forming the surface grid on a planar geometry (in the plane which is the cross section of the guided-wave structure, perpendicular to the direction of propagation), and then extruding the surface elements in the direction of propagation to form solid elements. The resulting grid is considered to be 2.5 dimensional because it cannot accommodate geometry variations along the extrusion direction. This is referred to as the 2.5D FDTD scheme. In the 2.5D FDTD scheme, the field variation along the direction of propagation is assumed constant. Assuming z is the propagation direction, and denoting the propagation constant as β, Maxwell's equation, as per the formulation in [48] for a lossless 2.5D case are shown below:

$$\mu \frac{\partial H_x}{\partial t} = \beta E_y - \frac{\partial E_z}{\partial y} - \rho H_x \tag{2.21}$$

$$\mu \frac{\partial H_y}{\partial t} = \frac{\partial E_z}{\partial x} - \beta E_x - \rho H_y \tag{2.22}$$

$$\mu\frac{\partial H_z}{\partial t} = \frac{\partial E_x}{\partial y} - \frac{\partial E_y}{\partial x} - \rho H_z \tag{2.23}$$

$$\epsilon\frac{\partial E_x}{\partial t} = \frac{\partial H_z}{\partial y} + \beta H_y - \sigma E_x \tag{2.24}$$

$$\epsilon\frac{\partial E_y}{\partial t} = -\beta H_x - \frac{\partial H_z}{\partial x} - \sigma E_y \tag{2.25}$$

$$\epsilon\frac{\partial E_z}{\partial t} = \frac{\partial H_y}{\partial x} - \frac{\partial H_x}{\partial y} - \sigma E_z \tag{2.26}$$

In the 2D FDTD method, the electromagnetic field varies only in two directions. For example, assuming no field variation in the z direction, all partial derivatives with respect to z can be set to zero leading to the following set of 2D-Maxwell's equations in a lossless medium:

$$\mu\frac{\partial H_x}{\partial t} = -\frac{\partial E_z}{\partial y} - \rho H_x \tag{2.27}$$

$$\mu\frac{\partial H_y}{\partial t} = \frac{\partial E_z}{\partial x} - \rho H_y \tag{2.28}$$

$$\mu\frac{\partial H_z}{\partial t} = \frac{\partial E_x}{\partial y} - \frac{\partial E_y}{\partial x} - \rho H_z \tag{2.29}$$

$$\epsilon\frac{\partial E_x}{\partial t} = \frac{\partial H_z}{\partial y} - \sigma E_x \tag{2.30}$$

$$\epsilon\frac{\partial E_y}{\partial t} = -\frac{\partial H_z}{\partial x} - \sigma E_y \tag{2.31}$$

$$\epsilon\frac{\partial E_z}{\partial t} = \frac{\partial H_y}{\partial x} - \frac{\partial H_x}{\partial y} - \sigma E_z \tag{2.32}$$

As expected, in the case of 1D propagation, the fields vary only in one direction (x) leading to the following Maxwell's equations in a lossless medium:

$$\mu\frac{\partial H_x}{\partial t} = -\rho H_x \tag{2.33}$$

$$\mu\frac{\partial H_y}{\partial t} = \frac{\partial E_z}{\partial x} - \rho H_y \tag{2.34}$$

$$\mu\frac{\partial H_z}{\partial t} = -\frac{\partial E_y}{\partial x} - \rho H_z \tag{2.35}$$

$$\epsilon\frac{\partial E_x}{\partial t} = -\sigma E_x \tag{2.36}$$

$$\epsilon\frac{\partial E_y}{\partial t} = -\frac{\partial H_z}{\partial x} - \sigma E_y \tag{2.37}$$

$$\epsilon\frac{\partial E_z}{\partial t} = \frac{\partial H_y}{\partial x} - \sigma E_z \tag{2.38}$$

2.4 On the Accuracy, Stability and Dispersion of FDTD Scheme

As seen earlier, the Yee algorithm of FDTD scheme results in an orthogonal grid where first order derivatives of Maxwell's equations are approximated using central-difference operators. It can be shown that the centered difference scheme leads to a solution with second order accuracy in space and time [49]. Thus high accuracy is obtained for smooth functions where the higher order derivatives are small over the spatial cell size. This condition requires that the grid size should be small compared to the wavelength of the propagating wave.

It is essential that a numerical scheme should be stabile, i.e, any numerical errors that result from the scheme should not grow as the simulation proceeds. Stability analysis of the FDTD scheme yields the following criterion [47]:

$$\Delta t \leq \frac{1}{c}\left(\frac{1}{\Delta x^2}+\frac{1}{\Delta x^2}+\frac{1}{\Delta x^2}\right)^{-\frac{1}{2}} \tag{2.39}$$

where c is the velocity of light in the medium that fills the computational domain.

The finite difference grid causes the velocity of propagating waves to be dependent on the resolution of the grid. The numerical dispersion that occurs can be quantified by following equation for the phase velocity of plane waves propagating on the grid:

$$v=\frac{\omega}{k}=\frac{2}{k\Delta t}\sin^{-1}\left(c\Delta t\left[\frac{\sin^2 k_x\Delta x/2}{\Delta x^2}+\frac{\sin^2 k_y\Delta y/2}{\Delta y^2}+\frac{\sin^2 k_z\Delta z/2}{\Delta z^2}\right]^{1/2}\right) \tag{2.40}$$

In this expression k is the wave number and is given by $k=\sqrt{k_x^2+k_y^2+k_z^2}$ where k_x, k_y and k_z are the x, y and z components of the wave number.

2.5 Boundary Conditions

To apply FDTD to circuit modeling, the treatment of boundary conditions and source term must be considered carefully. In this section, the treatment of Perfect electric and magnetic conductors, dielectric interfaces, open boundaries and source term in the FDTD scheme is presented.

2.5.1 Perfect Electric and Magnetic Conductors

The boundary conditions at a Perfect Electric Conductor (PEC) are that the tangential components of the E field or normal component of the H field should be zero. In the FDTD implementation, the tangential E field components of the unit cell corresponding to the PEC surfaces are set to zero.

Similarly, for a Perfect Magnetic Wall (PMC), the boundary condition of zero tangential H field or normal E field is imposed by zeroing the tangential H coefficients on the PMC surface.

2.5.2 Dielectric Interfaces

In the FDTD scheme, although permittivities are assigned uniquely to each unit cell, electric components which are located on the edges of the unit cell at the interface of dielectric discontinuity see a discontinuous permittivity. To cope with this problem, when calculating the field components located at the dielectric interface, the cells at the interface are assigned a permittivity which is equal to the average value of the permittivities of the two materials adjacent to it. Interfaces between materials with different permeabilities is handled in a similar manner.

2.5.3 Treatment of Open Boundaries

Many geometries of interest are defined in 'open' regions where the computational domain of interest is spatially unbounded in one or more directions. Since it is impossible to store the fields in an unlimited region in space, suitable boundary conditions which simulate an infinite extension of the computational domain need to be imposed at its perimeter. These boundary conditions are referred to as absorbing boundary conditions (ABC) and have been a subject of numerous investigations in literature [19], [20], [21], [22], [23], [24], [25], [26], [27]. While the techniques range from the simplest approach of eliminating reflections by padding the edge of computational domain with lossy regions [28] to utilizing the fact that waves reflected from Dirichlet and Neumann boundaries are of opposite signs [29], [30], the most common methods are based on asymptotic expansions of the one-way wave equation [19], [21], [31], [22]. Recently, the PML absorber was introduced which has surpassed the performance of all other ABC up to this point [32]. In [47], a detailed discussion of the different ABC's that were examined in literature has been presented. For the FDTD simulations in this work, Mur's 1st and 2nd order ABC's [22] in conjunction with Superabsorbers [27] was used. For some circuits, the PML absorber has been used as well.

2.5.4 Treatment of Source

Historically, the first source used in the FDTD scheme was the plane wave which is commonly used in the modeling of radar scattering problems. A detailed discussion of free space and waveguide incident-wave source conditions as well as lumped circuit load condition is presented in [47].

While the treatment of source or excitation depends on the problem that is being simulated, the source is imposed by forcing specific field components in the computation domain to be known functions of time and space. This very common FDTD source is called the 'hard source'

When using the 'hard source', precaution must be taken to ensure that source is removed from the algorithm after it has decayed exponentially to zero. This is because as time evolves in the FDTD algorithm, the field that is reflected from discontinuities arrives at the source location causing a non physical reflection of these waves. However, this approach cannot be used for continuous source waveforms. Practically, the hard source has been successfully applied for exciting numerical models of waveguides and striplines in 2D and 3D FDTD schemes. However in 1D FDTD simulations, the hard source limits the maximum number of time steps that can be run without spurious reflections [47].

In order to overcome these disadvantages, the 'total field' field formulation has been used. In this approach, the total electric and magnetic field components are decomposed into the incident and scattered fields [22], [33] with the incident field values assumed to be known at all space points in the FDTD mesh. The scattered fields are the unknown fields and FDTD discretized equations are applied with equal validity to the incident, scattered or total field components. To see how this excitation scheme works, consider the following analysis which was presented in [58]:

Consider the following discretized equation which shows the E_x component assuming no field validation in z-direction for a lossless medium:

$$
{}_{\lambda}E^{x}_{l'-1/2,m',n'} = {}_{\lambda-1}E^{x}_{l'-1/2,m',n'} + \frac{\Delta t}{\epsilon_{l',m',n'}} \left(\frac{{}_{\lambda-1/2}H^{z}_{l'-1/2,m'+1/2,n'} - {}_{\lambda-1/2}H^{z}_{l'-1/2,m'-1/2,n'}}{\Delta y} \right) \tag{2.41}
$$

Next, a time dependent term is added to the field component of interest. Denoting this term as Δs, we now obtain the following equation:

$$
\begin{aligned}
{}_{\lambda}E^{x}_{l'-1/2,m',n'} =& {}_{\lambda-1}E^{x}_{l'-1/2,m',n'} + \Delta s \\
&+ \frac{\Delta t}{\epsilon_{l',m',n'}} \left(\frac{{}_{\lambda-1/2}H^{z}_{l'-1/2,m'+1/2,n'} - {}_{\lambda-1/2}H^{z}_{l'-1/2,m'-1/2,n'}}{\Delta y} \right)
\end{aligned} \tag{2.42}
$$

If the circuit allows a conduction current to flow at the position where the source is applied, the source term can be seen as an impressed conduction current given by $\Delta s = \frac{\Delta t}{\epsilon} J_{cz}^{\lambda+1/2}$ On the other hand, if the circuit allows only for a displacement current, this term works as an additional term added to the field component. The modified discretized equation now becomes:

$$
{}_{\lambda}E^{x}_{l'-1/2,m',n'} - {}_{\lambda-1}E^{x}_{l'-1/2,m',n'} - \Delta s = + \frac{\Delta t}{\epsilon_{l',m',n'}} \left(\frac{{}_{\lambda-1/2}H^{z}_{l'-1/2,m'+1/2,n'} - {}_{\lambda-1/2}H^{z}_{l'-1/2,m'-1/2,n'}}{\Delta y} \right) \tag{2.43}
$$

corresponding to the following expression:

$$
\epsilon \frac{\partial E_x}{\partial t} - \frac{\partial s(t)}{\partial t} = \frac{\partial H_z}{\partial y} \tag{2.44}
$$

Thus the term which is added to the field component in this case is the derivative of the waveform that we want to obtain. Hence, in this technique, if the circuit allows for a conduction current term, the desired waveform is added to the field component. If only a displacement current exists, the derivative of the desired waveform is added. In most of the FDTD simulations here, a wideband Gaussian pulse (with nonzero DC content) was used as the excitation of the structures modeled. Other hard sources are the continuous sinusoidal wave function for use in 1D TM structures and a Gabor function which provides zero-dc content for applications in waveguide simulations.

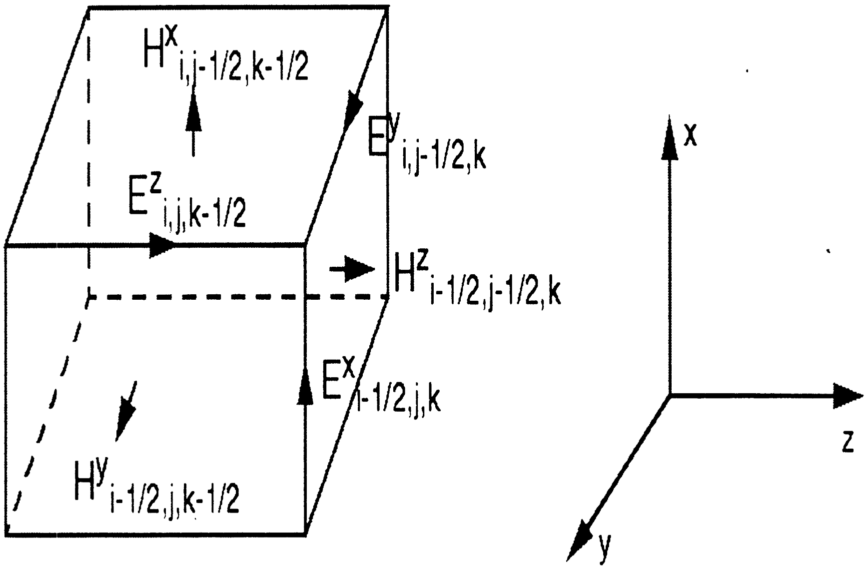

Figure 2.1: FDTD Cell: Field positions

CHAPTER 3

COPLANAR STRIPLINE CIRCUITS AND THEIR CHARACTERIZATION USING FDTD SCHEME

3.1 Brief Overview of Coplanar Circuits

The rapid growth of MIC and MMIC technology in recent years has lead to the extensive use of planar circuits based on planar transmission lines such as microstrip lines, slotlines, coplanar waveguides (CPW) and coplanar striplines (CPS). Among these, CPW, CPS and slotlines can be classified as uniplanar, or *coplanar* circuits, since all the conductors in these structures are in the same plane. In this chapter, CPS characteristics and CPS based microwave circuits has been presented.

Coplanar circuits enjoy several advantages over other non-uniplanar circuits such as microstrip. Some of these arise from 1) the ease in mounting of shunt and series active and passive devices and 2) the elimination of the need for wraparound and via holes to reach the ground plane, thereby reducing the additional parasitics [2]–[3]. Also, these circuits eliminate the need for back metalization, allow the circuits to be wafer probed at millimeter-wave frequencies [4]– [8] and allow circuits to be integrated with solid-state devices on a single surface [1]. The latter is particularly useful for devices such as MESFETS which are also coplanar in nature.

As the application moves to higher frequencies and the size of the substrate becomes critical in triggering parasitic modes and uncontrolled radiation, lines such as CPW and CPS, which show less dependence on wafer thickness, become better candidates. Of these lines, coplanar waveguide has attracted much more attention despite the limitations imposed by its large ground planes and the excitation of parallel plate parasitic modes. The use of many vias to suppress these parasitic modes introduces many difficulties in the design and fabrication, resulting in poor performance and high cost. In view of the above disadvantages, coplanar lines with finite size grounds such as CPS merit more attention.

CPS has the capability to provide excellent propagation [12]. When appropriately designed, it has small discontinuity parasitics and makes efficient use of the wafer area, resulting in lower cost and larger density of circuit functions [13]. Also, it can sustain back metalization without exciting parasitic modes within the range of the operating frequency. Lastly, CPS propagation parameters are independent of substrate thickness beyond a critical value, thereby simplifying heat sinking and packaging, a feature particularly useful in high power applications such as power amplifiers.

The aforementioned advantages suggest that CPS is a strong candidate for planar circuit applications. While Microstrip and CPW lines have been extensively studied, characterized and used, the same cannot be said of CPS lines and circuits. Therefore, in this work, a number of CPS discontinuities have been studied. Based on the results of these studies, a number of CPS circuits have been designed and characterized, thus demonstrating the potential of the interconnect technology.

Figure 3.1 shows the cross section of a Coplanar Stripline. It consists of two strips of width W separated by a slot of width S supported on a thin dielectric substrate of relative permittivity ϵ_r and thickness D. The electric field lines from the strip conductors extend across the slot as shown in Figure 3.1.

3.2 Coplanar Stripline Propagation Characteristics

In literature, a number of methods have been proposed to obtain the propagation characteristics of the CPS. In [2], CPS has been analyzed using Quasi-static (Conformal mapping) and Full-wave techniques (Galerkin's method in the spectral domain). A discussion and comparison of the expressions for the characteristic impedance and dielectric constant of the CPS is provided in [15]. Since these expressions are approximations in principle, they have been used as a design guide in this work. The FDTD technique has been utilized to perform the rigorous full wave analysis in studying the CPS here.

In this section results of the study of Coplanar Stripline dispersion and higher order modes is presented. The study of higher order mode behavior is necessary in order to assess the single-mode operating bandwidth.

Figure 3.2 shows a plot of the normalized propagation constant β/β_o as a function of frequency obtained using 2D-FDTD technique. For a CPS line with D = .03 inch, W = .065 inch, S = .004 inch and ϵ_r = 10.2, there are no higher order modes up to around 9.0 GHz. This has been confirmed by measuring the S-parameters. Smaller line dimensions and thinner substrates can push the cut-off frequency to even higher frequencies thus extending the operating range. For example, measurements on a through line with W = .025 inch, S = .004 inch, D = .01 inch and ϵ_r = 10.5 have shown that there is no onset of higher order modes up to 40 GHz.

3.3 Coplanar Stripline Discontinuities

Microwave circuits invariably consist of transmission lines with different types of transmission discontinuities. While some discontinuities are undesirable yet unavoidable , others are deliberately introduced into the circuit to perform the desired electrical function. In either case, characterization of discontinuities is essential in designing and analyzing the performance of circuits. A transmission line discontinuity can be represented as an equivalent circuit at some point on the line. Depending on the discontinuity, the equivalent circuit may be a simple shunt or series element, or more generally, a T- or Π- network. The values of the lumped elements depend depend on several factors, such as the geometrical parameters of the line, the type and geometry of the discontinuity, frequency of operation, etc. A thorough study and characterization of the transmission line discontinuities is essential in order to either compensate for their effects or to exploit them suitably for microwave circuit design as the case may be.

A number of CPS discontinuities have been characterized and studied in order to understand the applicability/suitability of CPS based microwave circuit [13], [16]. In the following sections results of the study of some of these are presented.

3.3.1 (a) Narrow Transverse Slit and a Symmetric Step in the CPS Strip Conductor

A symmetric narrow slit of width B and depth A in the CPS strip conductor is shown in Figure 3.3. The slit is modeled as a lumped inductor L located between the planes P1 - P1' and P2 - P2' in series with the line. The value of the inductance is determined from the discontinuity S-parameters of the circuit which are de-embedded from the measured S-parameters of the circuit using the NIST de-embedding software program [14].

Figures 3.4 and 3.5 show plots of the de-embedded and FDTD modeled scattering parameters as a function of frequency for a slit of depth A = 531.9 μm and width B = 180.3 μm. Figure 3.6 shows the value of the series inductance as a function of the slit depth A when the width B is held constant at 180.3 μm. As expected, the inductance increases with the slit depth. It is worth noting at this point that for small values of the slit width, the discontinuity can be accurately modeled as an inductance. The slight difference between the measured and FDTD results in Figures 3.4, 3.5 and 3.6 can be attributed to the difference in dimensions between the fabricated structure and the FDTD model. The dimensions of the structures modeled by the FDTD were rounded off and approximated so as to minimize the mesh size and memory requirements for circuit simulations. Using the exact dimensions of the circuit can lead to prohibitively large memory requirements when using the uniform grid adaptation of the FDTD scheme.

However, if the slit depth is kept constant and the slit width B is varied, the discontinuity can no longer be modeled purely as an inductive element. For larger slit widths, this discontinuity, now a CPS-step, needs to be modeled as a π-equivalent LC circuit where the capacitance, C, is the fringing capacitance and the inductance L is the series inductance. Figure 3.7 plots the lumped fringing capacitance C and the series inductance L for a CPS step as a function of the step width at a frequency of 6 GHz for a fixed depth A of 533.4 μm. These results have been obtained from the de-embedded measured S-parameters [1]. As expected, the capacitance is small initially, increases with step width and eventually saturates.

---

[1] The measured scattering parameters for a typical slit-step have been validated using the FDTD technique and are presented in Figures 3.4 and 3.5. Hence, the FDTD modeling was not repeated for the remaining step widths. Consequently Figure 3.7 excludes the FDTD modeled equivalent lumped circuit element values

3.3.2 (b) CPS Right Angle Bend

A CPS right angle bend is shown in Figure 3.8. Several CPS bends have been fabricated with slot width ranging from 110 μm (4.33 mils) to 230 μm (9.06 mils) and the strip width fixed at 762 μm (30 mils). In all cases it was seen that de-embedded measured S-parameters as well as FDTD show the reflection to be of the order -20 dB or lower. Figure 3.9 presents the results for a typical right angle bend in which the reflection coefficient is below -20 dB. Hence it can be concluded that compensation of the bend to improve VSWR is not required. Although Figure 3.9 indicates low reflection losses for measured as well as modeled cases, it can be seen that the return loss in case of FDTD modeling is lower. It is also seen that the measured magnitude of S21 is slightly lower than the S21 obtained by FDTD modeling. These differences can be attributed to the calibration accuracy of the measured results and to the fact that FDTD scheme adopted here does not take losses into account.

3.3.3 (c) CPS T-junction

A CPS in-phase T-junction is shown in Figure 3.10. The fact that a right angle bend does not contribute to significant parasitics has been favorably used in the design of this CPS T-junction where the line exhibits very low parasitics. The measured and FDTD modeled magnitude of S11, S21 and S31 as a function of frequency is shown in Figure 3.11. As seen from the figure, power is almost equally divided between the output ports 2 and 3. It was also observed that the phase of S31 and S21 is equal, as expected. From Figure 3.11 it is seen that there is a very good agreement between the measured and FDTD modeled power coupled to the two output ports.

3.4 Coplanar Stripline Filters

The results on CPS discontinuities above indicate potential applications in the emerging wireless communications industry in general, and in the design of low cost uniplanar microwave circuits such as filters, mixers and antennas in particular. This has been demonstrated by fabricating several band pass, band stop and lowpass filters using CPS discontinuities [?], [?]. The performance of a few of these filters is presented in the following sections. Here the measured filter response is compared with the results obtained by modeling the filter using the FDTD technique.

CPS filters have several unique features and advantages. Their uniplanar construction allows ease of fabrication. Also, these filters use series resonating elements which are fabricated within the 50Ω strip conductors and, hence, are extremely compact when compared to microstrip filters. In addition, they do not require bond wires and air bridges to suppress higher order modes at discontinuities, resulting in simpler designs when compared to conventional coplanar waveguide (CPW) filters.

3.4.1 (a) CPS Bandstop Filters

The configuration of a CPS spur-slot bandstop filter is shown in Figure 3.12. The spur-slot is convenient to use when W is large and S is small. It can be modeled as a short circuit stub of length L = $\lambda_{g(cps)}/4$ in series with the main line. At resonance, the stub prevents the flow of RF power to the load. The measured and modeled S11 and S21 for the geometry is shown in Figure 3.13.

On the other hand, the spur-strip is convenient to use when W is small and S is large and can be modeled as two open circuit stubs each of length L1 = $\lambda_{g(cps)}/4$ in parallel with the main line. Figure 3.14(a) shows the configuration of a CPS spur-strip bandstop filter with a taper on either ends. This is the configuration for which measurement has been performed. Figure 3.14(b) shows the configuration used to perform the FDTD modeling. Tapers were included in the measurement to accommodate a ground signal RF probe of 254 μm (10 mil) pitch. However, while simulating the results using FDTD, the tapers were eliminated due to memory constraints. Figure 3.15 shows the magnitude of measured and modeled S-parameters for the spur-strip filter. From Figures 3.13 and 3.15 we see that there is a good agreement in the measured and modeled resonance frequency for both the filters. However, Figure 3.15 shows a slight difference between the measured and modeled S21 for the spur-strip filter. This can be attributed to the tapers being excluded in the FDTD modeling. It is interesting to note that the spur-strip filter has a narrower bandwidth compared to the spur-slot filter indicating that the strip filter has a higher quality factor (Q) compared to the slot filter. As a point of interest, it is worthwhile mentioning that a spur-slot with 4 slots (with the two extra slots being a mirror image of the previous two) has the same resonance as the spur-slot structure in Figure 3.12 but a broader bandwidth (lower Q).

3.4.2 (b) CPS Lowpass and Bandpass Filters

The schematics of CPS lowpass (LP) and bandpass (BP) filters are shown in Figures 3.16 and 3.18 respectively. The filters consist of five sets of series stubs spaced 0.25 $\lambda_{g(cps)}$ apart where $\lambda_{g(cps)}$ is the guide wavelength in the CPS at the cut off frequency, f_c, of the lowpass filter and at the center frequency, f_o, of the bandpass filter respectively. Both the LP and BP filters have been fabricated on an RT/Duroid 6010 substrate of thickness 0.03 inch and $\epsilon_r = 10.2$. The design guidelines for the circuit elements are summarized as follows:

(1) **LP filter:** $L_1 = 0.062\ \lambda_{g(cps)}$, $L_2 = 0.125\ \lambda_{g(cps)}$, W = 0.065 inch, S = 0.004 inch, G = 0.008 inch.

(1) **BP filter:** L = 0.5 $\lambda_{g(cps)}$, W = 0.070 inch, S = 0.0035 inch, G = 0.008 inch.

The measured and FDTD-modeled insertion loss (S21) and return loss (S11) of the LP and BP filters are shown in Figures 3.17 and 3.19 respectively. Both filters exhibit excellent characteristics. The discrepancies between the measured and FDTD-modeled results for the filters are attributed to the zero-loss assumption incorporated in the FDTD, in addition to coarse FDTD gridding.

3.5 Conclusion

CPS as a transmission has all the advantages that other coplanar or uniplanar transmission lines enjoy. Some of these advantages include easy mounting of shunt and series active and passive devices, elimination of the need for back metalization, hence, allowing circuits to be wafer probed at millimeter-wave frequencies, elimination of wraparound and via holes to reach the ground plane and integration of microwave circuits with solid-state devices on a single surface. In addition, CPS makes efficient use of wafer area while maintaining excellent propagation and creating small discontinuity parasitics. In view of these advantages, CPS is a strong candidate in the design of microwave circuits. As a prelude to the study of the feasibility of CPS based circuits, a number of CPS discontinuities such as CPS slit, CPS, step, CPS right angle bend and CPS T-junction have been characterized as a function of both frequency and geometry. Study of these discontinuities has indicated several potential applications of CPS in the design of low cost circuits. This has been demonstrated by the design and characterization of several CPS circuits such as bandstop, bandpass and lowpass filters. The excellent performance of these circuits stands proof to the efficacy of CPS as a transmission line in the design of microwave circuits.

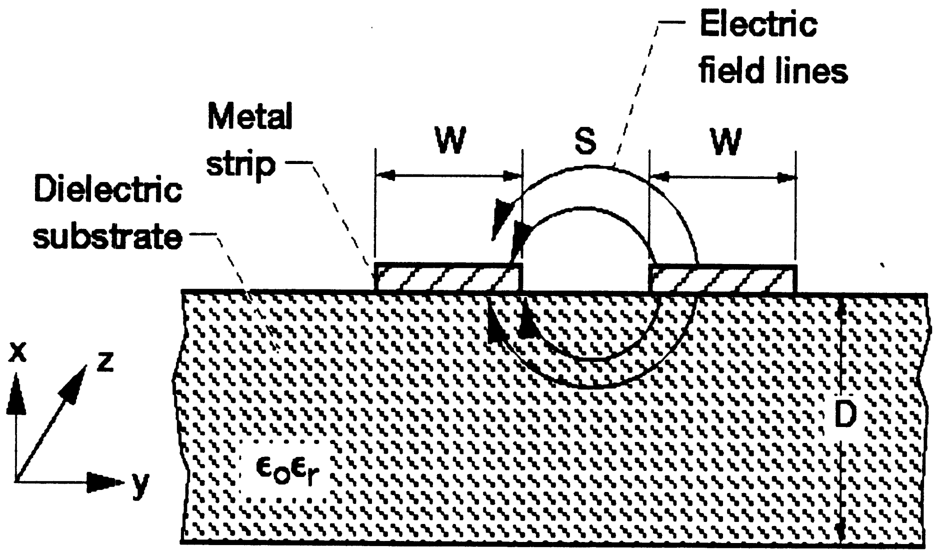

Figure 3.1: Cross Section of CPS

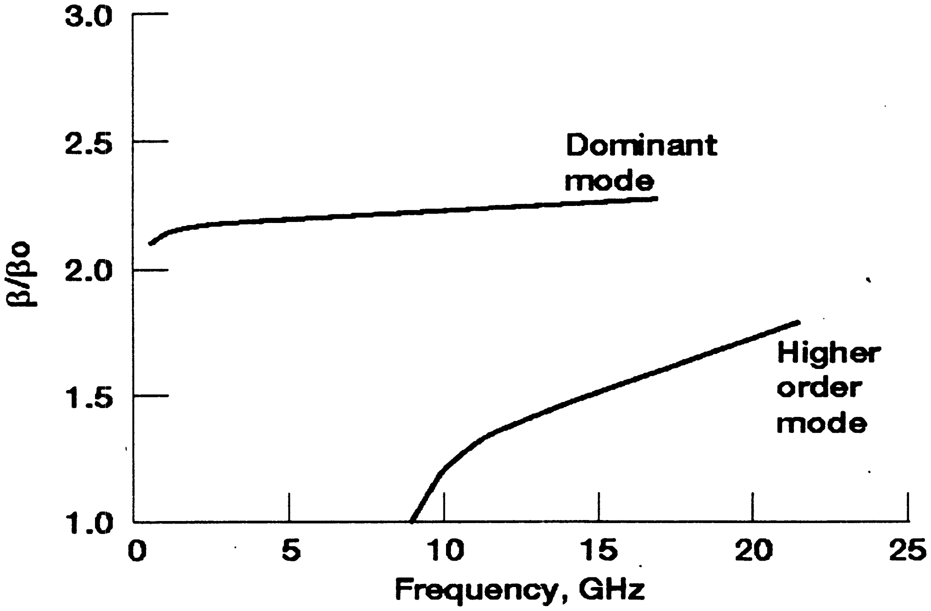

Figure 3.2: CPS Dispersion and Higher Order Modes.

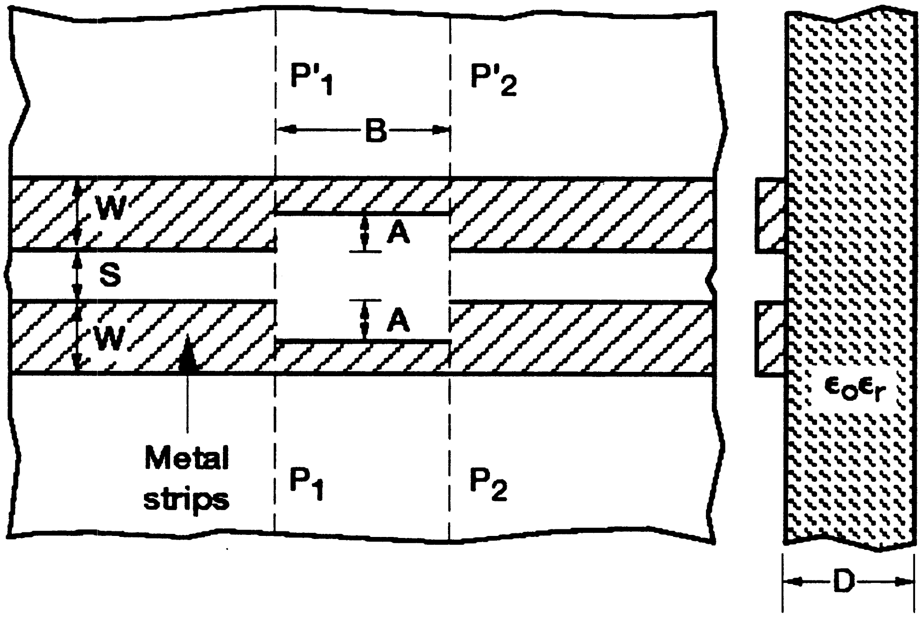

Figure 3.3: Symmetric transverse slit and a step in the CPS Strip conductors.

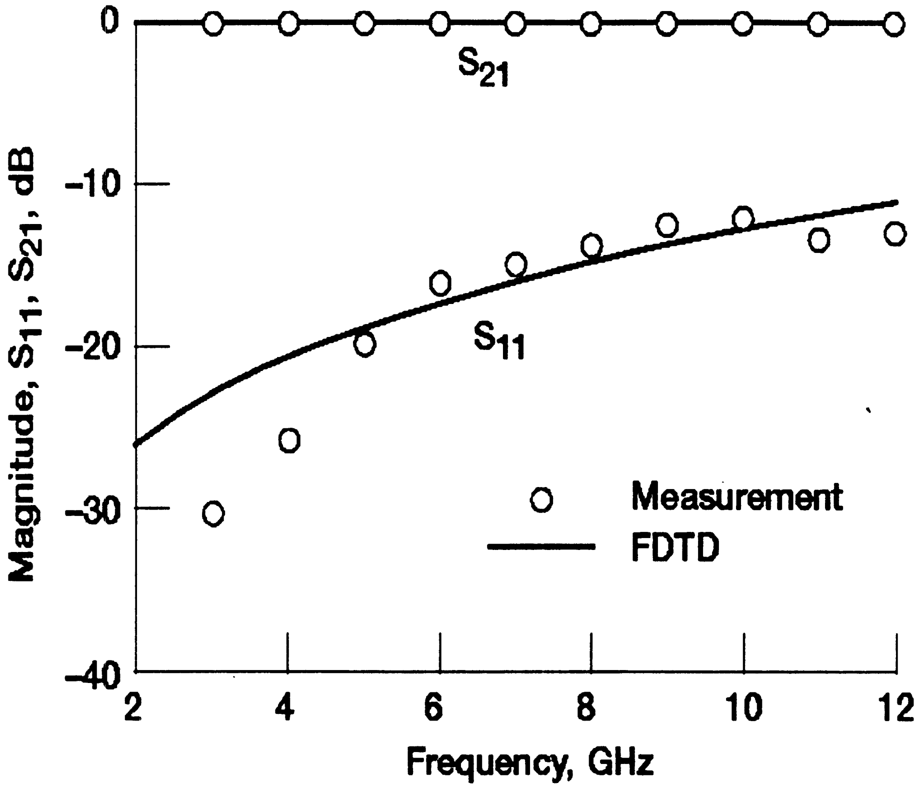

Figure 3.4: Experimental and FDTD modeled magnitude of S11 and S21 for CPS slit; A = 531.9 μm, B = 180.3 μm.

MISSING
PAGE

MISSING
PAGE

MISSING
PAGE

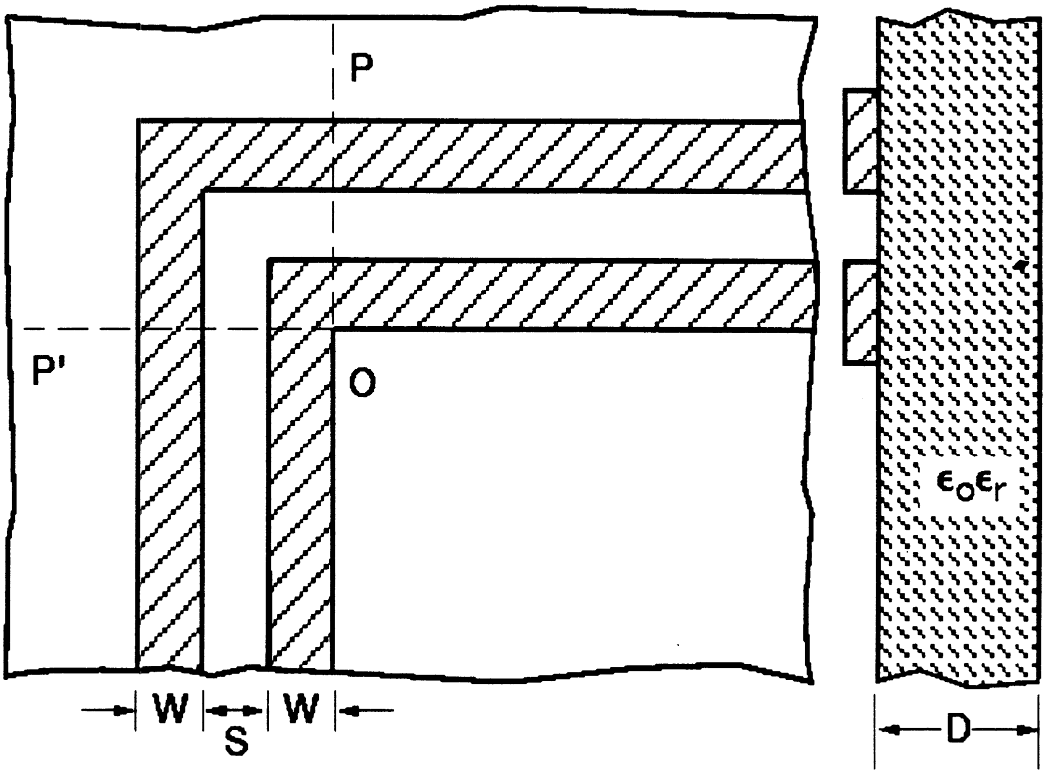

Figure 3.8: CPS Right Angle Bend.

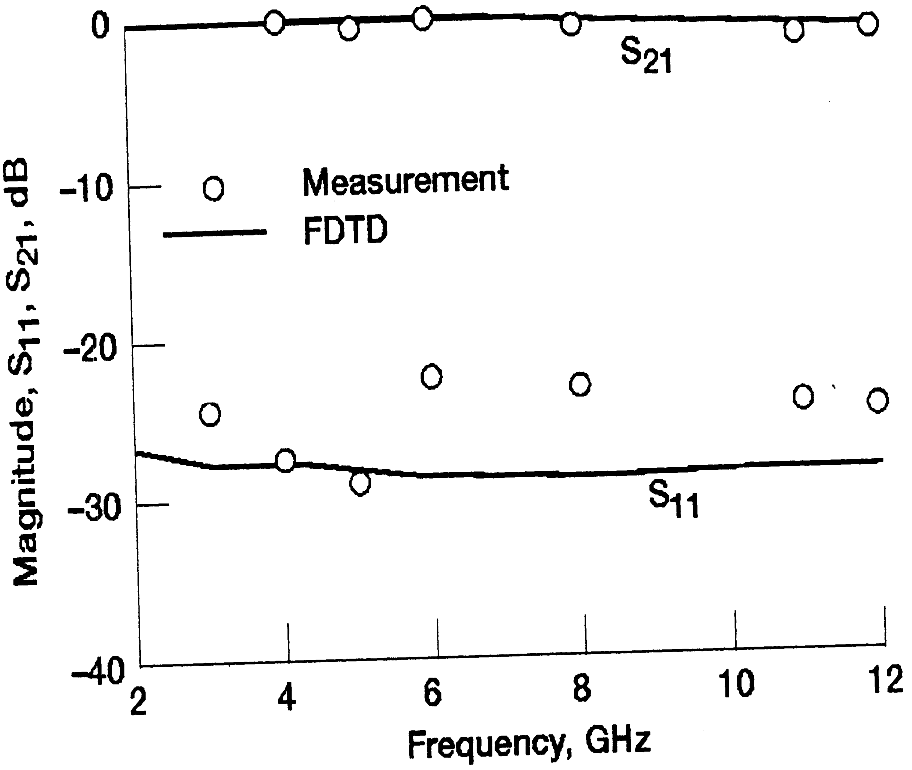

Figure 3.9: Experimental and FDTD modeled magnitudes of S11 and S21 as a function of frequency for CPS bend; S = 101.6 μm.

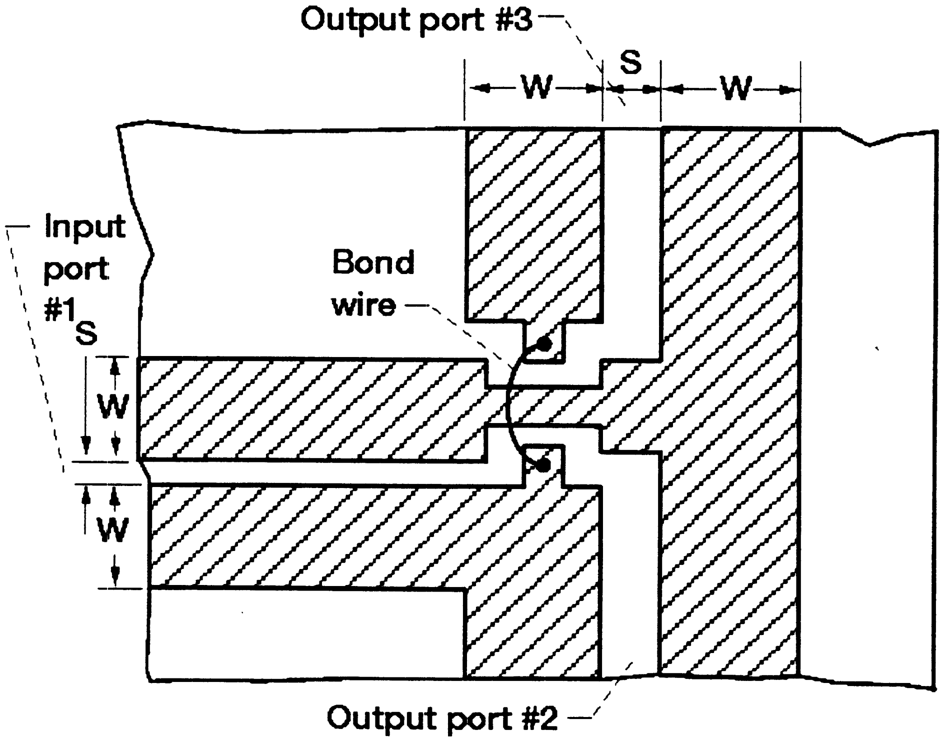

Figure 3.10: CPS T-junction.

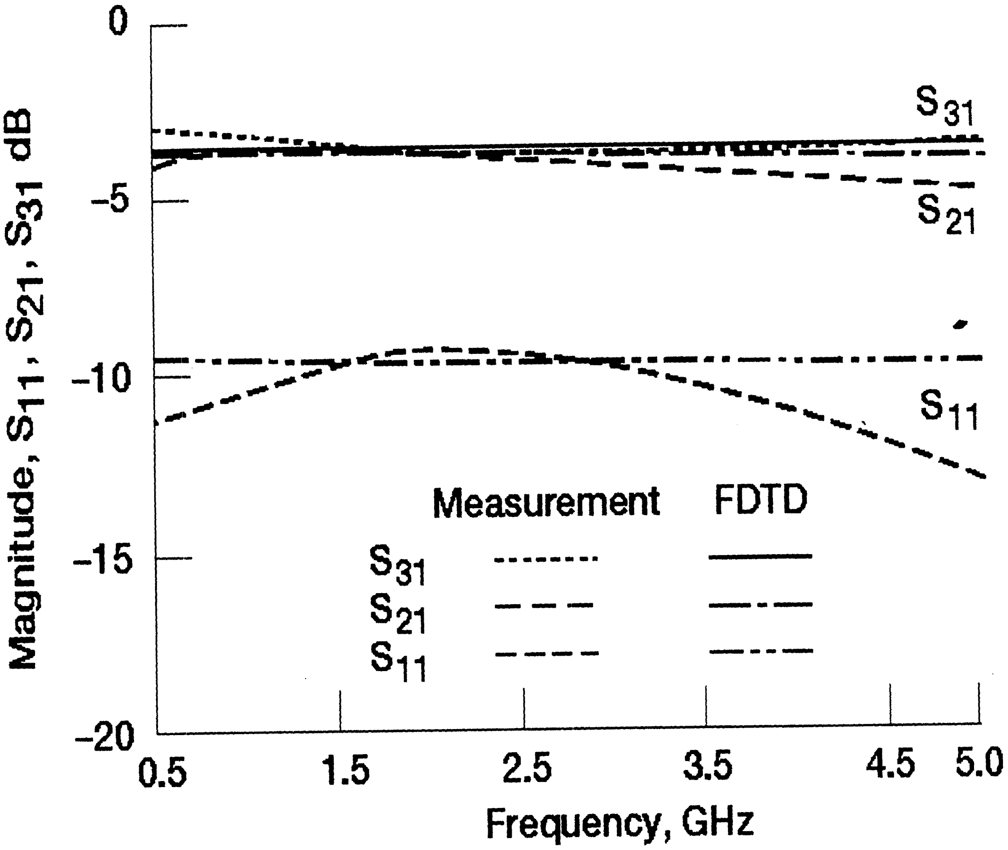

Figure 3.11: Experimental and FDTD modeled magnitudes of S11, S21 and S31 for a T-junction.

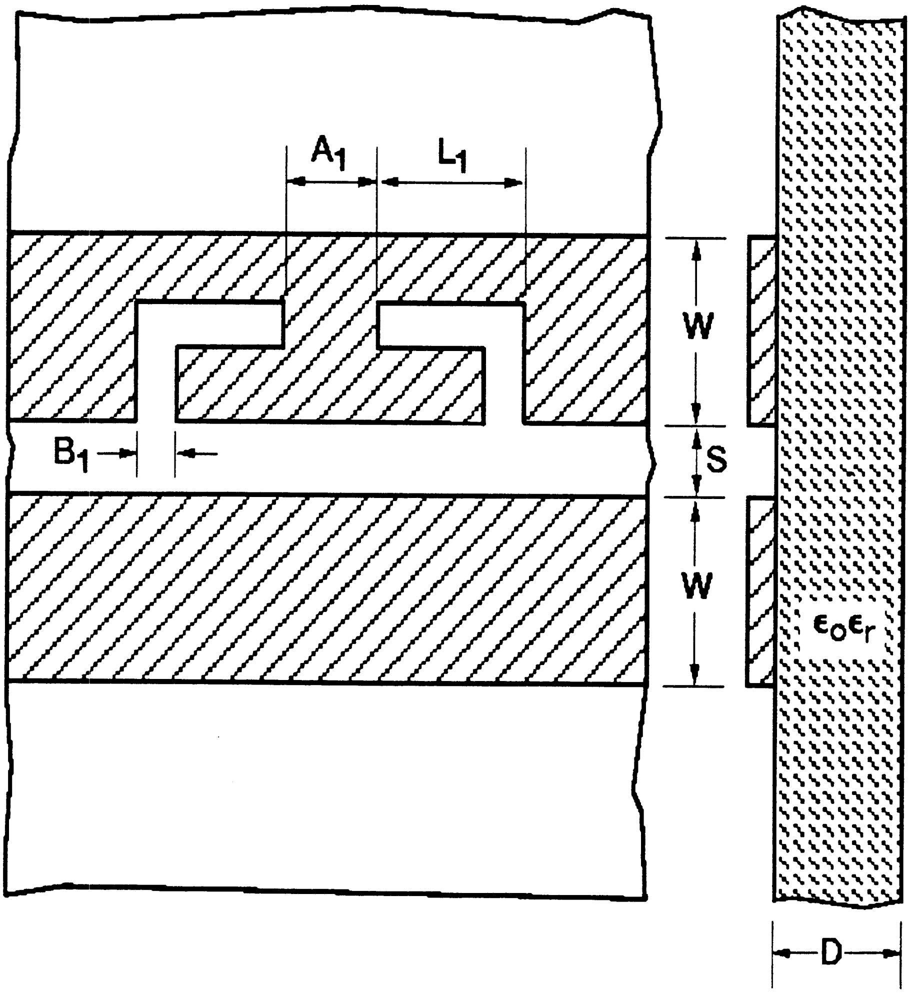

Figure 3.12: CPS Spur-slot Bandstop filter.

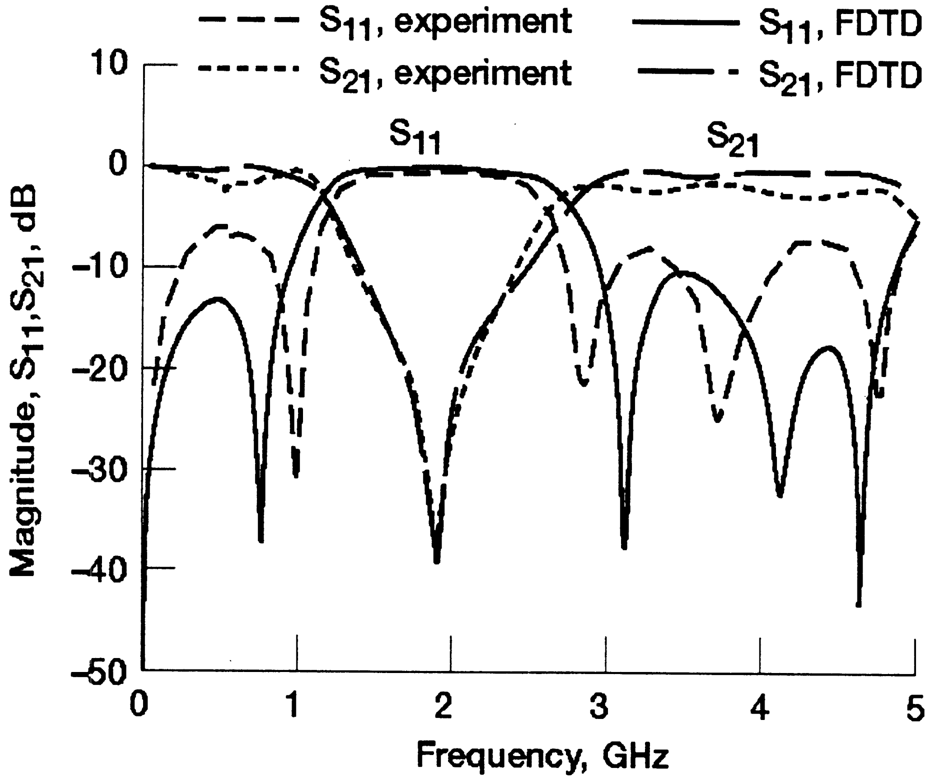

Figure 3.13: Experimental and FDTD modeled magnitudes of S11 and S21 for a spur-slot bandstop filter; A1=762 μm, B1=254 μm and L1=16.256mm.

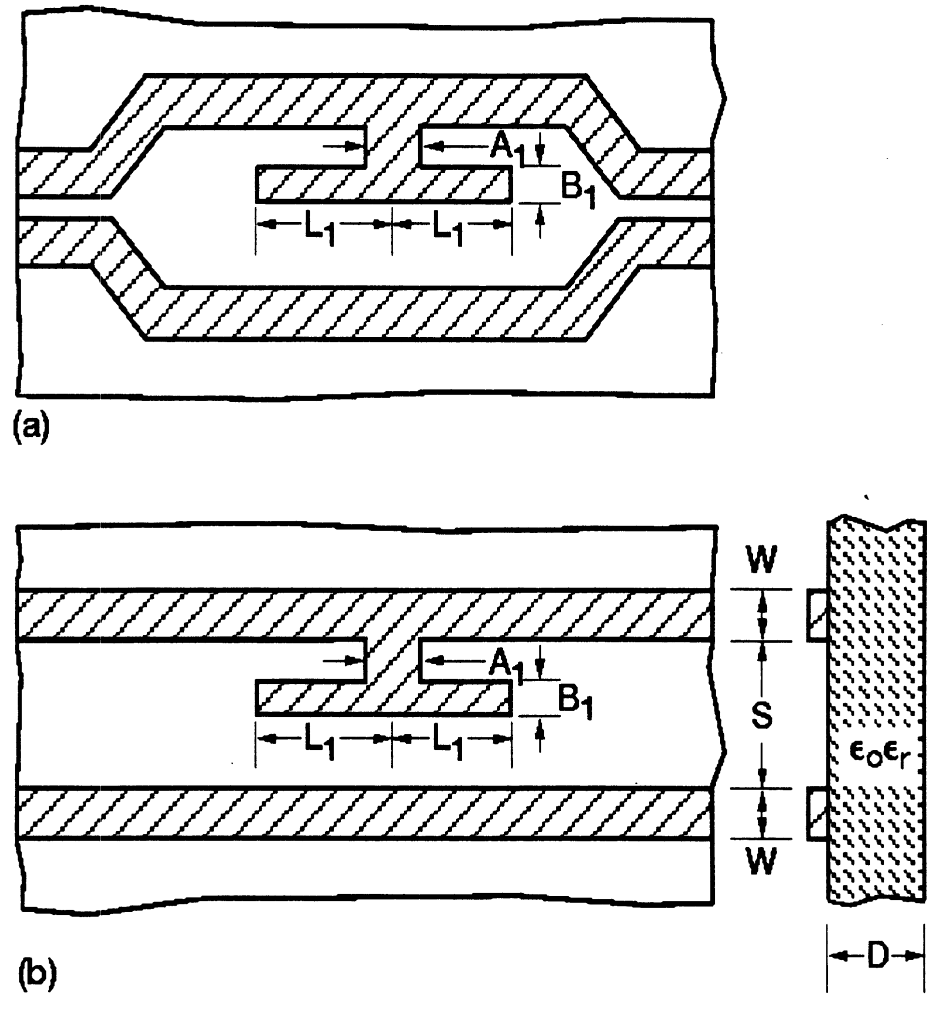

Figure 3.14: CPS Spur-strip Bandstop filter: (a) Measurement (b) FDTD modeling.

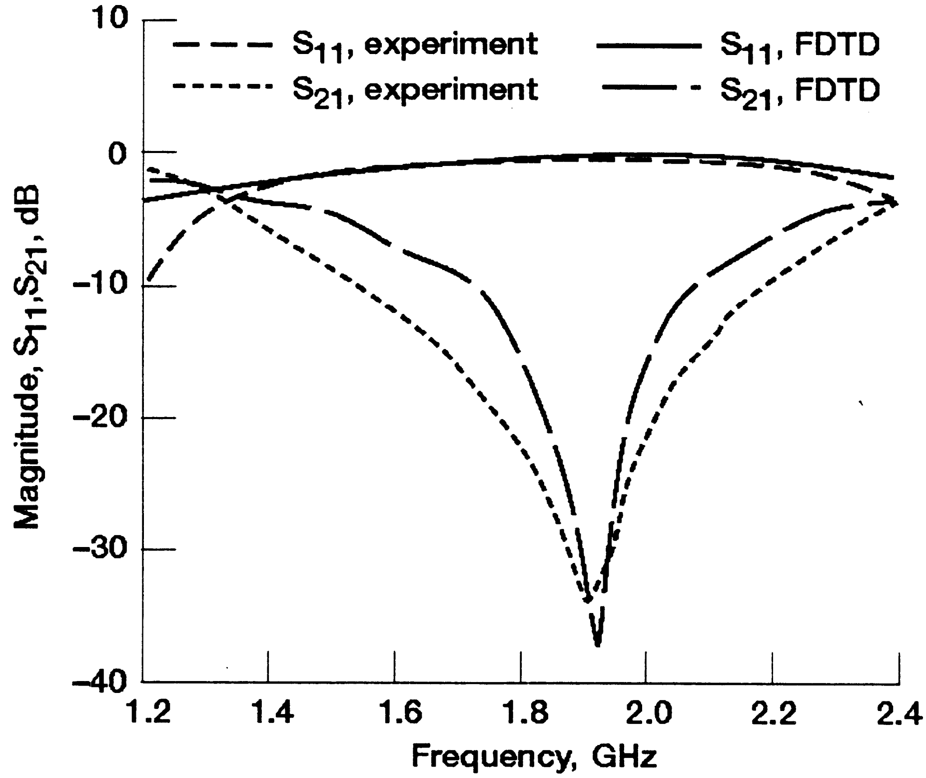

Figure 3.15: Experimental and FDTD modeled magnitudes of S11 and S21 for a spur-strip bandstop filter; A1=254 μm, B1=254 μm, L1=16.129mm and S=762 μm .

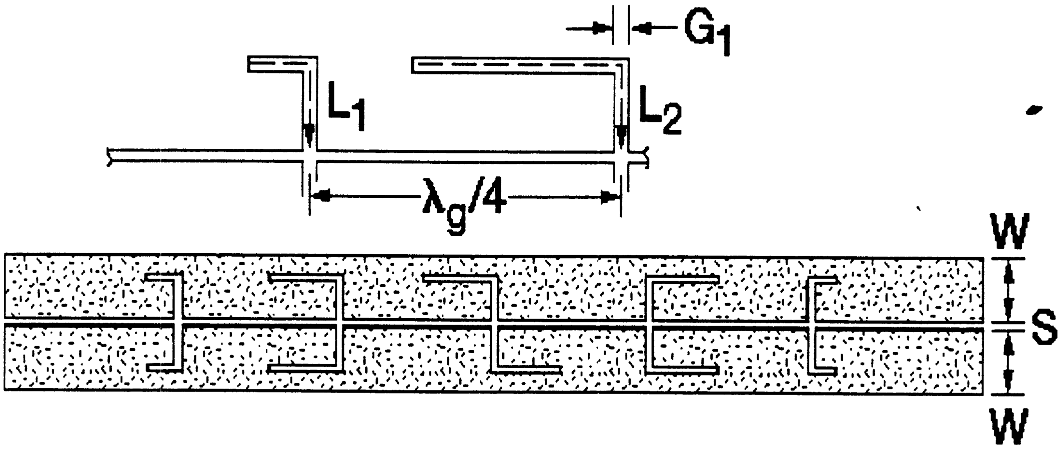

Figure 3.16: CPS Lowpass Filter.

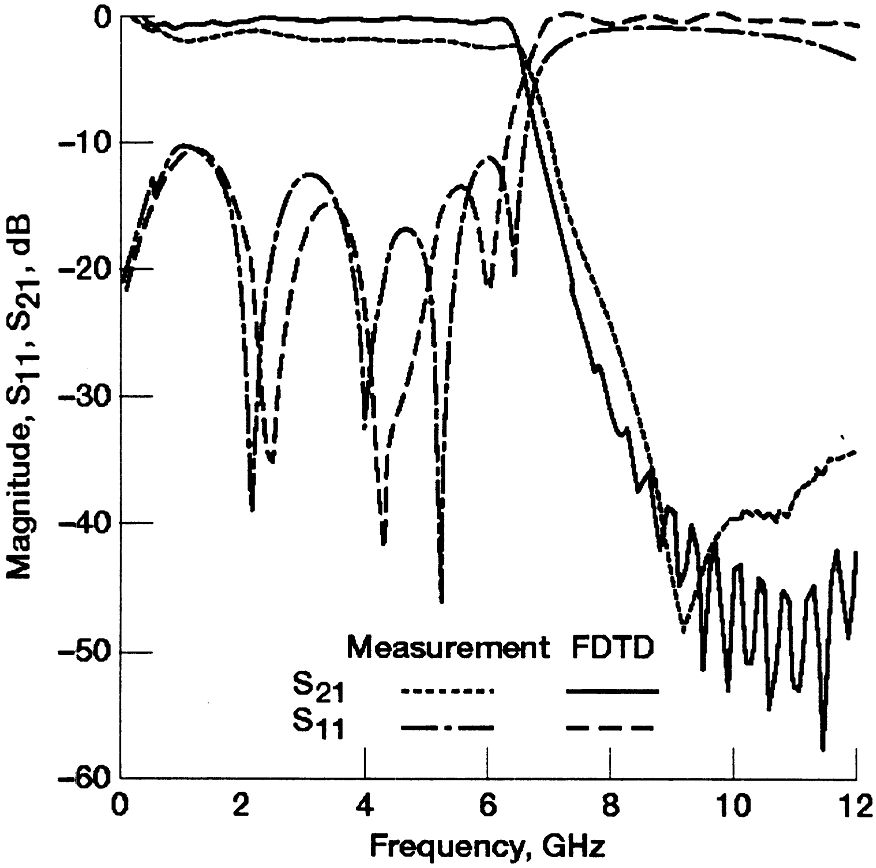

Figure 3.17: CPS Lowpass Filter Characteristics.

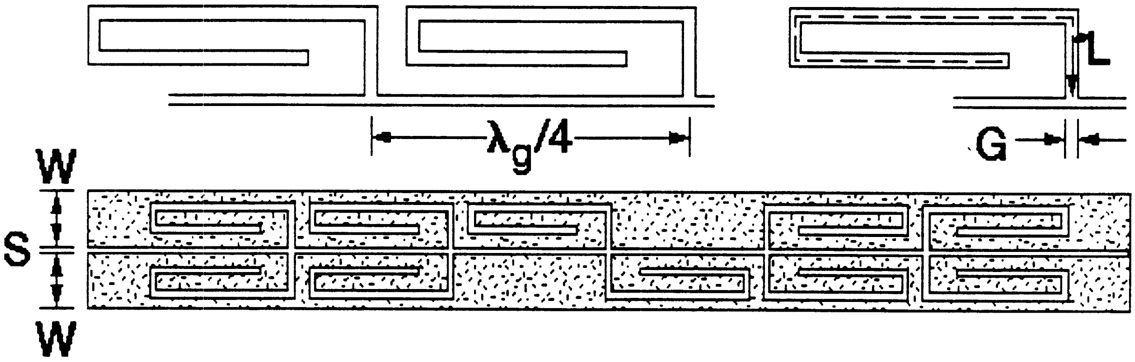

Figure 3.18: CPS Bandpass Filter.

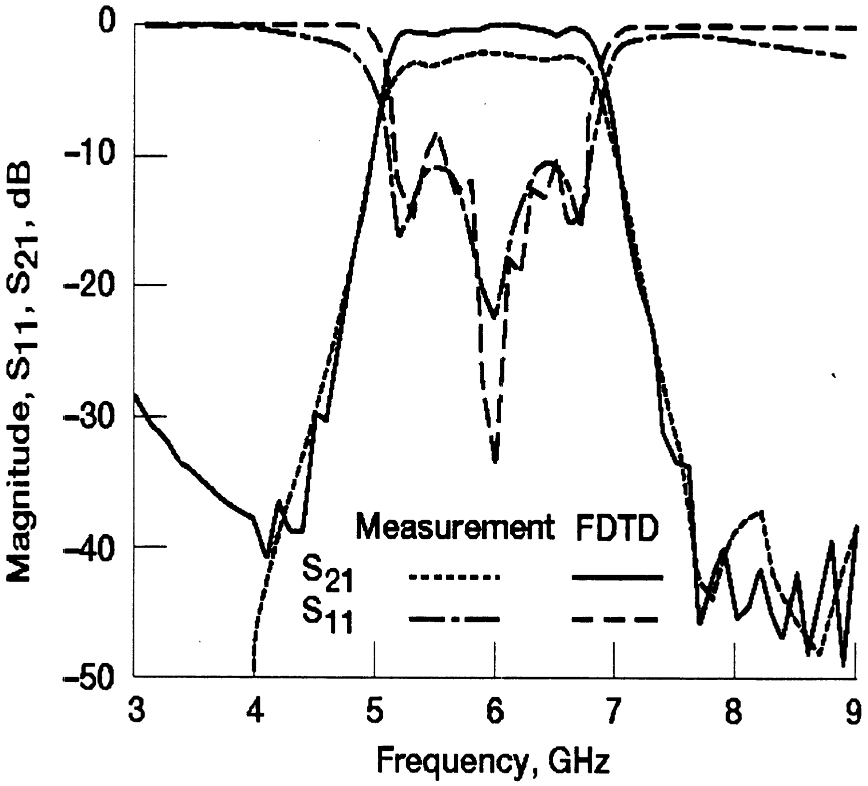

Figure 3.19: CPS Bandpass Filter Characteristics.

CHAPTER 4

NOVEL CIRCUITS FOR THREE DIMENSIONAL (3D) MICROWAVE CIRCUIT INTEGRATION AND THEIR ANALYSIS USING FDTD

4.1 Introduction

In chapter 3, the Coplanar Stripline (CPS) was introduced. Several CPS discontinuities were characterized and some novel CPS filters which emerged from the study of these discontinuities were characterized using the FDTD scheme and compared with measured results. In this chapter, novel circuit components based on minor variations of the CPS, which are suitable for applications in microwave circuit integration are presented. To begin with, the Micro-Coplanar Stripline, it's applications and characteristics are presented. This is followed by Coplanar Stripline based 3D interconnects for applications in microwave circuit integration. The FDTD scheme is used to perform the theoretical characterization of these circuits.

4.2 Micro-Coplanar Striplines (MCPS)

In recent years, wireless communications for audio, video and data transmission have witnessed tremendous growth. The essential requirements for these wireless systems are low cost for affordability and small size for portability. One approach in addressing low-cost requirements is to combine the available digital silicon processing technology with the high frequency silicon germanium device technology. The size and complexity issues that arise with this integration can be addressed by investigating novel integration techniques which rely on multilayer 3D transmission lines constructed using very thin glass or silicon dioxide layers. With appropriate interconnect technology available, customized innovative integrated packages can be realized by micromachining the silicon wafer [82]. These techniques, when realized, have the potential to meet the ever increasing demand to lower the cost and size of circuit components.

This chapter presents a new transmission line, the Micro-Coplanar Stripline (MCPS) [83]. Fig. 4.1 shows the geometry of MCPS. The MCPS is fabricated on a high resistivity silicon (HR Si) wafer and has a very thin spin-on-glass (SOG) as a spacer layer separating two strip conductors. MCPS has several advantages some of which are discussed here: 1) The dimensions of the strip conductors as well as the spacer layer are of the order of a few microns for a 50 Ω transmission line. Thus the transmission line is very compact, resulting in small amount of parasitics when combined with active devices. 2) The strip conductors are on two levels, thus making vertical as well as horizontal integration possible. This can be useful in applications such as mixers using broad-side couplers with tight coupling and wide bandwidth. MCPS has definite advantages over traditional lines such as microstrip in vertical integration because the ground plane in the MCPS can follow the signal line, eliminating the need for via holes in interconnects. 3) The spacer layer is very thin, hence making it possible to realize large capacitances in a small area. This feature is very desirable in the design of compact lowpass and bandpass filters. 4) The two strip conductors form a balanced line, making the MCPS an ideal line for feeding integrated antennas, such as, patches, bow-ties and dipoles. 5) MCPS offers wide design flexibility - small variations in the geometry lead to a very wide range of propagation characteristics.

Details of the fabrication process of the MCPS are presented in [84]. In the following sections, the characteristics of the MCPS which make it attractive for circuit integration applications are presented. In particular, the characteristic impedance (Z_o) and effective dielectric constant (ϵ_{eff}) is presented for a range of parameters of the MCPS, such as, strip width (W), overlap/separation (S) and conductor thickness has been presented. The 2D-FDTD technique scheme discussed in section 2.3, chapter 2 for a lossless medium has been used to obtain these propagation characteristics.

4.3 FDTD Modeled Propagation Characteristics of MCPS

To obtain the characteristic impedance (Z_o) and effective dielectric constant (ϵ_{eff}), the FDTD technique has been used. These propagation characteristics were studied for a range of parameters of the MCPS including the stripwidth (W), separation/overlap (S), SOG thickness (D_1) and thickness of the conductor. In [83], Z_o and ϵ_{eff} are presented for two wide lines of width (W) 135 μm and 94.5 μm. These results are also summarized in tables 4.1 and 4.2 respectively.

From Tables 4.1 and 4.2, it can be seen that for identical separation/overlap between the lines, as the linewidth decreases, Z_o increases. It can also be seen from the two tables that the MCPS lines can be designed to have a wide range of characteristic impedances. However, for integration circuit technology, lines with much smaller dimensions are required.

Table 4.1: Z_o **and** ϵ_{eff} **of SOG-on-Silicon MCPS:** D_1 **= 2.5**μ**m,** D_2 **= 400**μ**m, W = 135**μ**m**

Overlap S (μm)	Z_o (Ω)	ϵ_{eff}
+27.0	10.7	3.49
+13.5	14.0	3.67
0.0	22.4	4.02
-13.5	51.2	5.61
-27.0	59.0	5.89

In this section, the characteristics of MCPS lines with smaller dimensions are presented.

Fig. 4.7 shows Z_o as a function of separation/overlap between the MCPS conductors for a fixed stripwidth (W) (10μm), SOG thickness (D_1) of (1.35 μm) and conductor thickness of (0.45 μm). Fig. 4.7 shows the ϵ_{eff} for the same geometry. As seen from Figs. 4.7 and 4.7, by making small variations to the parameters involved, a very wide range of propagation characteristics can be obtained.

To obtain the results of Figs. 4.7 and 4.7, the conductor thickness was taken into account. This is because when the SOG layer (D_1) is very thin, the effect of conductor thickness on the propagation characteristics is significant. This can be seen in Table 4.3 which shown the characteristic impedance of an MCPS line with and without taking the conductor thickness into account for W =10μm, D_1 = 2.40μm and conductor thickness of 0.8μm. From this table it can be seen that the conductor thickness makes a significant difference to the characteristic impedance for thin layers of the SOG as expected.

Also, comparing the characteristic impedances of lines with separations 0, 2 and 4 μm in Table 4.3 and Fig. 4.7, it can be seen that as the thickness of the SOG increases, the

Table 4.2: Z_o **and** ϵ_{eff} **of SOG-on-Silicon MCPS:** $D_1 = 2.5\mu m$, $D_2 = 400\mu m$, **W =** $94.5\mu m$

Overlap S (μm)	Z_o (Ω)	ϵ_{eff}
+27.0	11.1	3.40
+13.5	14.6	3.59
0.0	23.9	3.94
-13.5	58.4	5.50
-27.0	66.6	5.79

characteristic impedance increases.

4.4 Applications of MCPS

As mentioned earlier, the MCPS an ideal line for feeding integrated antennas. This was demonstrated in [83] where an MCPS-Microstrip transition and an MCP-fed Patch antenna are presented. Also, in [84], an integrated Slot Antenna with Electromagnetically Coupled MCPS Feed is presented. These examples demonstrate the tremendous potential of MCPS circuits to provide extremely compact and low cost circuits with wide design flexibility.

4.5 Novel CPS based 3D Interconnects for Applications in Microwave Circuit Integration

4.5.1 Introduction

Recently, Microwave and RF integrated circuits (ICs) based on Silicon/ Silicon germanium device technology has emerged as a viable alternative to ICs based on III-V semi-

Table 4.3: Z_o **of MCPS with and without accounting for conductor thickness (.8μm) :D$_1$ = 2.4μm, D_2 = 400μm, W = 10.0μm**

Overlap S (μm)	Z_o (Ω) without conductor thickness	Z_o (ga) with conductor thickness
+0.0	79.24	61.51
+2.0	62.23	45.16
+4.0	49.46	35.70

conductor device technologies for wireless applications. The applications have experienced an exponential growth during the past few years. Current state-of the art digital ICs are also based on silicon technology and have the potential to be monolithically integrated with the above analogue ICs. Therefore it is apparent that future generation of silicon analog circuits would have integrated digital control functions to enable them to make intelligent decisions. These advanced silicon mixed signal ICs would require efficient interconnects to allow combining different transmission media, such as, Coplanar Stripline (CPS) and Coplanar Waveguide (CPW) for maximum design flexibility. In addition, they are useful for enhancing packing density in the vertical direction as in small hand held communication devices. The interconnects have to be small in size for low parasitic coupling capacitances, and simple to fabricate for high yield and low manufacturing cost.

In this section, several new design concepts for 3D interconnects on an HR silicon wafer are presented. The 3D interconnects constitute very small sections of CPS at two levels connected by metal filled vias and separated by a thin layer of spin-on-glass (SOG). CPS has the advantages of eliminating backside processing due to it's uniplanar construction, and greatly simplifying vertical integration by the use of metal filled vias. In addition, CPS being a slot type of transmission line allows easy integration of other transmission media, such as, slotline, CPW with finite width ground planes and micro-CPS [83] for greater design flexibility. The SOG has the advantage of low dielectric constant ($\epsilon_{r1} = 3.1$) and hence low parasitic coupling capacitance. The SOG also planarizes the circuits and this facilitates vertical integration [83]. The HR silicon wafer ($> 3000\Omega - cm$) has the advantage of lowering the signal attenuation in addition to improving the isolation between adjacent circuits.

The fabrication process of these interconnects and the performance characterization of some of these interconnects is presented in [85]. In the following section, the CPS vertically interconnected overpass with a crossover is presented.

4.5.2 CPS Vertically Interconnected Overpass with Crossover:

A CPS vertically interconnected overpass with a crossover on a HR silicon wafer ($\epsilon_r = 11.7$) of thickness $h = 400\mu m$ is shown in Fig. 4.7 In this interconnect, the CPS strip width $W_1 = W_2 =$ W and the separations $S_1 = S_2 =$ S are chosen such that the characteristic impedance $Z_{o(CPS)}$ is 50Ω. The thickness and dielectric constant of the SOG layer are h_1 and ϵ_{r1} respectively. The vertical interconnection between the first and the second level CPS conductors are provided by a pair of circular metal filled vias. Each via in a pair is symmetrically located on the strip conductor and has a diameter d. A via pair is designed as a small section of a vertical balanced transmission line with characteristic impedance $Z_{o(via)} = 50\Omega$. The $Z_{o(via)}$ is related to the diameter d, separation between vias in a pair S_2 and the dielectric constant of the medium surrounding the via ϵ_{r1} through the expression, $Z_{o(via)} = (60/sqrt(\epsilon_{r1}))Cosh^{-1}(N)$, where $N = 0.5[(2S_2/d)^2 - 2]$. The probe pad at the input and output for the characterization with microwave wafer probes is typically about

$100\mu m \times 100\mu m$ in size.

In order to study the performance of this interconnect, the scattering (S) parameters were computed using the FDTD scheme and they are shown in Fig.5. The computed S parameters for the overpass alone indicate that the insertion loss, (S21) is negligible and that the return loss (S11) is about -28 dB. The computed S parameters for the overpass with a crossover shows that the insertion loss is still very small. However, S11 has increased from -28dB to -12dB. This increase in S11 can be offset by providing a step compensation as shown in Fig. 4.7 Simulations with the step compensation are in progress. Computed S31 shows that the coupling between the overpass and the crossover is less than -40dB.

4.6 Conclusion

New 3D interconnect technology suitable for applications in microwave and RF integrated circuits has been proposed. Small sections of Coplanar Striplines connected by metal filled vias and separated by a thin layer of spin-on-glass have been used to realize a variety of broadband high performance circuits. This technology yields small sized interconnects which are simple to fabricate. In addition, the MCPS stuctures which offer wide design flexibility with very small changes in circuit parameters while maintaining small dimensions have been presented.

4.7 Comments on the Computational Aspects of Characterizing CPS and MCPS Circuits

While the FDTD technique has been very successfully applied in characterizing all the CPS and MCPS circuits in this chapter and chapter 3, it has been seen time and again that despite it's efficacy, this technique suffers from serious limitations in modeling large-scale problems due to the substantial computation resources required.

As the complexity of circuits increases, the size of the computational grid is expected to increase. However, it is often seen that some parts of the circuit are more complex than the other regions and require a fine mesh in order to be able to accurately characterize the circuit. In such cases the conventional FDTD scheme which uses a uniform mesh in the entire computational domain demands very extensive and sometimes formidable computation resources. A more efficient and economic scheme would use a non-uniform grid where a fine mesh is used only in selective sections of the circuit which have increased complexity and therefore, strong field variations, while using a coarse mesh elsewhere. The remaining portion of this research effort therefore focuses on developing an efficient nonuniform grid based FDTD scheme.

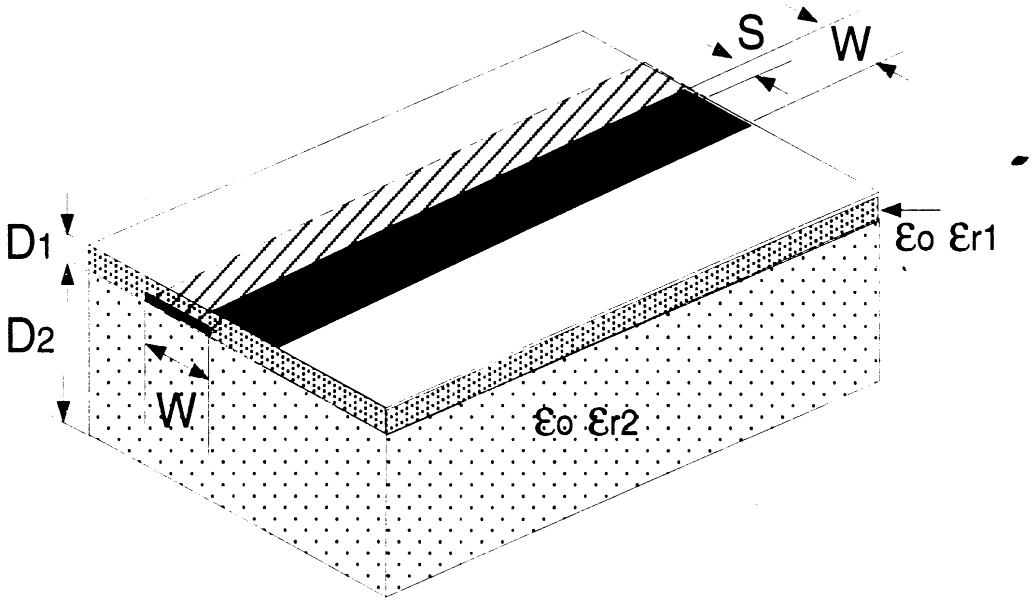

Figure 4.1: Geometry of MCPS line

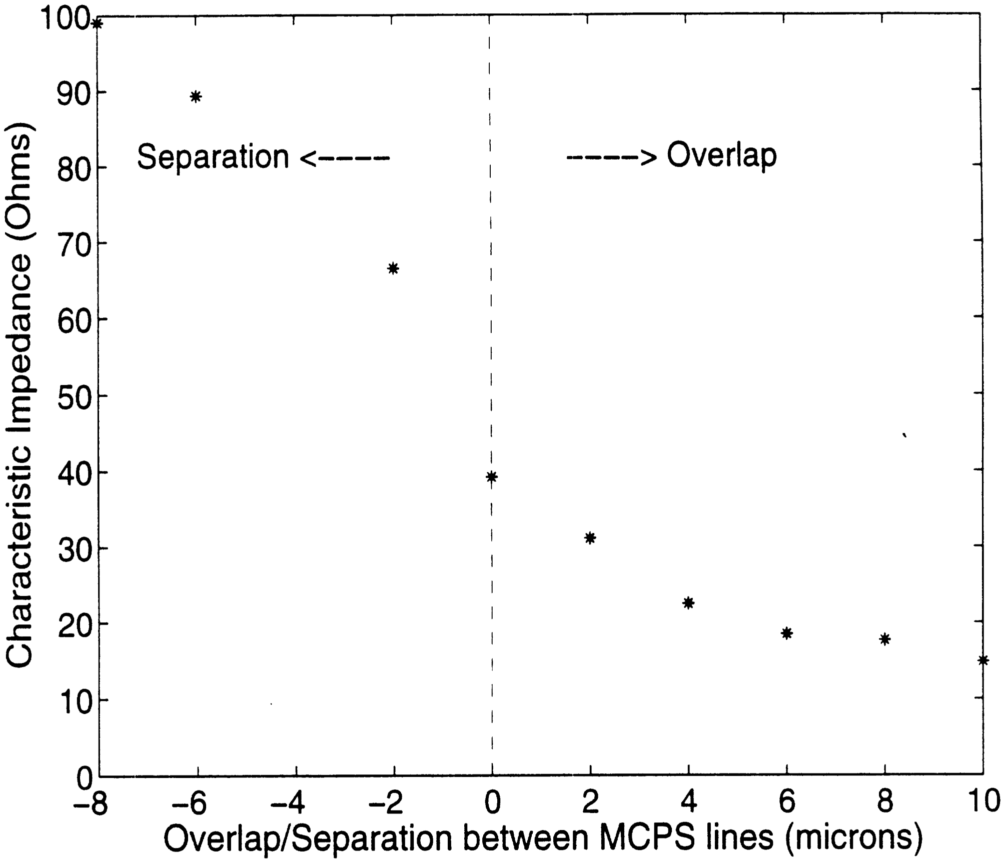

Figure 4.2: Characteristic Impedance of MCPS line for a fixed stripwidth (W) = 10μm, SOG thickness (D_1) = 1.35 μm and conductor thickness = 0.45 μm

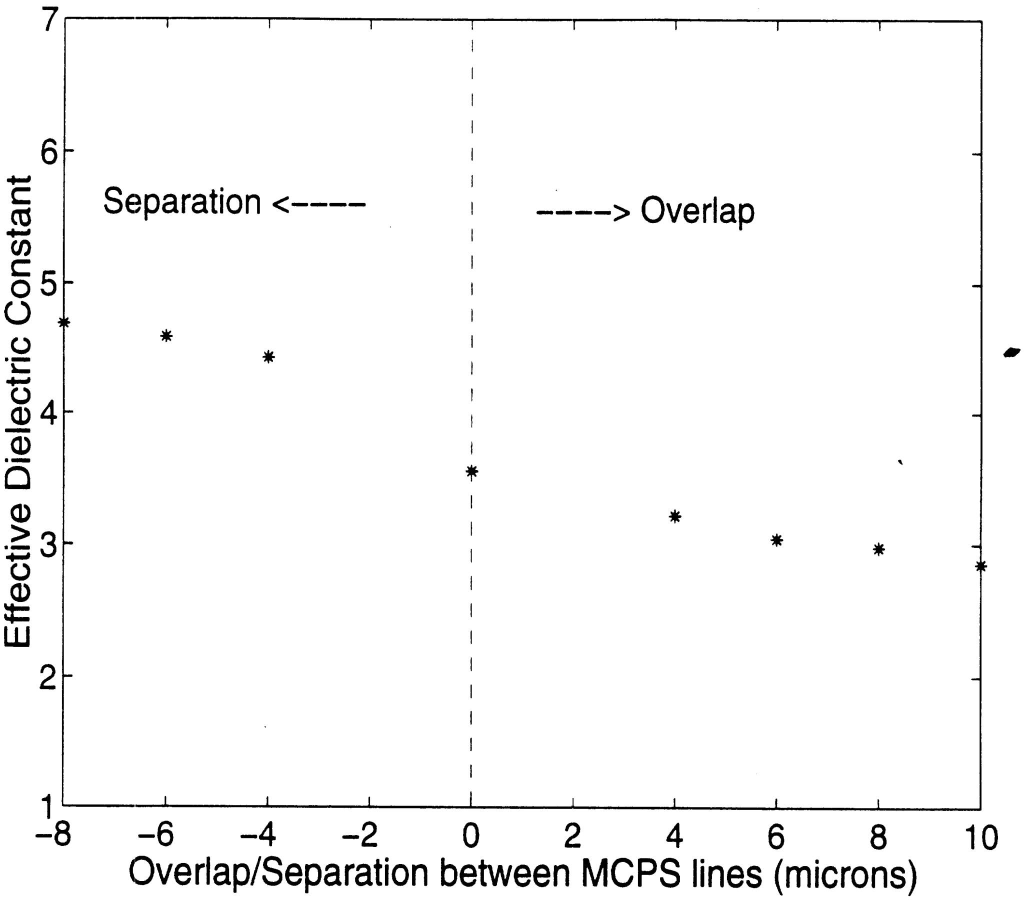

Figure 4.3: Effective Dielectric Constant of MCPS line for a fixed stripwidth (W) = 10μm, SOG thickness (D_1) = 1.35 μm and conductor thickness = 0.45 μm

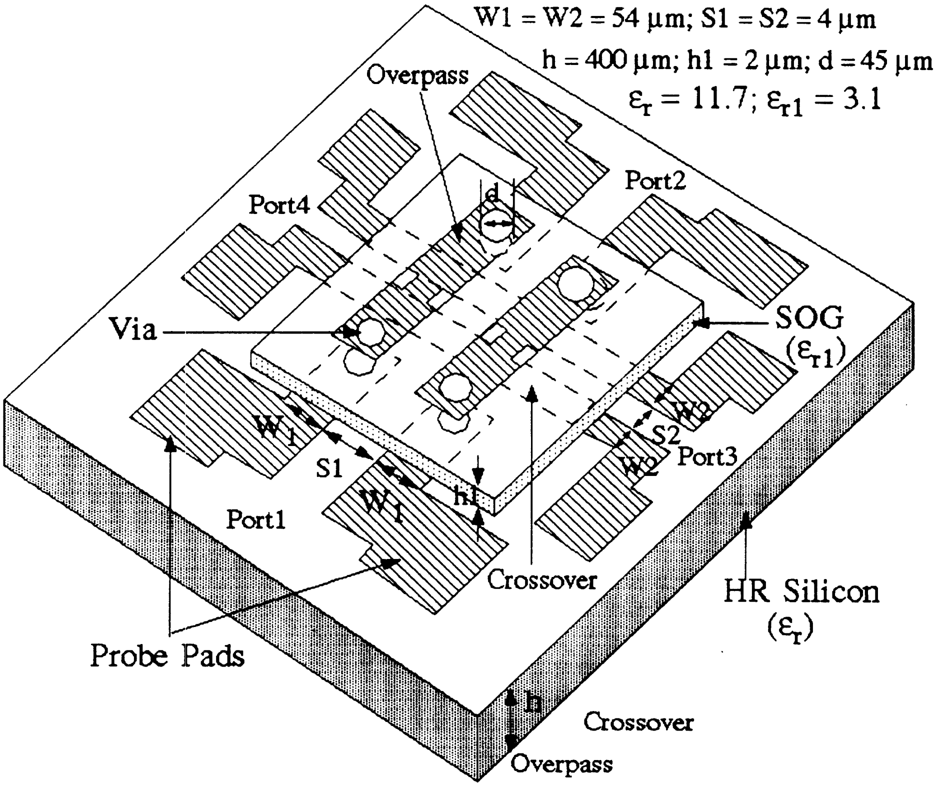

Figure 4.4: Geometry of CPS Overpass with Crossover

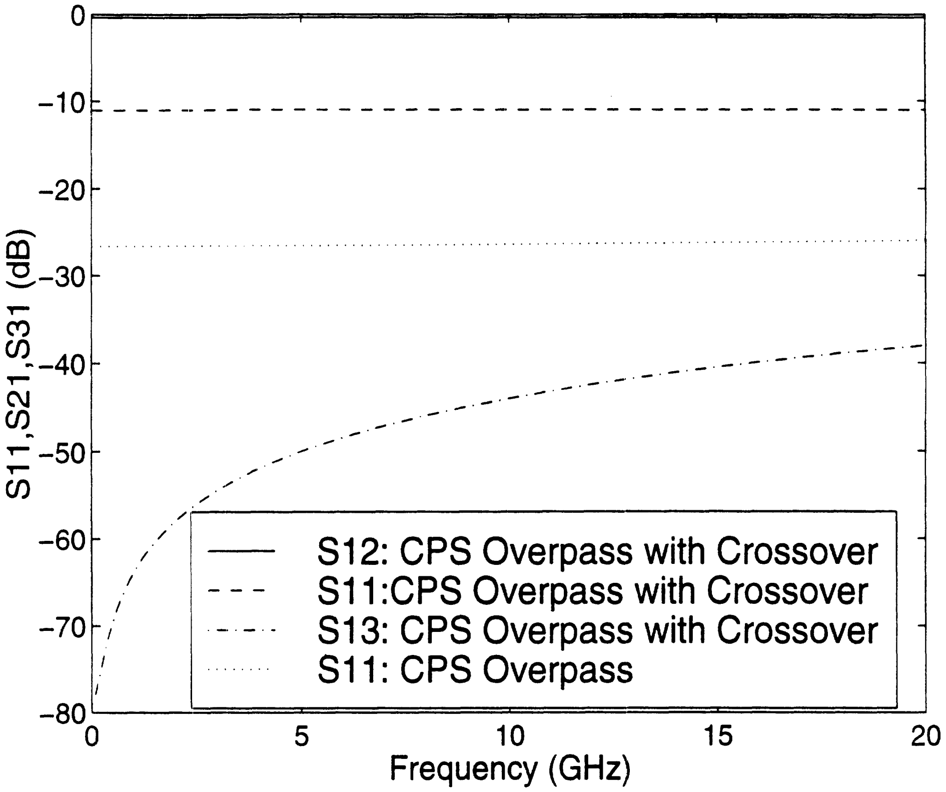

Figure 4.5: Computed Scattering Parameters for CPS Overpass with Crossover

CHAPTER 5

TIME DOMAIN MULTIRESOLUTION SCHEMES

5.1 Introduction to MRTD Schemes

Time domain schemes which result from the use of wavelet expansions or Multiresolution Analysis are called Multiresolution Time Domain (MRTD) schemes. Multiresolution analysis refers to the use of scaling and wavelet functions as a complete set of bases. The use of wavelets in the method of moments for the solution of integral equations in frequency domain has been known since the 1993 Antennas and Propagation Symposium in Ann Arbor, MI [61]. Recent publications have demonstrated that the application of the method of moments directly to Maxwell's equations allows for the use of multiresolution analysis in the time domain [64], [65], [66]. In fact, MRTD schemes based on Battle-Lemarie scaling functions have been shown to exhibit highly linear dispersion characteristics. In comparison to conventional FDTD, savings in computation time and memory of one and two orders of magnitude have been reported in [66]. Depending on the choice of basis functions, several different schemes result, each one carrying the signature of the basis functions used in MRA. It is also important to note that depending on the application, customized MRTD schemes which use one's own application-specific basis functions can be developed.

The objective of this work is to develop an FDTD multigrid using the Haar wavelet basis. It will be shown that MRTD technique which uses Haar scaling (pulse) functions as bases results in the FDTD technique. Motivation for this work stems from the theory of MRA which says that a function which is expanded in terms of scaling functions of a lower resolution level, m1, can be improved to a higher resolution level, m2, by using wavelets of the intermediate levels. In other words, expanding a function using scaling function of resolution level m1 and wavelets up to resolution level m2 gives the same accuracy as expanding the function using just the scaling functions of resolution m2. However, the use of wavelet expansions has major implications in memory savings due to the fact that wavelet expansion coefficients are significant only in areas of strong field variations. This allows for the capability to discard wavelet expansion coefficients at space/time locations where they are not significant, thereby leading to significant economy in memory. Different resolutions of wavelets can be combined so as to locally improve the accuracy of the approximation of the unknown function. This, combined with the fact that wavelet coefficients are significant only at abrupt field variations and discontinuities, allows MRTD to lend itself very naturally to a Multigrid implementation.

As mentioned above, the FDTD equations can be derived by applying the method of moments to Maxwell's equations using pulses as basis functions. Since pulse functions are the scaling functions in Haar system, FDTD technique can be considered as a specific MRTD scheme. Based on these ideas, in this chapter, an FDTD multigrid for the zero resolution level Haar wavelet is derived. This is followed by the performance of dispersion analysis to demonstrate the improvements gained by adding the multigrid feature to the regular FDTD scheme. The 2D MRTD scheme based on Haar basis functions is then developed and applied to solve for the Electromagnetic fields in a waveguide and a shielded stripline. The results obtained are compared with those computed using conventional FDTD technique. It will be shown that the wavelet coefficients are significant only at locations with abrupt field variations. This facilitates the gain of accurate solutions by combining the wavelet and scaling coefficients only in regions where the wavelet coefficients are significant (discontinuities).

5.2 Derivation of 1D Zero Resolution MRTD Scheme Using the Haar System

Consider the following equation obtained from the 1D wave equation:

$$\frac{1}{c}\frac{\partial E}{\partial t} = \frac{\partial E}{\partial z} \tag{5.1}$$

The discretization of this equation using FDTD and MRTD schemes will be presented in this section. To do so, the Haar basis is used for field expansions.

As known in the literature, the Haar system is generated by a scaling function $\phi(x)$ and a mother wavelet $\psi^0(x)$ given below:

$$\phi(x) = \begin{array}{ll} 1 & for\,|x| < \frac{1}{2} \\ \frac{1}{2} & for\,|x| = \frac{1}{2} \\ 0 & elsewhere \end{array}$$

and

$$\psi^0(x) = \begin{cases} \frac{1}{2} & for\, x = -\frac{1}{2} \\ 1 & for\ -\frac{1}{2} < x < 0 \\ 0 & for\, x = 0 \\ -1 & for\, 0 < x < \frac{1}{2} \\ -\frac{1}{2} & for\, x = \frac{1}{2} \\ 0 & elsewhere \end{cases}$$

Figure 5.2 shows these two generating functions. In the regular FDTD scheme, the electric and magnetic fields are expanded in terms of pulse functions as shown in the equation below:

$$E(x,t) = \Sigma_{k,m}\ {}_kE_m\ h_k(t)\ \phi_m(x) \tag{5.2}$$

where ${}_kE_m$ represents unknown constants which give the average values of the field and $h_k(t)$ and $\phi_m(x)$ are pulse functions centered at t_k and x_m.

Applying this expansion to Eq. 5.1 and using the method of moments (Galerkin's technique) we obtain the following discretized equation:

$$\frac{\Delta x}{c\Delta t}({}_{k+1}E_m -{}_{k-1} E_m) ={}_k E_{m+1} -{}_k E_{m-1} \tag{5.3}$$

which can also be denoted as:

$$D_tE ={}_k E_{m+1} -{}_k E_{m-1} \tag{5.4}$$

where D_t is the differential operator in the time domain. This is the regular FDTD discretization scheme To develop the zero resolution MRTD scheme, the scaling function as well as mother wavelet of the Haar system are used for field expansion as shown below :

$$E(x,t) = \Sigma_{k,m}h_k(t)[{}_kE^{\phi}_m\phi_m(x) +{}_k E^{\psi^0}_m\psi^0_m(x)] \tag{5.5}$$

where ${}_kE_m^{\phi}$ and ${}_kE_m^{\psi^0} representunknownconstantswhichgiveustheaveragevaluesofthefieldandthede$ is a pulse function centered around t_k and $\phi_m(x)$ and $\phi_m^0(x)$ are scaling and mother wavelet functions centered around x_m. Using Galerkin's method, the following discretized equations corresponding to Eq. 5.1 are obtained:

$$\frac{\Delta x}{c\Delta t}({}_{k+1}E_m^{\phi} -_{k-1} E_m^{\phi}) =_k E_{m+1}^{\phi} -_k E_{m-1}^{\phi} +_k E_{m+1}^{\psi^0} - 2_kE_m^{\psi^0} +_k E_{m-1}^{\psi^0} \tag{5.6}$$

$$\frac{\Delta x}{c\Delta t}({}_{k+1}E_m^{\psi^0} -_{k-1} E_m^{\psi^0}) =_k E_{m-1}^{\psi^0} -_k E_{m+1}^{\psi(0)} -_k E_{m+1}^{\phi} + 2_kE_m^{\phi} -_k E_{m-1}^{\phi} \tag{5.7}$$

These are the MRTD discretized equations. It it worth noting here that when the wavelet coefficient ${}_kE_m^{\psi^0}$ in Eq. 5.5 is set to zero, we obtain the FDTD scheme whose field expansion is:

$$E(x,t) = \Sigma_{k,m}h_k(t)[{}_kE_m^{\phi}\phi_m(x)] \tag{5.8}$$

The dispersion relation of the FDTD scheme is presented in chapter 2.

5.3 Dispersion Analysis of 1D Zero Resolution MRTD Scheme

In this section, dispersion analysis is performed on the FDTD and MRTD schemes in order to compare the dispersion characteristics of the MRTD scheme with that of the traditional FDTD technique. The dispersion relation of the FDTD and the MRTD scheme is calculated from the solution of the eigenvalue problem after transforming the discretized equations into the frequency domain [68], [69], [47]. For the 1D equation discussed above, the FDTD dispersion relation is shown below:

$$\frac{\Delta x}{c\Delta t}sin(\frac{\Omega}{2}) = sin(\frac{\chi}{2}) \tag{5.9}$$

where

$$\Omega = \omega\Delta t \tag{5.10}$$

and

$$\chi = \Delta x k_x \tag{5.11}$$

In the equations above, Δx and Δt are the space and time steps respectively and k_x is the magnitude of the wave vector. The dispersion relation for the zero resolution 1D MRTD mesh (FDTD multigrid) is given by the following equation:

$$\frac{\Delta x}{c\Delta t} sin(\frac{\Omega}{2}) = 2sin(\frac{\chi}{4}) \tag{5.12}$$

Figure 5.3 shows plots of the normalized wave vector component χ as a function of the normalized frequency Ω. These plots compare the dispersion of the MRTD scheme with coarse and dense grid FDTD schemes as well as the ideal case. The factor $\frac{\Delta x}{c\Delta t}$ is chosen to be 2.6131 in all the cases here. From the figure it can be seen that the dispersion curve of the MRTD scheme is the same as that of an FDTD scheme whose cell size is half that of the MRTD scheme. It is also seen that for the same grid size, MRTD dispersion appears to be much more linear and closer to ideal compared to FDTD dispersion. However, such a comparison is misleading since MRTD scheme inherently enhances the resolution of the FDTD scheme. In particular, the zero resolution MRTD scheme that uses scaling and mother wavelet functions offers double the resolution of the FDTD scheme of the same grid size. Hence, the MRTD dispersion should be compared to that of an FDTD scheme with doubled resolution. However, as will be shown later, the main advantage of using wavelets stems from the fact that wavelets can be used in selective regions of the computational domain to enhance field resolution while using scaling functions elsewhere. Hence, for a given accuracy, using wavelets selectively in the computational domain results in improved dispersion with very marginal increase in computational memory requirement.

Dispersion analysis has also been performed for the 2D MRTD scheme. When both scaling and wavelet functions are applied along one direction ($\hat{x}$) and only scaling functions along the other direction ($\hat{y}$), the following dispersion relation is obtained:

$$\frac{\Delta x}{c\Delta t}^2 sin^2(\frac{\Omega}{2}) = sin^2(\frac{\chi_x}{2}) + 4sin^2(\frac{\chi_y}{4}) \tag{5.13}$$

where $\chi_x = \Delta x k_x$ and $\chi_y = \Delta y k_y$. Also Δx and Δy are the space steps along $\hat{x}$ and $\hat{y}$ directions, Δt is the time step and k_x and k_y are the magnitudes of the wave vector components along $\hat{x}$ and $\hat{y}$ directions.

Similarly, dispersion analysis of 2D FDTD scheme leads to the following relation:

$$\frac{\Delta x}{c\Delta t}^2 sin^2(\frac{\Omega}{2}) = sin^2(\frac{\chi_x}{2}) + sin^2(\frac{\chi_y}{2}) \tag{5.14}$$

Figure 5.4 shows plots of χ as a function of Ω for the ideal case, the FDTD scheme with coarse and dense grids, and MRTD scheme. The plots are along the $\hat{x}$ (1,0,0) direction in which wavelets are applied. As expected, the dispersion of MRTD scheme is the same as that of the FDTD scheme with twice the resolution. Fig. 5.5 examines the plots of χ as a function of Ω for the ideal case, the FDTD technique with coarse and dense grids and MRTD scheme, along the $\hat{x} + \hat{y}$ (1,1,0) direction. Comparing Figs. 5.4 and 5.5, it can be seen that dispersion of MRTD scheme in (1,0,0) direction is closer to ideal compared to the dispersion in (1,1,0) direction. This improvement in the dispersion curve in the direction in which wavelets are applied is attributed to the enhancement in resolution due to wavelets.

Finally dispersion analysis of 2D MRTD scheme with wavelets along both x and y directions is performed resulting in the following dispersion relation:

$$\frac{\Delta x}{c\Delta t}^2 sin^2(\frac{\Omega}{2}) = 4sin^2(\frac{\chi_x}{4}) + 4sin^2(\frac{\chi_y}{4}) \tag{5.15}$$

Fig. 5.6 shows the dispersion plots along the $\hat{x}+\hat{y}$ (1,1,0) direction for the ideal case, the FDTD technique with coarse and dense grids and the MRTD scheme. Comparing this figure to Fig. 5.5, it can be seen that the MRTD dispersion along the given direction improves. This is intuitive, since the mesh resolution is now enhanced in all the relevant directions.

5.4 The Zero Resolution 2D-FDTD Multigrid Scheme

In this section, the 2D MRTD technique, which is also referred to as the FDTD Multigrid scheme, is presented. To begin with, a broad overview of the general procedure is presented. This is followed by a detailed look at the procedure to obtain the 2D MRTD discretized equations.

5.4.1 Overview of 2D-FDTD Multigrid Scheme

Consider the following 2-D scalar equation obtained from Maxwell's H-curl equation:

$$\epsilon\frac{\partial E_x}{\partial t} = \frac{\partial H_z}{\partial y} + \beta H_y \tag{5.16}$$

This equation can be rewritten in a differential operator form as shown below:

$$L_1(f_1(x,y,t)) + L_2(f_2(x,y,t)) = g \tag{5.17}$$

where L_1 and L_2 are the operators and f_1(x,y,t) and f_2(x,y,t) represent the electric/magnetic fields. We now expand the fields using Haar based MRA with scaling functions ϕ_n and mother wavelet functions ψ_n^0 to represent the fields. The field expansion can be represented as follows [80]:

$$f(x,y,t) = [A][\phi(x)\phi(y)] + [B][\phi(x)\psi^0(y)]$$
$$+[C][\psi^0(x)\phi(y)] + [D][\psi^0(x)\psi^0(y)] \tag{5.18}$$

where $[\phi(\mathrm{x})\phi(\mathrm{y})]$, $[\phi(\mathrm{x})\psi^0(\mathrm{y})]$, $[\psi^0(\mathrm{x})\phi(\mathrm{y})]$ and $[\psi^0(\mathrm{x})\psi^0(\mathrm{y})]$ represent matrices whose elements are the corresponding basis functions in the computational domain of interest and [A], [B], [C], [D] represent matrices of the unknown coefficients which give information about the fields and their derivatives.

Application of Galerkin's technique leads to 4 schemes which can be represented as follows:

$$< [\phi\phi], L_1(f_1) + L_2(f_2) > = < [\phi\phi], g >: \phi\phi - Scheme \tag{5.19}$$

$$< [\phi\psi^0], L_1(f_1) + L_2(f_2) > = < [\phi\psi^0], g >: \phi\psi^0 - Scheme \tag{5.20}$$

$$< [\psi^0\phi], L_1(f_1) + L_2(f_2) > = < [\psi^0\phi], g >: \psi^0\phi - Scheme \tag{5.21}$$

$$< [\psi^0\psi^0], L_1(f_1) + L_2(f_2) > = < [\psi^0\psi^0], g >: \psi^0\psi^0 - Scheme \tag{5.22}$$

From this system, we obtain a set of simultaneous discretized equations. For the zero resolution MRTD technique, the above four schemes decouple and coupling can be achieved only through the excitation term and the boundaries.

5.4.2 Derivation of Zero Resolution 2D-FDTD Multigrid Scheme using Haar Scaling Function and Mother Wavelet

In this section, the detailed derivation of the discretized equations for the zero resolution 2D-FDTD Multigrid scheme corresponding to Maxwell's H-curl equations is presented. The discretized equations corresponding to Maxwell's E-curl equation can be obtained in a similar manner.

Consider the following 2-D scalar equations obtained from Maxwell's H-curl equation with propagation along $\hat{z}$ direction:

$$\epsilon\frac{\partial E_x}{\partial t} = \frac{\partial H_z}{\partial y} + \beta H_y \tag{5.23}$$

$$\epsilon\frac{\partial E_y}{\partial t} = -\beta H_x - \frac{\partial H_z}{\partial x} \tag{5.24}$$

$$\epsilon\frac{\partial E_z}{\partial t} = \frac{\partial H_y}{\partial x} - \frac{\partial H_x}{\partial y} \tag{5.25}$$

We now expand the electric and magnetic fields using Haar based MRA with pulse functions in time and scaling functions ϕ_n and mother wavelet functions ψ_n^0 in space [80] as seen in Fig. 5.2. The electric and magnetic fields are interleaved in space and time as per the conventional Yee cell leap frog algorithm [43]. Figure 5.1 shows the location of the E and H fields in the MRTD cell. The field expansions can be represented as follows:

$$\begin{aligned} E_x(x,y,t) = & \sum_{k,l,m=-\infty}^{+\infty} {}_kE^{x,\phi\phi}_{l-1/2,m} h_k \phi_{l-1/2}(x)\phi_m(y) + \sum_{k,l,m=-\infty}^{+\infty} {}_kE^{x,\phi\psi^0}_{l-1/2,m} h_k \phi_{l-1/2}(x)\psi^0_m(y) + \\ & \sum_{k,l,m=-\infty}^{+\infty} {}_kE^{x,\psi^0\phi}_{l-1/2,m} h_k \psi^0_{l-1/2}(x)\phi_m(y) + \sum_{k,l,m=-\infty}^{+\infty} {}_kE^{x,\psi^0\psi^0}_{l-1/2,m} h_k \psi^0_{l-1/2}(x)\psi^0_m(y) \end{aligned} \tag{5.26}$$

$$\begin{aligned} E_y(x,y,t) = & \sum_{k,l,m=-\infty}^{+\infty} {}_kE^{y,\phi\phi}_{l,m-1/2} h_k \phi_l(x)\phi_{m-1/2}(y) + \sum_{k,l,m=-\infty}^{+\infty} {}_kE^{y,\phi\psi^0}_{l,m-1/2} h_k \phi_l(x)\psi^0_{m-1/2}(y) + \\ & \sum_{k,l,m=-\infty}^{+\infty} {}_kE^{y,\psi^0\phi}_{l,m-1/2} h_k \psi^0_l(x)\phi_{m-1/2}(y) + \sum_{k,l,m=-\infty}^{+\infty} {}_kE^{y,\psi^0\psi^0}_{l,m-1/2} h_k \psi^0_l(x)\psi^0_{m-1/2}(y) \end{aligned} \tag{5.27}$$

$$\begin{aligned} E_z(x,y,t) = & \sum_{k,l,m=-\infty}^{+\infty} {}_kE^{z,\phi\phi}_{l,m} h_k \phi_l(x)\phi_m(y) + \sum_{k,l,m=-\infty}^{+\infty} {}_kE^{z,\phi\psi^0}_{l,m} h_k \phi_l(x)\psi^0_m(y) + \\ & \sum_{k,l,m=-\infty}^{+\infty} {}_kE^{z,\psi^0\phi}_{l,m} h_k \psi^0_l(x)\phi_m(y) + \sum_{k,l,m=-\infty}^{+\infty} {}_kE^{z,\psi^0\psi^0}_{l,m} h_k \psi^0_l(x)\psi^0_m(y) \end{aligned} \tag{5.28}$$

$$\begin{aligned}H_x(x,y,t) = &\sum_{k,l,m=-\infty}^{+\infty} {}_{k-1/2}H^{x,\phi\phi}_{l,m-1/2} h_{k-1/2}\phi_l(x)\phi_{m-1/2}(y) + \\ &\sum_{k,l,m=-\infty}^{+\infty} {}_{k-1/2}H^{x,\phi\psi^0}_{l,m-1/2} h_{k-1/2}\phi_l(x)\psi^0_{m-1/2}(y) + \\ &\sum_{k,l,m=-\infty}^{+\infty} {}_{k-1/2}H^{x,\psi^0\phi}_{l,m-1/2} h_{k-1/2}\psi^0_l(x)\phi_{m-1/2}(y) + \\ &\sum_{k,l,m=-\infty}^{+\infty} {}_{k-1/2}H^{x,\psi^0\psi^0}_{l,m-1/2} h_{k-1/2}\psi^0_l(x)\psi^0_{m-1/2}(y) \qquad (5.29)\end{aligned}$$

$$\begin{aligned}H_y(x,y,t) = &\sum_{k,l,m=-\infty}^{+\infty} {}_{k-1/2}H^{y,\phi\phi}_{l-1/2,m} h_{k-1/2}\phi_{l-1/2}(x)\phi_m(y) + \\ &\sum_{k,l,m=-\infty}^{+\infty} {}_{k-1/2}H^{y,\phi\psi^0}_{l-1/2,m} h_{k-1/2}\phi_{l-1/2}(x)\psi^0_m(y) + \\ &\sum_{k,l,m=-\infty}^{+\infty} {}_{k-1/2}H^{y,\psi^0\phi}_{l-1/2,m} h_{k-1/2}\psi^0_{l-1/2}(x)\phi_m(y) + \\ &\sum_{k,l,m=-\infty}^{+\infty} {}_{k-1/2}H^{y,\psi^0\psi^0}_{l-1/2,m} h_{k-1/2}\psi^0_{l-1/2}(x)\psi^0_m(y) \qquad (5.30)\end{aligned}$$

$$\begin{aligned}H_z(x,y,t) = &\sum_{k,l,m=-\infty}^{+\infty} {}_{k-1/2}H^{z,\phi\phi}_{l-1/2,m-1/2} h_{k-1/2}\phi_{l-1/2}(x)\phi_{m-1/2}(y) + \\ &\sum_{k,l,m=-\infty}^{+\infty} {}_{k-1/2}H^{z,\phi\psi^0}_{l-1/2,m-1/2} h_{k-1/2}\phi_{l-1/2}(x)\psi^0_{m-1/2}(y) + \\ &\sum_{k,l,m=-\infty}^{+\infty} {}_{k-1/2}H^{z,\psi^0\phi}_{l-1/2,m-1/2} h_{k-1/2}\psi^0_{l-1/2}(x)\phi_{m-1/2}(y) + \\ &\sum_{k,l,m=-\infty}^{+\infty} {}_{k-1/2}H^{z,\psi^0\psi^0}_{l-1/2,m-1/2} h_{k-1/2}\psi^0_{l-1/2}(x)\psi^0_{m-1/2}(y) \qquad (5.31)\end{aligned}$$

where $\phi_n(x) = \phi(\frac{x}{\Delta x} - n)$ and $\psi^0_n(x) = \psi^0(\frac{x}{\Delta x} - n)$ represent the Haar scaling and mother wavelet (0-resolution wavelet) function respectively in space and $h_k(t)$ represents rectangular pulse functions in time. ${}_kE^{\kappa,\mu\nu}_{i,j}$ and ${}_{k-1/2}H^{\kappa,\mu\nu}_{i,j}$ where $\kappa = x, y, z$ and $\mu, \nu = \phi, \psi^0$ are the coefficients for field expansions in terms of scaling and wavelet functions. The indices i,j are discrete space indices related to space coordinates as follows: $x = i\Delta x, y = j\Delta y$ and the index k is a discrete time index related to time coordinate as follows: $t = k\Delta t$.

The expressions for the Haar scaling and mother wavelet functions are given in section 5.2. Also, since rectangular pulse functions are used as the time domain expansion function, we have $h_k(t) = h(\frac{t}{\Delta t} - k)$ where

$$h(t) = \begin{array}{ll} 1 & for\,|t| < \frac{1}{2} \\ \frac{1}{2} & for\,|t| = \frac{1}{2} \\ 0 & elsewhere \end{array}$$

To obtain the MRTD discretized equations, the field expansions in Eqs. 5.26 - 5.31 are inserted in Maxwell's differential equations shown in Eqs. 5.23 - 5.25. Next, Galerkin's technique is used to sample the resulting equations by using pulse functions as time-domain test functions and scaling/wavelet functions as space domain test functions. Since the zero resolution 2D MRTD scheme here uses pulse functions in time and scaling function and mother wavelet alone in space, 4 different schemes result from the sampling. For example, when sampling Eq. 5.23, the four schemes that result are:

$$< [h_{\lambda-1/2}(t)\phi_{l'-1/2}(x)\phi_{m'}(y)], [L_1(E_x(x,y,z,t)) = L_2(H_z(x,y,z,t)) + L_3(H_y(x,y,z,t))] > \quad \phi\phi - \textbf{Scheme:} \tag{5.32}$$

$$< [h_{\lambda-1/2}(t)\phi_{l'-1/2}(x)\psi^0_{m'}(y)], [L_1(E_x(x,y,z,t)) = L_2(H_z(x,y,z,t)) + L_3(H_y(x,y,z,t))] > \quad \phi\psi^0 - \textbf{Scheme:} \tag{5.33}$$

$$< [h_{\lambda-1/2}(t)\psi^0_{l'-1/2}(x)\phi_{m'}(y)], [L_1(E_x(x,y,z,t)) = L_2(H_z(x,y,z,t))+L_3(H_y(x,y,z,t))] >$$

$$\psi^0\phi - \textbf{Scheme}: \tag{5.34}$$

$$< [h_{\lambda-1/2}(t)\psi^0_{l'-1/2}(x)\psi^0_{m'}(y)], [L_1(E_x(x,y,z,t)) = L_2(H_z(x,y,z,t))+L_3(H_y(x,y,z,t))] >$$

$$\psi^0\psi^0 - \textbf{Scheme}: \tag{5.35}$$

In the equations above, the $\phi\phi$-Scheme corresponds to the case where the sampling function for the method of moments is the Haar scaling function in both x and y directions, $\phi\psi^0$-Scheme corresponds to the case where the sampling function is a scaling function in the x direction and wavelet function in the y direction, etc. Also, the operators L_1, L_2 and L_3 stand for the operations $\epsilon \times \frac{\partial}{\partial t}$, $\frac{\partial}{\partial y}$ and $\beta \times$ respectively. The expansions for $E_x(x,y,z,t)$, $H_y(x,y,z,t)$ and $H_z(x,y,z,t)$ are given in Eqs.(5.26), (5.30) and (5.31) respectively.

From Eqs. 5.32 - 5.35, we obtain the following set of discretized equations corresponding to Eq. 5.23:

$$\epsilon\Delta x\Delta y[{}_{\lambda}E^{x,\phi\phi}_{l'-1/2,m'} - {}_{\lambda-1}\,E^{x,\phi\phi}_{l'-1/2,m'}] = \Delta t\Delta x[{}_{\lambda-1/2}H^{z,\phi\phi}_{l'-1/2,m'+1/2} - {}_{\lambda-1/2}\,H^{z,\phi\phi}_{l'-1/2,m'-1/2}]$$
$$+ \beta\Delta t\Delta x\Delta y\,{}_{\lambda-1/2}H^{y,\phi\phi}_{l'-1/2,m'} \tag{5.36}$$

$$\epsilon\Delta x\Delta y[{}_{\lambda}E^{x,\phi\psi^0}_{l'-1/2,m'} - {}_{\lambda-1}\,E^{x,\phi\psi^0}_{l'-1/2,m'}] = \Delta t\Delta x[{}_{\lambda-1/2}H^{z,\phi\psi^0}_{l'-1/2,m'+1/2} - {}_{\lambda-1/2}\,H^{z,\phi\psi^0}_{l'-1/2,m'-1/2}]$$
$$+ \beta\Delta t\Delta x\Delta y\,{}_{\lambda-1/2}H^{y,\phi\psi^0}_{l'-1/2,m'} \tag{5.37}$$

$$\begin{aligned}\epsilon\Delta x\Delta y[{}_{\lambda}E^{x,\psi^0\phi}_{l'-1/2,m'} - {}_{\lambda-1}\,E^{x,\psi^0\phi}_{l'-1/2,m'}] &= \Delta t\Delta x[{}_{\lambda-1/2}H^{z,\psi^0\phi}_{l'-1/2,m'+1/2} - {}_{\lambda-1/2}\,H^{z,\psi^0\phi}_{l'-1/2,m'-1/2}] \\ &+ \beta\Delta t\Delta x\Delta y_{\lambda-1/2}H^{y,\psi^0\phi}_{l'-1/2,m'} \qquad (5.38)\end{aligned}$$

$$\begin{aligned}\epsilon\Delta x\Delta y[{}_{\lambda}E^{x,\psi^0\psi^0}_{l'-1/2,m'} - {}_{\lambda-1}\,E^{x,\psi^0\psi^0}_{l'-1/2,m'}] &= \Delta t\Delta x[{}_{\lambda-1/2}H^{z,\psi^0\psi^0}_{l'-1/2,m'+1/2} - {}_{\lambda-1/2}\,H^{z,\psi^0\psi^0}_{l'-1/2,m'-1/2}] \\ &+ \beta\Delta t\Delta x\Delta y_{\lambda-1/2}H^{y,\psi^0\psi^0}_{l'-1/2,m'} \qquad (5.39)\end{aligned}$$

Similarly, the discretized equations corresponding to Eqs. 5.24- 5.25 are as follows:

$$\begin{aligned}\epsilon\Delta x\Delta y[{}_{\lambda}E^{y,\phi\phi}_{l',m'-1/2} - {}_{\lambda-1}\,E^{y,\phi\phi}_{l',m'-1/2}] &= -\Delta t\Delta y[{}_{\lambda-1/2}H^{z,\phi\phi}_{l'+1/2,m'-1/2} - {}_{\lambda-1/2}\,H^{z,\phi\phi}_{l'-1/2,m'-1/2}] \\ &- \beta\Delta t\Delta x\Delta y_{\lambda-1/2}H^{x,\phi\phi}_{l',m'-1/2} \qquad (5.40)\end{aligned}$$

$$\begin{aligned}\epsilon\Delta x\Delta y[{}_{\lambda}E^{y,\phi\psi^0}_{l',m'-1/2} - {}_{\lambda-1}\,E^{y,\phi\psi^0}_{l',m'-1/2}] &= -\Delta t\Delta y[{}_{\lambda-1/2}H^{z,\phi\psi^0}_{l'+1/2,m'-1/2} - {}_{\lambda-1/2}\,H^{z,\phi\psi^0}_{l'-1/2,m'-1/2}] \\ &- \beta\Delta t\Delta x\Delta y_{\lambda-1/2}H^{x,\phi\psi^0}_{l',m'-1/2} \qquad (5.41)\end{aligned}$$

$$\begin{aligned}\epsilon\Delta x\Delta y[{}_{\lambda}E^{y,\psi^0\phi}_{l',m'-1/2} - {}_{\lambda-1}\,E^{y,\psi^0\phi}_{l',m'-1/2}] &= -\Delta t\Delta y[{}_{\lambda-1/2}H^{z,\psi^0\phi}_{l'+1/2,m'-1/2} - {}_{\lambda-1/2}\,H^{z,\psi^0\phi}_{l'-1/2,m'-1/2}] \\ &- \beta\Delta t\Delta x\Delta y_{\lambda-1/2}H^{x,\psi^0\phi}_{l',m'-1/2} \qquad (5.42)\end{aligned}$$

$$\begin{aligned}\epsilon\Delta x\Delta y[{}_{\lambda}E^{y,\psi^0\psi^0}_{l',m'-1/2} - {}_{\lambda-1}\,E^{y,\psi^0\psi^0}_{l',m'-1/2}] &= -\Delta t\Delta y[{}_{\lambda-1/2}H^{z,\psi^0\psi^0}_{l'+1/2,m'-1/2} - {}_{\lambda-1/2}\,H^{z,\psi^0\psi^0}_{l'-1/2,m'-1/2}] \\ &- \beta\Delta t\Delta x\Delta y_{\lambda-1/2}H^{x,\psi^0\psi^0}_{l',m'-1/2} \qquad (5.43)\end{aligned}$$

$$\epsilon\Delta x\Delta y[{}_{\lambda}E^{z,\phi\phi}_{l',m'} - {}_{\lambda-1}\,E^{z,\phi\phi}_{l',m'}] = -\Delta t\Delta y[{}_{\lambda-1/2}H^{y,\phi\phi}_{l'+1/2,m'} - {}_{\lambda-1/2}\,H^{y,\phi\phi}_{l'-1/2,m'}]$$

$$- \Delta t\Delta x[{}_{\lambda-1/2}H^{x,\phi\phi}_{l',m'+1/2} - {}_{\lambda-1/2}\,H^{x,\phi\phi}_{l',m'-1/2}] \qquad (5.44)$$

$$\epsilon\Delta x\Delta y[{}_{\lambda}E^{z,\phi\psi^0}_{l',m'} - {}_{\lambda-1}\,E^{z,\phi\psi^0}_{l',m'}] = -\Delta t\Delta y[{}_{\lambda-1/2}H^{y,\phi\psi^0}_{l'+1/2,m'} - {}_{\lambda-1/2}\,H^{y,\phi\psi^0}_{l'-1/2,m'}]$$

$$- \Delta t\Delta x[{}_{\lambda-1/2}H^{x,\phi\psi^0}_{l',m'+1/2} - {}_{\lambda-1/2}\,H^{x,\phi\psi^0}_{l',m'-1/2}] \qquad (5.45)$$

$$\epsilon\Delta x\Delta y[{}_{\lambda}E^{z,\psi^0\phi}_{l',m'} - {}_{\lambda-1}\,E^{z,\psi^0\phi}_{l',m'}] = -\Delta t\Delta y[{}_{\lambda-1/2}H^{y,\psi^0\phi}_{l'+1/2,m'} - {}_{\lambda-1/2}\,H^{y,\psi^0\phi}_{l'-1/2,m'}]$$

$$- \Delta t\Delta x[{}_{\lambda-1/2}H^{x,\psi^0\phi}_{l',m'+1/2} - {}_{\lambda-1/2}\,H^{x,\psi^0\phi}_{l',m'-1/2}] \qquad (5.46)$$

$$\epsilon\Delta x\Delta y[{}_{\lambda}E^{z,\psi^0\psi^0}_{l',m'}\;{}_{\lambda-1}E^{z,\psi^0\psi^0}_{l',m'}] = -\Delta t\Delta y[{}_{\lambda-1/2}H^{y,\psi^0\psi^0}_{l'+1/2,m'} - {}_{\lambda-1/2}\,H^{y,\psi^0\psi^0}_{l'-1/2,m'}]$$

$$- \Delta t\Delta x[{}_{\lambda-1/2}H^{x,\psi^0\psi^0}_{l',m'+1/2} - {}_{\lambda-1/2}\,H^{x,\psi^0\psi^0}_{l',m'-1/2}] \qquad (5.47)$$

The discretized equations for the E-curl equations are obtained following the same procedure.

As seen from the discretized Eqs. 5.36 - 5.47, the MRTD scheme based on Haar scaling and mother wavelet functions alone results in decoupled scaling and wavelet schemes. Coupling can be achieved only through the excitation term and the boundary conditions. When scaling and wavelet schemes decouple, boundary conditions need to be imposed on the fields and their derivatives in a very precise mathematical form. In chapter 6, the details of the treatment of Boundaries in decoupled MRTD schemes are presented. It will also be shown later that when higher resolution Haar wavelets are used, the scaling and wavelet schemes couple, thereby simplifying the implementation of boundary condition.

The 2D MRTD equations derived here are validated by applying them to analyze the electromagnetic fields in some simple shielded structures. These shielded structures are terminated with Perfect Electric Conductors (PEC). The boundary conditions are obtained by applying the natural boundary condition for the electric field on a PEC as shown below:

$$E_t^{\phi\phi}\phi(x)\phi(y) + E_t^{\phi\psi^0}\phi(x)\psi^0(y) + E_t^{\psi^0\phi}\psi^0(x)\phi(y) + E_t^{\psi^0\psi^0}\psi^0(x)\psi^0(y) = 0 \quad (5.48)$$

where $E_t^{\phi\phi}$, $E_t^{\phi\psi^0}$, $E_t^{\psi^0\phi}$ and $E_t^{\psi^0\psi^0}$ are the scaling and wavelet coefficients of the tangential electric field at the boundary nodes. As mentioned earlier, for decoupled schemes, boundary conditions need to be imposed on the fields and their derivatives. This topic is elaborately discussed in chapter 6. In the following section, some applications of the 2D MRTD scheme are presented and the multigrid capability and economy in memory that result from using MRTD schemes is demonstrated.

5.4.3 Applications of 2D FDTD Multigrid and Results

The 2-D MRTD scheme derived above has been applied to analyze the Electromagnetic fields in an empty waveguide and a shielded stripline.

(a) Waveguide

An empty waveguide with cross-section 12.7 x 25.4 mm has been chosen. A coarse 5 x 8 mesh is used to discretize this mesh and 2D MRTD technique has been applied to analyze the fields in this geometry. Figure 5.7 shows the amplitudes of the wavelet and scaling coefficients of the electric field obtained by using MRTD technique. From this figure it can be seen that only the $\phi\phi$ and $\phi\psi^0$ coefficients make a significant contribution to the field and that the contribution of $\psi^0\phi$ and $\psi^0\psi^0$ is negligible. From the computed coefficients, the total field is reconstructed using an appropriate combination of the scaling and significant wavelet coefficients. For the waveguide chosen here, elimination of the wavelet coefficients that have no significant contribution leads to 480 unknowns. The reconstructed field obtained by this mesh has the same accuracy as that of a 10 x 16 FDTD mesh with 960 unknowns. This is in agreement with the theory of MRA. Figure 5.8 shows the results of this comparison and demonstrates that the use of multigrid scheme provides a 50% economy in memory in this case.

(b) Shielded Stripline

Next, a stripline of width 1.27mm is considered. It is enclosed in a waveguide of cross section 12.7 x 12.7 mm so that the side walls are sufficiently far away so as to not affect the propagation. The strip is placed 1.27mm from the ground. A 40 x 40 mesh is used to analyze the fields in this geometry with the 2D MRTD technique. Figure 5.5 shows the computed scaling and wavelet coefficients of the normal electric field just below the strip. From the figure, it can be seen that among the wavelet coefficients, only $\psi^0\phi$ makes a significant contribution close to the vicinity of the strip where the field variation is rather abrupt. Figure 5.10 shows the comparision of the total reconstructed field obtained from a 40 x 40 MRTD mesh (using a combination of scaling coefficients and wavelet coefficients have have significant values) with those obtained from 40 x 40 and 80 x 80 FDTD meshes. From the figure it is clear that the field computed using the 40 x 40 MRTD mesh using only the significant wavelet coefficients follows the results of the finer 80x80 mesh very closely. Table 5.1 compares the memory requirements in the FDTD and MRTD schemes. From the table, it can be seen that MRTD scheme coupled with thresholding (to drop the wavelet coefficients that are insignificant) leads to a significant economy in memory. In addition to memory savings, MRTD offers to dual advantage of multigrid capability. Sections of the computational domain which use both scaling and wavelet coefficients correspond to a dense mesh while the remaining regions which use only scaling coefficients correspond to a coarse mesh, thus offering multigrid capability. Figure 5.11 shows the Normal Electric field plot of the strip and the variable mesh resulting from MRTD.

Table 5.1: **FDTD Vs. MRTD memory requirement for Shielded Stripline**

Technique	Unknown Coeff.
40x40 FDTD	9600
40x40 MRTD	11328
80x80 FDTD	38400

5.5 Conclusion

In this chapter, a mathematically consistent approach for implementing FDTD multigrid has been presented. Since FDTD technique is based on the expansion of the unknown fields using pulse functions, the principles of multiresolution analysis allows for a consistent additional field expansion in terms of Haar wavelets. The Haar wavelet based 2D MRTD scheme that has been developed here has been applied to analyze the fields in an empty waveguide and a shielded stripline. It has been shown that wavelet coefficients that are obtained are significant only in regions of strong field variations. Coefficients which are below the threshold level can be dropped without adversely affecting the condition numbering of the system. Thus the dual advantages of economy in memory and multigrid capability are realized.

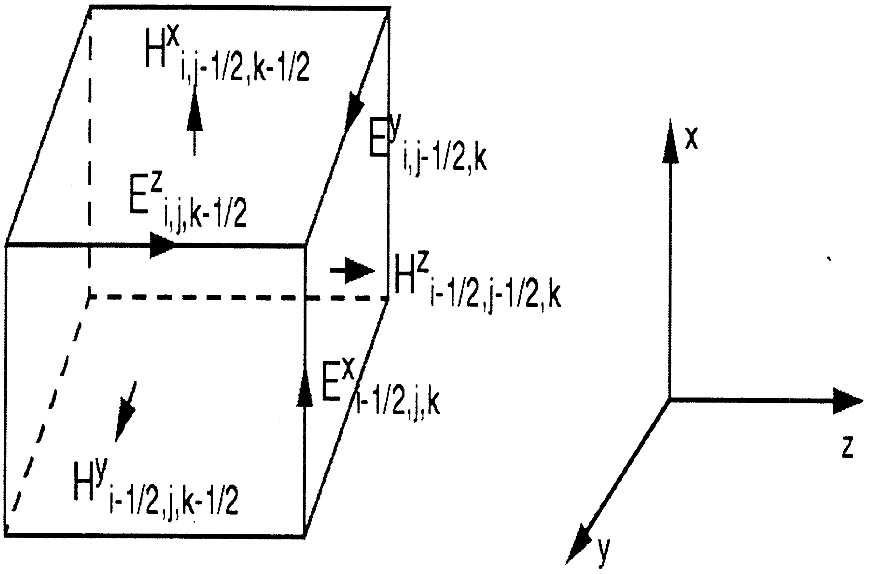

Figure 5.1: MRTD Cell: Field positions

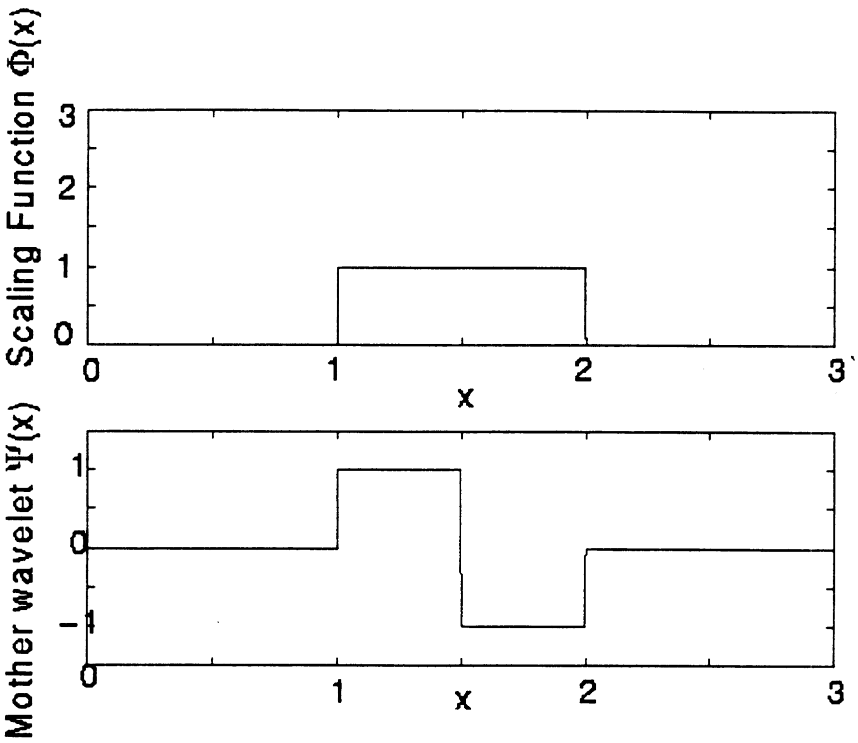

Figure 5.2: Scaling and Wavelet Functions.

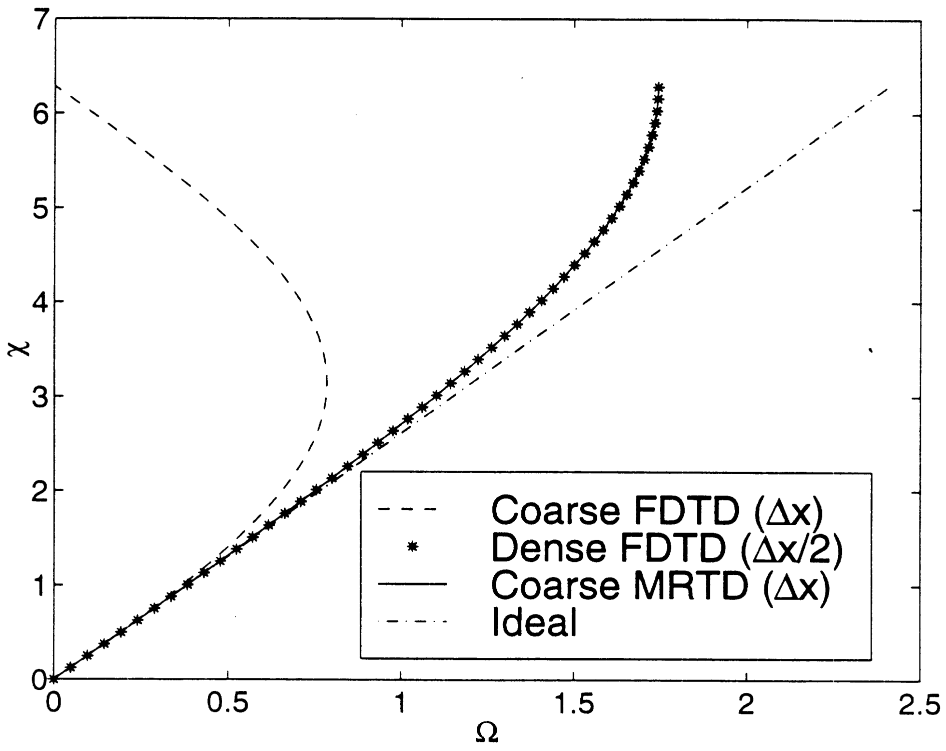

Figure 5.3: Dispersion of 1D MRTD Vs. FDTD and ideal dispersions.

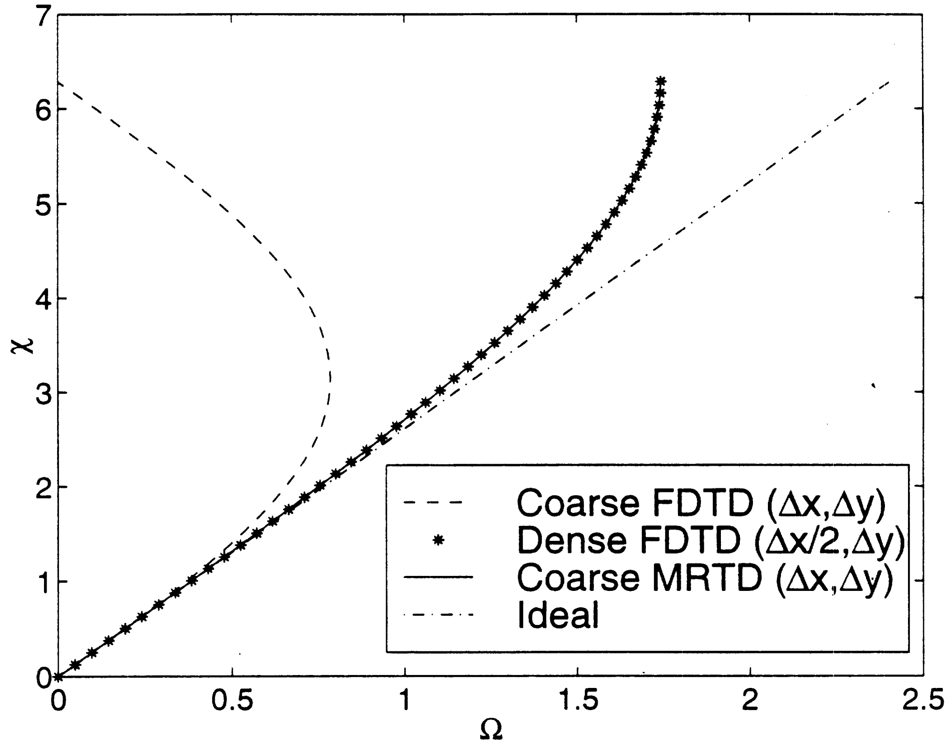

Figure 5.4: Dispersion of 2D MRTD (scaling and wavelet functions along $\hat{x}$ and only scaling functions along $\hat{y}$) Vs. FDTD and ideal dispersions looking in the (1,0,0) direction.

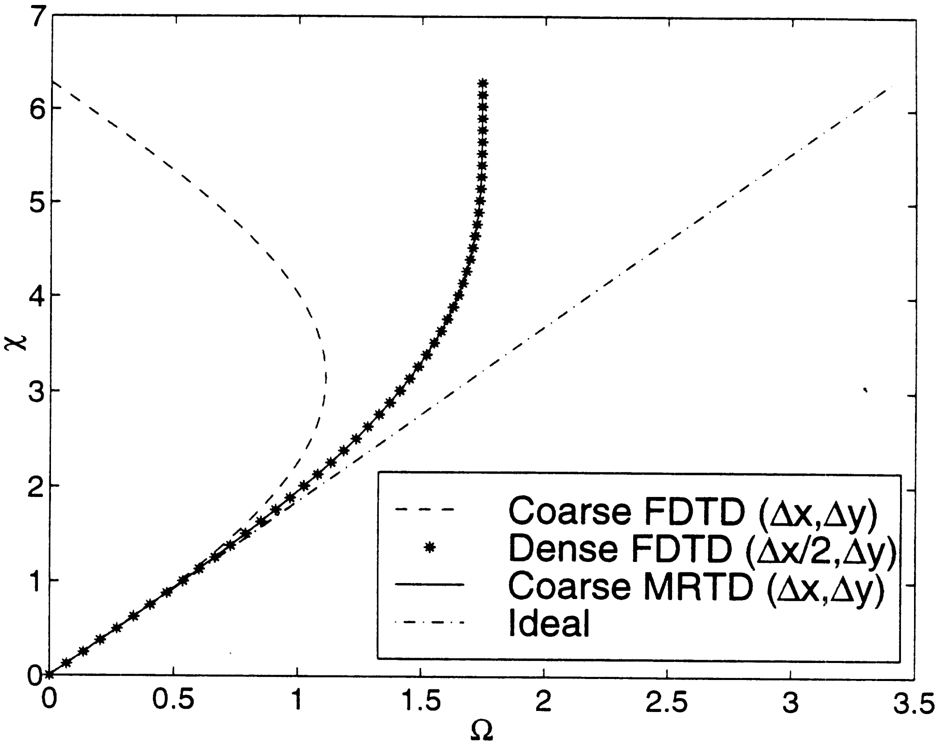

Figure 5.5: Dispersion of 2D MRTD (scaling and wavelet functions along $\hat{x}$ and only scaling functions along $\hat{y}$) Vs. FDTD and ideal dispersions looking in the (1,1,0) direction.

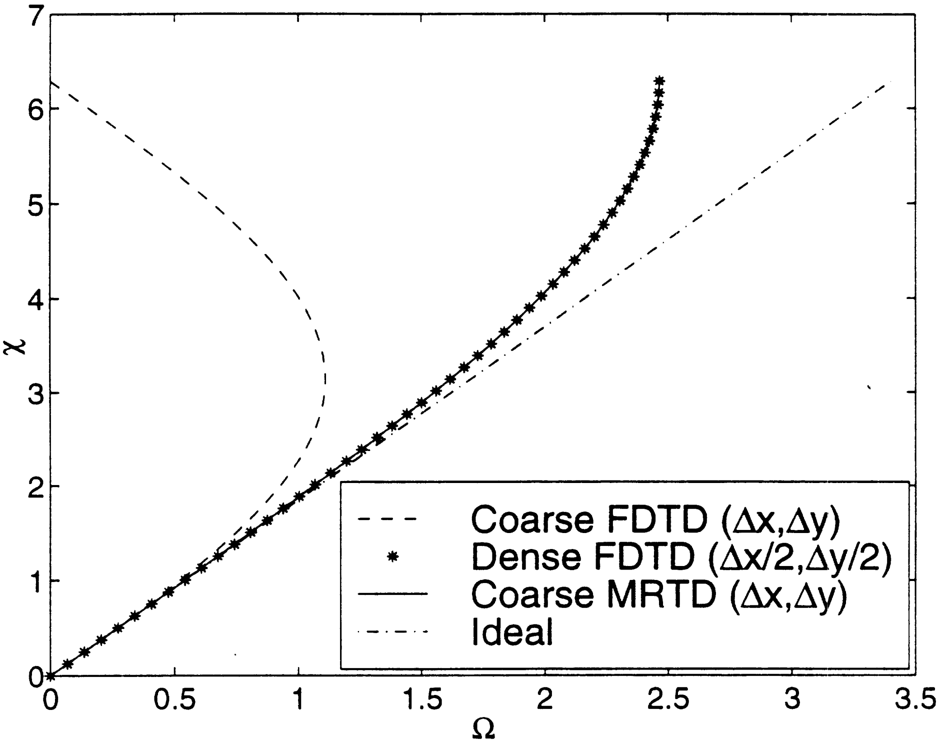

Figure 5.6: Dispersion of 2D MRTD (scaling and wavelet functions along $\hat{x}$ and $\hat{y}$) Vs. FDTD and ideal dispersions looking in the (1,1,0) direction.

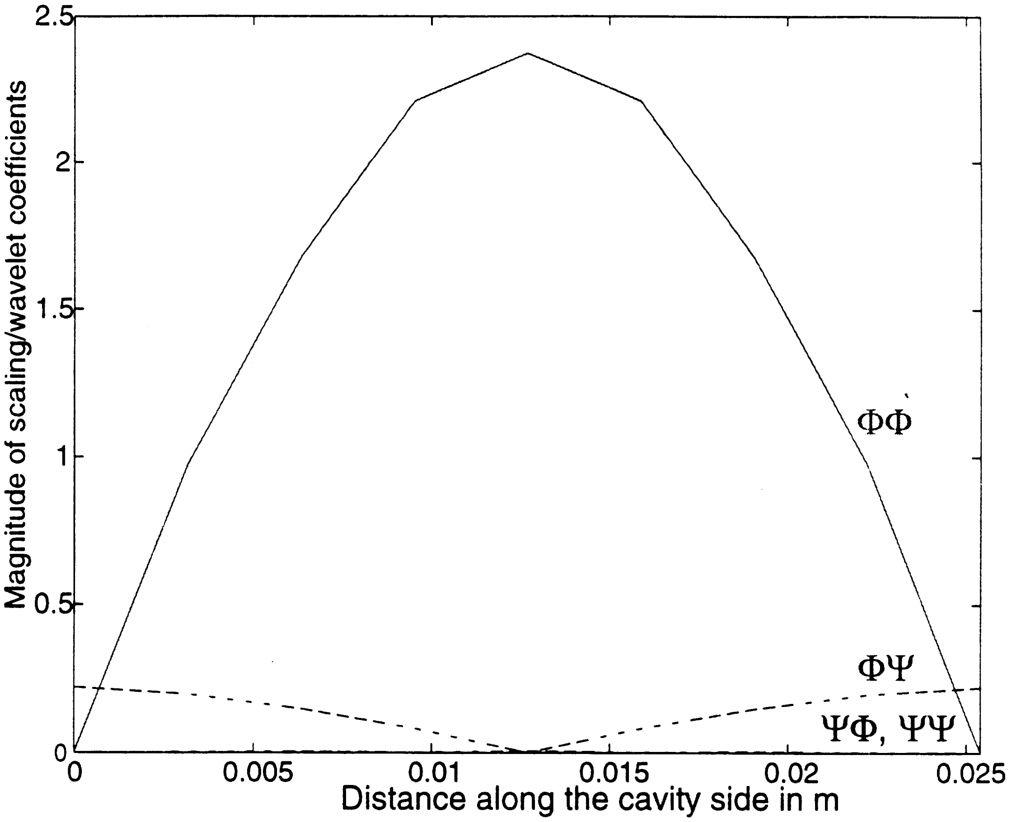

Figure 5.7: Amplitudes of Scaling and Wavelet Coefficients in a Waveguide.

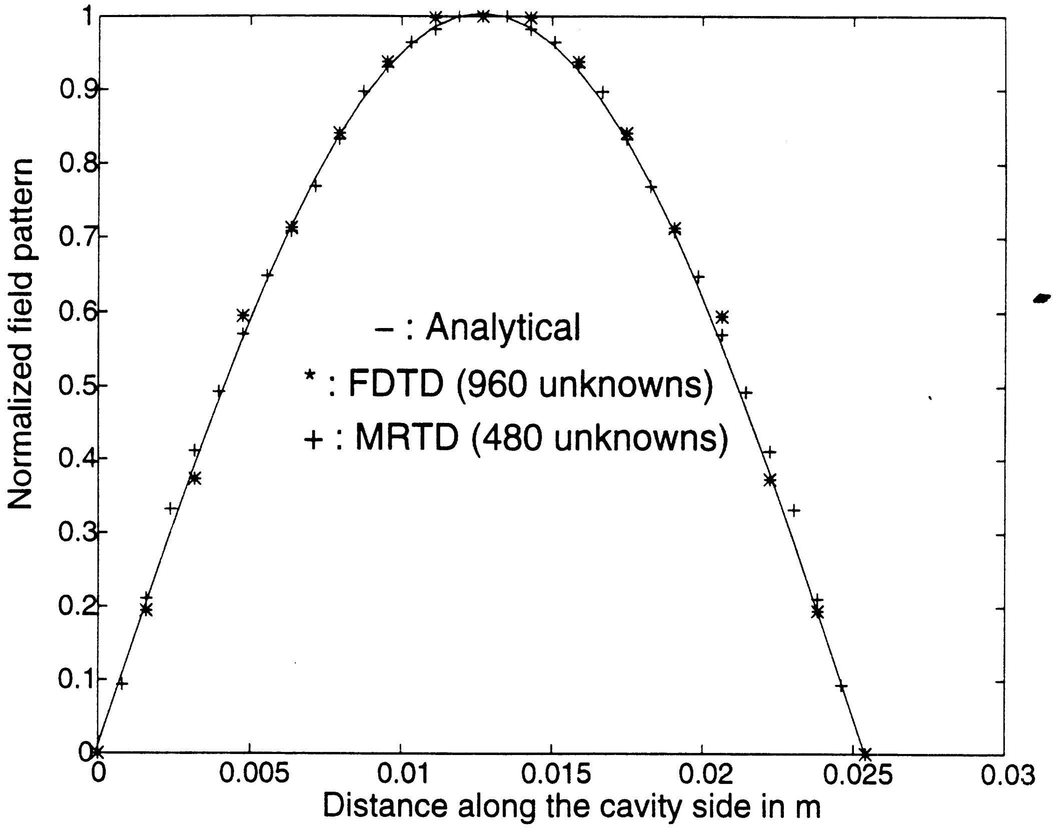

Figure 5.8: Comparison of MRTD , FDTD and Analytical Fields in a Waveguide.

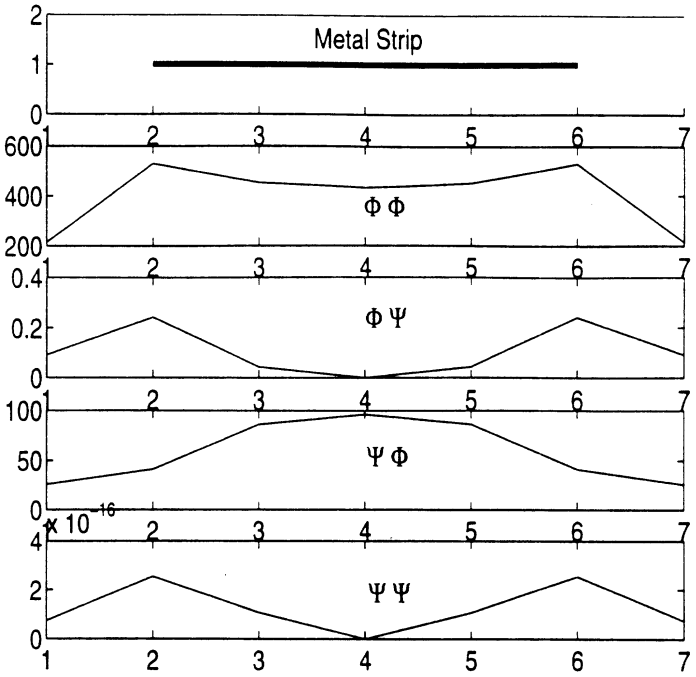

(a) Scaling, Wavelet Coeffs. just under the strip

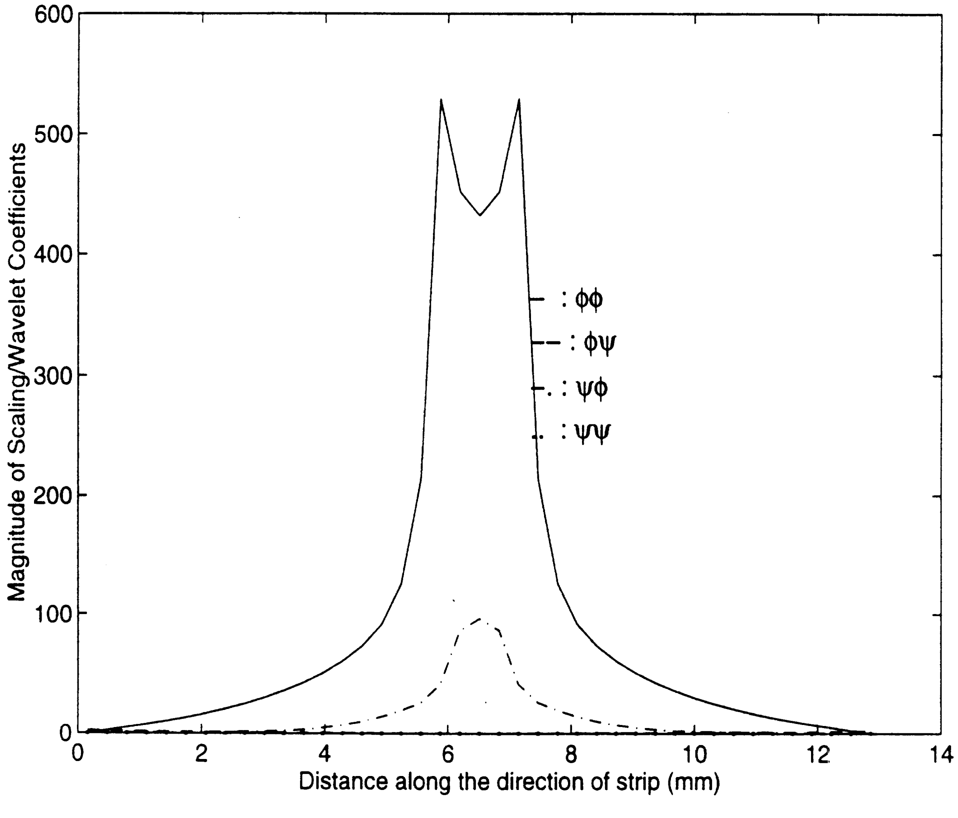

(b) Scaling, Wavelet Coeffs, all along the direction of strip

Figure 5.9: Normal Electric Field amplitudes of scaling and wavelet coefficients under the stripline

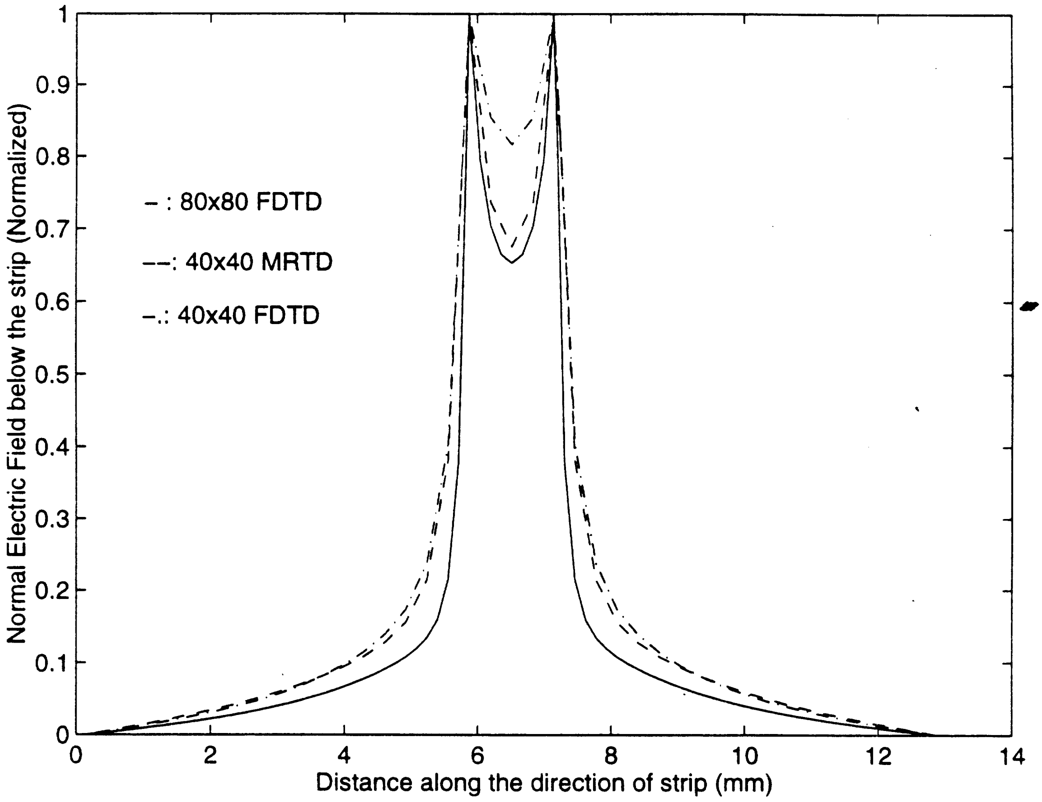

Figure 5.10: Comparison of Normal Electric Field under a stripline using MRTD and FDTD techniques.

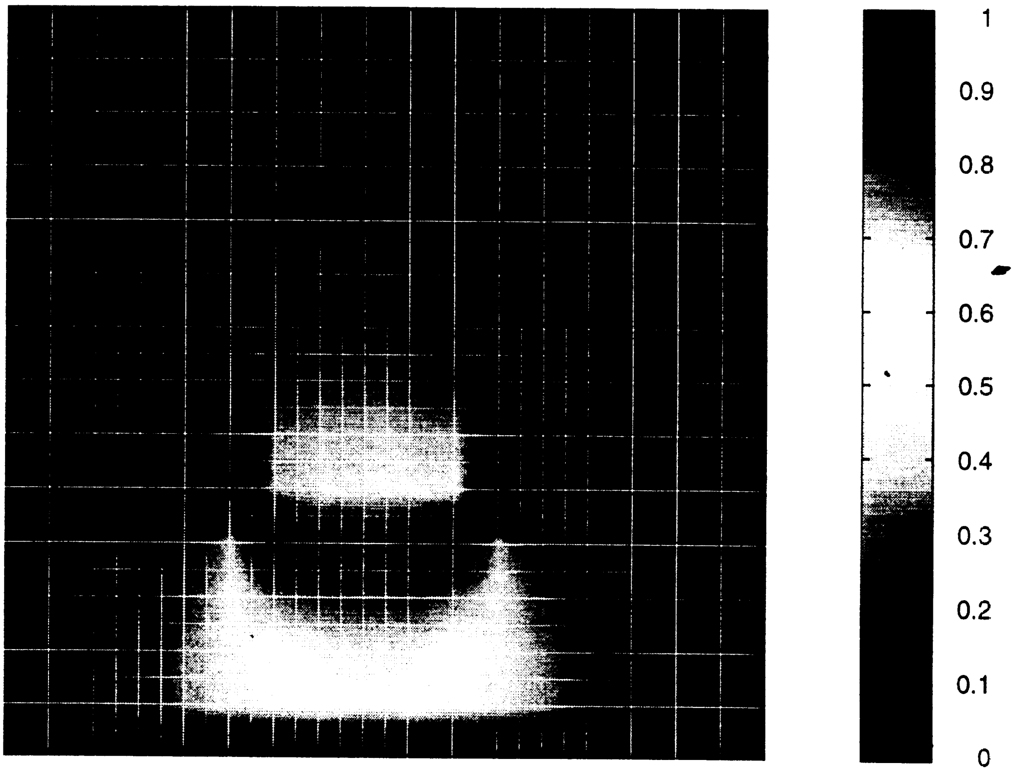

Figure 5.11: FDTD Multigrid and Field Plot of the Stripline.

CHAPTER 6

3D FIRST AND HIGHER RESOLUTION MRTD SCHEMES

In chapter 5, the zero resolution 2D MRTD (FDTD Multigrid) scheme was developed and applied to characterize some simple shielded structures. In this chapter, the 3D MRTD scheme is presented. To begin with, the zero resolution 3D MRTD scheme is developed. In this scheme, the scaling and wavelet schemes decouple. Thus the implementation of boundary conditions is more involved than it is in coupled schemes. Therefore, the details of implementation of boundary conditions for the zero resolution MRTD scheme are discussed. This is then followed by a derivation of first and higher resolution 3D MRTD schemes where it will be shown that the scaling and wavelet schemes couple, thereby simplifying the implementation of boundary conditions. Applications of boundary conditions in the MRTD method are presented. The MRTD scheme has been applied to characterize several 3D microwave circuits for validation.

6.1 Zero Resolution 3-D Haar-MRTD Scheme

The procedure to derive the zero resolution 3D Haar MRTD scheme is similar to that applied to derive the zero resolution 2D Haar MRTD scheme. Hence only a brief overview of the method is presented here. For simplicity, 3D MRTD scheme with wavelets along the $\hat{z}$ direction alone will be presented. Consider the following equation obtained from Maxwell's H-curl equation:

$$\epsilon\frac{\partial E_x}{\partial t} = \frac{\partial H_z}{\partial y} - \frac{\partial H_y}{\partial z} \tag{6.1}$$

This equation is rewritten in a differential operator form as shown below:

$$L_1(f_1(x,y,z,t)) + L_2(f_2(x,y,z,t)) = g \tag{6.2}$$

We now expand the fields using the Haar based MRA with scaling functions ϕ in all three directions and wavelet functions ψ^0 [78] in the z direction alone. The field expansion can be represented as follows:

$$\begin{aligned} f(x,y,z,t) &= [A][\phi(t)\phi(x)\phi(y)\phi(z)] \\ &+[B][\phi(t)\phi(x)\phi(y)\psi(z)] \end{aligned} \tag{6.3}$$

where $[\phi(\mathrm{t})\phi(\mathrm{x})\phi(\mathrm{y})\phi(\mathrm{z})]$ and $[\phi(\mathrm{t})\phi(\mathrm{x})\phi(\mathrm{y})\psi^0(\mathrm{z})]$ represent matrices whose elements are the corresponding basis functions in the computation domain of interest, and [A] and [B] represent the matrices of the unknown coefficients which give information about the fields and their derivatives.

Application of Galerkin's technique leads to the following schemes:

$$< [\phi\phi\phi], L_1(f_1) + L_2(f_2) >=< [\phi\phi\phi], g >: \phi\phi\phi Scheme$$

$$< [\phi\phi\psi^0], L_1(f_1) + L_2(f_2) >=< [\phi\phi\psi^0], g >: \phi\phi\psi^0 Scheme$$

Thus, by sampling Maxwell's differential equations with scaling and wavelet functions, we obtain a set of simultaneous discretized equations. For the zero resolution level of Haar wavelets, the above schemes decouple and coupling can be achieved only through the excitation term and boundaries. In the following sections, the conditions to be applied at these locations will be discussed.

To illustrate the treatment of boundary conditions in the zero resolution MRTD scheme, the parallel plate waveguide shown in Figure 6.1 is used. The plates are assumed to be infinite in width for simplicity and are separated by a distance of 24mm. A single mode (TEM) operation is chosen throughout this study.

To model the 'open' regions of the circuit, the Perfectly Matched Layer (PML) is used as an absorber. The details of PML implementation are in the zero resolution MRTD scheme are presented in section 6.3 The MRTD mesh is terminated by a PEC at the end of each PML layer.

6.2 Modeling of Excitation and Hard Boundaries in the Zero Resolution Haar-MRTD Scheme

6.2.1 Application of Source Term

To model excitation term in the conventional FDTD scheme, the excitation function is sampled with pulse functions to obtain the excitation coefficients. In MRTD scheme, the appropriate method of obtaining the scaling and wavelet excitation coefficients is to sample the excitation function with scaling and wavelet coefficients. However, in the zero resolution MRTD technique where the scaling and wavelet schemes decouple, to excite the wavelet scheme, continuity condition is applied at the interface between the source and its adjacent cell. To illustrate the treatment of the source term, the aforementioned parallel plate waveguide operating in TEM mode is analyzed. A signal with uniform spatial distribution along the waveguide cross section and Gaussian time distribution is chosen as the excitation. The amplitude of the scaling coefficients at the excitation plane is derived by sampling the excitation with pulse (Haar scaling) functions. The total electric field at the interface of the source and its adjacent cell must be continuous. Assuming that the field variation between these two cells is of the first order, it can be proved that the value of the wavelet coefficient is half that of the first derivative of the field. Thus, for a specific cell k with scaling and wavelet field amplitudes $E_k^{\phi\phi\phi}$ and $E_k^{\phi\phi\psi}$ respectively, the total field value at the position (k - 0.5)Δz equals $E_{tot,k-0.5}^{+} = E_k^{\phi\phi\phi} + 2E_k^{\phi\phi\psi}$ and location (k + 0.5)Δz equals $E_{tot,k+0.5}^{-} = E_k^{\phi\phi\phi} - 2E_k^{\phi\phi\psi}$. The amplitude of the wavelet coefficients at the excitation plane can be given by applying the continuity condition at the interface between the source and its adjacent cell: $E_{tot,k+0.5}^{-} = E_{tot,k+0.5}^{+}$. This leads to the following condition on the wavelet coefficients at the source location:

$$E_k^{\phi\phi\psi} = -0.5[E_{k+1}^{\phi\phi\phi} + 2E_{k+1}^{\phi\phi\psi} - E_k^{\phi\phi\phi}] \tag{6.4}$$

Figure 6.2 shows the scaling, wavelet and total electric fields, in the parallel plate waveguide which is shorted at one end with a PEC, without the use of the continuity condition, at an arbitrary time step after the incident pulse is reflected. It can be observed from the figure that the total field is not smooth; each cell interface introduces a spurious discontinuity. This implies that the values of the wavelet coefficients are not correct. Figure 6.3 on the other hand shows the scaling and wavelet coefficients along with the total field for the same geometry after applying the continuity condition given by Eq. 6.4. The smoothness of the total field here indicates that the wavelet coefficients have the correct magnitude and phase when the source condition is applied. Without the continuity condition, the boundary conditions are satisfied only for the average field values (scaling coefficients), whereas, continuity condition ensures that the appropriate boundary conditions are satisfied on the total field which depends on the average field as well as the derivatives of the field (wavelet coefficients).

6.2.2 Treatment of PECs

At the interface of a PEC, the total tangential Electric field is equal to 0. In the conventional FDTD scheme which uses scaling functions alone, consistency with image theory is implicit in the method of implementation of the boundary condition, where the scaling coefficients of the tangential electric field components at the location of the PEC are set equal to zero. Since the location of the origin (center) of the mother wavelet for the tangential electric field component in the zero resolution Haar MRTD scheme coincides with the location of the PEC, the requirement that the scaling coefficients of the tangential electric field components have a zero value at the PEC location is sufficient for the satisfaction of the boundary condition. However, since wavelet coefficients indicate the local derivatives of the field, they can have a nonzero value. Since the scaling and wavelet functions in zero resolution Haar MRTD scheme decouple, the value of the wavelet coefficients can be calculated by applying continuity condition on the tangential electric field as shown in Eq. 6.4 above. For a PEC located at cell k = 0, applying Eq. 6.4 and noting that the scaling coefficient of the tangential electric field $E_0^{\phi\phi\phi}$ is zero at the PEC, we obtain the following equation for the wavelet coefficients of the tangential electric field.

$$E_0^{\phi\phi\psi} = -0.5[E_1^{\phi\phi\phi} + 2E_1^{\phi\phi\psi}] \tag{6.5}$$

To validate this approach of treating PECs, the parallel plate shown in Fig. 6.1 is terminated by a PEC wall and characterized with and without applying the continuity condition given in Eq. 6.5. Figure 6.4 shows the reflected scaling, wavelet and total fields at an arbitrary instant of time without using Eq. 6.5. Figure 6.5 shows the same fields in the case where Eq. 6.5 is used. The smoothness of the total electric field obtained here in contrast to the total field seen in Figure 6.5 validates implementation of the PEC condition and demonstrates the necessity of applying the continuity condition at the PEC location.

6.2.3 Treatment of Dielectric Interfaces

In the conventional FDTD scheme, the field components which are located at the interface of two dielectrics are calculated by assigning the permittivity at that location to be the average value of the permittivity of the materials on either sides of the interface. It can be proved that dicretizing the constitutive relation, $D = \epsilon E$, by using pulse bases for field expansions followed by sampling using Galerkin's method leads to the FDTD approach of averaging the value of permittivities to model the fields at the interface. In the MRTD scheme, this approach needs to be appropriately generalized in order to accurately model dielectric interfaces. Consider a dielectric interface at location k (assume the dielectric interface to be perpendicular to the direction of propagation $\hat{z}$) for the parallel plate waveguide considered above. It is assumed here that the dielectric interface coincides with the cell boundary, implying that the same dielectric material fills the entire cell. Let the dielectric constant of the material to the left of the interface be ϵ_{r1} and that of the material to the right be ϵ_{r2}. By expanding the electric flux density (D) and electric field (E) in terms of the scaling and wavelet functions and applying the method of moments to the constitutive relationship, it can be shown that for the zero resolution MRTD scheme, at the interface location k, the coefficients of D and E are related by the following coupled equations:

$$D_k^{x,\phi\phi\phi} = 0.5\epsilon_0[(\epsilon_{r1} + \epsilon_{r2})E_k^{x,\phi\phi\phi} + (\epsilon_{r1} - \epsilon_{r2})E_k^{x,\phi\phi\psi^0}] \tag{6.6}$$

$$D_k^{x,\phi\phi\psi^0} = 0.5\epsilon_0[(\epsilon_{r1} + \epsilon_{r2})E_k^{x,\phi\phi\psi^0} + (\epsilon_{r1} - \epsilon_{r2})E_k^{x,\phi\phi\phi}] \tag{6.7}$$

$$D_k^{y,\phi\phi\phi} = 0.5\epsilon_0[(\epsilon_{r1} + \epsilon_{r2})E_k^{y,\phi\phi\phi} + (\epsilon_{r1} - \epsilon_{r2})E_k^{y,\phi\phi\psi^0}] \tag{6.8}$$

$$D_k^{y,\phi\phi\psi^0} = 0.5\epsilon_0[(\epsilon_{r1} + \epsilon_{r2})E_k^{y,\phi\phi\psi^0} + (\epsilon_{r1} - \epsilon_{r2})E_k^{y,\phi\phi\phi}] \tag{6.9}$$

When the dielectric interface is perpendicular to $\hat{z}$ and at the interface if two cells, as per the yee scheme relative field positions, seen in Fig. 5.1 the D_z and E_z components within each cell don't see any dielectric discontinuity. Hence, the discretized equations corresponding to E_z component become:

$$D_k^{z,\phi\phi\phi} = \epsilon_0\epsilon_{r1}E_k^{z,\phi\phi\phi} \tag{6.10}$$

$$D_k^{z,\phi\phi\psi^0} = \epsilon_0\epsilon_{r1}E_k^{z,\phi\phi\psi^0} \tag{6.11}$$

As seen from Eq. 6.6, when the wavelet component is set to zero, the FDTD approach of averaging the permittivity values is obtained.

In addition to the coupled Eqs. 6.6 and 6.7, in the zero resolution MRTD scheme, the continuity of the total tangential electric field at nodes adjacent to the interface needs to be ensured. Following the same procedure that leads to Eq. 6.4, we obtain the following equations for the electric field coefficients tangential to the dielectric interface k, to the left and right of the interface.

$$E_{k-1}^{\phi\phi\psi^0} = +0.5[E_{k-2}^{\phi\phi\phi} - 2E_{k-2}^{\phi\phi\psi^0} - E_{k-1}^{\phi\phi\phi}] \tag{6.12}$$

$$E_{k+1}^{\phi\phi\psi^0} = -0.5[E_{k+2}^{\phi\phi\phi} + 2E_{k+2}^{\phi\phi\psi^0} - E_{k+1}^{\phi\phi\phi}] \tag{6.13}$$

Figs. 6.6 and 6.7 show plots of the scaling, wavelet coefficients and total flux density with and without the use of the above continuity equations respectively, for the aforementioned parallel plate waveguide whose first half is filled with air and second half with a material of $\epsilon_r = 10$. As mentioned earlier, the plane of discontinuity in this case is perpendicular to the direction of propagation. The smoothness of the total field in Figure 6.7 in comparison to its roughness in Figures 6.6 validates the continuity conditions in Eqs. 6.12 and 6.13.

6.3 Modeling of Open boundaries in Zero Resolution Haar-MRTD Scheme using the Perfectly Matched Layer (PML) Absorber

To model 'open' regions so as to simulate an unbounded medium in the computational domain, the Perfectly Matched Layer (PML) absorber is used in the MRTD scheme here. The PML absorber which was originally proposed by Berenger [32] is based on creating a non physical absorbing medium adjacent to outer mesh boundary in the computational domain by splitting the E and H field components in the absorber area and assigning artificial electric and magnetic loss coefficients. In the zero resolution MRTD scheme here, a modified unsplit formulation of PML is applied where it is assumed that the conductivity is given in terms of scaling functions in space [79]. While the technique of expanding the conductivity in terms of scaling functions alone leads to a PML absorber with very good absorption for FDTD and zero resolution MRTD schemes, the performance of the PML based on scaling expansions deteriorates for higher resolution MRTD schemes. To address this problem, a modified PML implementation has been developed and will be presented in section 6.6.4.

In this section, the PML absorber which uses scaling functions alone for field expansions is presented. For the zero resolution MRTD scheme, this PML implementation leads to an absorption of reflections as low as -80dB. Let the PML area be characterized by permittivity and permeability (ϵ_o, μ_o) and electric and magnetic conductivities (σ_E, σ_H). The fields in the PML region can be modeled by adding the conductivity terms to Maxwell's equations as shown below:

$$\epsilon\frac{\partial E_x}{\partial t} + \sigma_E E_x = \frac{\partial H_z}{\partial y} - \frac{\partial H_y}{\partial z} \tag{6.14}$$

$$\epsilon\frac{\partial E_y}{\partial t} + \sigma_E E_y = \frac{\partial H_x}{\partial z} - \frac{\partial H_z}{\partial x} \tag{6.15}$$

$$\epsilon\frac{\partial E_z}{\partial t} + \sigma_E E_z = \frac{\partial H_y}{\partial x} - \frac{\partial H_x}{\partial y} \tag{6.16}$$

$$\mu\frac{\partial H_x}{\partial t} + \sigma_H H_x = \frac{\partial E_y}{\partial z} - \frac{\partial E_z}{\partial y} \tag{6.17}$$

$$\mu\frac{\partial H_y}{\partial t} + \sigma_H H_y = \frac{\partial E_z}{\partial x} - \frac{\partial E_x}{\partial z} \tag{6.18}$$

$$\mu\frac{\partial H_z}{\partial t} + \sigma_H H_z = \frac{\partial E_x}{\partial y} - \frac{\partial E_y}{\partial x} \tag{6.19}$$

In the interest of simplicity, MRTD scheme with wavelets and PML cells in $\hat{z}$ direction alone is considered. Extension to general case is straightforward. At each cell location z in the PML region, the electric and magnetic conductivities are chosen as follows:

$$\frac{\sigma_E(z)}{\epsilon_o} = \frac{\sigma_H(z)}{\mu_o} \tag{6.20}$$

The spatial distribution of $\sigma_{E,H}$ is modeled by assuming that the amplitudes of the scaling functions have a parabolic distribution as shown below:

$$\sigma_{E,H}(z) = \sigma_{E,H}^{max}(1 - \frac{z}{\delta})^2 \tag{6.21}$$

where δ is the thickness of the PML and $0 \leq z \leq \delta$ The PML area is terminated with a PEC. The maximum value $\sigma_{E,H}^{max}$ is determined by the designated reflection coefficient R at normal incidence and is obtained from the following equation [32]:

$$R = e^{-\frac{2}{\epsilon_o c}\int_0^\delta \sigma_E(z)dz} \tag{6.22}$$

To obtain the MRTD discretized equations in the PML region, Eqs. 6.14 -6.19 are discretized using Galerkin's technique in a similar approach used to obtain the regular MRTD discretized equation discussed in sections 6.1 and 6.4. However, as mentioned in [32], direct discretization of these equations leads to numerical reflections resulting from sharp variations of conductivity. To circumvent this problem, an exponential time stepping approach is adopted. To do this, the following equations are substituted in Eqs. 6.14-6.19:

$$E_i(x,y,z,t) = \tilde{E}_i(x,y,z,t)e^{-\sigma_E(z)t/\epsilon_o} \tag{6.23}$$

$$H_i(x,y,z,t) = \tilde{H}_i(x,y,z,t)e^{-\sigma_H(z)t/\mu_o} \tag{6.24}$$

where $i = x, y, z$

We thus obtain the following equations:

$$\epsilon\frac{\partial \tilde{E}_x}{\partial t} = \frac{\partial \tilde{H}_z}{\partial y} - \frac{\partial \tilde{H}_y}{\partial z} + \tilde{H}_y\frac{t}{\epsilon}\frac{\partial \sigma^E(z)}{\partial z} \tag{6.25}$$

$$\epsilon\frac{\partial \tilde{E}_y}{\partial t} = \frac{\partial \tilde{H}_x}{\partial z} - \tilde{H}_x\frac{t}{\epsilon}\frac{\partial \sigma^E(z)}{\partial z} - \frac{\partial \tilde{H}_z}{\partial x} \tag{6.26}$$

$$\epsilon\frac{\partial \tilde{E}_z}{\partial t} = \frac{\partial \tilde{H}_y}{\partial x} - \frac{\partial \tilde{H}_x}{\partial y} \tag{6.27}$$

$$\mu\frac{\partial \tilde{H}_x}{\partial t} = \frac{\partial \tilde{E}_y}{\partial z} - \tilde{E}_y\frac{t}{\mu}\frac{\partial \sigma^H(z)}{\partial z} - \frac{\partial \tilde{E}_z}{\partial y} \tag{6.28}$$

$$\mu\frac{\partial \tilde{H}_y}{\partial t} = \frac{\partial \tilde{E}_z}{\partial x} - \frac{\partial \tilde{E}_x}{\partial z} + \tilde{E}_x\frac{t}{\mu}\frac{\partial \sigma^H(z)}{\partial z} \tag{6.29}$$

$$\mu\frac{\partial \tilde{H}_z}{\partial t} = \frac{\partial \tilde{E}_x}{\partial y} - \frac{\partial \tilde{E}_y}{\partial x} \tag{6.30}$$

Since the functions $\sigma^E(z)$ and $\sigma^H(z)$ are expanded in terms of scaling functions, and since Haar scaling functions are pulse functions, it turns out that while sampling the equations above using Galerkin's technique, the terms involving $\frac{\partial \sigma^{H,E}(z)}{\partial z}$ in Eqs. 6.25-6.30 become zero. Hence it can be seen that Eqs. 6.25- 6.30 have the same form as Maxwell's equations in a lossless non-PML region. Therefore, to obtain the PML discretized equations, we follow the same approach that was used to obtain MRTD discretized equations:

The terms $\tilde{E}_x$, $\tilde{E}_y$, $\tilde{E}_z$, $\tilde{H}_x$, $\tilde{H}_y$ and $\tilde{H}_z$ in Eqs. 6.25- 6.30 are expanded as follows (assuming wavelets are applied in the $\hat{z}$ alone:

$$\begin{aligned}\tilde{E}_x(x,y,z,t) = & \sum_{k,l,m,n=-\infty}^{+\infty} {}_k\tilde{E}^{x,\phi\phi\phi}_{l-1/2,m,n} h_k(t)\phi_{l-1/2}(x)\phi_m(y)\phi_n(z) + \\ & \sum_{k,l,m=-\infty}^{+\infty} {}_k\tilde{E}^{x,\phi\phi\psi^0}_{l-1/2,m,n} h_k(t)\phi_{l-1/2}(x)\phi_m(y)\psi^0_n(z)\end{aligned} \tag{6.31}$$

$$\begin{aligned}\tilde{E}_y(x,y,z,t) = & \sum_{k,l,m,n=-\infty}^{+\infty} {}_k\tilde{E}^{y,\phi\phi\phi}_{l,m-1/2,n} h_k(t)\phi_l(x)\phi_{m-1/2}(y)\phi_n(z) + \\ & \sum_{k,l,m=-\infty}^{+\infty} {}_k\tilde{E}^{y,\phi\phi\psi^0}_{l,m-1/2,n} h_k(t)\phi_l(x)\phi_{m-1/2}(y)\psi^0_n(z)\end{aligned} \tag{6.32}$$

$$\begin{aligned}\tilde{E}_z(x,y,z,t) = & \sum_{k,l,m,n=-\infty}^{+\infty} {}_k\tilde{E}^{z,\phi\phi\phi}_{l,m,n-1/2} h_k(t)\phi_l(x)\phi_m(y)\phi_{n-1/2}(z) + \\ & \sum_{k,l,m=-\infty}^{+\infty} {}_k\tilde{E}^{z,\phi\phi\psi^0}_{l,m,n-1/2} h_k(t)\phi_l(x)\phi_m(y)\psi^0_{n-1/2}(z)\end{aligned} \tag{6.33}$$

$$\begin{aligned}\tilde{H}_x(x,y,z,t) = & \sum_{k,l,m,n=-\infty}^{+\infty} {}_k\tilde{H}^{x,\phi\phi\phi}_{l,m-1/2,n-1/2} h_k(t)\phi_l(x)\phi_{m-1/2}(y)\phi_{n-1/2}(z) + \\ & \sum_{k,l,m=-\infty}^{+\infty} {}_k\tilde{H}^{x,\phi\phi\psi^0}_{l,m-1/2,n-1/2} h_k(t)\phi_l(x)\phi_{m-1/2}(y)\psi^0_{n-1/2}(z)\end{aligned} \tag{6.34}$$

$$\begin{aligned}\tilde{H}_y(x,y,z,t) = & \sum_{k,l,m,n=-\infty}^{+\infty} {}_k\tilde{H}^{y,\phi\phi\phi}_{l-1/2,m,n-1/2} h_k(t)\phi_{l-1/2}(x)\phi_m(y)\phi_{n-1/2}(z) + \\ & \sum_{k,l,m=-\infty}^{+\infty} {}_k\tilde{H}^{y,\phi\phi\psi^0}_{l-1/2,m,n-1/2} h_k(t)\phi_{l-1/2}(x)\phi_m(y)\psi^0_{n-1/2}(z)\end{aligned} \tag{6.35}$$

$$\begin{aligned}\tilde{H}_z(x,y,z,t) = & \sum_{k,l,m,n=-\infty}^{+\infty} {}_k\tilde{H}^{z,\phi\phi\phi}_{l-1/2,m-1/2,n} h_k(t)\phi_{l-1/2}(x)\phi_{m-1/2}(y)\phi_n(z) + \\ & \sum_{k,l,m=-\infty}^{+\infty} {}_k\tilde{H}^{z,\phi\phi\psi^0}_{l-1/2,m-1/2,n} h_k(t)\phi_{l-1/2}(x)\phi_{m-1/2}(y)\psi^0_n(z)\end{aligned} \tag{6.36}$$

Next, Galerkin's technique is applied to obtain the discretized equations. Since the scaling and wavelet schemes decouple in the zero resolution MRTD technique, the discretized equations have the same form as the FDTD discretized equations for the scaling as well as wavelet schemes. The exact method of obtaining the discretized equations using Galerkin's technique is presented in greater detail in section 5.4.2. In this section, only the final results are presented. The discretized equations for the scaling scheme are presented below.

$$\epsilon\frac{{}^{\lambda}\tilde{E}^{x,\phi\phi\phi}_{l'-1/2,m',n'} - {}^{\lambda-1}\tilde{E}^{x,\phi\phi\phi}_{l'-1/2,m',n'}}{\Delta t} = \frac{{}^{\lambda-1/2}\tilde{H}^{z,\phi\phi\phi}_{l'-1/2,m'+1/2,n'} - {}^{\lambda-1/2}\tilde{H}^{z,\phi\phi\phi}_{l'-1/2,m'-1/2,n'}}{\Delta y} - \frac{{}^{\lambda-1/2}\tilde{H}^{y,\phi\phi\phi}_{l'-1/2,m',n'+1/2} - {}^{\lambda-1/2}\tilde{H}^{y,\phi\phi\phi}_{l'-1/2,m',n'-1/2}}{\Delta z} \tag{6.37}$$

$$\epsilon\frac{{}^{\lambda}\tilde{E}^{y,\phi\phi\phi}_{l',m'-1/2,n'} - {}^{\lambda-1}\tilde{E}^{y,\phi\phi\phi}_{l',m'-1/2,n'}}{\Delta t} = \frac{{}^{\lambda-1/2}\tilde{H}^{x,\phi\phi\phi}_{l',m'-1/2,n'+1/2} - {}^{\lambda-1/2}\tilde{H}^{x,\phi\phi\phi}_{l',m'-1/2,n'-1/2}}{\Delta z} - \frac{{}^{\lambda-1/2}\tilde{H}^{z,\phi\phi\phi}_{l'+1/2,m'-1/2,n'} - {}^{\lambda-1/2}\tilde{H}^{z,\phi\phi\phi}_{l'-1/2,m'-1/2,n'}}{\Delta x} \tag{6.38}$$

$$\epsilon\frac{{}^{\lambda}\tilde{E}^{z,\phi\phi\phi}_{l',m',n'-1/2} - {}^{\lambda-1}\tilde{E}^{z,\phi\phi\phi}_{l',m',n'-1/2}}{\Delta t} = \frac{{}^{\lambda-1/2}\tilde{H}^{y,\phi\phi\phi}_{l'+1/2,m',n'-1/2} - {}^{\lambda-1/2}\tilde{H}^{y,\phi\phi\phi}_{l'-1/2,m',n'-1/2}}{\Delta x} - \frac{{}^{\lambda-1/2}\tilde{H}^{x,\phi\phi\phi}_{l',m'+1/2,n'-1/2} - {}^{\lambda-1/2}\tilde{H}^{x,\phi\phi\phi}_{l',m'-1/2,n'-1/2}}{\Delta y} \tag{6.39}$$

$$\mu\frac{{}^{\lambda+1/2}\tilde{H}^{x,\phi\phi\phi}_{l',m'-1/2,n'-1/2} - {}^{\lambda-1/2}\tilde{H}^{x,\phi\phi\phi}_{l',m'-1/2,n'-1/2}}{\Delta t} = -\frac{{}^{\lambda}\tilde{E}^{z,\phi\phi\phi}_{l',m',n'-1/2} - {}^{\lambda}\tilde{E}^{z,\phi\phi\phi}_{l',m'-1,n'-1/2}}{\Delta y} + \frac{{}^{\lambda}\tilde{E}^{y,\phi\phi\phi}_{l',m'-1/2,n'} - {}^{\lambda}\tilde{E}^{y,\phi\phi\phi}_{l',m'-1/2,n'-1}}{\Delta z} \tag{6.40}$$

$$\mu\frac{{}^{\lambda+1/2}\tilde{H}^{y,\phi\phi\phi}_{l'-1/2,m',n'-1/2} - {}^{\lambda-1/2}\tilde{H}^{y,\phi\phi\phi}_{l'-1/2,m',n'-1/2}}{\Delta t} = -\frac{{}^{\lambda}\tilde{E}^{x,\phi\phi\phi}_{l'-1/2,m',n'} - {}^{\lambda}\tilde{E}^{x,\phi\phi\phi}_{l'-1/2,m',n'-1}}{\Delta z} + \frac{{}^{\lambda}\tilde{E}^{z,\phi\phi\phi}_{l',m',n'-1/2} - {}^{\lambda}\tilde{E}^{z,\phi\phi\phi}_{l'-1,m',n'-1/2}}{\Delta x} \tag{6.41}$$

$$\mu \frac{{}_{\lambda+1/2}\tilde{H}^{z,\phi\phi\phi}_{l'-1/2,m'-1/2,n'} - {}_{\lambda-1/2}\tilde{H}^{z,\phi\phi\phi}_{l'-1/2,m'-1/2,n'}}{\Delta t} =$$
$$- \frac{{}_{\lambda}\tilde{E}^{y,\phi\phi\phi}_{l',m'-1/2,n'} - {}_{\lambda}\tilde{E}^{y,\phi\phi\phi}_{l'-1,m'-1/2,n'}}{\Delta x}$$
$$+ \frac{{}_{\lambda}\tilde{E}^{x,\phi\phi\phi}_{l'-1/2,m',n'} - {}_{\lambda}\tilde{E}^{x,\phi\phi\phi}_{l'-1/2,m'-1,n'}}{\Delta y} \qquad (6.42)$$

The final step in obtaining the discretized equations for the PML region is to write the equations above in terms of the electric and magnetic field coefficients. To do this, Eq. 6.23 and 6.24 need to be discretized. This is done by expanding $\tilde{E_x}$, $\tilde{E_y}$, $\tilde{E_z}$, $\tilde{H_x}$, $\tilde{H_y}$ and $\tilde{H_z}$ in Eqs. 6.23- 6.24 are expanded using Eqs. 6.31-6.36. E_x, E_y, E_z, H_x, H_y and H_z are expanded similarly using the following equations:

$$E_x(x,y,z,t) = \sum_{k,l,m,n=-\infty}^{+\infty} {}_kE^{x,\phi\phi\phi}_{l-1/2,m,n} h_k(t)\phi_{l-1/2}(x)\phi_m(y)\phi_n(z) + \sum_{k,l,m=-\infty}^{+\infty} {}_kE^{x,\phi\phi\psi^0}_{l-1/2,m,n} h_k(t)\phi_{l-1/2}(x)\phi_m(y)\psi^0_n(z) \qquad (6.43)$$

$$E_y(x,y,z,t) = \sum_{k,l,m,n=-\infty}^{+\infty} {}_kE^{y,\phi\phi\phi}_{l,m-1/2,n} h_k(t)\phi_l(x)\phi_{m-1/2}(y)\phi_n(z) + \sum_{k,l,m=-\infty}^{+\infty} {}_kE^{y,\phi\phi\psi^0}_{l,m-1/2,n} h_k(t)\phi_l(x)\phi_{m-1/2}(y)\psi^0_n(z) \qquad (6.44)$$

$$E_z(x,y,z,t) = \sum_{k,l,m,n=-\infty}^{+\infty} {}_kE^{z,\phi\phi\phi}_{l,m,n-1/2} h_k(t)\phi_l(x)\phi_m(y)\phi_{n-1/2}(z) + \sum_{k,l,m=-\infty}^{+\infty} {}_kE^{z,\phi\phi\psi^0}_{l,m,n-1/2} h_k(t)\phi_l(x)\phi_m(y)\psi^0_{n-1/2}(z) \qquad (6.45)$$

$$
\begin{aligned}
H_x(x,y,z,t) = & \sum_{k,l,m,n=-\infty}^{+\infty} {}_kH^{x,\phi\phi\phi}_{l,m-1/2,n-1/2} h_k(t)\phi_l(x)\phi_{m-1/2}(y)\phi_{n-1/2}(z) + \\
& \sum_{k,l,m=-\infty}^{+\infty} {}_kH^{x,\phi\phi\psi^0}_{l,m-1/2,n-1/2} h_k(t)\phi_l(x)\phi_{m-1/2}(y)\psi^0_{n-1/2}(z)
\end{aligned}
\tag{6.46}
$$

$$
\begin{aligned}
H_y(x,y,z,t) = & \sum_{k,l,m,n=-\infty}^{+\infty} {}_kH^{y,\phi\phi\phi}_{l-1/2,m,n-1/2} h_k(t)\phi_{l-1/2}(x)\phi_m(y)\phi_{n-1/2}(z) + \\
& \sum_{k,l,m=-\infty}^{+\infty} {}_kH^{y,\phi\phi\psi^0}_{l-1/2,m,n-1/2} h_k(t)\phi_{l-1/2}(x)\phi_m(y)\psi^0_{n-1/2}(z)
\end{aligned}
\tag{6.47}
$$

$$
\begin{aligned}
H_z(x,y,z,t) = & \sum_{k,l,m,n=-\infty}^{+\infty} {}_kH^{z,\phi\phi\phi}_{l-1/2,m-1/2,n} h_k(t)\phi_{l-1/2}(x)\phi_{m-1/2}(y)\phi_n(z) + \\
& \sum_{k,l,m=-\infty}^{+\infty} {}_kH^{z,\phi\phi\psi^0}_{l-1/2,m-1/2,n} h_k(t)\phi_{l-1/2}(x)\phi_{m-1/2}(y)\psi^0_n(z)
\end{aligned}
\tag{6.48}
$$

The above equations for fields are substituted into Eqs. 6.23- 6.24 and sampled using Galerkin's technique. For example, when sampling Eq. 6.23 with E_x field component, we obtain the following two schemes for the zero resolution MRTD technique:

$$
\begin{aligned}
< [h_\lambda(t)\phi_{l'-1/2}(x)\phi_{m'}(y)\phi_{n'}(z)], (& \sum_{k,l,m=-\infty}^{+\infty} [{}_kE^{x,\phi\phi\phi}_{l-1/2,m,n} h_k(t)\phi_{l-1/2}(x)\phi_m(y)\phi_n(z) + \\
& \sum_{k,l,m=-\infty}^{+\infty} {}_kE^{x,\phi\phi\psi^0}_{l-1/2,m,n} h_k(t)\phi_{l-1/2}(x)\phi_m(y)\psi^0_n(z)) = \\
e^{-\sigma_E(z)t/\epsilon}(& \sum_{k,l,m=-\infty}^{+\infty} [{}_k\tilde{E}^{x,\phi\phi\phi}_{l-1/2,m,n} h_k(t)\phi_{l-1/2}(x)\phi_m(y)\phi_n(z) + \\
& \sum_{k,l,m=-\infty}^{+\infty} {}_k\tilde{E}^{x,\phi\phi\psi^0}_{l-1/2,m,n} h_k(t)\phi_{l-1/2}(x)\phi_m(y)\psi^0_n(z)) >
\end{aligned}
\tag{6.49}
$$

$$< [h_\lambda(t)\phi_{l'-1/2}(x)\phi_{m'}(y)\psi^0_{n'}(z)],(\sum_{k,l,m=-\infty}^{+\infty} [{}_kE^{x,\phi\phi\phi}_{l-1/2,m,n}h_k(t)\phi_{l-1/2}(x)\phi_m(y)\phi_n(z) +$$

$$\sum_{k,l,m=-\infty}^{+\infty} {}_kE^{x,\phi\phi\psi^0}_{l-1/2,m,n}h_k(t)\phi_{l-1/2}(x)\phi_m(y)\psi^0_n(z)) =$$

$$e^{-\sigma_E(z)t/\epsilon}(\sum_{k,l,m=-\infty}^{+\infty} [{}_k\tilde{E}^{x,\phi\phi\phi}_{l-1/2,m,n}h_k(t)\phi_{l-1/2}(x)\phi_m(y)\phi_n(z) +$$

$$\sum_{k,l,m=-\infty}^{+\infty} {}_k\tilde{E}^{x,\phi\phi\psi^0}_{l-1/2,m,n}h_k(t)\phi_{l-1/2}(x)\phi_m(y)\psi^0_n(z)) > \quad (6.50)$$

Simplifying Eqs. 6.49 and 6.50 involves using the integral

$$\int_{-\infty}^{+\infty} h_\lambda(t)h_k(t)e^{-\sigma_E(z)t/\epsilon}dt = \delta_{\lambda,k}\Delta t\frac{sinh(\frac{\sigma_E(z)t}{2\epsilon})}{\frac{\sigma_E(z)t}{2\epsilon}}e^{-\sigma_E(z)\lambda\Delta t/\epsilon} \quad (6.51)$$

Note that while evaluating the integrals, even though the expression $e^{-\sigma_E(z)t/\epsilon}$ has spatial as well as time dependence, it is assumed to be part of the time integral. This is because the conductivity is expanded in terms of scaling functions in space and hence for the Haar-MRTD scheme, the terms is constant over the spatial window of the integral. The amplitude of the scaling coefficients of the conductivity terms are parabolic as mentioned earlier. We thus obtain the following relations after simplifying Eqs. 6.49 and 6.50:

$${}_kE^{x,\phi\phi\phi}_{l-1/2,m,n} ={}_k \tilde{E}^{x,\phi\phi\phi}_{l-1/2,m,n}e^{-\sigma_E^n\lambda\Delta t/\epsilon}\frac{sinh(\frac{\sigma_E(z)\Delta t}{2\epsilon})}{(\frac{\sigma_E(z)\Delta t}{2\epsilon})} \quad (6.52)$$

$${}_kE^{x,\phi\phi\psi^0}_{l-1/2,m,n} ={}_k \tilde{E}^{x,\phi\phi\psi^0}_{l-1/2,m,n}e^{-\sigma_E^n\lambda\Delta t/\epsilon}\frac{sinh(\frac{\sigma_E(z)\Delta t}{2\epsilon})}{(\frac{\sigma_E(z)\Delta t}{2\epsilon})} \quad (6.53)$$

For most practical cases, $\frac{\sigma_E(z)t}{2\epsilon}$ is a very small value. Hence using the approximation $sinh(x)/x \approx 1$ for $x \to 0$, we obtain the following simplification of Eqs. 6.52 and 6.53

$${}_kE^{x,\phi\phi\phi}_{l-1/2,m,n} ={}_k \tilde{E}^{x,\phi\phi\phi}_{l-1/2,m,n}e^{-\sigma_E^n\lambda\Delta t/\epsilon} \quad (6.54)$$

$$ {}_kE^{x,\phi\phi\psi^0}_{l-1/2,m,n} = {}_k\tilde{E}^{x,\phi\phi\psi^0}_{l-1/2,m,n}e^{-\sigma_E^n\lambda\Delta t/\epsilon} \tag{6.55}$$

In Eqs. 6.54 and 6.55, the term σ_E^n corresponds to the coefficients of the conductivity term which can be evaluated by the following integral:

$$\sigma_E^n = \int_{(n-1/2)\Delta z}^{(n+1/2)\Delta z} \sigma_E(z)\phi_n(z)dz \tag{6.56}$$

Similarly, expressions for ${}_kE^{y,\phi\phi\phi}_{l,m-1/2,n}$, ${}_kE^{y,\phi\phi\psi^0}_{l,m-1/2,n}$, ${}_kE^{z,\phi\phi\phi}_{l,m,n-1/2}$, ${}_kE^{z,\phi\phi\psi^0}_{l,m,n-1/2}$, ${}_kH^{x,\phi\phi\phi}_{l,m-1/2,n-1/2}$, ${}_kH^{x,\phi\phi\psi^0}_{l,m-1/2,n-1/2}$, ${}_kH^{y,\phi\phi\phi}_{l-1/2,m,n-1/2}$, ${}_kH^{y,\phi\phi\psi^0}_{l-1/2,m,n-1/2}$, ${}_kH^{z,\phi\phi\phi}_{l-1/2,m-1/2,n}$ and ${}_kH^{z,\phi\phi\psi^0}_{l-1/2,m-1/2,n}$ in terms of ${}_k\tilde{E}^{y,\phi\phi\phi}_{l,m-1/2,n}$, ${}_k\tilde{E}^{y,\phi\phi\psi^0}_{l,m-1/2,n}$, ${}_k\tilde{E}^{z,\phi\phi\phi}_{l,m,n-1/2}$, ${}_k\tilde{E}^{z,\phi\phi\psi^0}_{l,m,n-1/2}$, ${}_k\tilde{H}^{x,\phi\phi\phi}_{l,m-1/2,n-1/2}$, ${}_k\tilde{H}^{x,\phi\phi\psi^0}_{l,m-1/2,n-1/2}$, ${}_k\tilde{H}^{y,\phi\phi\phi}_{l-1/2,m,n-1/2}$, ${}_k\tilde{H}^{y,\phi\phi\psi^0}_{l-1/2,m,n-1/2}$, ${}_k\tilde{H}^{z,\phi\phi\phi}_{l-1/2,m-1/2,n}$ and ${}_k\tilde{H}^{z,\phi\phi\psi^0}_{l-1/2,m-1/2,n}$ respectively, can be derived.

From these, the following final discretized equations are obtained for the defining the scaling scheme in the PML region:

$$\begin{aligned}
&\epsilon\frac{{}_\lambda E^{x,\phi\phi\phi}_{l'-1/2,m',n'} - e^{-\sigma_E^n\Delta t/\epsilon}_{\lambda-1}E^{x,\phi\phi\phi}_{l'-1/2,m',n'}}{\Delta t} = \\
&e^{-\sigma_E^n 0.5\Delta t/\epsilon}\left(\frac{{}_{\lambda-1/2}H^{z,\phi\phi\phi}_{l'-1/2,m'+1/2,n'} - {}_{\lambda-1/2}H^{z,\phi\phi\phi}_{l'-1/2,m'-1/2,n'}}{\Delta y}\right) - \\
&e^{-\sigma_E^n 0.5\Delta t/\epsilon}\left(\frac{{}_{\lambda-1/2}H^{y,\phi\phi\phi}_{l'-1/2,m',n'+1/2} - {}_{\lambda-1/2}H^{y,\phi\phi\phi}_{l'-1/2,m',n'-1/2}}{\Delta z}\right)
\end{aligned} \tag{6.57}$$

$$\begin{aligned}
&\epsilon\frac{{}_\lambda E^{y,\phi\phi\phi}_{l',m'-1/2,n'} - e^{-\sigma_E^n\Delta t/\epsilon}_{\lambda-1}E^{y,\phi\phi\phi}_{l',m'-1/2,n'}}{\Delta t} = \\
&e^{-\sigma_E^n 0.5\Delta t/\epsilon}\left(\frac{{}_{\lambda-1/2}H^{x,\phi\phi\phi}_{l',m'-1/2,n'+1/2} - {}_{\lambda-1/2}H^{x,\phi\phi\phi}_{l',m'-1/2,n'-1/2}}{\Delta z}\right) - \\
&e^{-\sigma_E^n 0.5\Delta t/\epsilon}\left(\frac{{}_{\lambda-1/2}H^{z,\phi\phi\phi}_{l'+1/2,m'-1/2,n'} - {}_{\lambda-1/2}H^{z,\phi\phi\phi}_{l'-1/2,m'-1/2,n'}}{\Delta x}\right)
\end{aligned} \tag{6.58}$$

$$\epsilon\frac{{}_{\lambda}E^{z,\phi\phi\phi}_{l',m',n'-1/2}-e^{-\sigma_E^{n-1/2}\Delta t/\epsilon}\,{}_{\lambda-1}E^{z,\phi\phi\phi}_{l',m',n'-1/2}}{\Delta t}=$$
$$e^{-\sigma_E^{n-1/2}0.5\Delta t/\epsilon}\left(\frac{{}_{\lambda-1/2}H^{y,\phi\phi\phi}_{l'+1/2,m',n'-1/2}-{}_{\lambda-1/2}H^{y,\phi\phi\phi}_{l'-1/2,m',n'-1/2}}{\Delta x}\right)-$$
$$e^{-\sigma_E^{n-1/2}0.5\Delta t/\epsilon}\left(\frac{{}_{\lambda-1/2}H^{x,\phi\phi\phi}_{l',m'+1/2,n'-1/2}-{}_{\lambda-1/2}H^{x,\phi\phi\phi}_{l',m'-1/2,n'-1/2}}{\Delta y}\right) \tag{6.59}$$

$$\mu\frac{{}_{\lambda+1/2}H^{x,\phi\phi\phi}_{l',m'-1/2,n'-1/2}-e^{-\sigma_H^{n-1/2}\Delta t/\mu}\,{}_{\lambda-1/2}H^{x,\phi\phi\phi}_{l',m'-1/2,n'-1/2}}{\Delta t}=$$
$$-\,e^{-\sigma_H^{n-1/2}0.5\Delta t/\mu}\left(\frac{{}_{\lambda}E^{z,\phi\phi\phi}_{l',m',n'-1/2}-{}_{\lambda}E^{z,\phi\phi\phi}_{l',m'-1,n'-1/2}}{\Delta y}\right)$$
$$+\,e^{-\sigma_H^{n-1/2}0.5\Delta t/\mu}\left(\frac{{}_{\lambda}E^{y,\phi\phi\phi}_{l',m'-1/2,n'}-{}_{\lambda}E^{y,\phi\phi\phi}_{l',m'-1/2,n'-1}}{\Delta z}\right) \tag{6.60}$$

$$\mu\frac{{}_{\lambda+1/2}H^{y,\phi\phi\phi}_{l'-1/2,m',n'-1/2}-e^{-\sigma_H^{n-1/2}\Delta t/\mu}\,{}_{\lambda-1/2}H^{y,\phi\phi\phi}_{l'-1/2,m',n'-1/2}}{\Delta t}=$$
$$-\,e^{-\sigma_H^{n-1/2}0.5\Delta t/\mu}\left(\frac{{}_{\lambda}E^{x,\phi\phi\phi}_{l'-1/2,m',n'}-{}_{\lambda}E^{x,\phi\phi\phi}_{l'-1/2,m',n'-1}}{\Delta z}\right)$$
$$+\,e^{-\sigma_H^{n-1/2}0.5\Delta t/\mu}\left(\frac{{}_{\lambda}E^{z,\phi\phi\phi}_{l',m',n'-1/2}-{}_{\lambda}E^{z,\phi\phi\phi}_{l'-1,m',n'-1/2}}{\Delta x}\right) \tag{6.61}$$

$$\mu\frac{{}_{\lambda+1/2}H^{z,\phi\phi\phi}_{l'-1/2,m'-1/2,n'}-e^{-\sigma_H^{n-1/2}\Delta t/\mu}\,{}_{\lambda-1/2}H^{z,\phi\phi\phi}_{l'-1/2,m'-1/2,n'}}{\Delta t}=$$
$$-\,e^{-\sigma_H^{n-1/2}0.5\Delta t/\mu}\left(\frac{{}_{\lambda}E^{y,\phi\phi\phi}_{l',m'-1/2,n'}-{}_{\lambda}E^{y,\phi\phi\phi}_{l'-1,m'-1/2,n'}}{\Delta x}\right)$$
$$+\,e^{-\sigma_H^{n-1/2}0.5\Delta t/\mu}\left(\frac{{}_{\lambda}E^{x,\phi\phi\phi}_{l'-1/2,m',n'}-{}_{\lambda}E^{x,\phi\phi\phi}_{l'-1/2,m'-1,n'}}{\Delta y}\right) \tag{6.62}$$

The equations for the wavelet scheme can be derived similarly and have the same form.

6.4 Limitations of Zero Resolution Haar-MRTD Scheme

As seen from the examples above, the zero resolution Haar MRTD scheme has been successfully applied to characterize simple circuits. However, it has been seen that because the scaling and wavelet schemes in this method decouple, the implementation of the boundary conditions involves the application of boundary conditions on the fields as well as their derivatives. For complex circuits and circuits with many modes, this method is prone to numerical errors. As an example, consider the geometry in Figure 6.8 which shows a parallel plate waveguide junction with separations 24 mm and 14.4 mm between the plates. Figure 6.9 shows the scaling and wavelet coefficients along with the total reconstructed field of the dominant electric field component obtained by analyzing this geometry using zero resolution MRTD scheme.

From this figure, it is clear that the complications in implementing boundary conditions due to the decoupling of the scaling and wavelet schemes leads to numerical errors in complex geometries. An obvious solution to this problem is obtained by including higher order Haar wavelets in the MRTD scheme which leads to coupled MRTD discretized equations. The following section focuses on the details of the development of the higher resolution MRTD scheme.

6.5 First Resolution Haar-MRTD Scheme

6.5.1 Derivation of First Resolution 3-D Haar-MRTD Scheme

For simplicity we present the derivation of the 3D MRTD scheme with wavelets along the $\hat{z}$ direction alone. Consider the following 3D scalar equations obtained from Maxwell's

H-curl equation:

$$\epsilon\frac{\partial E_x}{\partial t} = \frac{\partial H_z}{\partial y} - \frac{\partial H_y}{\partial z} \tag{6.63}$$

$$\epsilon\frac{\partial E_y}{\partial t} = \frac{\partial H_x}{\partial z} - \frac{\partial H_z}{\partial x} \tag{6.64}$$

$$\epsilon\frac{\partial E_z}{\partial t} = \frac{\partial H_y}{\partial x} - \frac{\partial H_x}{\partial y} \tag{6.65}$$

$$\mu\frac{\partial H_x}{\partial t} = \frac{\partial E_y}{\partial z} - \frac{\partial E_z}{\partial y} \tag{6.66}$$

$$\mu\frac{\partial H_y}{\partial t} = \frac{\partial E_z}{\partial x} - \frac{\partial E_x}{\partial z} \tag{6.67}$$

$$\mu\frac{\partial H_z}{\partial t} = \frac{\partial E_x}{\partial y} - \frac{\partial E_y}{\partial x} \tag{6.68}$$

We now expand the Electric and Magnetic fields using the Haar based MRA with scaling functions in all three directions and wavelet functions in the $\hat{z}$ direction alone. In deriving the zero resolution MRTD scheme, only the scaling function ϕ and mother wavelet ψ^0 were used. To derive the higher resolution MRTD schemes, scaling function and wavelets of different resolution levels (including the mother wavelet) are used in the field expansions.

For the first resolution MRTD scheme, the field expansions can be represented as follows:

$$\begin{aligned} E_x(x,y,z,t) = & \sum_{k,l,m,n=-\infty}^{+\infty} {}_kE^{x,\phi\phi\phi}_{l-1/2,m,n} h_k(t)\phi_{l-1/2}(x)\phi_m(y)\phi_n(z) + \\ & \sum_{k,l,m=-\infty}^{+\infty} {}_kE^{x,\phi\phi\psi^0}_{l-1/2,m,n} h_k(t)\phi_{l-1/2}(x)\phi_m(y)\psi^0_n(z) + \\ & \sum_{k,l,m=-\infty}^{+\infty} {}_kE^{x,\phi\phi\psi^1_0}_{l-1/2,m,n} h_k(t)\phi_{l-1/2}(x)\phi_m(y)\psi^1_{n,0}(z) + \\ & \sum_{k,l,m=-\infty}^{+\infty} {}_kE^{x,\phi\phi\psi^1_1}_{l-1/2,m,n} h_k(t)\phi_{l-1/2}(x)\phi_m(y)\psi^1_{n,1}(z) \end{aligned} \tag{6.69}$$

$$\begin{aligned}E_y(x,y,z,t) = & \sum_{k,l,m,n=-\infty}^{+\infty} {}_kE^{y,\phi\phi\phi}_{l,m-1/2,n} h_k(t)\phi_l(x)\phi_{m-1/2}(y)\phi_n(z) + \\ & \sum_{k,l,m=-\infty}^{+\infty} {}_kE^{y,\phi\phi\psi^0}_{l,m-1/2,n} h_k(t)\phi_l(x)\phi_{m-1/2}(y)\psi^0_n(z) + \\ & \sum_{k,l,m=-\infty}^{+\infty} {}_kE^{y,\phi\phi\psi^1_0}_{l,m-1/2,n} h_k(t)\phi_l(x)\phi_{m-1/2}(y)\psi^1_{n,0}(z) + \\ & \sum_{k,l,m=-\infty}^{+\infty} {}_kE^{y,\phi\phi\psi^1_1}_{l,m-1/2,n} h_k(t)\phi_l(x)\phi_{m-1/2}(y)\psi^1_{n,1}(z) \end{aligned} \tag{6.70}$$

$$\begin{aligned}E_z(x,y,z,t) = & \sum_{k,l,m,n=-\infty}^{+\infty} {}_kE^{z,\phi\phi\phi}_{l,m,n-1/2} h_k(t)\phi_l(x)\phi_m(y)\phi_{n-1/2}(z) + \\ & \sum_{k,l,m=-\infty}^{+\infty} {}_kE^{z,\phi\phi\psi^0}_{l,m,n-1/2} h_k(t)\phi_l(x)\phi_m(y)\psi^0_{n-1/2}(z) + \\ & \sum_{k,l,m=-\infty}^{+\infty} {}_kE^{z,\phi\phi\psi^1_0}_{l,m,n-1/2} h_k(t)\phi_l(x)\phi_m(y)\psi^1_{n-1/2,0}(z) + \\ & \sum_{k,l,m=-\infty}^{+\infty} {}_kE^{z,\phi\phi\psi^1_1}_{l,m,n-1/2} h_k(t)\phi_l(x)\phi_m(y)\psi^1_{n-1/2,1}(z) \end{aligned} \tag{6.71}$$

$$\begin{aligned}H_x(x,y,z,t) = & \sum_{k,l,m,n=-\infty}^{+\infty} {}_kH^{x,\phi\phi\phi}_{l,m-1/2,n-1/2} h_k(t)\phi_l(x)\phi_{m-1/2}(y)\phi_{n-1/2}(z) + \\ & \sum_{k,l,m=-\infty}^{+\infty} {}_kH^{x,\phi\phi\psi^0}_{l,m-1/2,n-1/2} h_k(t)\phi_l(x)\phi_{m-1/2}(y)\psi^0_{n-1/2}(z) + \\ & \sum_{k,l,m=-\infty}^{+\infty} {}_kH^{x,\phi\phi\psi^1_0}_{l,m-1/2,n-1/2} h_k(t)\phi_l(x)\phi_{m-1/2}(y)\psi^1_{n-1/2,0}(z) + \\ & \sum_{k,l,m=-\infty}^{+\infty} {}_kH^{x,\phi\phi\psi^1_1}_{l,m-1/2,n-1/2} h_k(t)\phi_l(x)\phi_{m-1/2}(y)\psi^1_{n-1/2,1}(z) \end{aligned} \tag{6.72}$$

$$\begin{aligned} H_y(x,y,z,t) = & \sum_{k,l,m,n=-\infty}^{+\infty} {}_kH^{y,\phi\phi\phi}_{l-1/2,m,n-1/2} h_k(t)\phi_{l-1/2}(x)\phi_m(y)\phi_{n-1/2}(z) + \\ & \sum_{k,l,m=-\infty}^{+\infty} {}_kH^{y,\phi\phi\psi^0}_{l-1/2,m,n-1/2} h_k(t)\phi_{l-1/2}(x)\phi_m(y)\psi^0_{n-1/2}(z) + \\ & \sum_{k,l,m=-\infty}^{+\infty} {}_kH^{y,\phi\phi\psi^1_0}_{l-1/2,m,n-1/2} h_k(t)\phi_{l-1/2}(x)\phi_m(y)\psi^1_{n-1/2,0}(z) + \\ & \sum_{k,l,m=-\infty}^{+\infty} {}_kH^{y,\phi\phi\psi^1_1}_{l-1/2,m,n-1/2} h_k(t)\phi_{l-1/2}(x)\phi_m(y)\psi^1_{n-1/2,1}(z) \end{aligned} \tag{6.73}$$

$$\begin{aligned} H_z(x,y,z,t) = & \sum_{k,l,m,n=-\infty}^{+\infty} {}_kH^{z,\phi\phi\phi}_{l-1/2,m-1/2,n} h_k(t)\phi_{l-1/2}(x)\phi_{m-1/2}(y)\phi_n(z) + \\ & \sum_{k,l,m=-\infty}^{+\infty} {}_kH^{z,\phi\phi\psi^0}_{l-1/2,m-1/2,n} h_k(t)\phi_{l-1/2}(x)\phi_{m-1/2}(y)\psi^0_n(z) + \\ & \sum_{k,l,m=-\infty}^{+\infty} {}_kH^{z,\phi\phi\psi^1_0}_{l-1/2,m-1/2,n} h_k(t)\phi_{l-1/2}(x)\phi_{m-1/2}(y)\psi^1_{n,0}(z) + \\ & \sum_{k,l,m=-\infty}^{+\infty} {}_kH^{z,\phi\phi\psi^1_1}_{l-1/2,m-1/2,n} h_k(t)\phi_{l-1/2}(x)\phi_{m-1/2}(y)\psi^1_{n,1}(z) \end{aligned} \tag{6.74}$$

where $\phi_n(x) = \phi(\frac{x}{\Delta x} - n)$ and $\psi^0_n(x) = \psi(\frac{x}{\Delta x} - n)$ represent the Haar scaling and mother wavelet (0-resolution wavelet) functions respectively in space and $\psi^r_{n,p}(x) = 2^{r/2}\psi^0(2^r[\frac{x}{\Delta x} - n] - p)$ represents the r resolution Haar scaling function. As seen from the expression above, higher resolution wavelets are shifted and dilated versions of the mother or 0-resolution wavelet. Since their domain is a fraction of the 0-resolution wavelet, there are going to be multiple higher resolution wavelet coefficients for each MRTD cell. For a resolution of r, at the nth cell, there are going to be 2^r wavelet coefficients located at $\frac{x}{\Delta x} = n + \frac{p}{(2^r+1)}$. ${}_kE^{\kappa,\mu\nu\gamma}_{l,m,n}$ and ${}_{k-1/2}H^{\kappa,\mu\nu\gamma}_{l,m,n}$ where $\kappa = x, y, z$ and $\mu, \nu, \gamma = \phi, \psi^0, \psi^{r'}_p$ with $r' = 0, 1 ... r$ and $p = 0, 1, 2, ... 2^{r'} - 1$ are the coefficients for field expansions in terms of scaling and wavelet functions. As before, the indices l, m and n are discrete space indices related to space coordinates as $x = l\Delta x, y = m\Delta y, z = n\Delta z$ and the index k is a discrete time index related to time coordinate as $t = k\Delta t$.

By inserting Eqs. 6.69-6.74 in Eqs. 6.63 - 6.65 and applying Galerkin's technique, we obtain the following MRTD discretized equations corresponding to Maxwell's curl-E equation:

$$\begin{aligned}
&\epsilon\frac{{}_{\lambda}E^{x,\phi\phi\phi}_{l'-1/2,m',n'} - {}_{\lambda-1}E^{x,\phi\phi\phi}_{l'-1/2,m',n'}}{\Delta t} = \\
&\frac{{}_{\lambda-1/2}H^{z,\phi\phi\phi}_{l'-1/2,m'+1/2,n'} - {}_{\lambda-1/2}H^{z,\phi\phi\phi}_{l'-1/2,m'-1/2,n'}}{\Delta y} - \\
&\frac{{}_{\lambda-1/2}H^{y,\phi\phi\phi}_{l'-1/2,m',n'+1/2} - {}_{\lambda-1/2}H^{y,\phi\phi\phi}_{l'-1/2,m',n'-1/2}}{\Delta z} + \\
&\frac{{}_{\lambda-1/2}H^{y,\phi\phi\psi_0^1}_{l'-1/2,m',n'+1/2} - {}_{\lambda-1/2}H^{y,\phi\phi\psi_0^1}_{l'-1/2,m',n'-1/2}}{\sqrt{2}\Delta z} - \\
&\frac{{}_{\lambda-1/2}H^{y,\phi\phi\psi_1^1}_{l'-1/2,m',n'+1/2} - {}_{\lambda-1/2}H^{y,\phi\phi\psi_1^1}_{l'-1/2,m',n'-1/2}}{\sqrt{2}\Delta z}
\end{aligned} \tag{6.75}$$

$$\begin{aligned}
&\epsilon\frac{{}_{\lambda}E^{x,\phi\phi\psi^0}_{l'-1/2,m',n'} - {}_{\lambda-1}E^{x,\phi\phi\psi^0}_{l'-1/2,m',n'}}{\Delta t} = \\
&\frac{{}_{\lambda-1/2}H^{z,\phi\phi\psi^0}_{l'-1/2,m'+1/2,n'} - {}_{\lambda-1/2}H^{z,\phi\phi\psi^0}_{l'-1/2,m'-1/2,n'}}{\Delta y} - \\
&\frac{{}_{\lambda-1/2}H^{y,\phi\phi\psi^0}_{l'-1/2,m',n'+1/2} - {}_{\lambda-1/2}H^{y,\phi\phi\psi^0}_{l'-1/2,m',n'-1/2}}{\Delta z} - \\
&\frac{3\,{}_{\lambda-1/2}H^{y,\phi\phi\psi_0^1}_{l'-1/2,m',n'+1/2} + {}_{\lambda-1/2}H^{y,\phi\phi\psi_0^1}_{l'-1/2,m',n'-1/2}}{\sqrt{2}\Delta z} + \\
&\frac{{}_{\lambda-1/2}H^{y,\phi\phi\psi_1^1}_{l'-1/2,m',n'+1/2} + 3\,{}_{\lambda-1/2}H^{y,\phi\phi\psi_1^1}_{l'-1/2,m',n'-1/2}}{\sqrt{2}\Delta z}
\end{aligned} \tag{6.76}$$

$$\begin{aligned}
&\epsilon\frac{{}_{\lambda}E^{x,\phi\phi\psi_0^1}_{l'-1/2,m',n'} - {}_{\lambda-1}\,E^{x,\phi\phi\psi_0^1}_{l'-1/2,m',n'}}{\Delta t} = \\
&\frac{{}_{\lambda-1/2}H^{z,\phi\phi\psi_0^1}_{l'-1/2,m'+1/2,n'} - {}_{\lambda-1/2}\,H^{z,\phi\phi\psi_0^1}_{l'-1/2,m'-1/2,n'}}{\Delta y} + \\
&\frac{{}_{\lambda-1/2}H^{y,\phi\phi\psi_0^1}_{l'-1/2,m',n'+1/2} - {}_{\lambda-1/2}\,H^{y,\phi\phi\psi_0^1}_{l'-1/2,m',n'-1/2}}{\Delta z} + \\
&\frac{{}_{\lambda-1/2}H^{y,\phi\phi\phi}_{l'-1/2,m',n'+1/2} - {}_{\lambda-1/2}\,H^{y,\phi\phi\phi}_{l'-1/2,m',n'-1/2}}{\sqrt{2}\Delta z} + \\
&\frac{{}_{\lambda-1/2}H^{y,\phi\phi\psi^0}_{l'-1/2,m',n'+1/2} + 3{}_{\lambda-1/2}H^{y,\phi\phi\psi^0}_{l'-1/2,m',n'-1/2}}{\sqrt{2}\Delta z}
\end{aligned} \tag{6.77}$$

$$\begin{aligned}
&\epsilon\frac{{}_{\lambda}E^{x,\phi\phi\psi_1^1}_{l'-1/2,m',n'} - {}_{\lambda-1}\,E^{x,\phi\phi\psi_1^1}_{l'-1/2,m',n'}}{\Delta t} = \\
&\frac{{}_{\lambda-1/2}H^{z,\phi\phi\psi_1^1}_{l'-1/2,m'+1/2,n'} - {}_{\lambda-1/2}\,H^{z,\phi\phi\psi_1^1}_{l'-1/2,m'-1/2,n'}}{\Delta y} + \\
&\frac{{}_{\lambda-1/2}H^{y,\phi\phi\psi_1^1}_{l'-1/2,m',n'+1/2} - {}_{\lambda-1/2}\,H^{y,\phi\phi\psi_1^1}_{l'-1/2,m',n'-1/2}}{\Delta z} - \\
&\frac{{}_{\lambda-1/2}H^{y,\phi\phi\phi}_{l'-1/2,m',n'+1/2} - {}_{\lambda-1/2}\,H^{y,\phi\phi\phi}_{l'-1/2,m',n'-1/2}}{\sqrt{2}\Delta z} - \\
&\frac{3{}_{\lambda-1/2}H^{y,\phi\phi\psi^0}_{l'-1/2,m',n'+1/2} + {}_{\lambda-1/2}\,H^{y,\phi\phi\psi^0}_{l'-1/2,m',n'-1/2}}{\sqrt{2}\Delta z}
\end{aligned} \tag{6.78}$$

$$\begin{aligned}
&\epsilon\frac{{}_{\lambda}E^{y,\phi\phi\phi}_{l',m'-1/2,n'} - {}_{\lambda-1}\,E^{y,\phi\phi\phi}_{l',m'-1/2,n'}}{\Delta t} = \\
&\frac{{}_{\lambda-1/2}H^{x,\phi\phi\phi}_{l',m'-1/2,n'+1/2} - {}_{\lambda-1/2}\,H^{x,\phi\phi\phi}_{l',m'-1/2,n'-1/2}}{\Delta z} - \\
&\frac{{}_{\lambda-1/2}H^{x,\phi\phi\psi_0^1}_{l',m'-1/2,n'+1/2} - {}_{\lambda-1/2}\,H^{x,\phi\phi\psi_0^1}_{l',m'-1/2,n'-1/2}}{\sqrt{2}\Delta z} + \\
&\frac{{}_{\lambda-1/2}H^{x,\phi\phi\psi_1^1}_{l',m'-1/2,n'+1/2} - {}_{\lambda-1/2}\,H^{x,\phi\phi\psi_1^1}_{l',m'-1/2,n'-1/2}}{\sqrt{2}\Delta z} - \\
&\frac{{}_{\lambda-1/2}H^{z,\phi\phi\phi}_{l'+1/2,m'-1/2,n'} - {}_{\lambda-1/2}\,H^{z,\phi\phi\phi}_{l'-1/2,m'-1/2,n'}}{\Delta x}
\end{aligned} \tag{6.79}$$

$$
\begin{aligned}
&\epsilon\frac{{}^{\lambda}E^{y,\phi\phi\psi^{0}}_{l',m'-1/2,n'} - {}^{\lambda-1}E^{y,\phi\phi\psi^{0}}_{l',m'-1/2,n'}}{\Delta t} = \\
&\frac{{}^{\lambda-1/2}H^{x,\phi\phi\psi^{0}}_{l',m'-1/2,n'+1/2} - {}^{\lambda-1/2}H^{x,\phi\phi\psi^{0}}_{l',m'-1/2,n'-1/2}}{\Delta z} + \\
&\frac{3\,{}^{\lambda-1/2}H^{x,\phi\phi\psi^{1}_{0}}_{l',m'-1/2,n'+1/2} + {}^{\lambda-1/2}H^{x,\phi\phi\psi^{1}_{0}}_{l',m'-1/2,n'-1/2}}{\sqrt{2}\Delta z} - \\
&\frac{{}^{\lambda-1/2}H^{x,\phi\phi\psi^{1}_{1}}_{l',m'-1/2,n'+1/2} + 3\,{}^{\lambda-1/2}H^{x,\phi\phi\psi^{1}_{1}}_{l',m'-1/2,n'-1/2}}{\sqrt{2}\Delta z} - \\
&\frac{{}^{\lambda-1/2}H^{z,\phi\phi\psi^{0}}_{l'+1/2,m'-1/2,n'} - {}^{\lambda-1/2}H^{z,\phi\phi\psi^{0}}_{l'-1/2,m'-1/2,n'}}{\Delta x}
\end{aligned}
\tag{6.80}
$$

$$
\begin{aligned}
&\epsilon\frac{{}^{\lambda}E^{y,\phi\phi\psi^{1}_{0}}_{l',m'-1/2,n'} - {}^{\lambda-1}E^{y,\phi\phi\psi^{1}_{0}}_{l',m'-1/2,n'}}{\Delta t} = \\
&\frac{{}^{\lambda-1/2}H^{x,\phi\phi\psi^{1}_{0}}_{l',m'-1/2,n'-1/2} - {}^{\lambda-1/2}H^{x,\phi\phi\psi^{01}}_{l',m'-1/2,n'+1/2}}{\Delta z} - \\
&\frac{3\,{}^{\lambda-1/2}H^{x,\phi\phi\psi^{0}}_{l',m'-1/2,n'+1/2} + {}^{\lambda-1/2}H^{x,\phi\phi\psi^{0}}_{l',m'-1/2,n'-1/2}}{\sqrt{2}\Delta z} - \\
&\frac{{}^{\lambda-1/2}H^{x,\phi\phi\phi}_{l',m'-1/2,n'+1/2} - {}^{\lambda-1/2}H^{x,\phi\phi\phi}_{l',m'-1/2,n'-1/2}}{\sqrt{2}\Delta z} - \\
&\frac{{}^{\lambda-1/2}H^{z,\phi\phi\psi^{1}_{0}}_{l'+1/2,m'-1/2,n'} - {}^{\lambda-1/2}H^{z,\phi\phi\psi^{1}_{0}}_{l'-1/2,m'-1/2,n'}}{\Delta x}
\end{aligned}
\tag{6.81}
$$

$$
\begin{aligned}
&\epsilon\frac{{}^{\lambda}E^{y,\phi\phi\psi^{1}_{1}}_{l',m'-1/2,n'} - {}^{\lambda-1}E^{y,\phi\phi\psi^{1}_{1}}_{l',m'-1/2,n'}}{\Delta t} = \\
&\frac{{}^{\lambda-1/2}H^{x,\phi\phi\psi^{1}_{1}}_{l',m'-1/2,n'-1/2} - {}^{\lambda-1/2}H^{x,\phi\phi\psi^{1}_{1}}_{l',m'-1/2,n'+1/2}}{\Delta z} + \\
&\frac{3\,{}^{\lambda-1/2}H^{x,\phi\phi\psi^{0}}_{l',m'-1/2,n'+1/2} + {}^{\lambda-1/2}H^{x,\phi\phi\psi^{0}}_{l',m'-1/2,n'-1/2}}{\sqrt{2}\Delta z} + \\
&\frac{{}^{\lambda-1/2}H^{x,\phi\phi\phi}_{l',m'-1/2,n'+1/2} - {}^{\lambda-1/2}H^{x,\phi\phi\phi}_{l',m'-1/2,n'-1/2}}{\sqrt{2}\Delta z} - \\
&\frac{{}^{\lambda-1/2}H^{z,\phi\phi\psi^{1}_{1}}_{l'+1/2,m'-1/2,n'} - {}^{\lambda-1/2}H^{z,\phi\phi\psi^{1}_{1}}_{l'-1/2,m'-1/2,n'}}{\Delta x}
\end{aligned}
\tag{6.82}
$$

$$\epsilon\frac{{}^{\lambda}E^{z,\phi\phi\phi}_{l',m',n'-1/2} - {}^{\lambda-1}E^{z,\phi\phi\phi}_{l',m',n'-1/2}}{\Delta t} = \frac{{}^{\lambda-1/2}H^{y,\phi\phi\phi}_{l'+1/2,m',n'-1/2} - {}^{\lambda-1/2}H^{y,\phi\phi\phi}_{l'-1/2,m',n'-1/2}}{\Delta x} - \frac{{}^{\lambda-1/2}H^{x,\phi\phi\phi}_{l',m'+1/2,n'-1/2} - {}^{\lambda-1/2}H^{x,\phi\phi\phi}_{l',m'-1/2,n'-1/2}}{\Delta y} \tag{6.83}$$

$$\epsilon\frac{{}^{\lambda}E^{z,\phi\phi\psi^0}_{l',m',n'-1/2} - {}^{\lambda-1}E^{z,\phi\phi\psi^0}_{l',m',n'-1/2}}{\Delta t} = \frac{{}^{\lambda-1/2}H^{y,\phi\phi\psi^0}_{l'+1/2,m',n'-1/2} - {}^{\lambda-1/2}H^{y,\phi\phi\psi^0}_{l'-1/2,m',n'-1/2}}{\Delta x} - \frac{{}^{\lambda-1/2}H^{x,\phi\phi\psi^0}_{l',m'+1/2,n'-1/2} - {}^{\lambda-1/2}H^{x,\phi\phi\psi^0}_{l',m'-1/2,n'-1/2}}{\Delta y} \tag{6.84}$$

$$\epsilon\frac{{}^{\lambda}E^{z,\phi\phi\psi^1_0}_{l',m',n'-1/2} - {}^{\lambda-1}E^{z,\phi\phi\psi^1_0}_{l',m',n'-1/2}}{\Delta t} = \frac{{}^{\lambda-1/2}H^{y,\phi\phi\psi^1_0}_{l'+1/2,m',n'-1/2} - {}^{\lambda-1/2}H^{y,\phi\phi\psi^1_0}_{l'-1/2,m',n'-1/2}}{\Delta x} - \frac{{}^{\lambda-1/2}H^{x,\phi\phi\psi^1_0}_{l',m'+1/2,n'-1/2} - {}^{\lambda-1/2}H^{x,\phi\phi\psi^1_0}_{l',m'-1/2,n'-1/2}}{\Delta y} \tag{6.85}$$

$$\epsilon\frac{{}^{\lambda}E^{z,\phi\phi\psi^1_1}_{l',m',n'-1/2} - {}^{\lambda-1}E^{z,\phi\phi\psi^1_1}_{l',m',n'-1/2}}{\Delta t} = \frac{{}^{\lambda-1/2}H^{y,\phi\phi\psi^1_1}_{l'+1/2,m',n'-1/2} - {}^{\lambda-1/2}H^{y,\phi\phi\psi^1_1}_{l'-1/2,m',n'-1/2}}{\Delta x} - \frac{{}^{\lambda-1/2}H^{x,\phi\phi\psi^1_1}_{l',m'+1/2,n'-1/2} - {}^{\lambda-1/2}H^{x,\phi\phi\psi^1_1}_{l',m'-1/2,n'-1/2}}{\Delta y} \tag{6.86}$$

The discretized equations for Maxwell's curl-H equation are obtained following a similar procedure and are summarized below:

$$
\begin{aligned}
&\mu\frac{{}_{\lambda+1/2}H^{x,\phi\phi\phi}_{l',m'-1/2,n'-1/2}-{}_{\lambda-1/2}\,H^{x,\phi\phi\phi}_{l',m'-1/2,n'-1/2}}{\Delta t}=-\\
&\frac{{}_{\lambda}E^{z,\phi\phi\phi}_{l',m',n'-1/2}-{}_{\lambda}\,E^{z,\phi\phi\phi}_{l',m'-1,n'-1/2}}{\Delta y}+\\
&\frac{{}_{\lambda}E^{y,\phi\phi\phi}_{l',m'-1/2,n'}-{}_{\lambda}\,E^{y,\phi\phi\phi}_{l',m'-1/2,n'-1}}{\Delta z}+\\
&\frac{-{}_{\lambda}E^{y,\phi\phi\psi_0^1}_{l',m'-1/2,n'}+{}_{\lambda}\,E^{y,\phi\phi\psi_0^1}_{l',m'-1/2,n'-1}}{\sqrt{2}\Delta z}+\\
&\frac{{}_{\lambda}E^{y,\phi\phi\psi_1^1}_{l',m'-1/2,n'}-{}_{\lambda}\,E^{y,\phi\phi\psi_1^1}_{l',m'-1/2,n'-1}}{\sqrt{2}\Delta z}
\end{aligned}
\tag{6.87}
$$

$$
\begin{aligned}
&\mu\frac{{}_{\lambda+1/2}H^{x,\phi\phi\psi^0}_{l',m'-1/2,n'-1/2}-{}_{\lambda-1/2}\,H^{x,\phi\phi\psi^0}_{l',m'-1/2,n'-1/2}}{\Delta t}=-\\
&\frac{{}_{\lambda}E^{z,\phi\phi\psi^0}_{l',m',n'-1/2}-{}_{\lambda}\,E^{z,\phi\phi\psi^0}_{l',m'-1,n'-1/2}}{\Delta y}+\\
&\frac{{}_{\lambda}E^{y,\phi\phi\psi^0}_{l',m'-1/2,n'}-{}_{\lambda}\,E^{y,\phi\phi\psi^0}_{l',m'-1/2,n'-1}}{\Delta z}+\\
&\frac{3{}_{\lambda}E^{y,\phi\phi\psi_0^1}_{l',m'-1/2,n'}+{}_{\lambda}\,E^{y,\phi\phi\psi_0^1}_{l',m'-1/2,n'}}{\sqrt{2}\Delta z}-\\
&\frac{{}_{\lambda}E^{y,\phi\phi\psi_1^1}_{l',m'-1/2,n'}+3{}_{\lambda}E^{y,\phi\phi\psi_1^1}_{l',m'-1/2,n'-1}}{\sqrt{2}\Delta z}
\end{aligned}
\tag{6.88}
$$

$$
\begin{aligned}
&\mu\frac{{}_{\lambda+1/2}H^{x,\phi\phi\psi_0^1}_{l',m'-1/2,n'-1/2}-{}_{\lambda-1/2}\,H^{x,\phi\phi\psi_0^1}_{l',m'-1/2,n'-1/2}}{\Delta t}=-\\
&\frac{{}_{\lambda}E^{z,\phi\phi\psi_0^1}_{l',m',n'-1/2}-{}_{\lambda}\,E^{z,\phi\phi\psi_0^1}_{l',m'-1,n'-1/2}}{\Delta y}-\\
&\frac{{}_{\lambda}E^{y,\phi\phi\psi_0^1}_{l',m'-1/2,n'-1}-{}_{\lambda}\,E^{y,\phi\phi\psi_0^1}_{l',m'-1/2,n'}}{\Delta z}-\\
&\frac{{}_{\lambda}E^{y,\phi\phi\phi}_{l',m'-1/2,n'}-{}_{\lambda}\,E^{y,\phi\phi\phi}_{l',m'-1/2,n'-1}}{\sqrt{2}\Delta z}-\\
&\frac{{}_{\lambda}E^{y,\phi\phi\psi^0}_{l',m'-1/2,n'}+3{}_{\lambda}E^{y,\phi\phi\psi^0}_{l',m'-1/2,n'-1}}{\sqrt{2}\Delta z}
\end{aligned}
\tag{6.89}
$$

$$\begin{aligned}
&\mu\frac{{}_{\lambda+1/2}H^{x,\phi\phi\psi_1^1}_{l',m'-1/2,n'-1/2} - {}_{\lambda-1/2}H^{x,\phi\phi\psi_1^1}_{l',m'-1/2,n'-1/2}}{\Delta t} = -\\
&\frac{{}_{\lambda}E^{z,\phi\phi\psi_1^1}_{l',m',n'-1/2} - {}_{\lambda}E^{z,\phi\phi\psi_1^1}_{l',m'-1,n'-1/2}}{\Delta y} -\\
&\frac{{}_{\lambda}E^{y,\phi\phi\psi_1^1}_{l',m'-1/2,n'} - {}_{\lambda}E^{y,\phi\phi\psi_1^1}_{l',m'-1/2,n'-1}}{\Delta z} +\\
&\frac{{}_{\lambda}E^{y,\phi\phi\phi}_{l',m'-1/2,n'} - {}_{\lambda}E^{y,\phi\phi\phi}_{l',m'-1/2,n'-1}}{\sqrt{2}\Delta z} +\\
&\frac{3{}_{\lambda}E^{y,\phi\phi\psi^0}_{l',m'-1/2,n'} + {}_{\lambda}E^{y,\phi\phi\psi^0}_{l',m'-1/2,n'-1}}{\sqrt{2}\Delta z}
\end{aligned}\tag{6.90}$$

$$\begin{aligned}
&\mu\frac{{}_{\lambda+1/2}H^{y,\phi\phi\phi}_{l'-1/2,m',n'-1/2} - {}_{\lambda-1/2}H^{y,\phi\phi\phi}_{l'-1/2,m',n'-1/2}}{\Delta t} = -\\
&\frac{{}_{\lambda}E^{x,\phi\phi\phi}_{l'-1/2,m',n'} - {}_{\lambda}E^{x,\phi\phi\phi}_{l'-1/2,m',n'-1}}{\Delta z} +\\
&\frac{{}_{\lambda}E^{x,\phi\phi\psi_0^1}_{l'-1/2,m',n'} - {}_{\lambda}E^{x,\phi\phi\psi_0^1}_{l'-1/2,m',n'-1}}{\sqrt{2}\Delta z} -\\
&\frac{{}_{\lambda}E^{x,\phi\phi\psi_1^1}_{l'-1/2,m',n'} - {}_{\lambda}E^{x,\phi\phi\psi_1^1}_{l'-1/2,m',n'-1}}{\sqrt{2}\Delta z} +\\
&\frac{{}_{\lambda}E^{z,\phi\phi\phi}_{l',m',n'-1/2} - {}_{\lambda}E^{z,\phi\phi\phi}_{l'-1,m',n'-1/2}}{\Delta x}
\end{aligned}\tag{6.91}$$

$$\begin{aligned}
&\mu\frac{{}_{\lambda+1/2}H^{y,\phi\phi\psi^0}_{l'-1/2,m',n'-1/2} - {}_{\lambda-1/2}H^{y,\phi\phi\psi^0}_{l'-1/2,m',n'-1/2}}{\Delta t} = -\\
&\frac{{}_{\lambda}E^{x,\phi\phi\psi^0}_{l'-1/2,m',n'} - {}_{\lambda}E^{x,\phi\phi\psi^0}_{l'-1/2,m',n'-1}}{\Delta z} -\\
&\frac{3{}_{\lambda}E^{x,\phi\phi\psi_0^1}_{l'-1/2,m',n'} + {}_{\lambda}E^{x,\phi\phi\psi_0^1}_{l'-1/2,m',n'-1}}{\sqrt{2}\Delta z} +\\
&\frac{{}_{\lambda}E^{x,\phi\phi\psi_1^1}_{l'-1/2,m',n'} + 3{}_{\lambda-1/2}E^{x,\phi\phi\psi_1^1}_{l'-1/2,m',n'-1}}{\sqrt{2}\Delta z} +\\
&\frac{{}_{\lambda}E^{z,\phi\phi\psi^0}_{l',m',n'-1/2} - {}_{\lambda}E^{z,\phi\phi\psi^0}_{l'-1,m',n'-1/2}}{\Delta x}
\end{aligned}\tag{6.92}$$

$$\begin{aligned}
&\mu\frac{{}^{\lambda+1/2}H^{y,\phi\phi\psi_0^1}_{l'-1/2,m',n'-1/2} - {}^{\lambda-1/2}\,H^{y,\phi\phi\psi_0^1}_{l'-1/2,m',n'-1/2}}{\Delta t} = - \\
&\frac{{}^{\lambda}E^{x,\phi\phi\psi_0^1}_{l'-1/2,m',n'} - {}^{\lambda}\,E^{x,\phi\phi\psi^{01}}_{l'-1/2,m',n'-1}}{\Delta z} + \\
&\frac{3\,{}^{\lambda}E^{x,\phi\phi\psi^0}_{l'-1/2,m',n'-1} + {}^{\lambda}\,E^{x,\phi\phi\psi^0}_{l'-1/2,m',n'}}{\sqrt{2}\Delta z} + \\
&\frac{{}^{\lambda}E^{x,\phi\phi\phi}_{l'-1/2,m',n'} - {}^{\lambda}\,E^{x,\phi\phi\phi}_{l'-1/2,m',n'-1}}{\sqrt{2}\Delta z} + \\
&\frac{{}^{\lambda}E^{z,\phi\phi\psi_0^1}_{l',m',n'-1/2} - {}^{\lambda}\,E^{z,\phi\phi\psi_0^1}_{l'-1,m',n'-1/2}}{\Delta x}
\end{aligned} \tag{6.93}$$

$$\begin{aligned}
&\mu\frac{{}^{\lambda+1/2}H^{y,\phi\phi\psi_1^1}_{l'-1/2,m',n'-1/2} - {}^{\lambda-1/2}\,H^{y,\phi\phi\psi_1^1}_{l'-1/2,m',n'-1/2}}{\Delta t} = - \\
&\frac{{}^{\lambda}E^{x,\phi\phi\psi_1^1}_{l'-1/2,m',n'} - {}^{\lambda}\,E^{x,\phi\phi\psi_1^1}_{l'-1/2,m',n'-1}}{\Delta z} - \\
&\frac{3\,{}^{\lambda}E^{x,\phi\phi\psi^0}_{l'-1/2,m',n'} + {}^{\lambda}\,E^{x,\phi\phi\psi^0}_{l'-1/2,m',n'-1}}{\sqrt{2}\Delta z} - \\
&\frac{{}^{\lambda}E^{x,\phi\phi\phi}_{l'-1/2,m',n'} - {}^{\lambda}\,E^{x,\phi\phi\phi}_{l'-1/2,m',n'-1}}{\sqrt{2}\Delta z} + \\
&\frac{{}^{\lambda}E^{z,\phi\phi\psi_1^1}_{l',m',n'-1/2} - {}^{\lambda}\,E^{z,\phi\phi\psi_1^1}_{l'-1,m',n'-1/2}}{\Delta z}
\end{aligned} \tag{6.94}$$

$$\begin{aligned}
&\mu\frac{{}^{\lambda+1/2}H^{z,\phi\phi\phi}_{l'-1/2,m'-1/2,n'} - {}^{\lambda-1/2}\,H^{z,\phi\phi\phi}_{l'-1/2,m'-1/2,n'}}{\Delta t} = - \\
&\frac{{}^{\lambda}E^{y,\phi\phi\phi}_{l',m'-1/2,n'} - {}^{\lambda}\,E^{y,\phi\phi\phi}_{l'-1,m'-1/2,n'}}{\Delta x} + \\
&\frac{{}^{\lambda}E^{x,\phi\phi\phi}_{l'-1/2,m',n'} - {}^{\lambda}\,E^{x,\phi\phi\phi}_{l'-1/2,m'-1,n'}}{\Delta y}
\end{aligned} \tag{6.95}$$

$$\mu\frac{{}^{\lambda+1/2}H^{z,\phi\phi\psi^{0}}_{l'-1/2,m'-1/2,n'} - {}^{\lambda-1/2}H^{z,\phi\phi\psi^{0}}_{l'-1/2,m'-1/2,n'}}{\Delta t} = - \frac{{}^{\lambda}E^{y,\phi\phi\psi^{0}}_{l',m'-1/2,n'} - {}^{\lambda}E^{y,\phi\phi\psi^{0}}_{l'-1,m'-1/2,n'}}{\Delta x} + \frac{{}^{\lambda}E^{x,\phi\phi\psi^{0}}_{l'-1/2,m',n'} - {}^{\lambda}E^{x,\phi\phi\psi^{0}}_{l'-1/2,m'-1,n'}}{\Delta y} \tag{6.96}$$

$$\mu\frac{{}^{\lambda+1/2}H^{z,\phi\phi\psi^{1}_{0}}_{l'-1/2,m'-1/2,n'} - {}^{\lambda-1/2}H^{z,\phi\phi\psi^{1}_{0}}_{l'-1/2,m'-1/2,n'}}{\Delta t} = - \frac{{}^{\lambda}E^{y,\phi\phi\psi^{1}_{0}}_{l',m'-1/2,n'} - {}^{\lambda}E^{y,\phi\phi\psi^{1}_{0}}_{l'-1,m'-1/2,n'}}{\Delta x} + \frac{{}^{\lambda}E^{x,\phi\phi\psi^{1}_{0}}_{l'-1/2,m',n'} - {}^{\lambda}E^{x,\phi\phi\psi^{1}_{0}}_{l'-1/2,m'-1,n'}}{\Delta y} \tag{6.97}$$

$$\mu\frac{{}^{\lambda+1/2}H^{z,\phi\phi\psi^{1}_{1}}_{l'-1/2,m'-1/2,n'} - {}^{\lambda-1/2}H^{z,\phi\phi\psi^{1}_{1}}_{l'-1/2,m'-1/2,n'}}{\Delta t} = - \frac{{}^{\lambda}E^{y,\phi\phi\psi^{1}_{1}}_{l',m'-1/2,n'} - {}^{\lambda}E^{y,\phi\phi\psi^{1}_{1}}_{l'-1,m'-1/2,n'}}{\Delta x} + \frac{{}^{\lambda}E^{x,\phi\phi\psi^{1}_{1}}_{l'-1/2,m',n'} - {}^{\lambda}E^{x,\phi\phi\psi^{1}_{1}}_{l'-1/2,m'-1,n'}}{\Delta y} \tag{6.98}$$

As seen before, sampling Maxwell's differential equations with scaling and wavelet functions leads to a set of simultaneous discretized equations. Also, unlike the previous scheme with zero resolution wavelet alone, we see from the discretized equations 6.75 - 6.98 that using higher resolution wavelets leads to coupled MRTD schemes. This enables a straightforward implementation of boundary conditions as will be seen in the next section.

6.5.2 MRTD Schemes of Arbitrary Resolution

To obtain the MRTD discretized equations so as to include ‘r_t’ resolutions of wavelets, the electric and magnetic field components are expanded in terms of scaling function and wavelets up to resolution $'r_t'$. As an example, the equations for field components in MRTD scheme where wavelet functions are used in z-direction alone are shown below:

$$E_x(x,y,z,t) = \sum_{k,l,m,n=-\infty}^{+\infty} h_k(t)\phi_{l-1/2}(x)\phi_m(y) \times \left[{}_kE^{x,\phi\phi\phi}_{l-1/2,m,n}\phi_n(z) + \sum_{r=0}^{r_t}\sum_{p=0}^{2^r-1} {}_kE^{x,\phi\phi\psi^r_p}_{l-1/2,m,n}\psi^r_{n,p}(z) \right] \tag{6.99}$$

$$E_y(x,y,z,t) = \sum_{k,l,m,n=-\infty}^{+\infty} h_k(t)\phi_l(x)\phi_{m-1/2}(y) \times \left[{}_kE^{y,\phi\phi\phi}_{l,m-1/2,n}\phi_n(z) + \sum_{r=0}^{r_t}\sum_{p=0}^{2^r-1} {}_kE^{y,\phi\phi\psi^r_p}_{l,m-1/2,n}\psi^r_{n,p}(z) \right] \tag{6.100}$$

$$E_z(x,y,z,t) = \sum_{k,l,m,n=-\infty}^{+\infty} h_k(t)\phi_l(x)\phi_m(y) \times \left[{}_kE^{z,\phi\phi\phi}_{l,m,n-1/2}\phi_{n-1/2}(z) + \sum_{r=0}^{r_t}\sum_{p=0}^{2^r-1} {}_kE^{z,\phi\phi\psi^r_p}_{l,m,n-1/2}\psi^r_{n-1/2,p}(z) \right] \tag{6.101}$$

$$H_x(x,y,z,t) = \sum_{k,l,m,n=-\infty}^{+\infty} h_k(t)\phi_l(x)\phi_{m-1/2}(y) \times \left[{}_kH^{x,\phi\phi\phi}_{l,m-1/2,n-1/2}\phi_{n-1/2}(z) + \sum_{r=0}^{r_t}\sum_{p=0}^{2^r-1} {}_kH^{x,\phi\phi\psi^r_p}_{l,m-1/2,n-1/2}\psi^r_{n-1/2,p}(z) \right] \tag{6.102}$$

$$H_y(x,y,z,t) = \sum_{k,l,m,n=-\infty}^{+\infty} h_k(t)\phi_{l-1/2}(x)\phi_m(y) \times \left[{}_kH^{y,\phi\phi\phi}_{l-1/2,m,n-1/2}\phi_{n-1/2}(z) + \sum_{r=0}^{r_t}\sum_{p=0}^{2^r-1} {}_kH^{x,\phi\phi\psi^r_p}_{l-1/2,m,n-1/2}\psi^r_{n-1/2,p}(z) \right] \tag{6.103}$$

$$H_z(x,y,z,t) = \sum_{k,l,m,n=-\infty}^{+\infty} h_k(t)\phi_{l-1/2}(x)\phi_{m-1/2}(y) \times \left[{}_kH^{y,\phi\phi\phi}_{l-1/2,m-1/2,n}\phi_n(z) + \sum_{r=0}^{r_t}\sum_{p=0}^{2^r-1} {}_kH^{x,\phi\phi\psi^r_p}_{l-1/2,m-1/2,n}\psi^r_{n,p}(z) \right] \tag{6.104}$$

To derive the discretized equations for the MRTD scheme of arbitrary resolution r_t, Eqs. 6.99-6.104 are substituted into Eqs 6.63-6.68. As mentioned in the previous sections, the resulting equations are then sampled using Galerkin's technique to obtain the MRTD discretized equations. The integrals that are encountered in the process of applying Galerkin's technique to obtain the discretized equations can be generalized as shown below.

For sampling in the time domain, the relevant integrals are:

$$\int_{-\infty}^{+\infty} h_\lambda(t)h_{\lambda'}(t)dt = \Delta t\delta_{\lambda,\lambda'} \tag{6.105}$$

$$\int_{-\infty}^{+\infty} h_{\lambda'-1/2}(z)\frac{\partial h_\lambda(z)}{\partial t}dt = \delta_{\lambda',\lambda}(t) - \delta_{\lambda',\lambda+1}(t) \tag{6.106}$$

$$\int_{-\infty}^{+\infty} h_{\lambda'}(t)\frac{\partial h_{\lambda-1/2}(t)}{\partial t}dt = \delta_{\lambda',\lambda-1}(t) - \delta_{\lambda',\lambda}(t) \tag{6.107}$$

For sampling in the space domain, the integrals needed are as follows:

$$\int_{-\infty}^{+\infty} \phi_n(z)\phi_{n'}(z)dz = \Delta z\delta_{n,n'} \tag{6.108}$$

$$\int_{-\infty}^{+\infty} \phi_n(z)\psi^{r}_{n',p}{}'(z)dz = 0, \forall r, p \tag{6.109}$$

$$\int_{-\infty}^{+\infty} \psi^{r}_{n,p}(z)\psi^{r'}_{n',p'}(z)dz = \Delta z \delta_{n,n'}\delta_{r,r'}\delta_{p,p'} \tag{6.110}$$

$$\int_{-\infty}^{+\infty} \phi_{n'}(z)\frac{\partial \phi_{n-1/2}(z)}{\partial z}dz = \delta_{n',n-1}(z) - \delta_{n',n}(z) \tag{6.111}$$

$$\int_{-\infty}^{+\infty} \phi_{n'-1/2}(z)\frac{\partial \phi_{n}(z)}{\partial z}dz = \delta_{n',n}(z) - \delta_{n',n+1}(z) \tag{6.112}$$

$$\begin{aligned}\int_{-\infty}^{+\infty} \phi_{n'}(z)\frac{\partial \psi^{r}_{n-1/2,p}(z)}{\partial z}dz =& 2^{\frac{r}{2}}\delta_{n,n'+1}(z) \times \left[\frac{1}{2}\delta_{p,2^{r-1}} + U\left(\frac{p}{2^{r-1}}\right) - \delta_{r,0} - 2U\left(\frac{p+1/2}{2^{r-1}}\right) + \right.\\ & \left. U\left(\frac{p+1}{2^{r-1}}\right) + \frac{1}{2}\delta_{p,2^{r-1}-1}\right] + \\ & 2^{\frac{r}{2}}\delta_{n,n'}(z) \times \left[\frac{1}{2}\delta_{p,2^{r-1}} + L\left(\frac{p}{2^{r-1}}\right) - \delta_{r,0} - 2L\left(\frac{p+1/2}{2^{r-1}}\right) + \right.\\ & \left. L\left(\frac{p+1}{2^{r-1}}\right) + \frac{1}{2}\delta_{p,2^{r-1}-1}\right]\end{aligned} \tag{6.113}$$

$$\begin{aligned}\int_{-\infty}^{+\infty} \phi_{n'-1/2}(z)\frac{\partial \psi^{r}_{n,p}(z)}{\partial z}dz =& 2^{\frac{r}{2}}\delta_{n,n'-1}(z) \times \left[\frac{1}{2}\delta_{p,2^{r-1}} + L\left(\frac{p}{2^{r-1}}\right) - \delta_{r,0} - 2L\left(\frac{p+1/2}{2^{r-1}}\right) + \right.\\ & \left. L\left(\frac{p+1}{2^{r-1}}\right) + \frac{1}{2}\delta_{p,2^{r-1}-1}\right] + \\ & 2^{\frac{r}{2}}\delta_{n,n'}(z) \times \left[\frac{1}{2}\delta_{p,2^{r-1}} + U\left(\frac{p}{2^{r-1}}\right) - \delta_{r,0} - 2U\left(\frac{p+1/2}{2^{r-1}}\right) + \right.\\ & \left. U\left(\frac{p+1}{2^{r-1}}\right) + \frac{1}{2}\delta_{p,2^{r-1}-1}\right]\end{aligned} \tag{6.114}$$

$$\int_{-\infty}^{+\infty} \psi^{r'}_{n',p'}(z)\frac{\partial \phi_{n-1/2}(z)}{\partial z}dz = \frac{2^{\frac{r'}{2}}}{2}\left[(\delta_{n,n'+1}-\delta_{n,n'})(\delta_{p',2^{r'-1}}-\delta_{p',2^{r'-1}-1})\right] \tag{6.115}$$

$$\int_{-\infty}^{+\infty} \psi^{r'}_{n'-1/2,p'}(z)\frac{\partial \phi_{n}(z)}{\partial z}dz = \frac{2^{\frac{r'}{2}}}{2}\left[(\delta_{n,n'-1}-\delta_{n,n'})(\delta_{p',2^{r'-1}-1}-\delta_{p',2^{r'-1}})\right] \tag{6.116}$$

$$\begin{aligned}\int_{-\infty}^{+\infty} \psi^{r'}_{n',p'}(z)\frac{\partial \psi^{r}_{n-1/2,p}(z)}{\partial z}dz =& 2^{\frac{r'+r}{2}}\left(\delta_{n,n'}+\delta_{n,n'+1}\right)\times \\ &\Big[\psi^0(2^{r'}[n-1+p2^{-r}-n']+2^{r'-1}-\frac{1}{2}-p') \\ &-2\psi^0(2^{r'}[n-1+2^{-r-1}+p2^{-r}-n']+2^{r'-1}-\frac{1}{2}-p') \\ &+\psi^0(2^{r'}[n-1+2^{-r}+p2^{-r}-n']+2^{r'-1}-\frac{1}{2}-p')\Big]\end{aligned} \tag{6.117}$$

$$\begin{aligned}\int_{-\infty}^{+\infty} \psi^{r'}_{n'-1/2,p'}(z)\frac{\partial \psi^{r}_{n,p}(z)}{\partial z}dz =& 2^{\frac{r'+r}{2}}\left(\delta_{n,n'}+\delta_{n,n'-1}\right)\times \\ &\Big[\psi^0(2^{r'}[n-n'+p2^{-r}]+2^{r'-1}-\frac{1}{2}-p') \\ &-2\psi^0(2^{r'}[n-n'+2^{-r-1}+p2^{-r}]+2^{r'-1}-\frac{1}{2}-p') \\ &+\psi^0(2^{r'}[n-n'+2^{-r}+p2^{-r}]+2^{r'-1}-\frac{1}{2}-p')\Big]\end{aligned} \tag{6.118}$$

where $\delta_{n,n'}$ is the Kronecker delta function defined by,

$$\delta_{n,n'} = \begin{cases} 1 & \text{if } n = n' \\ 0 & \text{if } n \neq n' \end{cases}$$

the function $U(k)$ is defined as,

$$U(k) = \begin{cases} 1 & \text{if } 0 \leq k < 1 \\ 0 & \text{otherwise} \end{cases}$$

and the function $L(k)$ is defined as,

$$L(k) = \begin{cases} 1 & \text{if } k > 1 \\ 0 & \text{otherwise} \end{cases}$$

Also, as mentioned in section 5.2, $\psi^0(k)$ is the mother wavelet given by:

$$\psi^0(x) = \begin{cases} \frac{1}{2} & for\, x = -\frac{1}{2} \\ 1 & for\ -\frac{1}{2} < x < 0 \\ 0 & for\, x = 0 \\ -1 & for\, 0 < x < \frac{1}{2} \\ -\frac{1}{2} & for\, x = \frac{1}{2} \\ 0 & elsewhere \end{cases}$$

Thus, using the expressions for the integrals given above, the MRTD discretized equations can be developed so as to include any arbitrary resolution of wavelets.

6.6 Application of Boundary Conditions in the Higher Resolution Haar-MRTD Scheme

6.6.1 Application of source term in the First and Higher Resolution Haar-MRTD Schemes

As mentioned previously, to obtain the amplitude of the scaling and wavelet coefficients at the excitation plane, the excitation function is sampled with Haar scaling and wavelet functions respectively. Since the scaling and wavelet schemes for the first and upward resolutions couple, no additional conditions are necessary to ensure field continuity at the interface of the source cell and it's neighbor. This is demonstrated by applying the higher resolution 3D MRTD scheme to analyze the parallel plate waveguide shown in Figure 6.1 The source of excitation is an equipotential plane with Gaussian time distribution perpendicular to the direction of propagation. The source is applied by sampling the excitation function with scaling and wavelet coefficients. The resulting total field, along with the scaling and wavelet coefficients that are generated by this excitation is shown in Figure 6.10. The smoothness of the total reconstructed field validates the method of implementation of the source condition.

6.6.2 Treatment of PECs in the First and Higher Resolution Haar-MRTD Schemes

The coupled MRTD discretized equations lead to a straightforward implementation of PEC boundary conditions. To implement the PEC condition of zero tangential electric field in first and higher resolution Haar MRTD schemes, image theory is explicitly applied at the location of the PEC. This is because the total value of the field components in these schemes depends on the value of wavelet coefficients on the other side of the PEC surface. Using image theory it can be shown that the scaling and mother wavelet coefficients of the tangential electric field components in the Haar MRTD scheme are zero at the location of the PEC. The remaining higher order wavelet coefficients are obtained by explicitly imposing image theory at the PEC location.

For example, consider a PEC wall at z = 0 plane. The general discretized equations for tangential E_x component at z = 0 are given by Eqs. 6.75 - 6.78. For a PEC wall at z = 0, image theory yields:

$$_{k-1/2}H^{z,\phi\phi\phi}_{l-1/2,m-1/2,0} = 0 \tag{6.119}$$

$$ {}_{k-1/2}H^{z,\phi\phi\psi^0}_{l-1/2,m-1/2,0} = 0 \tag{6.120}$$

$$ {}_{k-1/2}H^{y,\phi\phi\phi}_{l-1/2,m,1/2} = {}_{k-1/2}\, H^{y,\phi\phi\phi}_{l-1/2,m,-1/2} \tag{6.121}$$

$$ {}_{k-1/2}H^{y,\phi\phi\psi^0}_{l-1/2,m,1/2} = -{}_{k-1/2}H^{y,\phi\phi\psi^0}_{l-1/2,m,-1/2} \tag{6.122}$$

$$ {}_{k-1/2}H^{y,\phi\phi\psi^1_0}_{l-1/2,m,1/2} = -{}_{k-1/2}H^{y,\phi\phi\psi^1_0}_{l-1/2,m,-1/2} \tag{6.123}$$

$$ {}_{k-1/2}H^{y,\phi\phi\psi^1_1}_{l-1/2,m,1/2} = -{}_{k-1/2}H^{y,\phi\phi\psi^1_1}_{l-1/2,m,-1/2} \tag{6.124}$$

This leads to the following conditions for tangential E_x field at PEC location z = 0:

$$ \epsilon_\lambda E^{x,\phi\phi\phi}_{l'-1/2,m',0} = 0 \tag{6.125}$$

$$ \epsilon_\lambda E^{x,\phi\phi\psi^0}_{l'-1/2,m',0} = 0 \tag{6.126}$$

$$ \begin{aligned} &\epsilon\frac{{}_\lambda E^{x,\phi\phi\psi^1_1}_{l'-1/2,m',0} - {}_{\lambda-1}\, E^{x,\phi\phi\psi^1_1}_{l'-1/2,m',0}}{\Delta t} = \\ &\frac{{}_{\lambda-1/2}H^{z,\phi\phi\psi^1_1}_{l'-1/2,m'+1/2,0} - {}_{\lambda-1/2}\, H^{z,\phi\phi\psi^1_1}_{l'-1/2,m'-1/2,0}}{\Delta y} + \\ &\frac{{}_{\lambda-1/2}H^{y,\phi\phi\psi^1_1}_{l'-1/2,m',+1/2} + {}_{\lambda-1/2}\, H^{y,\phi\phi\psi^1_0}_{l'-1/2,m',+1/2}}{\Delta z} - \\ &\frac{2\,{}_{\lambda-1/2}H^{y,\phi\phi\psi^0}_{l'-1/2,m',+1/2}}{\sqrt{2}\Delta z} \end{aligned} \tag{6.127}$$

The equations for other tangential Electric field component E_y and normal Magnetic field H_z are obtained in a similar manner. The validation of PEC implementation is obtained by analyzing the aforementioned parallel plate waveguide terminated with a PEC. Figure 6.11 shows the reflected scaling, wavelet and total fields at an arbitrary instant of time after the incident field is reflected by the PEC. The smoothness of the total electric field obtained here validates the methodology of implementing PEC conditions here.

6.6.3 Treatment of Dielectric Interfaces in the First and Higher Resolution Haar-MRTD Schemes

As mentioned before, the fields at a Dielectric interface are modeled by using equations that are obtained by discretizing the constitutive relation $D = \epsilon E$ by expanding the flux density D and electric field E in terms of scaling and wavelet functions and sampling using Galerkin's technique. Since the higher resolution MRTD scheme is coupled, no additional continuity conditions are necessary for modeling dielectric interfaces. When the dielectric interface coincides with the edge of MRTD cell, and the dielectric materials on either sides of the interface completely fill the cells as shown in Fig. 6.12, the following discrete equations are obtained: (Note that the dielectric interface is assumed to be a plane perpendicular to the $\hat{z}$ direction in this case.)

$$D_k^{x,\phi\phi\phi} = 0.5\epsilon_0[(\epsilon_{r1} + \epsilon_{r2})E_k^{x,\phi\phi\phi} + (\epsilon_{r1} - \epsilon_{r2})E_k^{x,\phi\phi\psi^0}] \tag{6.128}$$

$$D_k^{x,\phi\phi\psi^0} = 0.5\epsilon_0[(\epsilon_{r1} + \epsilon_{r2})E_k^{x,\phi\phi\psi^0} + (\epsilon_{r1} - \epsilon_{r2})E_k^{x,\phi\phi\phi}] \tag{6.129}$$

$$D_k^{x,\phi\phi\psi_0^1} = \epsilon_0\epsilon_{r1}E_k^{x,\phi\phi\psi_0^1} \tag{6.130}$$

$$D_k^{x,\phi\phi\psi_1^1} = \epsilon_0\epsilon_{r2}E_k^{x,\phi\phi\psi_1^1} \tag{6.131}$$

$$D_k^{y,\phi\phi\phi} = 0.5\epsilon_0[(\epsilon_{r1}+\epsilon_{r2})E_k^{y,\phi\phi\phi} + (\epsilon_{r1}-\epsilon_{r2})E_k^{y,\phi\phi\psi^0}] \tag{6.132}$$

$$D_k^{y,\phi\phi\psi^0} = 0.5\epsilon_0[(\epsilon_{r1}+\epsilon_{r2})E_k^{y,\phi\phi\psi^0} + (\epsilon_{r1}-\epsilon_{r2})E_k^{y,\phi\phi\phi}] \tag{6.133}$$

$$D_k^{y,\phi\phi\psi_0^1} = \epsilon_0\epsilon_{r1}E_k^{y,\phi\phi\psi_0^1} \tag{6.134}$$

$$D_k^{y,\phi\phi\psi_1^1} = \epsilon_0\epsilon_{r2}E_k^{y,\phi\phi\psi_1^1} \tag{6.135}$$

$$D_k^{z,\phi\phi\phi} = \epsilon_0\epsilon_{r1}E_k^{z,\phi\phi\phi} \tag{6.136}$$

$$D_k^{z,\phi\phi\psi^0} = \epsilon_0\epsilon_{r1}E_k^{z,\phi\phi\psi^0} \tag{6.137}$$

$$D_k^{z,\phi\phi\psi_0^1} = \epsilon_0\epsilon_{r1}E_k^{z,\phi\phi\psi_0^1} \tag{6.138}$$

$$D_k^{z,\phi\phi\psi_1^1} = \epsilon_0\epsilon_{r1}E_k^{z,\phi\phi\psi_1^1} \tag{6.139}$$

However, ϵ can be an arbitrary function of space coordinates and hence, dielectrics of arbitrary distribution can be modeled using the same approach. This is particularly useful in modeling geometries with thin dielectrics such as those presented in section 8.3 where the dielectric material is thinner than the chosen MRTD cell size. As an example, consider a thin dielectric slab of thickness equal to half of the MRTD cell dimension as shown in Fig. 6.13. The discretized equations obtained for this particular geometry (assuming that the diclectric interface is perpendicular to $\hat{z}$) are as follows:

$$D_{k-1}^{x,\phi\phi\phi} = 0.5\epsilon_0[(\epsilon_{r1}+\epsilon_{r2})E_{k-1}^{x,\phi\phi\phi} + (\epsilon_{r1}-\epsilon_{r2})E_{k-1}^{x,\phi\phi\psi^0}] \tag{6.140}$$

$$D_{k-1}^{x,\phi\phi\psi^0} = 0.5\epsilon_0[(\epsilon_{r1} + \epsilon_{r2})E_{k-1}^{x,\phi\phi\psi^0} + (\epsilon_{r1} - \epsilon_{r2})E_{k-1}^{x,\phi\phi\phi}] \tag{6.141}$$

$$D_{k-1}^{x,\phi\phi\psi_0^1} = \epsilon_0\epsilon_{r1}E_{k-1}^{x,\phi\phi\psi_0^1} \tag{6.142}$$

$$D_{k-1}^{x,\phi\phi\psi_1^1} = \epsilon_0\epsilon_{r2}E_{k-1}^{x,\phi\phi\psi_1^1} \tag{6.143}$$

$$D_{k-1}^{y,\phi\phi\phi} = 0.5\epsilon_0[(\epsilon_{r1} + \epsilon_{r2})E_{k-1}^{y,\phi\phi\phi} + (\epsilon_{r1} - \epsilon_{r2})E_{k-1}^{y,\phi\phi\psi^0}] \tag{6.144}$$

$$D_{k-1}^{y,\phi\phi\psi^0} = 0.5\epsilon_0[(\epsilon_{r1} + \epsilon_{r2})E_{k-1}^{y,\phi\phi\psi^0} + (\epsilon_{r1} - \epsilon_{r2})E_{k-1}^{y,\phi\phi\phi}] \tag{6.145}$$

$$D_{k-1}^{y,\phi\phi\psi_0^1} = \epsilon_0\epsilon_{r1}E_{k-1}^{y,\phi\phi\psi_0^1} \tag{6.146}$$

$$D_{k-1}^{y,\phi\phi\psi_1^1} = \epsilon_0\epsilon_{r2}E_{k-1}^{y,\phi\phi\psi_1^1} \tag{6.147}$$

$$D_k^{z,\phi\phi\phi} = 0.5\epsilon_0[(\epsilon_{r2} + \epsilon_{r3})E_k^{z,\phi\phi\phi} + (\epsilon_{r2} - \epsilon_{r3})E_k^{z,\phi\phi\psi^0}] \tag{6.148}$$

$$D_k^{z,\phi\phi\psi^0} = 0.5\epsilon_0[(\epsilon_{r2} + \epsilon_{r3})E_k^{z,\phi\phi\psi^0} + (\epsilon_{r2} - \epsilon_{r3})E_k^{z,\phi\phi\phi}] \tag{6.149}$$

$$D_k^{z,\phi\phi\psi_0^1} = \epsilon_0\epsilon_{r2}E_k^{z,\phi\phi\psi_0^1} \tag{6.150}$$

$$D_k^{z,\phi\phi\psi_1^1} = \epsilon_0\epsilon_{r3}E_k^{z,\phi\phi\psi_1^1} \tag{6.151}$$

It is important to note in this approach that while the MRTD cell size can be greater than the thickness of the dielectric, the cell size has to be chosen such that the dielectric thickness is at least equal to and integral multiple of the extent of the highest resolution wavelet in the MRTD scheme.

The technique of modeling dielectric interfaces is validated by analyzing the parallel plate waveguide of Figure 6.1 which is half filled with air and half with a material of $\epsilon_r = 20$.

Figure 6.14 shows the scaling and wavelet coefficients of the total flux density in the parallel plate waveguide. As seen from the figure, this generalized approach for modeling dielectics results in accurate scaling and wavelet coefficients and leads to smooth reconstruction of the total fields and an enhancement in field resolution.

6.6.4 Modeling of PML Absorber in the First and Higher Resolution Haar-MRTD Schemes

As mentioned in section 6.3, the PML absorber is used to model 'open' boundaries in the MRTD scheme. In section 6.3, an implementation of PML technique was presented where the electric and magnetic conductivities were expanded in terms of scaling functions. While the performance of such a PML scheme was found to be very good for zero resolution MRTD scheme, it has been seen that for higher resolution MRTD schemes, using the scaling functions alone for the expansion of conductivity term is not a very good approximation. For the zero resolution MRTD scheme, while the technique of using scaling expands leads to a PML absorber with reflections of the order of -80 dB, for higher resolution Haar-MRTD schemes, the performance of this PML scheme deteriorates, leading to reflectrion of the order of -35dB in some cases. This is attributed to the numerical errors which accumulate by making the approximation that conductivity varies in 'steps' where the step size is the size of the scaling function. This approximation leads to high reflections in the total reflected fields due to the numerical errors which are manifested in the form of 'amplifications' of the higher order wavelets.

To address this problem, a modified PML implementation has been develoved here which uses scaling and wavelet expansions for the electric and magnetic conductivities. Here, the derivation of PML discretized equation for the E_x field component of the first resolution

Haar-MRTD scheme is presented. Expressions for the other field components in the PML region in first resolution MRTD scheme and the PML field components in higher resolution MRTD schemes can be derived similarly. Also, for simplicity, PML cells only in the $\hat{z}$ direction are considered.

As discussed in section 6.3, we start by adding conductivity terms to Maxwell's equation. A parabolic distribution is assumed for the electric and magnetic conductivities as given in Eq. 6.21. Consider the equation which leads to E_x field component as shown below:

$$\epsilon \frac{\partial E_x}{\partial t} + \sigma_E E_x = \frac{\partial H_z}{\partial y} - \frac{\partial H_y}{\partial z} \tag{6.152}$$

The field components E_x, H_y and H_z are expanded using scaling and wavelet components and electric/magnetic conductivities (σ_E, σ_H) as shown below:

$$\begin{aligned} E_x(x,y,z,t) = & \sum_{k,l,m,n=-\infty}^{+\infty} {}_k\tilde{E}^{x,\phi\phi\phi}_{l-1/2,m,n} h_k(t) e^{-\sigma^n_{E\phi} t/\epsilon_o} \phi_{l-1/2}(x)\phi_m(y)\phi_n(z) + \\ & \sum_{k,l,m=-\infty}^{+\infty} {}_k\tilde{E}^{x,\phi\phi\psi^0}_{l-1/2,m,n} h_k(t) e^{-\sigma^n_{E\psi^0} t/\epsilon_o} \phi_{l-1/2}(x)\phi_m(y)\psi^0_n(z) + \\ & \sum_{k,l,m=-\infty}^{+\infty} {}_k\tilde{E}^{x,\phi\phi\psi^1_0}_{l-1/2,m,n} h_k(t) e^{-\sigma^n_{E\psi^1_0} t/\epsilon_o} \phi_{l-1/2}(x)\phi_m(y)\psi^1_{n,0}(z) + \\ & \sum_{k,l,m=-\infty}^{+\infty} {}_k\tilde{E}^{x,\phi\phi\psi^1_1}_{l-1/2,m,n} h_k(t) e^{-\sigma^n_{E\psi^1_1} t/\epsilon_o} \phi_{l-1/2}(x)\phi_m(y)\psi^1_{n,1}(z) \end{aligned} \tag{6.153}$$

$$\begin{aligned} H_y(x,y,z,t) = & \sum_{k,l,m,n=-\infty}^{+\infty} {}_k\tilde{H}^{y,\phi\phi\phi}_{l-1/2,m,n-1/2} h_k(t) e^{-\sigma^{n-1/2}_{H\phi} t/\mu_o} \phi_{l-1/2}(x)\phi_m(y)\phi_{n-1/2}(z) + \\ & \sum_{k,l,m=-\infty}^{+\infty} {}_k\tilde{H}^{y,\phi\phi\psi^0}_{l-1/2,m,n-1/2} h_k(t) e^{-\sigma^{n-1/2}_{H\psi^0} t/\mu_o} \phi_{l-1/2}(x)\phi_m(y)\psi^0_{n-1/2}(z) + \\ & \sum_{k,l,m=-\infty}^{+\infty} {}_k\tilde{H}^{y,\phi\phi\psi^1_0}_{l-1/2,m,n-1/2} h_k(t) e^{-\sigma^{n-1/2}_{H\psi^1_0} t/\mu_o} \phi_{l-1/2}(x)\phi_m(y)\psi^1_{n-1/2,0}(z) + \\ & \sum_{k,l,m=-\infty}^{+\infty} {}_k\tilde{H}^{y,\phi\phi\psi^1_1}_{l-1/2,m,n-1/2} h_k(t) e^{-\sigma^{n-1/2}_{H\psi^1_1} t/\mu_o} \phi_{l-1/2}(x)\phi_m(y)\psi^1_{n-1/2,1}(z) \end{aligned} \qquad (6.154)$$

$$\begin{aligned} H_z(x,y,z,t) = & \sum_{k,l,m,n=-\infty}^{+\infty} {}_k\tilde{H}^{z,\phi\phi\phi}_{l-1/2,m-1/2,n} h_k(t) e^{-\sigma^{n}_{H\phi} t/\mu_o} \phi_{l-1/2}(x)\phi_{m-1/2}(y)\phi_n(z) + \\ & \sum_{k,l,m=-\infty}^{+\infty} {}_k\tilde{H}^{z,\phi\phi\psi^0}_{l-1/2,m-1/2,n} h_k(t) e^{-\sigma^{n}_{H\psi^0} t/\mu_o} \phi_{l-1/2}(x)\phi_{m-1/2}(y)\psi^0_n(z) + \\ & \sum_{k,l,m=-\infty}^{+\infty} {}_k\tilde{H}^{z,\phi\phi\psi^1_0}_{l-1/2,m-1/2,n} h_k(t) e^{-\sigma^{n}_{H\psi^1_0} t/\mu_o} \phi_{l-1/2}(x)\phi_{m-1/2}(y)\psi^1_{n,0}(z) + \\ & \sum_{k,l,m=-\infty}^{+\infty} {}_k\tilde{H}^{z,\phi\phi\psi^1_1}_{l-1/2,m-1/2,n} h_k(t) e^{-\sigma^{n}_{H\psi^1_1} t/\mu_o} \phi_{l-1/2}(x)\phi_{m-1/2}(y)\psi^1_{n,1}(z) \end{aligned} \qquad (6.155)$$

Substituting Eqs. 6.153-6.155 in 6.152, we obtain the following equation:

$$
\begin{array}{l}
\epsilon \displaystyle\sum_{k,l,m,n=-\infty}^{+\infty} \frac{\partial h_k(t)}{\partial t} \phi_{l-1/2}(x)\phi_m(y)[{}_k\tilde{E}^{x,\phi\phi\phi}_{l-1/2,m,n} e^{-\sigma^n_{E\phi} t/\epsilon_o} \phi_n(z) + {}_k\tilde{E}^{x,\phi\phi\psi^0}_{l-1/2,m,n} e^{-\sigma^n_{E\psi^0} t/\epsilon_o} \psi^0_n(z) + \\
{}_k\tilde{E}^{x,\phi\phi\psi^1_0}_{l-1/2,m,n} h_k(t) e^{-\sigma^n_{E\psi^1_0} t/\epsilon_o} \psi^1_{n,0}(z) + {}_k\tilde{E}^{x,\phi\phi\psi^1_1}_{l-1/2,m,n} h_k(t) e^{-\sigma^n_{E\psi^1_1} t/\epsilon_o} \psi^1_{n,1}(z)] \\
\displaystyle\sum_{k,l,m,n=-\infty}^{+\infty} h_k(t)\phi_{l-1/2}(x)\phi_m(y)[{}_k\tilde{E}^{x,\phi\phi\phi}_{l-1/2,m,n}(-\sigma^n_{E\phi} + \sigma_E(z))\phi_n(z) + \\
{}_k\tilde{E}^{x,\phi\phi\psi^0}_{l-1/2,m,n}(-\sigma^n_{E\psi^0} + \sigma_E(z))\psi^0_n(z) {}_k\tilde{E}^{x,\phi\phi\psi^1_0}_{l-1/2,m,n} h_k(t)(-\sigma^n_{E\psi^1_0} + \sigma_E(z))\psi^1_{n,0}(z) + \\
{}_k\tilde{E}^{x,\phi\phi\psi^1_1}_{l-1/2,m,n} h_k(t)(-\sigma^n_{E\psi^1_1} + \sigma_E(z))\psi^1_{n,1}(z)] = \\
\displaystyle\sum_{k,l,m,n=-\infty}^{+\infty} {}_k h_{k-1/2}(t)\phi_{l-1/2}(x)\frac{\partial \phi_{m-1/2}(y)}{\partial y}[{}_k\tilde{H}^{z,\phi\phi\phi}_{l-1/2,m-1/2,n}\phi_n(z) e^{-\sigma^n_{H\phi} t/\mu_o} + \\
{}_k\tilde{H}^{z,\phi\phi\psi^0}_{l-1/2,m-1/2,n}\psi^0_n(z) e^{-\sigma^n_{H\psi^0} t/\mu_o} + {}_k\tilde{H}^{z,\phi\phi\psi^1_0}_{l-1/2,m-1/2,n}\psi^1_{n,0}(z) e^{-\sigma^n_{H\psi^1_0} t/\mu_o} + \\
{}_k\tilde{H}^{z,\phi\phi\psi^1_1}_{l-1/2,m-1/2,n}\psi^1_{n,1}(z) e^{-\sigma^n_{H\psi^1_1} t/\mu_o}] - \\
\displaystyle\sum_{k,l,m,n=-\infty}^{+\infty} h_{k-1/2}(t)\phi_{l-1/2}(x)\phi_m(y)[\tilde{H}^{y,\phi\phi\phi}_{l-1/2,m,n-1/2} e^{-\sigma^{n-1/2}_{H\phi} t/\mu_o} \frac{\partial \phi_{n-1/2}(z)}{\partial z} + \\
{}_k\tilde{H}^{y,\phi\phi\psi^0}_{l-1/2,m,n-1/2} e^{-\sigma^{n-1/2}_{H\psi^0} t/\mu_o} \dfrac{\partial \psi^0_{n-1/2}(z)}{\partial z} + {}_k\tilde{H}^{y,\phi\phi\psi^1_0}_{l-1/2,m,n-1/2} e^{-\sigma^{n-1/2}_{H\psi^1_0} t/\mu_o} \dfrac{\partial \psi^1_{n-1/2,0}(z)}{\partial z} + \\
{}_k\tilde{H}^{y,\phi\phi\psi^1_1}_{l-1/2,m,n-1/2} e^{-\sigma^{n-1/2}_{H\psi^1_1} t/\mu_o} \dfrac{\partial \psi^1_{n-1/2,1}(z)}{\partial z}]
\end{array}
\qquad (6.156)
$$

In Eq. 6.156 above, the values of $\sigma^n_{E\phi}$, $\sigma^n_{E\psi^0}$, $\sigma^n_{E\psi^1_0}$ and $\sigma^n_{E\psi^1_1}$ are chosen as follows:

$$\int_{-\infty}^{\infty} \phi_{n'}(z)\phi_n(z)\sigma^n_{E\phi} dz = \int_{-\infty}^{\infty} \phi_{n'}(z)\phi_n(z)\sigma_E(z) dz \qquad (6.157)$$

$$\int_{-\infty}^{\infty} \psi^0_{n'}(z)\psi^0_n(z)\sigma^n_{E\psi^0} dz = \int_{-\infty}^{\infty} \psi^0_{n'}(z)\psi^0_n(z)\sigma_E(z) dz \qquad (6.158)$$

$$\int_{-\infty}^{\infty} \psi^1_{n',0}(z)\psi^1_{n,0}(z)\sigma^n_{E\psi^1_0} dz = \int_{-\infty}^{\infty} \psi^1_{n',0}(z)\psi^1_{n,0}(z)\sigma_E(z) dz \qquad (6.159)$$

$$\int_{-\infty}^{\infty} \psi^1_{n',1}(z)\psi^1_{n,1}(z)\sigma^n_{E\psi^1_1} dz = \int_{-\infty}^{\infty} \psi^1_{n',1}(z)\psi^1_{n,1}(z)\sigma_E(z) dz \qquad (6.160)$$

Eq. 6.156 is sampled using Galerkin's technique to obtain discretized equations as discussed in sections 6.3 and 6.1. Since the PML implementation discussed here is for the first resolution MRTD scheme with wavelets in $\hat{z}$ direction alone, the four sampling functions that are used are:

$$h_{\lambda-1/2}(t)\phi_{l'-1/2}(x)\phi_{m'}(y)\phi_{n'}(z) \qquad : for \phi\phi\phi scheme \qquad (6.161)$$

$$h_{\lambda-1/2}(t)\phi_{l'-1/2}(x)\phi_{m'}(y)\psi^{0}_{n'}(z) \qquad : for \phi\phi\psi^{0} scheme \qquad (6.162)$$

$$h_{\lambda-1/2}(t)\phi_{l'-1/2}(x)\phi_{m'}(y)\phi^{1}_{n',0}(z) \qquad : for \phi\phi\psi^{1}_{0} scheme \qquad (6.163)$$

$$h_{\lambda-1/2}(t)\phi_{l'-1/2}(x)\phi_{m'}(y)\phi^{1}_{n',1}(z) \qquad : for \phi\phi\psi^{1}_{1} scheme \qquad (6.164)$$

From these, a system of four equations is obtained which can be solved to obtain the discretized PML equations corresponding to Eq. 6.152. As in section 6.3, to obtain the final discretized equations, Eqs. 6.153-6.155 need to be discretized as well, so as to express the equations in terms of electric and magnetic field coefficients. For example, discretization of Eq. 6.153 involves writing E_x as follows:

$$\begin{aligned} E_x(x,y,z,t) = & \sum_{k,l,m,n=-\infty}^{+\infty} {}_kE^{x,\phi\phi\phi}_{l-1/2,m,n} h_k(t)\phi_{l-1/2}(x)\phi_m(y)\phi_n(z) + \\ & \sum_{k,l,m=-\infty}^{+\infty} {}_kE^{x,\phi\phi\psi^0}_{l-1/2,m,n} h_k(t)\phi_{l-1/2}(x)\phi_m(y)\psi^0_n(z) + \\ & \sum_{k,l,m=-\infty}^{+\infty} {}_kE^{x,\phi\phi\psi^1_0}_{l-1/2,m,n} h_k(t)\phi_{l-1/2}(x)\phi_m(y)\psi^1_{n,0}(z) + \\ & \sum_{k,l,m=-\infty}^{+\infty} {}_kE^{x,\phi\phi\psi^1_1}_{l-1/2,m,n} h_k(t)\phi_{l-1/2}(x)\phi_m(y)\psi^1_{n,1}(z) \\ = & \\ & \sum_{k,l,m,n=-\infty}^{+\infty} {}_k\tilde{E}^{x,\phi\phi\phi}_{l-1/2,m,n} h_k(t) e^{-\sigma^n_{E\phi} t/lon_o} \phi_{l-1/2}(x)\phi_m(y)\phi_n(z) + \\ & \sum_{k,l,m=-\infty}^{+\infty} {}_k\tilde{E}^{x,\phi\phi\psi^0}_{l-1/2,m,n} h_k(t) e^{-\sigma^n_{E\psi^0} t/\epsilon_o} \phi_{l-1/2}(x)\phi_m(y)\psi^0_n(z) + \\ & \sum_{k,l,m=-\infty}^{+\infty} {}_k\tilde{E}^{x,\phi\phi\psi^1_0}_{l-1/2,m,n} h_k(t) e^{-\sigma^n_{E\psi^1_0} t/\epsilon_o} \phi_{l-1/2}(x)\phi_m(y)\psi^1_{n,0}(z) + \\ & \sum_{k,l,m=-\infty}^{+\infty} {}_k\tilde{E}^{x,\phi\phi\psi^1_1}_{l-1/2,m,n} h_k(t) e^{-\sigma^n_{E\psi^1_1} t/\epsilon_o} \phi_{l-1/2}(x)\phi_m(y)\psi^1_{n,1}(z) \end{aligned} \qquad (6.165)$$

Applying Galerkin's technique to sample as discussed in section 6.3, we obtain the following relations:

$$ {}_kE^{x,\phi\phi\phi}_{l-1/2,m,n} = {}_k\,\tilde{E}^{x,\phi\phi\phi}_{l-1/2,m,n} e^{-\sigma^n_{E\phi} k\Delta t/\epsilon} \frac{sinh(\frac{\sigma^n_{E\phi}\Delta t}{2\epsilon})}{(\frac{\sigma^n_{E\phi}\Delta t}{2\epsilon})} \qquad (6.166)$$

$$ {}_kE^{x,\phi\phi\psi^0}_{l-1/2,m,n} = {}_k\,\tilde{E}^{x,\phi\phi\psi^0}_{l-1/2,m,n} e^{-\sigma^n_{E\psi^0} k\Delta t/\epsilon} \frac{sinh(\frac{\sigma^n_{E\psi^0}\Delta t}{2\epsilon})}{(\frac{\sigma^n_{E\psi^0}\Delta t}{2\epsilon})} \qquad (6.167)$$

$$ {}_kE^{x,\phi\phi\psi^1_0}_{l-1/2,m,n} = {}_k\,\tilde{E}^{x,\phi\phi\psi^1_0}_{l-1/2,m,n} e^{-\sigma^n_{E\psi^1_0} k\Delta t/\epsilon} \frac{sinh(\frac{\sigma^n_{E\psi^1_0}\Delta t}{2\epsilon})}{(\frac{\sigma^n_{E\psi^1_0}\Delta t}{2\epsilon})} \qquad (6.168)$$

$$
{}_{k}E^{x,\phi\phi\psi_1^1}_{l-1/2,m,n} = {}_{k}\tilde{E}^{x,\phi\phi\psi_1^1}_{l-1/2,m,n} e^{-\sigma^n_{E\psi_1^1} k\Delta t/\epsilon} \frac{sinh(\frac{\sigma^n_{E\psi_1^1}\Delta t}{2\epsilon})}{(\frac{\sigma^n_{E\psi_1^1}\Delta t}{2\epsilon})} \tag{6.169}
$$

Also, as mentioned in section 6.3, the argument of the functions of form $sinh(x)/(x)$ in Eqs. 6.166-6.169 is so small for most practical cases that the approximation $sinh(x)/(x) \approx 1$ can be used. This approximation is used in the discretized equations presented here. Eqs. 6.154 and 6.155 can be discretized in a similar manner.

The final discretized equations corresponding to Eq. 6.152 which are obtained by following the procedure described in this section are as follows:

$$
\begin{aligned}
&\epsilon \frac{{}_{\lambda}E^{x,\phi\phi\phi}_{l'-1/2,m',n'} - {}_{\lambda-1}E^{x,\phi\phi\phi}_{l'-1/2,m',n'}}{\Delta t} + \\
&\frac{I_{\phi}^{\psi^0} e^{-\sigma^n_{E\phi}0.5\Delta t/\epsilon}}{\Delta z}[-{}_{\lambda}E^{x,\phi\phi\psi^0}_{l'-1/2,m',n'}(\frac{1-e^{\sigma^n_{E\psi^0}0.5\Delta t/\epsilon}}{\sigma^n_{E\psi^0}\Delta t}) + \\
&{}_{\lambda-1}E^{x,\phi\phi\psi^0}_{l'-1/2,m',n'} e^{\sigma^n_{E\psi^0}\Delta t/\epsilon}(\frac{1-e^{-\sigma^n_{E\psi^0}0.5\Delta t/\epsilon}}{\sigma^n_{E\psi^0}\Delta t})] + \\
&\frac{I_{\phi}^{\psi_0^1} e^{-\sigma^n_{E\phi}0.5\Delta t/\epsilon}}{\Delta z}[-{}_{\lambda}E^{x,\phi\phi\psi_0^1}_{l'-1/2,m',n'}(\frac{1-e^{\sigma^n_{E\psi_0^1}0.5\Delta t/\epsilon}}{\sigma^n_{E\psi_0^1}\Delta t}) + \\
&{}_{\lambda-1}E^{x,\phi\phi\psi_0^1}_{l'-1/2,m',n'} e^{\sigma^n_{E\psi_0^1}\Delta t/\epsilon}(\frac{1-e^{-\sigma^n_{E\psi_0^1}0.5\Delta t/\epsilon}}{\sigma^n_{E\psi_0^1}\Delta t})] + \\
&\frac{I_{\phi}^{\psi_1^1} e^{-\sigma^n_{E\phi}0.5\Delta t/\epsilon}}{\Delta z}[-{}_{\lambda}E^{x,\phi\phi\psi_1^1}_{l'-1/2,m',n'}(\frac{1-e^{\sigma^n_{E\psi_1^1}0.5\Delta t/\epsilon}}{\sigma^n_{E\psi_1^1}\Delta t}) + \\
&{}_{\lambda-1}E^{x,\phi\phi\psi_1^1}_{l'-1/2,m',n'} e^{\sigma^n_{E\psi_1^1}\Delta t/\epsilon}(\frac{1-e^{-\sigma^n_{E\psi_1^1}0.5\Delta t/\epsilon}}{\sigma^n_{E\psi_1^1}\Delta t})] = \\
&e^{-\sigma^n_{E\phi}0.5\Delta t/\epsilon}(\frac{{}_{\lambda-1/2}H^{z,\phi\phi\phi}_{l'-1/2,m'+1/2,n'} - {}_{\lambda-1/2}H^{z,\phi\phi\phi}_{l'-1/2,m'-1/2,n'}}{\Delta y}) - \\
&e^{-\sigma^n_{E\phi}0.5\Delta t/\epsilon}(\frac{{}_{\lambda-1/2}H^{y,\phi\phi\phi}_{l'-1/2,m',n'+1/2} - {}_{\lambda-1/2}H^{y,\phi\phi\phi}_{l'-1/2,m',n'-1/2}}{\Delta z}) + \\
&e^{-\sigma^n_{E\phi}0.5\Delta t/\epsilon}(\frac{{}_{\lambda-1/2}H^{y,\phi\phi\psi_0^1}_{l'-1/2,m',n'+1/2} - {}_{\lambda-1/2}H^{y,\phi\phi\psi_0^1}_{l'-1/2,m',n'-1/2}}{\sqrt{2}\Delta z}) - \\
&e^{-\sigma^n_{E\phi}0.5\Delta t/\epsilon}(\frac{{}_{\lambda-1/2}H^{y,\phi\phi\psi_1^1}_{l'-1/2,m',n'+1/2} - {}_{\lambda-1/2}H^{y,\phi\phi\psi_1^1}_{l'-1/2,m',n'-1/2}}{\sqrt{2}\Delta z})
\end{aligned} \tag{6.170}
$$

$$
\begin{aligned}
&\epsilon\frac{{}_{\lambda}E^{x,\phi\phi\psi^0}_{l'-1/2,m',n'}-{}_{\lambda-1}E^{x,\phi\phi\psi^0}_{l'-1/2,m',n'}}{\Delta t}+\\
&\frac{I^{\phi}_{\psi^0}e^{-\sigma^n_{E\psi^0}0.5\Delta t/\epsilon}}{\Delta z}[-{}_{\lambda}E^{x,\phi\phi\phi}_{l'-1/2,m',n'}(\frac{1-e^{\sigma^n_{E\phi}0.5\Delta t/\epsilon}}{\sigma^n_{E\phi}\Delta t})+\\
&{}_{\lambda-1}E^{x,\phi\phi\phi}_{l'-1/2,m',n'}e^{\sigma^n_{E\phi}\Delta t/\epsilon}(\frac{1-e^{-\sigma^n_{E\phi}0.5\Delta t/\epsilon}}{\sigma^n_{E\phi}\Delta t})]+\\
&\frac{I^{\psi^1_0}_{\psi^0}e^{-\sigma^n_{E\psi^0}0.5\Delta t/\epsilon}}{\Delta z}[-{}_{\lambda}E^{x,\phi\phi\psi^1_0}_{l'-1/2,m',n'}(\frac{1-e^{\sigma^n_{E\psi^1_0}0.5\Delta t/\epsilon}}{\sigma^n_{E\psi^1_0}\Delta t})+\\
&{}_{\lambda-1}E^{x,\phi\phi\psi^1_0}_{l'-1/2,m',n'}e^{\sigma^n_{E\psi^1_0}\Delta t/\epsilon}(\frac{1-e^{-\sigma^n_{E\psi^1_0}0.5\Delta t/\epsilon}}{\sigma^n_{E\psi^1_0}\Delta t})]+\\
&\frac{I^{\psi^1_1}_{\psi^0}e^{-\sigma^n_{E\psi^0}0.5\Delta t/\epsilon}}{\Delta z}[-{}_{\lambda}E^{x,\phi\phi\psi^1_1}_{l'-1/2,m',n'}(\frac{1-e^{\sigma^n_{E\psi^1_1}0.5\Delta t/\epsilon}}{\sigma^n_{E\psi^1_1}\Delta t})+\\
&{}_{\lambda-1}E^{x,\phi\phi\psi^1_1}_{l'-1/2,m',n'}e^{\sigma^n_{E\psi^1_1}\Delta t/\epsilon}(\frac{1-e^{-\sigma^n_{E\psi^1_1}0.5\Delta t/\epsilon}}{\sigma^n_{E\psi^1_1}\Delta t})]=\\
&e^{-\sigma^n_{E\psi^0}0.5\Delta t/\epsilon}(\frac{{}_{\lambda-1/2}H^{z,\phi\phi\psi^0}_{l'-1/2,m'+1/2,n'}-{}_{\lambda-1/2}H^{z,\phi\phi\psi^0}_{l'-1/2,m'-1/2,n'}}{\Delta y})-\\
&e^{-\sigma^n_{E\psi^0}0.5\Delta t/\epsilon}(\frac{{}_{\lambda-1/2}H^{y,\phi\phi\psi^0}_{l'-1/2,m',n'+1/2}-{}_{\lambda-1/2}H^{y,\phi\phi\psi^0}_{l'-1/2,m',n'-1/2}}{\Delta z})-\\
&e^{-\sigma^n_{E\psi^0}0.5\Delta t/\epsilon}(\frac{3\,{}_{\lambda-1/2}H^{y,\phi\phi\psi^1_0}_{l'-1/2,m',n'+1/2}+{}_{\lambda-1/2}H^{y,\phi\phi\psi^1_0}_{l'-1/2,m',n'-1/2}}{\sqrt{2}\Delta z})+\\
&e^{-\sigma^n_{E\psi^0}0.5\Delta t/\epsilon}(\frac{{}_{\lambda-1/2}H^{y,\phi\phi\psi^1_1}_{l'-1/2,m',n'+1/2}+3\,{}_{\lambda-1/2}H^{y,\phi\phi\psi^1_1}_{l'-1/2,m',n'-1/2}}{\sqrt{2}\Delta z})
\end{aligned}
\tag{6.171}
$$

$$
\begin{aligned}
&\epsilon\frac{{}_{\lambda}E^{x,\phi\phi\psi_0^1}_{l'-1/2,m',n'} - {}_{\lambda-1}E^{x,\phi\phi\psi_0^1}_{l'-1/2,m',n'}}{\Delta t} + \\
&\frac{I^{\phi}_{\psi_0^1} e^{-\sigma^n_{E\psi_0^1} 0.5\Delta t/\epsilon}}{\Delta z}\Big[-{}_{\lambda}E^{x,\phi\phi\phi}_{l'-1/2,m',n'}\Big(\frac{1-e^{\sigma^n_{E\phi}0.5\Delta t/\epsilon}}{\sigma^n_{E\phi}\Delta t}\Big) + \\
&{}_{\lambda-1}E^{x,\phi\phi\phi}_{l'-1/2,m',n'} e^{\sigma^n_{E\phi}\Delta t/\epsilon}\Big(\frac{1-e^{-\sigma^n_{E\phi}0.5\Delta t/\epsilon}}{\sigma^n_{E\phi}\Delta t}\Big)\Big] + \\
&\frac{I^{\psi_0^1}_{\psi_0^1} e^{-\sigma^n_{E\psi_0^1} 0.5\Delta t/\epsilon}}{\Delta z}\Big[-{}_{\lambda}E^{x,\phi\phi\psi^0}_{l'-1/2,m',n'}\Big(\frac{1-e^{\sigma^n_{E\psi^0}0.5\Delta t/\epsilon}}{\sigma^n_{E\psi^0}\Delta t}\Big) + \\
&{}_{\lambda-1}E^{x,\phi\phi\psi^0}_{l'-1/2,m',n'} e^{\sigma^n_{E\psi^0}\Delta t/\epsilon}\Big(\frac{1-e^{-\sigma^n_{E\psi^0}0.5\Delta t/\epsilon}}{\sigma^n_{E\psi^0}\Delta t}\Big)\Big] + \\
&\frac{I^{\psi_1^1}_{\psi_0^1} e^{-\sigma^n_{E\psi_0^1} 0.5\Delta t/\epsilon}}{\Delta z}\Big[-{}_{\lambda}E^{x,\phi\phi\psi_1^1}_{l'-1/2,m',n'}\Big(\frac{1-e^{\sigma^n_{E\psi_1^1}0.5\Delta t/\epsilon}}{\sigma^n_{E\psi_1^1}\Delta t}\Big) + \\
&{}_{\lambda-1}E^{x,\phi\phi\psi_1^1}_{l'-1/2,m',n'} e^{\sigma^n_{E\psi_1^1}\Delta t/\epsilon}\Big(\frac{1-e^{-\sigma^n_{E\psi_1^1}0.5\Delta t/\epsilon}}{\sigma^n_{E\psi_1^1}\Delta t}\Big)\Big] = \\
&e^{-\sigma^n_{E\psi_0^1}0.5\Delta t/\epsilon}\Big(\frac{{}_{\lambda-1/2}H^{z,\phi\phi\psi_0^1}_{l'-1/2,m'+1/2,n'} - {}_{\lambda-1/2}H^{z,\phi\phi\psi_0^1}_{l'-1/2,m'-1/2,n'}}{\Delta y}\Big) + \\
&e^{-\sigma^n_{E\psi_0^1}0.5\Delta t/\epsilon}\Big(\frac{{}_{\lambda-1/2}H^{y,\phi\phi\psi_0^1}_{l'-1/2,m',n'+1/2} - {}_{\lambda-1/2}H^{y,\phi\phi\psi_0^1}_{l'-1/2,m',n'-1/2}}{\Delta z}\Big) + \\
&e^{-\sigma^n_{E\psi_0^1}0.5\Delta t/\epsilon}\Big(\frac{{}_{\lambda-1/2}H^{y,\phi\phi\phi}_{l'-1/2,m',n'+1/2} - {}_{\lambda-1/2}H^{y,\phi\phi\phi}_{l'-1/2,m',n'-1/2}}{\sqrt{2}\Delta z}\Big) + \\
&e^{-\sigma^n_{E\psi_0^1}0.5\Delta t/\epsilon}\Big(\frac{{}_{\lambda-1/2}H^{y,\phi\phi\psi^0}_{l'-1/2,m',n'+1/2} + 3\,{}_{\lambda-1/2}H^{y,\phi\phi\psi^0}_{l'-1/2,m',n'-1/2}}{\sqrt{2}\Delta z}\Big)
\end{aligned} \tag{6.172}
$$

$$
\begin{gathered}
\epsilon\frac{{}_{\lambda}E^{x,\phi\phi\psi_1^1}_{l'-1/2,m',n'}-{}_{\lambda-1}E^{x,\phi\phi\psi_1^1}_{l'-1/2,m',n'}}{\Delta t}+ \\
\frac{I^{\phi}_{\psi_1^1}e^{-\sigma^n_{E\psi_1^1}0.5\Delta t/\epsilon}}{\Delta z}[-{}_{\lambda}E^{x,\phi\phi\phi}_{l'-1/2,m',n'}(\frac{1-e^{\sigma^n_{E\phi}0.5\Delta t/\epsilon}}{\sigma^n_{E\phi}\Delta t})+ \\
{}_{\lambda-1}E^{x,\phi\phi\phi}_{l'-1/2,m',n'}e^{\sigma^n_{E\phi}\Delta t/\epsilon}(\frac{1-e^{-\sigma^n_{E\phi}0.5\Delta t/\epsilon}}{\sigma^n_{E\phi}\Delta t})]+ \\
\frac{I^{\psi^0}_{\psi_1^1}e^{-\sigma^n_{E\psi_1^1}0.5\Delta t/\epsilon}}{\Delta z}[-{}_{\lambda}E^{x,\phi\phi\psi^0}_{l'-1/2,m',n'}(\frac{1-e^{\sigma^n_{E\psi^0}0.5\Delta t/\epsilon}}{\sigma^n_{E\psi^0}\Delta t})+ \\
{}_{\lambda-1}E^{x,\phi\phi\psi^0}_{l'-1/2,m',n'}e^{\sigma^n_{E\psi^0}\Delta t/\epsilon}(\frac{1-e^{-\sigma^n_{E\psi^0}0.5\Delta t/\epsilon}}{\sigma^n_{E\psi^0}\Delta t})]+ \\
\frac{I^{\psi_0^1}_{\psi_1^1}e^{-\sigma^n_{E\psi_0^1}0.5\Delta t/\epsilon}}{\Delta z}[-{}_{\lambda}E^{x,\phi\phi\psi_0^1}_{l'-1/2,m',n'}(\frac{1-e^{\sigma^n_{E\psi_0^1}0.5\Delta t/\epsilon}}{\sigma^n_{E\psi_0^1}\Delta t})+ \\
{}_{\lambda-1}E^{x,\phi\phi\psi_0^1}_{l'-1/2,m',n'}e^{\sigma^n_{E\psi_0^1}\Delta t/\epsilon}(\frac{1-e^{-\sigma^n_{E\psi_0^1}0.5\Delta t/\epsilon}}{\sigma^n_{E\psi_0^1}\Delta t})]= \\
e^{-\sigma^n_{E\psi_1^1}0.5\Delta t/\epsilon}(\frac{{}_{\lambda-1/2}H^{z,\phi\phi\psi_1^1}_{l'-1/2,m'+1/2,n'}-{}_{\lambda-1/2}H^{z,\phi\phi\psi_1^1}_{l'-1/2,m'-1/2,n'}}{\Delta y})+ \\
e^{-\sigma^n_{E\psi_1^1}0.5\Delta t/\epsilon}(\frac{{}_{\lambda-1/2}H^{y,\phi\phi\psi_1^1}_{l'-1/2,m',n'+1/2}-{}_{\lambda-1/2}H^{y,\phi\phi\psi_1^1}_{l'-1/2,m',n'-1/2}}{\Delta z})- \\
e^{-\sigma^n_{E\psi_1^1}0.5\Delta t/\epsilon}(\frac{{}_{\lambda-1/2}H^{y,\phi\phi\phi}_{l'-1/2,m',n'+1/2}-{}_{\lambda-1/2}H^{y,\phi\phi\phi}_{l'-1/2,m',n'-1/2}}{\sqrt{2}\Delta z})- \\
e^{-\sigma^n_{E\psi_1^1}0.5\Delta t/\epsilon}(\frac{3\,{}_{\lambda-1/2}H^{y,\phi\phi\psi^0}_{l'-1/2,m',n'+1/2}+{}_{\lambda-1/2}H^{y,\phi\phi\psi^0}_{l'-1/2,m',n'-1/2}}{\sqrt{2}\Delta z})
\end{gathered}
\tag{6.173}
$$

In the equations above, terms which have the form I^{f2}_{f1} are given by the following equation:

$$
\delta_{n,n'}I^{f2}_{f1}=\int_{-\infty}^{+\infty}f1(z)f2(z)\sigma_E(z)dz \tag{6.174}
$$

where $f1(z), f2(z)$ stand for $\phi(z), \psi^0(z), \psi^1_0(z), \psi^1_1(z)$ and $\sigma_E(z)$ is the parabolic function given in Eq. 6.21.

The PML equations for the remaining field components are derived in a similar way. Also, the same procedure can be used to derive the PML condition for any arbitrary resolution of wavelets. It can be shown very easily that when only scaling functions are used for field expansions (FDTD scheme), the PML equations above reduce to those given in Eqs. 6.57-6.62 in section 6.3 where PML implementation using only scaling expansions of electric and magnetic conductivities is presented. Thus it can be seen that the methodology presented here for the PML implementation is very general and can be used to develop the PML implementation for MRTD scheme of arbitrary resolution.

6.7 Applications of First Resolution 3-D Haar-MRTD Schemes

The first resolution MRTD scheme that has been derived in section 6.5.1 can be used to analyze complex electromagnetic circuits. In this section, this scheme is used to analyze the fields in the parallel plate waveguide junction shown in Figure 6.8.

As mentioned earlier, using zero resolution Haar MRTD scheme to analyze this geometry leads to numerical errors. This error is seen in Figure 6.9 where the incorrect values of the scaling and wavelet coefficients lead to a total reconstructed field pattern that is not smooth. This error is attributed to the numerical errors that crop up in the decoupled scaling and wavelet MRTD schemes of the zero resolution during the implementation of boundary conditions.

However, we have seen that using higher resolution wavelets leads to coupled MRTD schemes and simplifies the treatment of boundary conditions. Figure 6.15 shows the scaling, wavelet coefficients and total field reconstructed field obtained by analyzing the parallel plate waveguide junction using first resolution MRTD scheme. As seen from the figure, the total field is now smooth, indicating that the scaling and wavelet coefficients have been accurately evaluated using the higher resolution MRTD scheme.

6.8 Conclusion

For the first time in literature, a mathematically correct approach to implement an FDTD multigrid has been proposed. Since FDTD is based on the expansion of the unknown fields in terms of pulse functions, the principles of multiresolution analysis allows for consistent additional field expansion in terms of Haar wavelets. The Haar wavelet based MRTD scheme that has been developed here has been successfully applied to analyze the fields in some simple 3D microwave circuits.

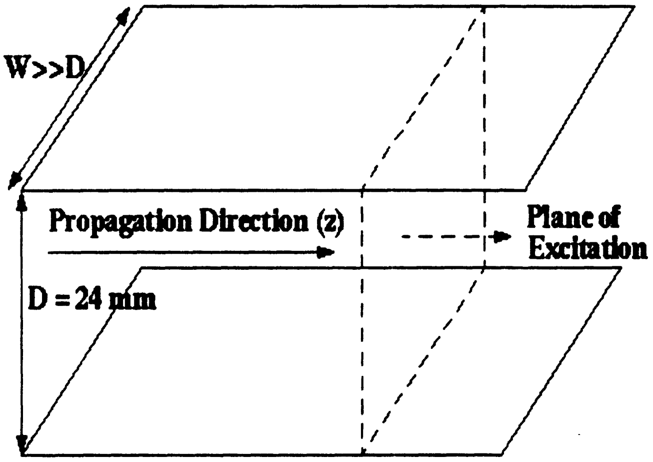

Figure 6.1: Parallel Plate Waveguide

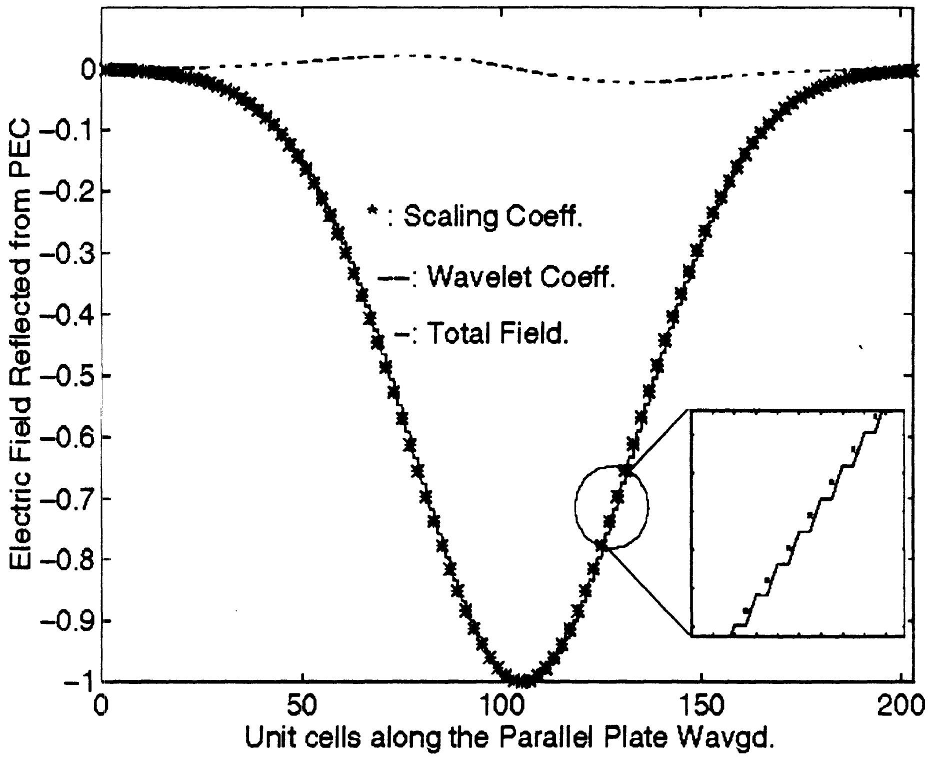

Figure 6.2: E field without wavelet excitation condition in a Parallel Plate Waveguide.

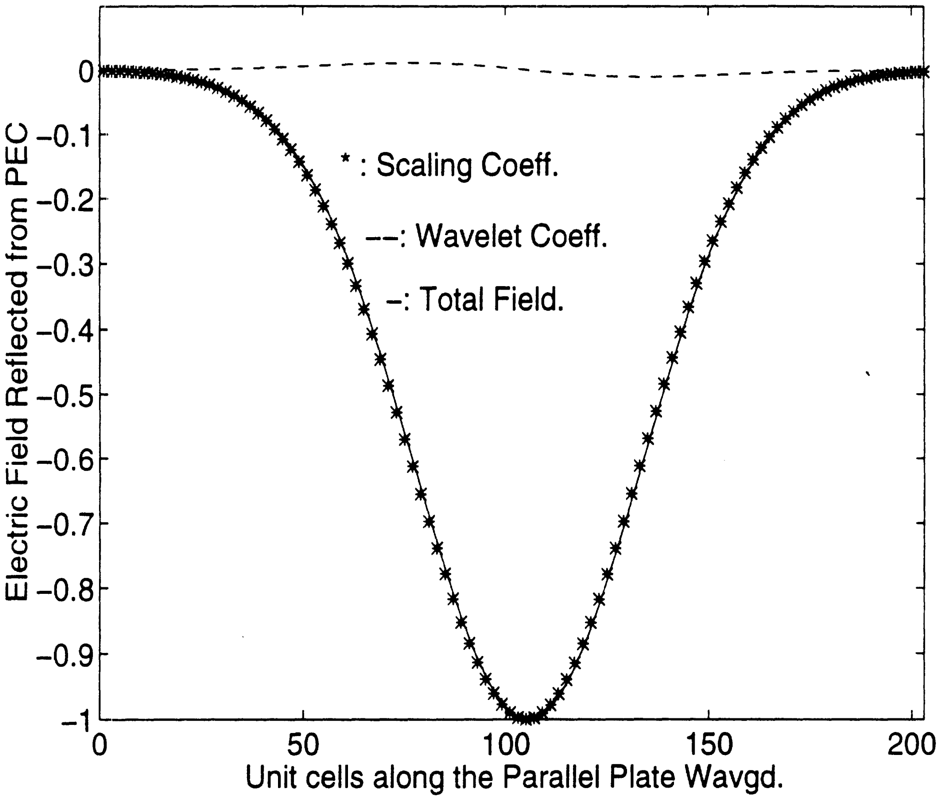

Figure 6.3: E field with wavelet excitation condition in a Parallel Plate Waveguide.

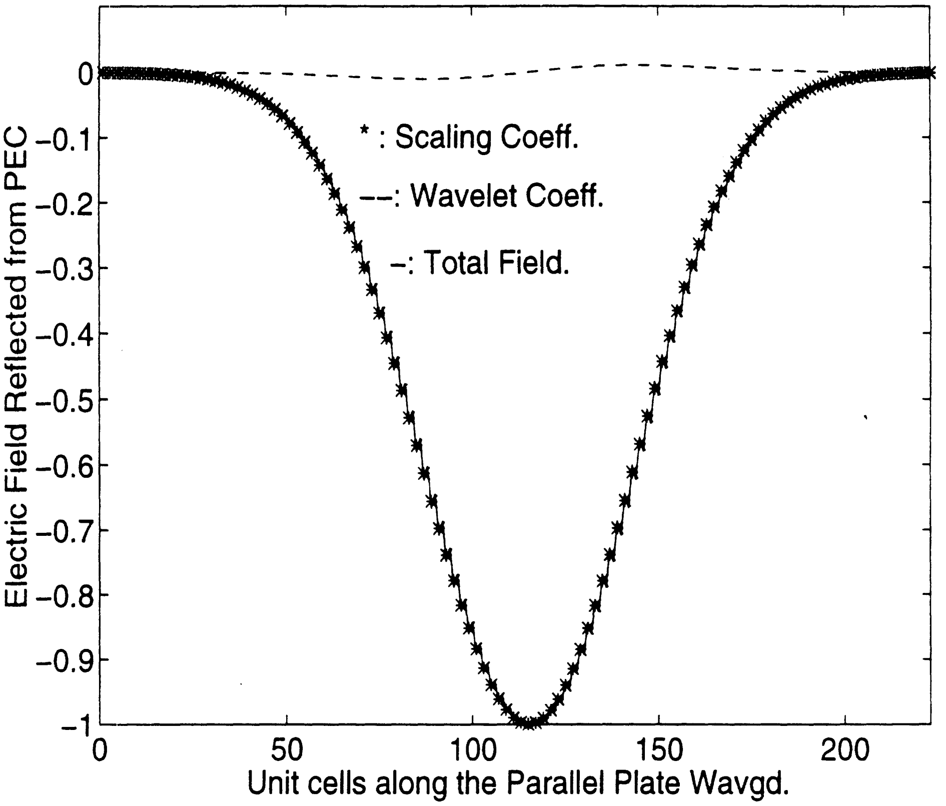

Figure 6.4: E field without continuity condition at PEC in a Parallel Plate Waveguide shorted at one end.

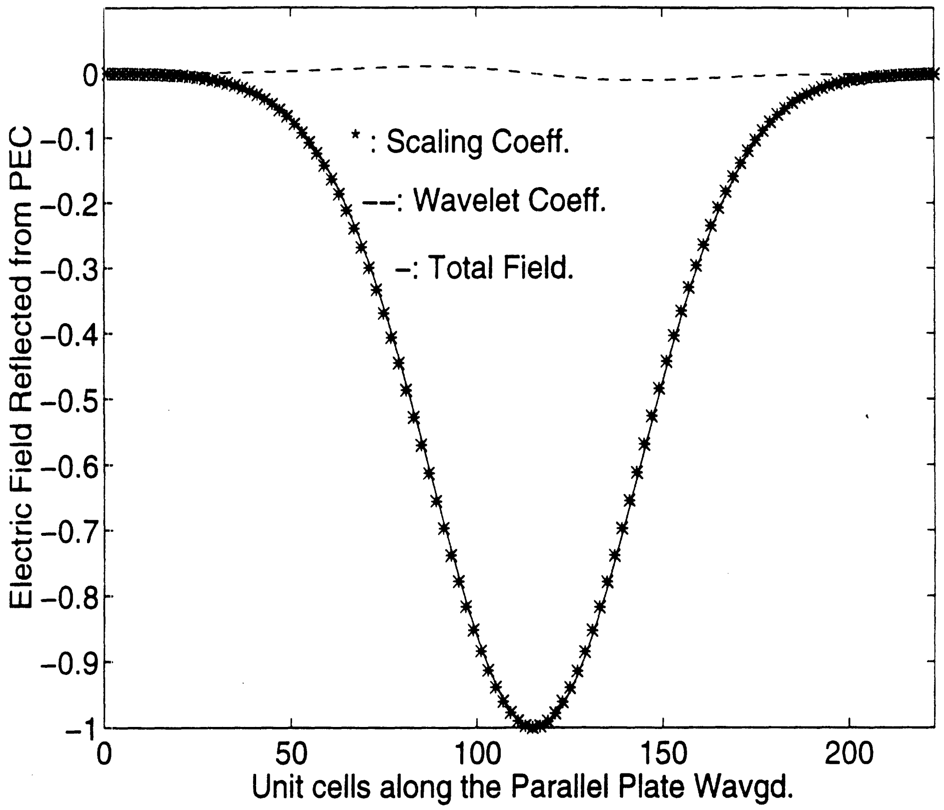

Figure 6.5: E field with continuity condition at PEC in a Parallel Plate Waveguide shorted at one end.

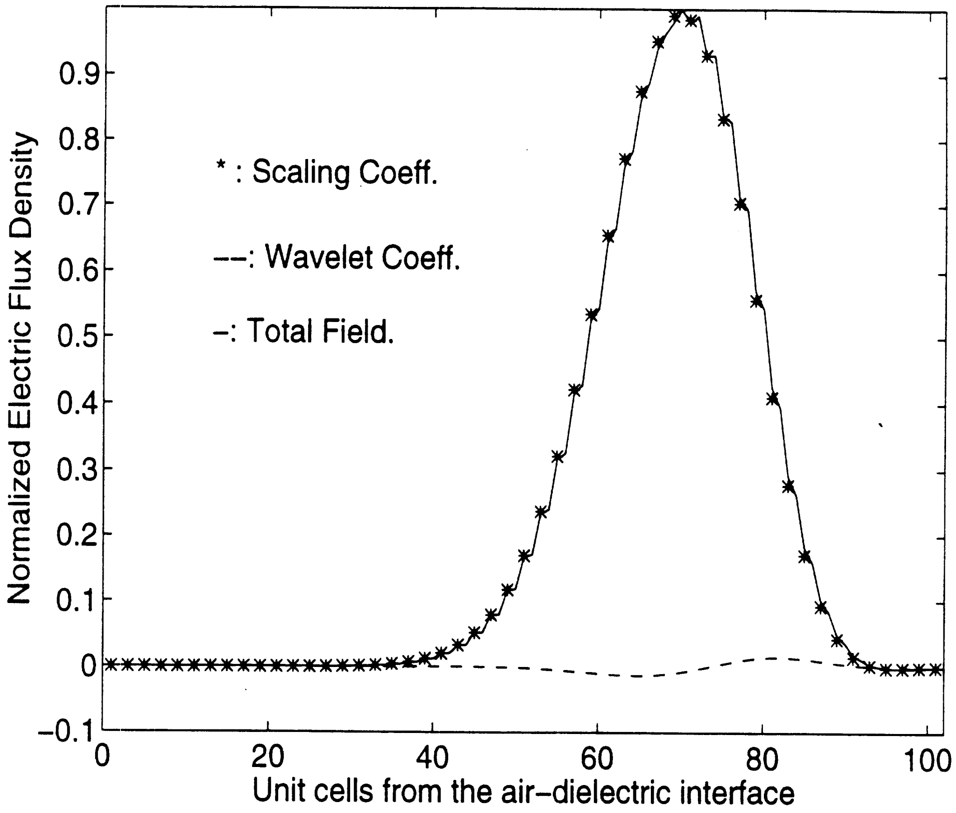

Figure 6.6: Flux density (D) without wavelet continuity conditions in a Parallel Plate Waveguide half filled with dielectric of $\epsilon_r = 10$.

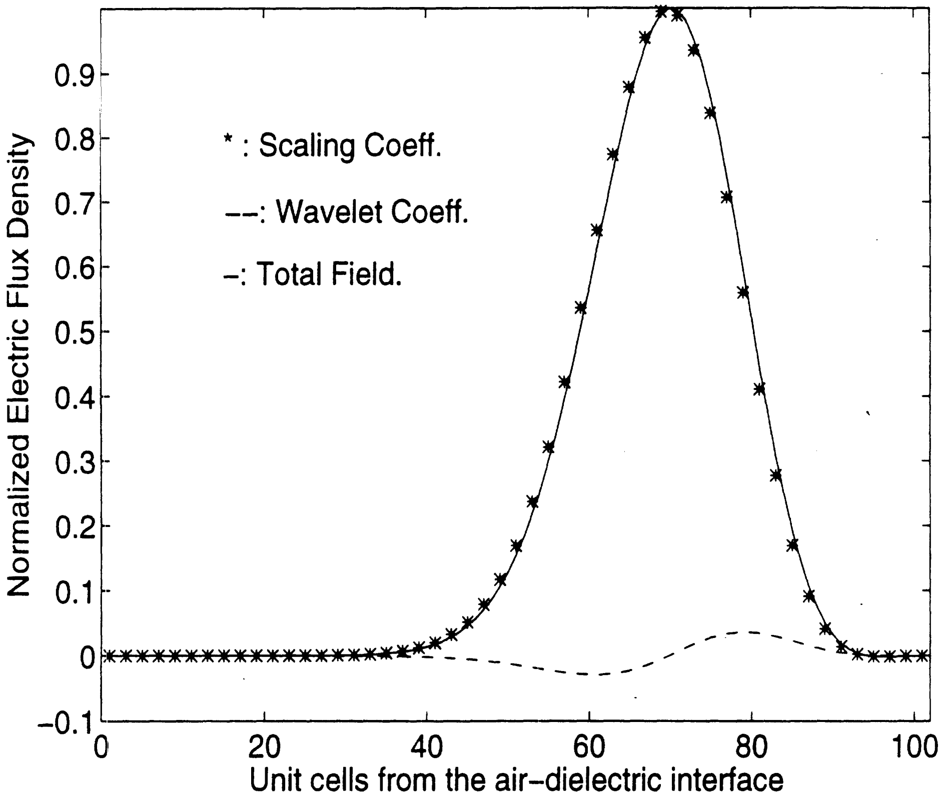

Figure 6.7: Flux density (D) with wavelet continuity conditions in a Parallel Plate Waveguide half filled with dielectric of $\epsilon_r = 10$.

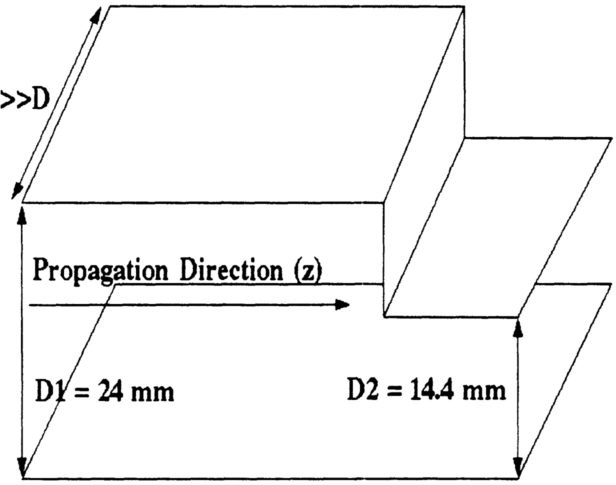

Figure 6.8: Parallel Plate Waveguide Junction

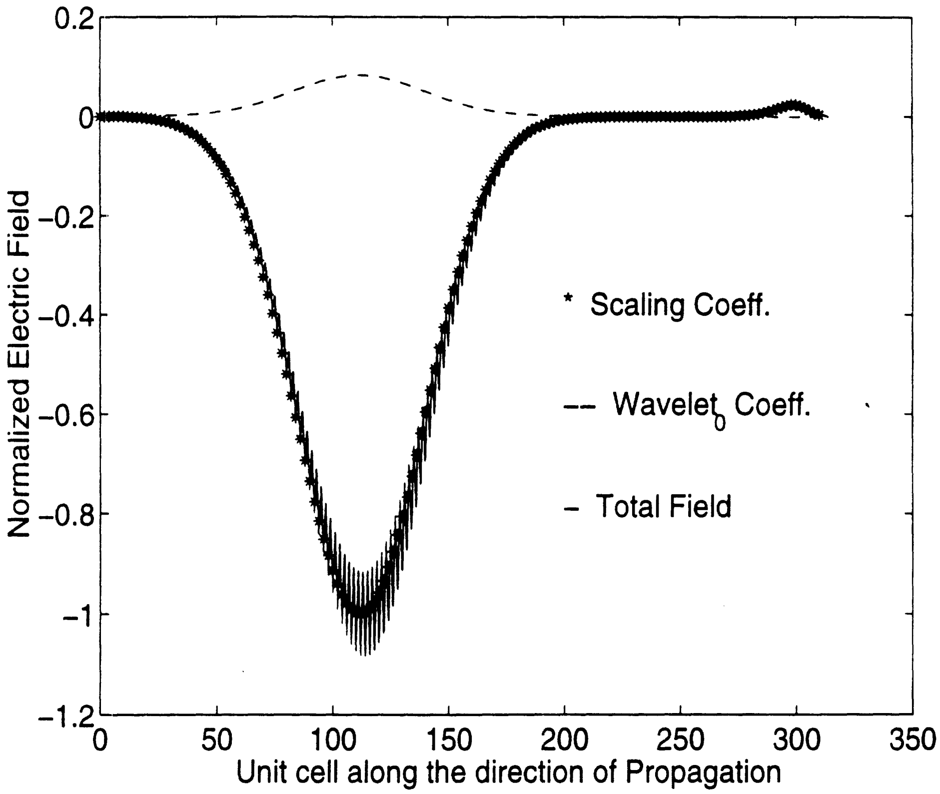

Figure 6.9: Zero Resolution MRTD Modeled Electric Field in a Parallel Plate Waveguide Junction at an arbitrary instant of time after the incident field sees the discontinuity

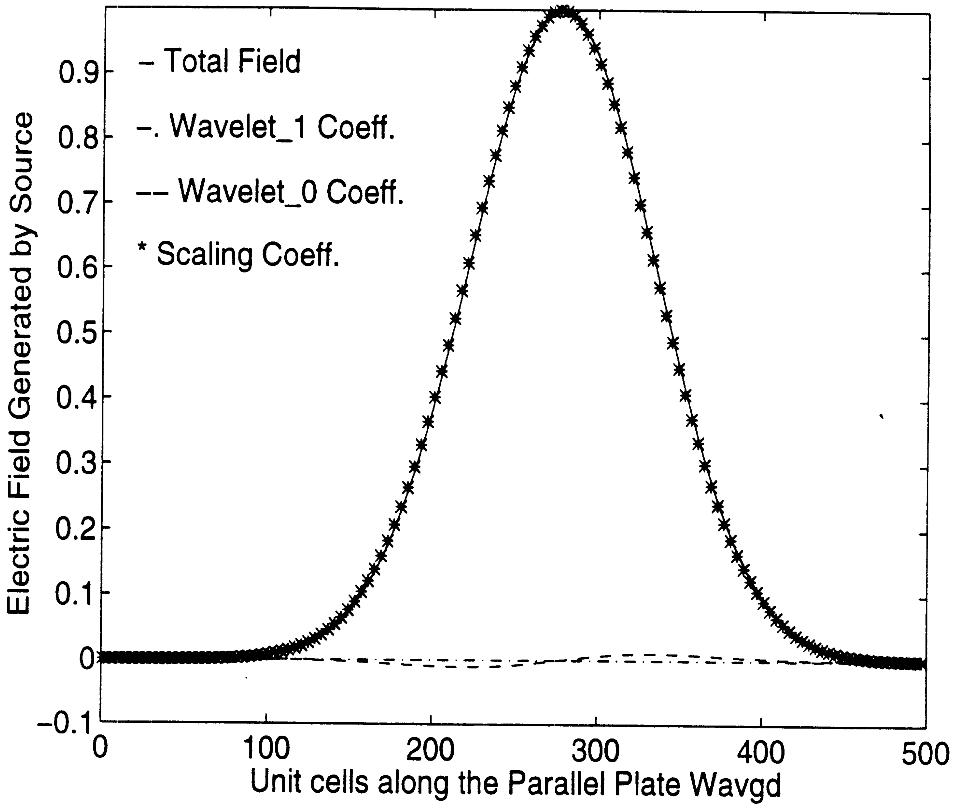

Figure 6.10: Electric field generated in a Parallel Plate waveguide by applying source condition of First Resolution MRTD scheme.

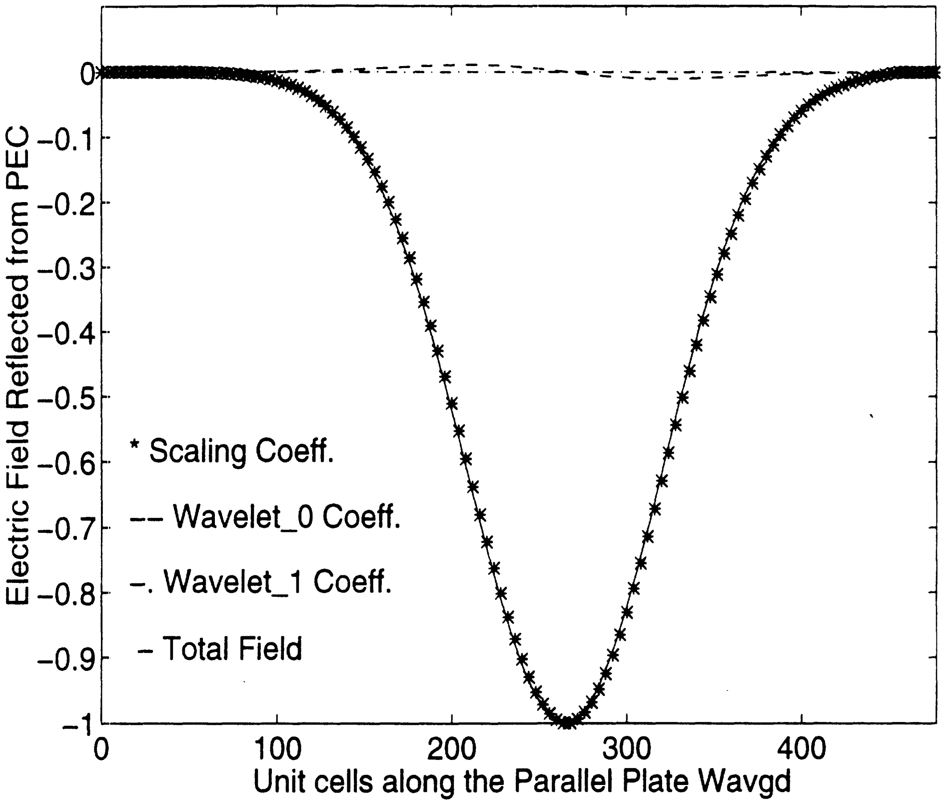

Figure 6.11: Reflected Electric Field obtained from First Resolution MRTD Scheme by applying PEC boundary condition in a Parallel plate waveguide terminated with a PEC

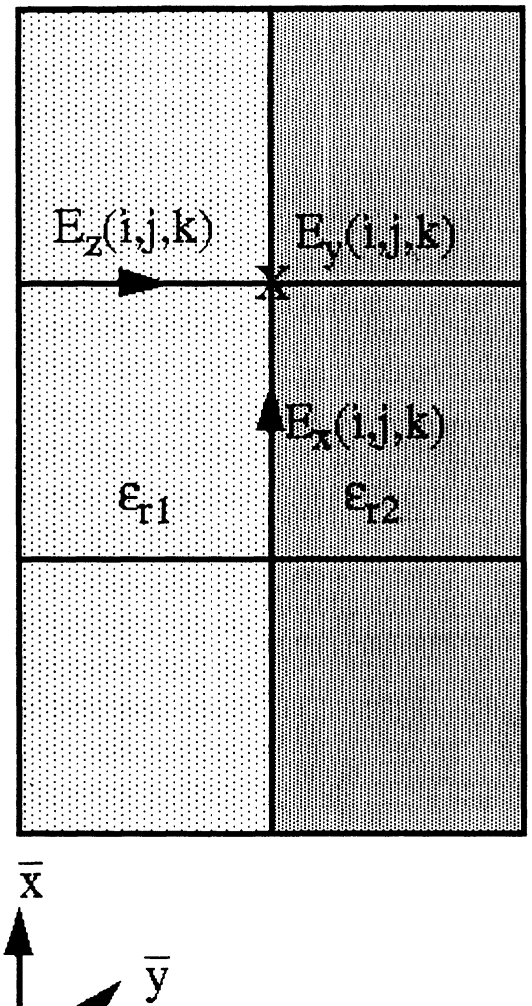

Figure 6.12: Dielectric interface with homogeneous dielectric material in each cell

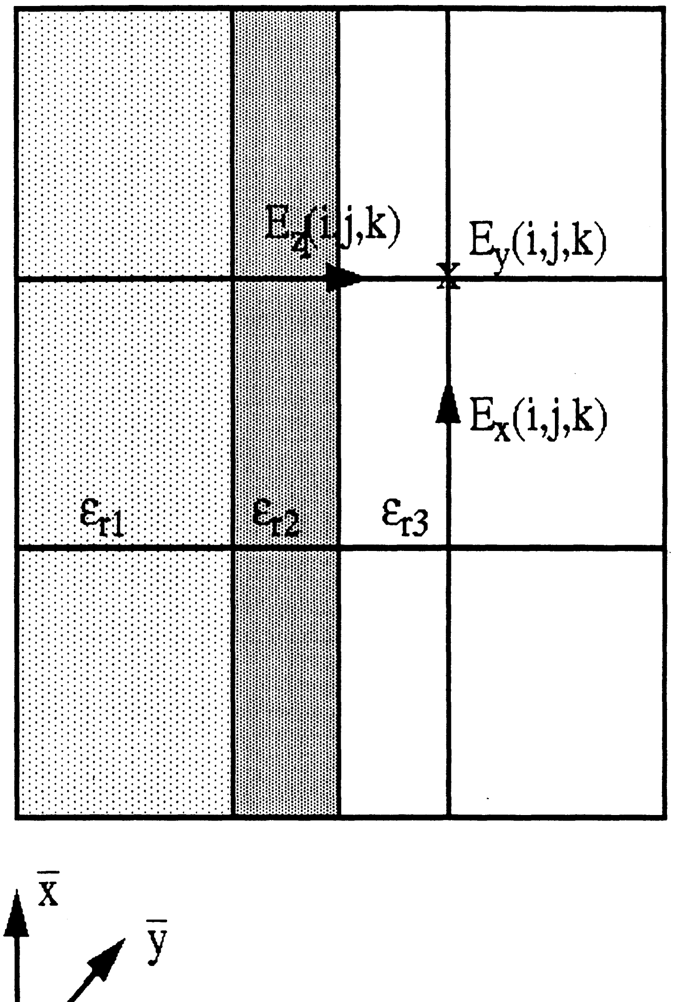

Figure 6.13: Dielectric interface with inhomogeneous dielectric material in cells

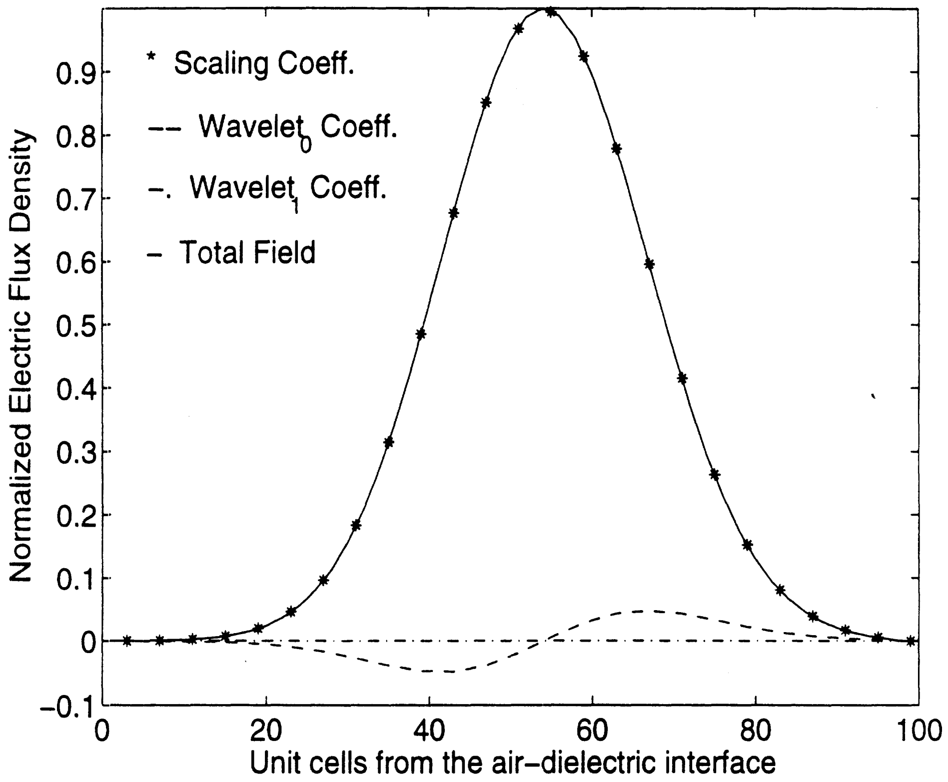

Figure 6.14: Electric Flux density (D) in a parallel Plate waveguide half filled with dielectric of $\epsilon_r = 20$

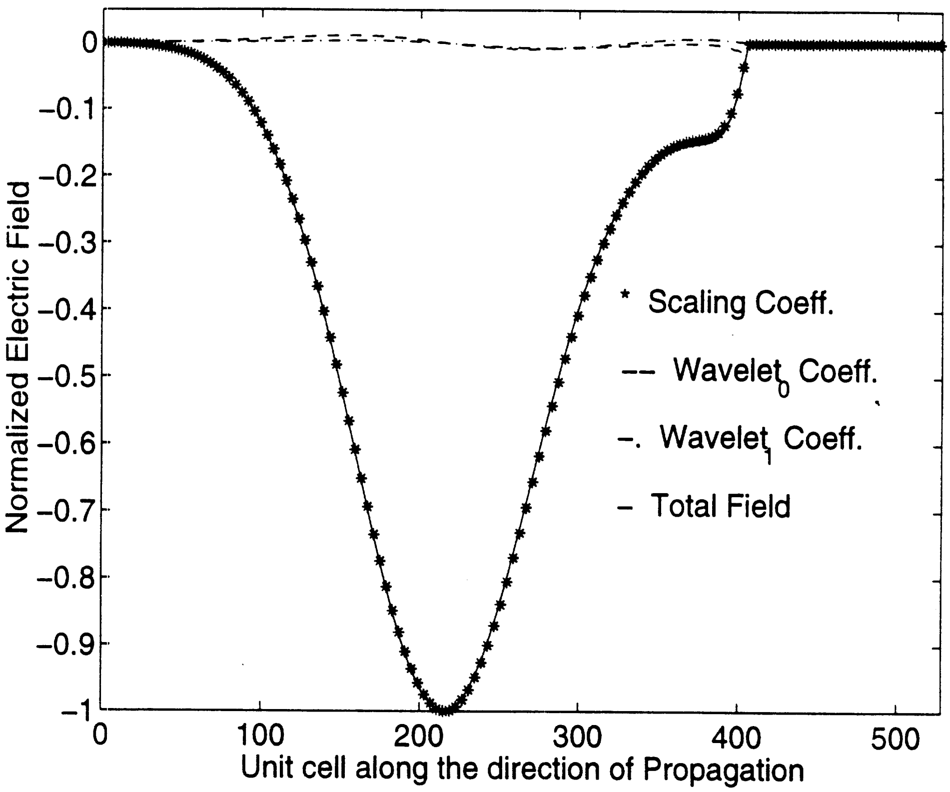

Figure 6.15: First Resolution MRTD modeled Electric Field in a Parallel Plate Waveguide Junction at an arbitrary instant of time after the incident field sees the discontinuity

CHAPTER 7

STABILITY AND DISPERSION ANALYSIS OF HAAR BASED MULTIRESOLUTION TIME DOMAIN SCHEMES

7.1 Introduction

In order to evaluate the usefulness of a discretized time domain scheme, it is very important to evaluate it's numerical stability and dispersion. Numerical stability analysis is necessary to ensure that the time domain scheme leads to stable solutions, i.e, any numerical errors in the scheme must not grow as simulation time progresses. In order to ensure stability, the time step Δt used in the discretized schemes have a specific bound relative to the space steps Δx, Δy and Δz. In addition to stability consideration, it is also necessary to evaluate the numerical dispersion resulting from discretized schemes. Dispersion is defined as the variation of a propagating wave's wavelength with frequency. It occurs due to the discretization scheme in the grid which causes the velocity of waves propagating on the grid to be dependent on the resolution of the grid and smoothness of the wave on the grid. In chapter 2, the dispersion and stability of the FDTD scheme were discussed. In this chapter, the stability and dispersion of the Haar-based MRTD scheme of arbitrary resolution will be presented.

7.2 Stability Analysis

The stability analysis method for the FDTD scheme is discussed in detail in [47]. To perform the stability analysis of the Haar-MRTD scheme, the same methodology of decomposing the MRTD equations into separate time and space eigenvalue problems is adopted. To begin with, the stability analysis is performed for 1D first resolution MRTD scheme (which uses Haar scaling function, mother wavelet and first resolution wavelets). The results are then generalized to include the general 3D MRTD scheme of arbitrary resolution. The reason for starting with the first resolution MRTD scheme is that the zero resolution Haar MRTD scheme leads to decoupled scaling and wavelet schemes where the discretized equations of each of these schemes are the same as those of the FDTD scheme and hence the stability analysis leads to the same stability criterion as that of the FDTD scheme. Since the first and higher resolution MRTD schemes are coupled, the stability analysis is presented for the first resolution MRTD scheme and eventually generalized to obtain the stability criterion for the Haar-MRTD scheme of arbitrary resolution.

Consider Maxwell's 1D equations as shown below:

$$\mu \frac{\partial H_x}{\partial t} = \frac{\partial E_y}{\partial z} \tag{7.1}$$

$$\epsilon \frac{\partial E_y}{\partial t} = \frac{\partial H_x}{\partial z} \tag{7.2}$$

Following the approach discussed in chapter 6, the following discretized equations can be obtained for the first resolution Haar-MRTD scheme:

$$\mu\frac{{}^{\lambda+1/2}H^{x,\phi}_{n'-1/2} -_{\lambda-1/2} H^{x,\phi}_{n'-1/2}}{\Delta t} = \frac{{}^{\lambda}E^{y,\phi}_{n'} -_{\lambda} E^{y,\phi}_{n'-1}}{\Delta z} +$$
$$\frac{-_{\lambda}E^{y,\psi^1_0}_{n'} +_{\lambda} E^{y,\psi^1_0}_{n'-1}}{\sqrt{2}\Delta z} + \frac{{}^{\lambda}E^{y,\psi^1_1}_{n'} -_{\lambda} E^{y,\psi^1_1}_{n'-1}}{\sqrt{2}\Delta z} \tag{7.3}$$

$$\mu\frac{{}^{\lambda+1/2}H^{x,\psi^0}_{n'-1/2} -_{\lambda-1/2} H^{x,\psi^0}_{n'-1/2}}{\Delta t} = \frac{{}^{\lambda}E^{y,\psi^0}_{n'} -_{\lambda} E^{y,\psi^0}_{n'-1}}{\Delta z} +$$
$$\frac{3_{\lambda}E^{y,\psi^1_0}_{n'} +_{\lambda} E^{y,\psi^1_0}_{n'}}{\sqrt{2}\Delta z} - \frac{{}^{\lambda}E^{y,\psi^1_1}_{n'} + 3_{\lambda}E^{y,\psi^1_1}_{n'-1}}{\sqrt{2}\Delta z} \tag{7.4}$$

$$\mu\frac{{}^{\lambda+1/2}H^{x,\psi^1_0}_{n'-1/2} -_{\lambda-1/2} H^{x,\psi^1_0}_{n'-1/2}}{\Delta t} = \frac{{}^{\lambda}E^{y,\psi^1_0}_{n'-1} -_{\lambda} E^{y,\psi^1_0}_{n'}}{\Delta z} -$$
$$\frac{{}^{\lambda}E^{y,\phi}_{n'} -_{\lambda} E^{y,\phi}_{n'-1}}{\sqrt{2}\Delta z} - \frac{{}^{\lambda}E^{y,\psi^0}_{n'} + 3_{\lambda}E^{y,\psi^0}_{n'-1}}{\sqrt{2}\Delta z} \tag{7.5}$$

$$\mu\frac{{}^{\lambda+1/2}H^{x,\psi^1_1}_{n'-1/2} -_{\lambda-1/2} H^{x,\psi^1_1}_{n'-1/2}}{\Delta t} = \frac{{}^{\lambda}E^{y,\psi^1_1}_{n'} -_{\lambda} E^{y,\psi^1_1}_{n'-1}}{\Delta z} +$$
$$\frac{{}^{\lambda}E^{y,\phi}_{n'} -_{\lambda} E^{y,\phi}_{n'-1}}{\sqrt{2}\Delta z} + \frac{3_{\lambda}E^{y,\psi^0}_{n'} +_{\lambda} E^{y,\psi^0}_{n'-1}}{\sqrt{2}\Delta z} \tag{7.6}$$

$$\epsilon\frac{{}^{\lambda}E^{y,\phi}_{n'} -_{\lambda-1} E^{y,\phi}_{n'}}{\Delta t} = \frac{{}^{\lambda-1/2}H^{x,\phi}_{n'+1/2} -_{\lambda-1/2} H^{x,\phi}_{n'-1/2}}{\Delta z} -$$
$$\frac{{}^{\lambda-1/2}H^{x,\psi^1_0}_{n'+1/2} -_{\lambda-1/2} H^{x,\psi^1_0}_{n'-1/2}}{\sqrt{2}\Delta z} + \frac{{}^{\lambda-1/2}H^{x,\psi^1_1}_{n'+1/2} -_{\lambda-1/2} H^{x,\psi^1_1}_{n'-1/2}}{\sqrt{2}\Delta z} \tag{7.7}$$

$$\epsilon\frac{{}^{\lambda}E^{y,\psi^0}_{n'} -_{\lambda-1} E^{y,\psi^0}_{n'}}{\Delta t} = \frac{{}^{\lambda-1/2}H^{x,\psi^0}_{n'+1/2} -_{\lambda-1/2} H^{x,\psi^0}_{n'-1/2}}{\Delta z} +$$
$$\frac{3_{\lambda-1/2}H^{x,\psi^1_0}_{n'+1/2} +_{\lambda-1/2} H^{x,\psi^1_0}_{n'-1/2}}{\sqrt{2}\Delta z} - \frac{{}^{\lambda-1/2}H^{x,\psi^1_1}_{n'+1/2} + 3_{\lambda-1/2}H^{x,\psi^1_1}_{n'-1/2}}{\sqrt{2}\Delta z} \tag{7.8}$$

$$\epsilon\frac{{}_{\lambda}E_{n'}^{y,\psi_0^1} - {}_{\lambda-1}\,E_{n'}^{y,\psi_0^1}}{\Delta t} = \frac{{}_{\lambda-1/2}H_{n'-1/2}^{x,\psi_0^1} - {}_{\lambda-1/2}\,H_{n'+1/2}^{x,\psi^{01}}}{\Delta z} - \\ \frac{3{}_{\lambda-1/2}H_{n'+1/2}^{x,\psi^0} + {}_{\lambda-1/2}\,H_{n'-1/2}^{x,\psi^0}}{\sqrt{2}\Delta z} - \frac{{}_{\lambda-1/2}H_{n'+1/2}^{x,\phi} - {}_{\lambda-1/2}\,H_{n'-1/2}^{x,\phi}}{\sqrt{2}\Delta z} \tag{7.9}$$

$$\epsilon\frac{{}_{\lambda}E_{n'}^{y,\psi_1^1} - {}_{\lambda-1}\,E_{n'}^{y,\psi_1^1}}{\Delta t} = \frac{{}_{\lambda-1/2}H_{n'-1/2}^{x,\psi_1^1} - {}_{\lambda-1/2}\,H_{n'+1/2}^{x,\psi_1^1}}{\Delta z} + \\ \frac{3{}_{\lambda-1/2}H_{n'+1/2}^{x,\psi^0} + {}_{\lambda-1/2}\,H_{n'-1/2}^{x,\psi^0}}{\sqrt{2}\Delta z} + \frac{{}_{\lambda-1/2}H_{n'+1/2}^{x,\phi} - {}_{\lambda-1/2}\,H_{n'-1/2}^{x,\phi}}{\sqrt{2}\Delta z} \tag{7.10}$$

To perform the stability analysis, the time-differentiation parts of Eqs. 7.1 - 7.2 are written as eigenvalue problems as shown below:

$$\frac{{}_{\lambda+1/2}H_{n'-1/2}^{x,\phi} - {}_{\lambda-1/2}\,H_{n'-1/2}^{x,\phi}}{\Delta t} = \Lambda_{\lambda}H_{n'-1/2} \tag{7.11}$$

$$\frac{{}_{\lambda}E_{n'}^{y,\phi} - {}_{\lambda-1}\,E_{n'}^{y,\phi}}{\Delta t} = \Lambda_{\lambda-1/2}E_{n'} \tag{7.12}$$

It can be shown that in order to ensure that none of the spatial modes in the scheme increase without limit during normal time stepping, the following condition has to be enforced on Λ which is a pure imaginary number [47]:

$$-\frac{2}{\Delta t} \leq Im(\Lambda) \leq \frac{2}{\Delta t} \tag{7.13}$$

Next, the space-eigenvalue problem is addressed. For this, the space differentiations are also written as eigenvalue problems as shown below:

$$\frac{1}{\mu}\left(\frac{{}_\lambda E^{y,\phi}_{n'} -{}_\lambda E^{y,\phi}_{n'-1}}{\Delta z} + \frac{-{}_\lambda E^{y,\psi^1_0}_{n'} +{}_\lambda E^{y,\psi^1_0}_{n'-1}}{\sqrt{2}\Delta z} + \frac{{}_\lambda E^{y,\psi^1_1}_{n'} -{}_\lambda E^{y,\psi^1_1}_{n'-1}}{\sqrt{2}\Delta z}\right) = \Lambda_\lambda H^{x,\phi}_{n'-1/2} \tag{7.14}$$

$$\frac{1}{\mu}\left(\frac{{}_\lambda E^{y,\psi^0}_{n'} -{}_\lambda E^{y,\psi^0}_{n'-1}}{\Delta z} + \frac{3{}_\lambda E^{y,\psi^1_0}_{n'} +{}_\lambda E^{y,\psi^1_0}_{n'}}{\sqrt{2}\Delta z} - \frac{{}_\lambda E^{y,\psi^1_1}_{n'} + 3{}_\lambda E^{y,\psi^1_1}_{n'-1}}{\sqrt{2}\Delta z}\right) = \Lambda_\lambda H^{x,\psi^0}_{n'-1/2} \tag{7.15}$$

$$\frac{1}{\mu}\left(\frac{{}_\lambda E^{y,\psi^1_0}_{n'-1} -{}_\lambda E^{y,\psi^1_0}_{n'}}{\Delta z} - \frac{{}_\lambda E^{y,\phi}_{n'} -{}_\lambda E^{y,\phi}_{n'-1}}{\sqrt{2}\Delta z} - \frac{{}_\lambda E^{y,\psi^0}_{n'} + 3{}_\lambda E^{y,\psi^0}_{n'-1}}{\sqrt{2}\Delta z}\right) = \Lambda_\lambda H^{x,\psi^1_0}_{n'-1/2} \tag{7.16}$$

$$\frac{1}{\mu}\left(\frac{{}_\lambda E^{y,\psi^1_1}_{n'} -{}_\lambda E^{y,\psi^1_1}_{n'-1}}{\Delta z} + \frac{{}_\lambda E^{y,\phi}_{n'} -{}_\lambda E^{y,\phi}_{n'-1}}{\sqrt{2}\Delta z} + \frac{3{}_\lambda E^{y,\psi^0}_{n'} +{}_\lambda E^{y,\psi^0}_{n'-1}}{\sqrt{2}\Delta z}\right) = \Lambda_\lambda H^{x,\psi^1_1}_{n'-1/2} \tag{7.17}$$

$$\begin{aligned}&\frac{1}{\epsilon}\frac{{}_{\lambda-1/2}H^{x,\phi}_{n'+1/2} -{}_{\lambda-1/2} H^{x,\phi}_{n'-1/2}}{\Delta z} - \frac{{}_{\lambda-1/2}H^{x,\psi^1_0}_{n'+1/2} -{}_{\lambda-1/2} H^{x,\psi^1_0}_{n'-1/2}}{\sqrt{2}\Delta z} + \\ &\frac{{}_{\lambda-1/2}H^{x,\psi^1_1}_{n'+1/2} -{}_{\lambda-1/2} H^{x,\psi^1_1}_{n'-1/2}}{\sqrt{2}\Delta z} = \Lambda\epsilon_\lambda E^{y,\phi}_{n'}\end{aligned} \tag{7.18}$$

$$\begin{aligned}&\frac{1}{\epsilon}\frac{{}_{\lambda-1/2}H^{x,\psi^0}_{n'+1/2} -{}_{\lambda-1/2} H^{x,\psi^0}_{n'-1/2}}{\Delta z} + \frac{3{}_{\lambda-1/2}H^{x,\psi^1_0}_{n'+1/2} +{}_{\lambda-1/2} H^{x,\psi^1_0}_{n'-1/2}}{\sqrt{2}\Delta z} - \\ &\frac{{}_{\lambda-1/2}H^{x,\psi^1_1}_{n'+1/2} + 3{}_{\lambda-1/2}H^{x,\psi^1_1}_{n'-1/2}}{\sqrt{2}\Delta z} = \Lambda\epsilon_\lambda E^{y,\psi^0}_{n'}\end{aligned} \tag{7.19}$$

$$\begin{aligned}&\frac{1}{\epsilon}\frac{{}_{\lambda-1/2}H^{x,\psi^1_0}_{n'-1/2} -{}_{\lambda-1/2} H^{x,\psi^{01}}_{n'+1/2}}{\Delta z} - \frac{3{}_{\lambda-1/2}H^{x,\psi^0}_{n'+1/2} +{}_{\lambda-1/2} H^{x,\psi^0}_{n'-1/2}}{\sqrt{2}\Delta z} - \\ &\frac{{}_{\lambda-1/2}H^{x,\phi}_{n'+1/2} -{}_{\lambda-1/2} H^{x,\phi}_{n'-1/2}}{\sqrt{2}\Delta z} = \Lambda\epsilon_\lambda E^{y,\psi^1_0}_{n'}\end{aligned} \tag{7.20}$$

$$\frac{1}{\epsilon}\frac{{}_{\lambda-1/2}H^{x,\psi_1^1}_{n'-1/2} - {}_{\lambda-1/2}\,H^{x,\psi_1^1}_{n'+1/2}}{\Delta z} + \frac{3{}_{\lambda-1/2}H^{x,\psi^0}_{n'+1/2} + {}_{\lambda-1/2}\,H^{x,\psi^0}_{n'-1/2}}{\sqrt{2}\Delta z} +$$
$$\frac{{}_{\lambda-1/2}H^{x,\phi}_{n'+1/2} - {}_{\lambda-1/2}\,H^{x,\phi}_{n'-1/2}}{\sqrt{2}\Delta z} = \Lambda\epsilon_\lambda E^{y,\psi_1^1}_{n'} \tag{7.21}$$

At any time step λ, the instantaneous values of the electric and magnetic fields in the grid can be Fourier transformed with respect to the grid coordinate n' to provide a spectrum of sinusoidal modes. Assuming k_z to be the wavevector, we can specify the modes of frequency spectrum as follows:

$$E^y_{n'} = E_{yo}e^{jk_z n'\Delta z} \tag{7.22}$$

$$H^x_{n'} = H_{xo}e^{jk_z n'\Delta z} \tag{7.23}$$

Substituting the eigenmode expressions of Eq. 7.22 and 7.23 in Eqs. 7.14- 7.21 and simplifying the expressions to solve for Λ, we obtain the following expression:

$$\Lambda^2 = -\frac{1}{\epsilon\mu}\frac{16}{\Delta z^2}\sin^2\left(\frac{k_z\Delta z}{4}\right) \tag{7.24}$$

From Eq. 7.24, it can be inferred that Λ is a purely imaginary number and has the following bounds:

$$-\frac{4}{c}\frac{1}{\Delta z} \leq Im(\Lambda) \leq \frac{4}{c}\frac{1}{\Delta z} \tag{7.25}$$

where $c = 1/sqrt(\mu\epsilon)$ is the velocity of propagation of light in the material being modeled.

To maintain numerical stability for any arbitrary spatial mode, the range of eigenvalues for the spatial mode must be contained within the stability range of the time eigenvalues given by Eq. 7.13. This implies the following stability condition for 1D first resolution MRTD scheme:

$$\Delta t \leq \frac{1}{2c\frac{1}{\Delta z}} \tag{7.26}$$

Following the approach shown here, the following expression is obtained for the stability analysis of a 3D first resolution Haar-MRTD scheme (with wavelets in all three directions):

$$\Delta t \leq \frac{1}{2c\sqrt{(\frac{1}{\Delta x^2} + \frac{1}{\Delta y^2} + \frac{1}{\Delta z^2}}}) \tag{7.27}$$

For an arbitrary resolution MRTD scheme say rth resolution scheme (which uses up to r-1 resolution of wavelets, the stability criterion is as follows:

$$\Delta t \leq \frac{1}{2^{r-1}c\sqrt{(\frac{1}{\Delta x^2} + \frac{1}{\Delta y^2} + \frac{1}{\Delta z^2}}}) \tag{7.28}$$

If different resolutions are used in different directions, say, r_x, r_y and r_z in x, y and z directions respectively, the stability condition becomes:

$$\Delta t \leq \frac{1}{c\sqrt{(\frac{2^{2r_x-2}}{\Delta x^2} + \frac{2^{2r_y-2}}{\Delta y^2} + \frac{2^{2r_z-2}}{\Delta z^2}}}) \tag{7.29}$$

When the stability time step for MRTD scheme is compared to that of the FDTD scheme which is given by $\Delta t \leq \frac{1}{c\sqrt{(\frac{1}{\Delta x^2}+\frac{1}{\Delta x^2}+\frac{1}{\Delta x^2}}})$, we notice that for zero resolution MRTD scheme, the stability equation is the same as FDTD as expected since zero resolution MRTD scheme reduces to the FDTD scheme. Also, the stability time step is small for the MRTD scheme compared to the FDTD scheme. This is also as expected since MRTD effectively enhances the resolution of the mesh which is equivalent to choosing smaller grid sizes.

7.3 Dispersion Analysis

In this section, the method of deriving the dispersion relation for Haar-MRTD scheme is presented. The approach is the same as that used to obtain the FDTD dispersion relation [47]. For the same reasons discussed in section 7.2, the dispersion analysis is presented for a 1D first resolution MRTD scheme and then generalized to obtain the dispersion relation for an MRTD scheme of arbitrary resolution.

Consider Maxwell's 1D Eqs. 7.1-7.2 and the first resolution MRTD discretized Eqs. 7.3-7.10. The procedure for the dispersion analysis involves substitution of plane monochromatic traveling-wave solutions into the discretized MRTD equations. For the 1D MRTD case here, these equations are shown below:

$$ {}_{\lambda}E^{y}_{n'} = E_{yo}e^{jk_z n'\Delta z - \omega\lambda\Delta t} \tag{7.30} $$

$$ {}_{\lambda}H^{x}_{n'} = H_{xo}e^{jk_z n'\Delta z - \omega\lambda\Delta t} \tag{7.31} $$

Eqs. 7.30 and 7.31 are substituted into MRTD discretized Eqs. 7.3-7.10. After some algebraic manipulations of the resulting equations, the following dispersion relation which relates the numerical wavevector, wavefrequency and grid space and time steps is obtained for the first resolution 1D MRTD scheme:

$$\left[\frac{1}{c\Delta t}\sin(\frac{\omega\Delta t}{2})\right]^2 = \left[\frac{2}{\Delta x}\sin(\frac{k_z\Delta z}{4})\right]^2 \tag{7.32}$$

For a first resolution 3D MRTD scheme, following the same procedure discussed above, the following dispersion relation is obtained:

$$\left[\frac{1}{c\Delta t}\sin(\frac{\omega\Delta t}{2})\right]^2 = \left[\frac{2}{\Delta x}\sin(\frac{k_x\Delta x}{4})\right]^2 + \left[\frac{2}{\Delta y}\sin(\frac{k_y\Delta y}{4})\right]^2 + \left[\frac{2}{\Delta z}\sin(\frac{k_z\Delta z}{4})\right]^2 \tag{7.33}$$

For a general rth order 3D MRTD scheme, the dispersion relation is given as follows:

$$\left[\frac{1}{c\Delta t}\sin(\frac{\omega\Delta t}{2})\right]^2 = \left[\frac{2^{r-1}}{\Delta x}\sin(\frac{k_x\Delta x}{2^r})\right]^2 + \left[\frac{2^{r-1}}{\Delta y}\sin(\frac{k_y\Delta y}{2^r})\right]^2 + \left[\frac{2^{r-1}}{\Delta z}\sin(\frac{k_z\Delta z}{2^r})\right]^2 \tag{7.34}$$

For a 3D MRTD scheme whose resolution is r_x, r_y and r_z in x, y and z directions respectively, the dispersion relation is given as follows:

$$\left[\frac{1}{c\Delta t}\sin(\frac{\omega\Delta t}{2})\right]^2 = \left[\frac{2^{r_x-1}}{\Delta x}\sin(\frac{k_x\Delta x}{2^r_x})\right]^2 + \left[\frac{2^{r_y-1}}{\Delta y}\sin(\frac{k_y\Delta y}{2^r_y})\right]^2 + \left[\frac{2^{r_z-1}}{\Delta z}\sin(\frac{k_z\Delta z}{2^r_z})\right]^2 \tag{7.35}$$

Comparing the dispersion relation of the MRTD scheme with that of the FDTD scheme which is given by $\left[\frac{1}{c\Delta t}\sin(\frac{\omega\Delta t}{2})\right]^2 = \left[\frac{1}{\Delta x}\sin(\frac{k_x\Delta x}{2})\right]^2 + \left[\frac{1}{\Delta y}\sin(\frac{k_y\Delta y}{2})\right]^2 + \left[\frac{1}{\Delta z}\sin(\frac{k_z\Delta z}{2})\right]^2$, we observe that for the zero resolution MRTD scheme, the dispersion relation becomes the same as that of the FDTD scheme as expected. In addition, it is also observed that MRTD dispersion appears to be much more linear compared to FDTD dispersion. This is because as mention earlier, MRTD scheme enhances the resolution of the FDTD scheme and effectively provides finer grid sizes.

7.4 Conclusion

The stability and dispersion analysis of Haar-MRTD schemes has been presented. The compact Haar bases leads to simple analytical expressions for stability and dispersion of the MRTD scheme. As expected, the MRTD dispersion and stability become the same as that of FDTD for zero resolution MRTD. Also, comparing the stability and dispersion relations of MRTD scheme with that of FDTD scheme, it can be seen that for any choice of resolution of MRTD scheme, the same stability and dispersion relations can be obtained by choosing a finer mesh in the conventional FDTD scheme. This is also intuitive because the Haar-MRTD scheme effectively enhances the resolution of the conventional FDTD scheme.

CHAPTER 8

APPLICATIONS OF MRTD IN THE ANALYSIS OF COMPLEX MICROWAVE CIRCUITS

8.1 Introduction

In the previous chapters, the Haar wavelet based MRTD scheme was developed. It was demonstrated that the resolution of a function can be enhanced from a coarse level to a fine level either by using fine resolution scaling functions or a combination of coarse resolution scaling functions and intermediate level wavelets. Furthermore, it was shown that while the same resolution can be achieved by both methods, using a combination of coarse scaling functions with the necessary intermediate resolution wavelets (to obtain the desired resolution) is more beneficial. This is because as it was shown in the examples in the previous chapters, wavelet expansion coefficients are significant only in areas of strong field variations. Wavelet coefficients which are below a certain threshold level can be discarded without adversely affecting the condition numbering of the system [57]. Thus multiresolution analysis in conjunction with selective thresholding leads to enhanced field resolution while significantly reducing memory requirements.

As mentioned earlier, zero resolution Haar MRTD technique leads to decoupled scaling and wavelet schemes and hence boundary conditions need to be imposed separately on the fields and their derivatives [81]. It was shown that while simple geometries could be characterized with satisfactory accuracy using this scheme, this technique is prone to numerical errors for complex circuits and structures. In order to resolve these issues, a general higher order MRTD scheme (with the scaling function, mother wavelet and one or more higher order wavelets) has been developed and presented in chapter 6. It was shown that from the first resolution level onwards, the Haar MRTD leads to coupled schemes, thereby facilitating a straightforward implementation of boundary conditions and providing accurate characterization of circuits. It was also shown that coupled schemes result in improved accuracy in the characterization of complex circuits.

This chapter focuses on the capability of the MRTD scheme to characterize complex 3D Microwave circuits that are computationally intensive. It will be shown that by using this technique, circuits having fine geometrical details can be modeled with improved accuracy and economy in memory. This is accomplished by using a coarse (scaling) cell discretization globally while locally adding higher resolution wavelets to pick up the fine geometrical details.

8.2 Characterization of a Parallel Plate Waveguide with a very Thin Dielectric Layer using MRTD Technique

A parallel plate waveguide with a very thin dielectric layer as shown in Fig. 8.1 has been analyzed using the first resolution MRTD scheme for two different choices of cell sizes. In the first MRTD implementation, the scaling cell size was chosen to be twice that of the dielectric thickness. Hence, only the first order wavelet function covered the entire span of the dielectric material. In the second implementation, MRTD with double the spatial resolution was chosen such that the scaling cell size is now equal to the dielectric thickness. Hence, in this case, the scaling and wavelet functions span across the extent of the dielectric. Fig. 8.4 shows the instantaneous Magnetic Flux density D_x (at an arbitrary snapshot of time after the incident wave encounters the dielectric interface) obtained by applying the coarse grid MRTD scheme and Fig.8.4 shows the results obtained from the finer grid. Since the resolutions of two schemes are different, the focus is not the direct comparison of the fields obtained from these scheme. Instead, however, the ability of the coarse mesh MRTD where the dielectric extends only across half the cell to to characterize the dielectric discontinuity is the central motive behind this study.

By observing the total field in the figures Fig. 8.4 and Fig.8.4, it is seen that the coarse mesh is as effective as the dense mesh in modeling the this dielectric slab. Thus, by choosing wavelets to pick up the electrical details of the smallest resolution, 50% economy in memory was achieved in this case. This can be improved further by choosing higher resolutions of wavelets to locally enhance field resolution while maintaining a coarse grid globally.

8.3 Analysis of CPS based Vertical Interconnect using MRTD

While it has been demonstrated that MRTD scheme can be used successfully to characterize circuits, it can be seen from section 8.2 that the true benefit of using this technique lies in the fact that field resolution can be enhanced locally by adding wavelets where desired while using scaling functions elsewhere. This aspect of MRTD technique comes in very handy in the analysis of circuits similar to the one shown in Fig. 8.4. The figure shows a Coplanar Stripline with a thin SOG layer on top, which was introduced in chapter 4 as a medium conducive for providing 3D vertical interconnects. The thickness of the silicon substrate is $200\mu m$ and that of the SOG layer is $4\mu m$. The conductor strip width and slot width are $56\mu m$ and $4mum$ respectively. From the dimensions of this circuits, it can be seen that to model this circuit using conventional tools like FDTD can lead to formidable computational resources. This is because the smallest dimensions (e.g, the SOG thickness) determine the largest cell size in the FDTD grid and this cell size is maintained throughout the computational domain due to the uniform mesh.

MRTD can be very efficiently employed in modeling such circuits. When using MRTD, the scaling cell dimension can be chosen to be very coarse compared to the physical dimension of the geometry (with Nyquist limit dictating the upper limit of the coarseness of the cell). Instead, higher order wavelets can be introduced in the region with fine geometrical details. This concept was demonstrated in section 8.2 for the analysis of the parallel plate waveguide with thin dielectric substrate. The same approach is used to characterize the circuit is Fig. 8.4. This circuit is analyzed using first resolution MRTD scheme with two different cell sizes. In the first case, MRTD scheme where scaling cell size is equal to the thickness is the SOG has been used to characterize this circuit and in the second case, MRTD scheme whose scaling cell size is equal twice the SOG thickness has been used. In the MRTD scheme here, wavelets are used only along the direction normal to the substrate. Let $\hat{x}$ be the axis along the propagation direction, $\hat{y}$ the axis in the direction of the line width and $\hat{z}$ the axis which is normal to the substrate. Using this notation, the cell size of the dense MRTD mesh is $\Delta x = 12\mu m \times \Delta y = 4\mu m \times \Delta z = 4\mu m$ and the cell size of the coarse mesh is $\Delta x = 12\mu m \times \Delta y = 4\mu m \times \Delta z = 8\mu m$. The time step in both cases is chosen to be 2.2949e-15 sec which corresponds to $.25dt_{max}$ for the dense mesh and $.2008dt_{max}$ for the coarse mesh where dt_{max} is the maximum Courant limit for an FDTD scheme with the cell sizes specified above. The PML absorber is used in both cases to simulate the open boundaries of the circuit.

Fig. ?? shows a comparison of the total dominant electric field component (E_y) propagating along the line ($\hat{x}$) using the coarse and dense MRTD grids. Fig. ?? shows a comparison of the reflection coefficients (S_{11}) of the circuit using the coarse and dense grid MRTD schemes. Form Figs. ?? and refxxxx, it can be seen that the coarse MRTD mesh characterizes the circuit as effectively as the dense MRTD mesh. However, by choosing the MRTD cell size to be twice the dielectric thickness, up to 50% economy in memory can be achieved. This fact that be utilized very effectively in the characterizing complex microwave circuits with geometrically fine but electrically important details such as the MCPS and CPS vertical interconnects discussed in chapter 4.

8.4 Conclusion

Applications of MRTD in the analysis of 3D microwave circuits has been presented. It has been shown that the upper limit of the coarse scaling cell size does not have to be decided by the smallest geometrical detail as in the case of the FDTD scheme. Instead, wavelets can be added locally to enhance field resolution. This demonstrates the tremendous potential that MRTD scheme holds in characterizing circuits with fine geometrical details.

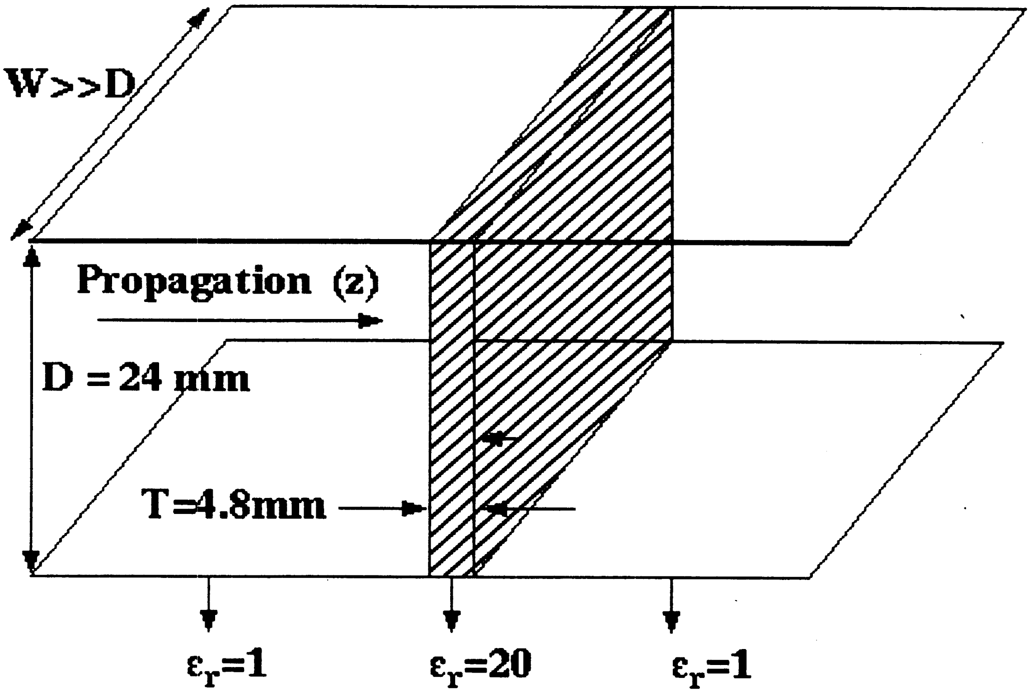

Figure 8.1: Parallel Plate Waveguide filled with a thin dielectric layer

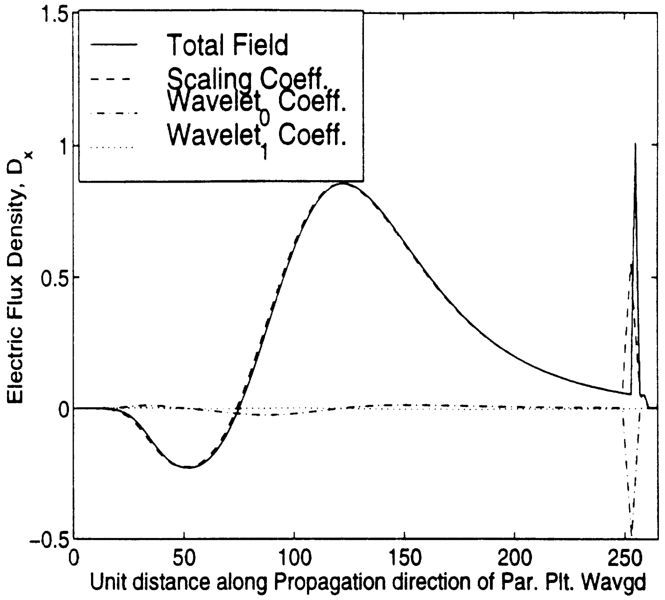

(a) Scaling, wavelet coefficients and total Flux density all along the propagation direction

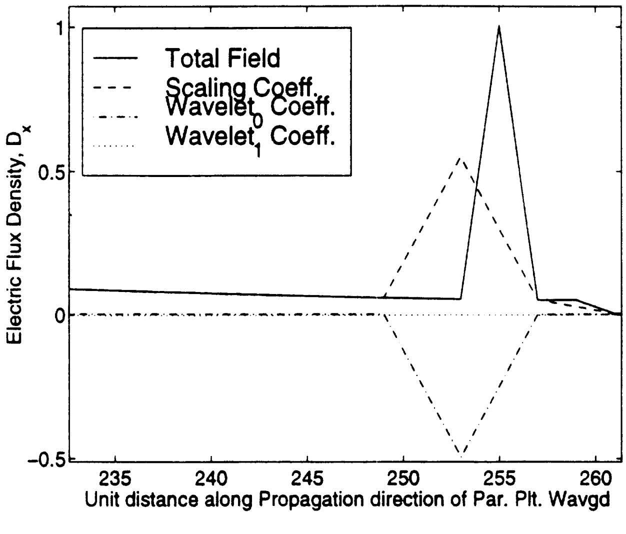

(b) Scaling, wavelet coefficients and total Flux density zooming into the vicinity of the dielectric slab

Figure 8.2: Total field, Scaling and wavelet Coeffs. in the Partially Filled Par. Plt Waveguide obtained from First Resolution MRTD; scaling cell size (9.6mm);dielectric thickness (4.8mm)

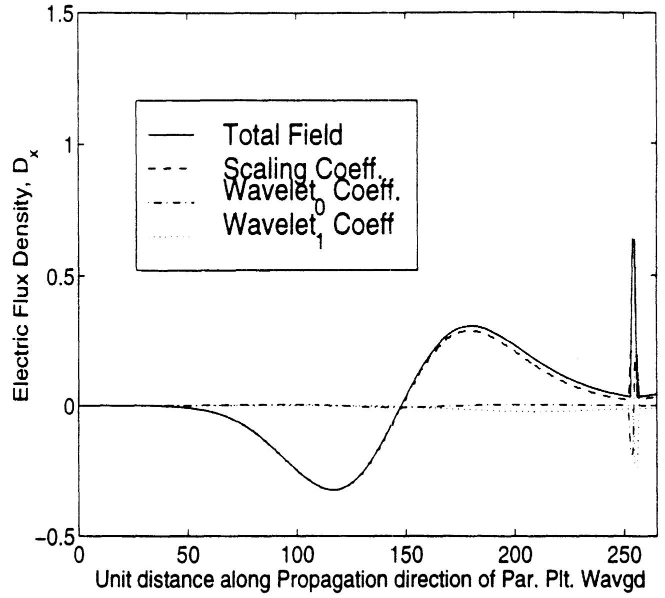

(a) Scaling, wavelet coefficients and total Flux density all along the propagation direction

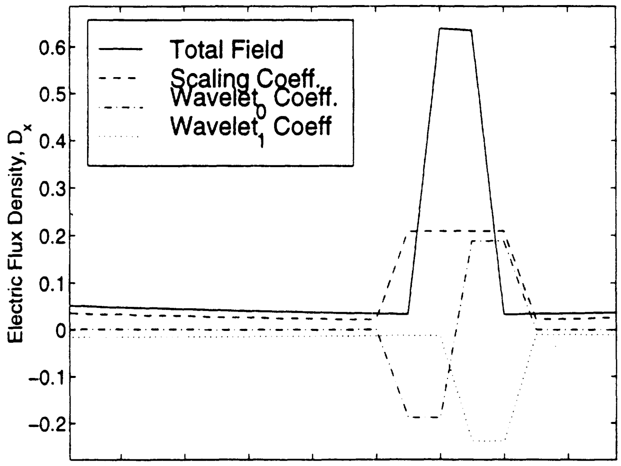

(b) Scaling, wavelet coefficients and total Flux density zooming into the vicinity of the dielectric slab

Figure 8.3: Total field, Scaling and wavelet Coeffs. in the Partially Filled Par. Plt Waveguide obtained from First Resolution MRTD; scaling cell size (4.8mm);dielectric thickness (4.8mm)

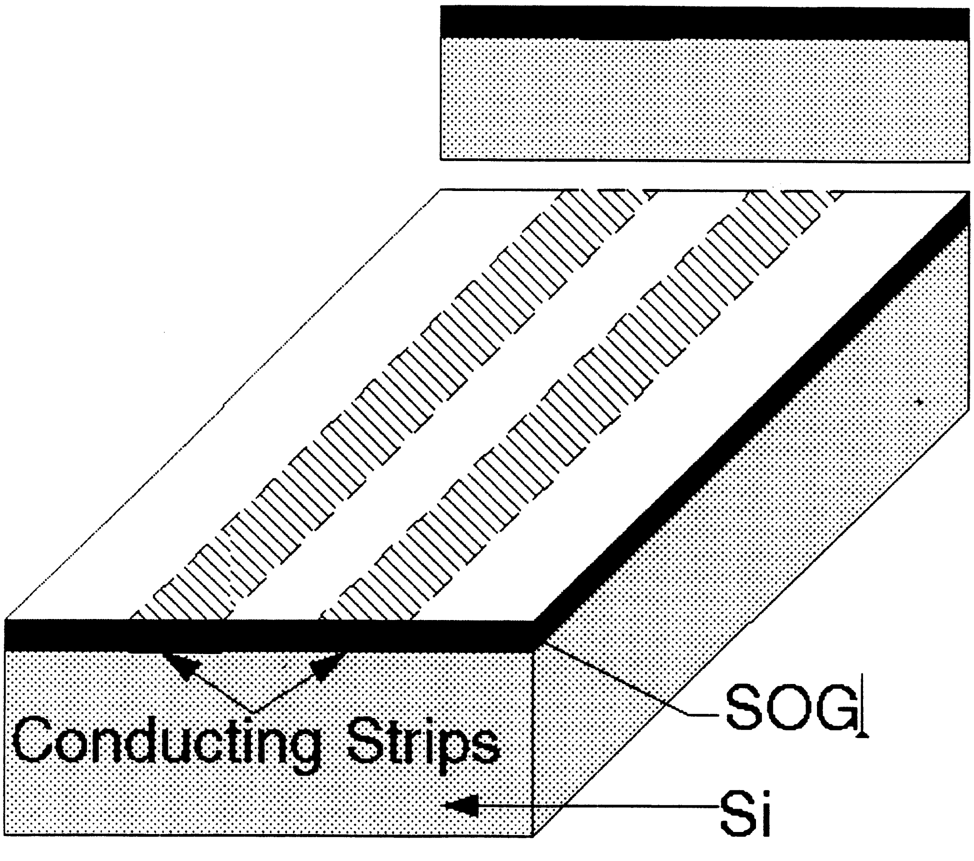

Figure 8.4: CPS throughline with a thin SOG layer on top

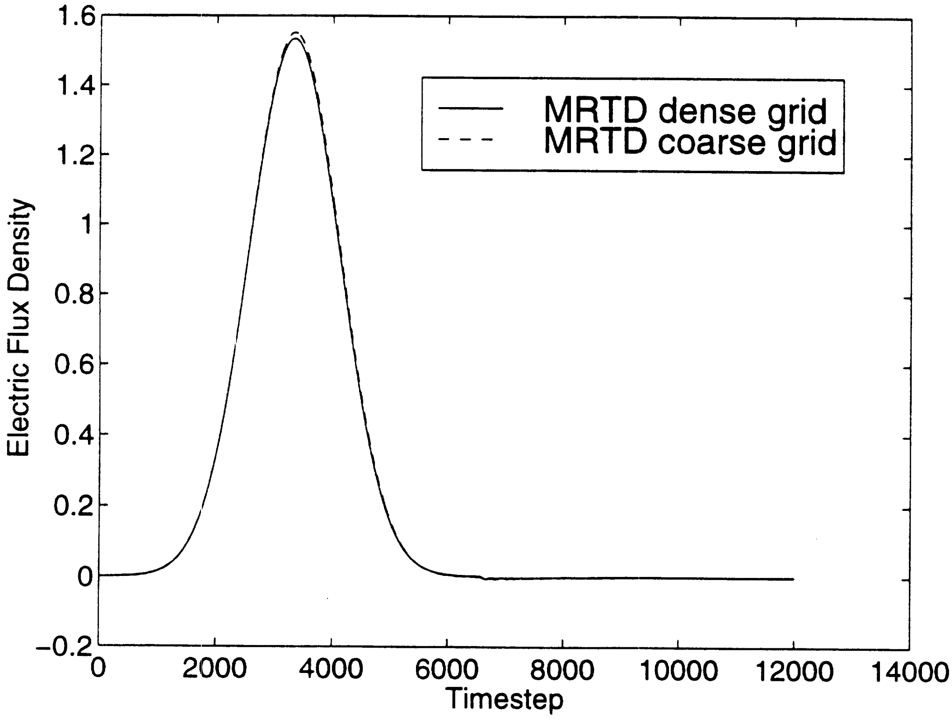

Figure 8.5: Total Electric Flux Density of the CPS throughline with SOG

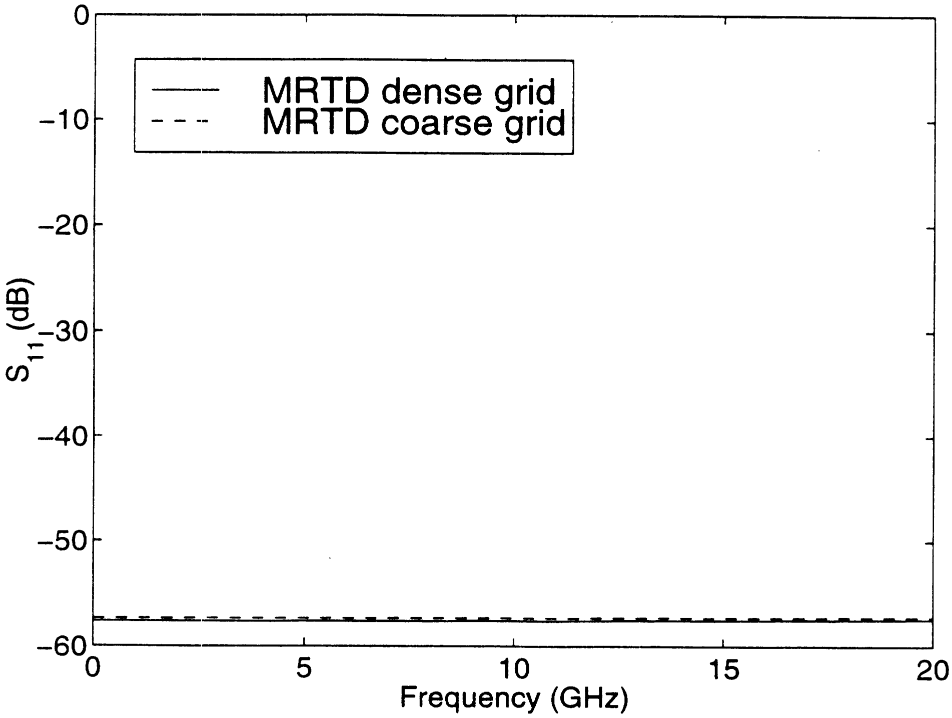
MRTD dense grid
MRTD coarse grid
0
−10
−20
−30
−40
−50
−60
S_{11} (dB)
0
5
10
15
20
Frequency (GHz)

CHAPTER 9

SUMMARY

9.1 Summary of Accomplishments

The focus of this work was to apply time domain techniques to characterize microwave circuits. To being with, the well known FDTD scheme was applied to analyze novel Coplanar Stripline circuits. In addition the FDTD technique was also used to analyze Coplanar and Micro-Coplanar Stripline based circuits and interconnects that are suitable for circuit integration. Through these applications, the simplicity, efficiency and ease of implementation of the conventional Yee FDTD scheme, features which make it a very attractive tool for circuit microwave characterization, were demonstrated.

However, it was seen that the uniform grid implementation of the FDTD scheme was a serious limitation in modeling large scale problems. To circumvent this limitation, the core of this research effort focussed on developing an FDTD multigrid using Haar wavelet based multiresolution analysis. The Haar basis was chosen due to the fact that pulse functions, which are used for field expansions in the FDTD scheme form the scaling function of the Haar system. Hence FDTD can be thought of as a special case of a more general scheme, referred to here as the MRTD technique, which used Haar scaling and wavelet resolutions for field expansions. MRTD scheme has the capability of enhancing the resolution in selective regions of the computational domain by using a combination of scaling and wavelet bases for field expansions. In sections of the computational domain where a coarse resolution is sufficient, only the scaling functions are used for field expansions. Thus an FDTD multigrid is implemented using Haar based Multiresolution.

In conjunction with developing the discretized equations for the MRTD scheme, the details of implementation of the relevant boundary conditions and 'open' boundaries were presented. The MRTD scheme was validated and efficiency and advantages of demonstrated by characterizing several circuits using MRTD scheme. From these applications, it can be concluded that MRTD is a very powerful time domain scheme which has all the advantages of the the conventional FDTD scheme, such as simplicity, efficiency, and ease of implementation. In addition, MRTD offers improved accuracy due to enhanced resolution and economy in memory due to selective enhancement in the resolution. Thus Haar based MRTD scheme has several potential applications in the characterization of complex microwave circuits.

9.2 Recommendations for Future Work

While the details of developing the Haar-based MRTD technique for an arbitrary resolution MRTD scheme have been presented, all the applications in this work used MRTD schemes up to resolution 1. Future work on the Haar based MRTD scheme should use higher resolutions for enhanced benefits. A systematic study of the improvement in accuracy by adding higher resolutions in different complex geometries should be evaluated. In addition, developing the Haar-wavelet based MRTD scheme to model nonlinear circuits will be very useful in broadening the genre of circuits that can be characterized using this scheme.

CHAPTER 10

BIBLIOGRAPHY

BIBLIOGRAPHY

BIBLIOGRAPHY

[1] M. Muraguchi, et al., "Uniplanar MMIC's and their applications", IEEE Trans. Microwave Theory Tech., Vol. 36, pp. 1896-1900, Dec. 1988.

[2] K. C. Gupta, R. Garg and I. J. Bahl, Microstrip lines and slotlines, Dedham, MA: Artech House, 1979, Chap. 7 on Coplanar lines, pp. 257 - 301.

[3] R. Goyal, Editor, Monolithic Microwave Integrated Circuits: Technology and Design, Nowood, MA: Artech House, 1989, Chap. 4, Section 4.7 on Transmission Lines, pp. 347 - 382.

[4] M. Houdart, "Coplanar lines: Application to broadband microwave integrated circuits," Proc. 6th European Microwave Conf., pp. 49 - 53, Rome, 1976.

[5] R. A. Pucel, "Design considerations for monolithic microwave circuits," IEEE Trans. Microwave Theory Tech., Vol. 29, pp. 513-534, June 1981.

[6] R. W. Jackson, "Considerations in the use of coplanar waveguide for millimeter wave integrated circuits," IEEE Trans. Microwave Theory Tech., Vol. 34, pp. 1450 - 1456, Dec. 1986.

[7] M. Riaziat, E. Par, G. Zdasiuk, S. Bandy and M. Glenn, "Monolithic millimeter wave CPW circuits," 1989 IEEE MTT-S Int. Microwave Symp. Dig., pp. 525 - 528, Long Beach, CA.

[8] T. Hirota, Y. Tarusawa and H. Ogawa, "Uniplanar MMIC hybrids - A Proposed new MMIC structure," IEEE Trans. Microwave Theory Tech., Vol. 35, pp. 576 - 581, June 1987.

[9] J. B. Knorr and K. D. Kuchler, "Analysis of coupled Slots and Coplanar Strips on Dielectric Substrate", IEEE Trans. Microwave Theory Tech., Vol. MTT-23, No. 7, pp. 541 - 548, July 1975.

[10] R. N. Simons, G. E. Ponchak, R. Q. Lee and N. S. Fernandez, "Coplanar Waveguide Fed Phased array Antenna", Digest of the 1990 IEEE Antennas and Propagat. International Symposium., Vol. 4, pp. 1778 - 1781.

[11] R. N. Simons, N. I. Dib, R. Q. Lee and L. P. B. Katehi, "Integrated Uniplanar transition for Linearly Tapered Slot Antenna", IEEE Trans. Antennas and Propagat., Vol. 43, pp. 998 - 1002, Sept. 1995.

[12] M.-Y. Frankel, J. F. Whitaker and G. A. Mourou, "Optoelectronic Transient characterization of Ultrafast Devices", IEEE Journal of Quantum Electronics, Vol. 28, pp. 2313 - 2324, Oct. 1992.

[13] R. N. Simons, N. I. Dib and L. P. B. Katehi, "Modeling of Coplanar Stripline Discontinuities.", IEEE Trans. Microwave Theory Tech., Vol. 44, No. 5, May 1996, pp. 711 - 716.

[14] NIST De-embedding Software, Program DEEMBED, Revision 4.04, 1994.

[15] G. Ghione and C. Naldi, "Analytical Formulas For For Coplanar Lines In Hybrid And Monolithic MICs", Electronic Letters, Vol. 20, No. 4, Feb. 1984.

[16] K. Goverdhanam, R. N. Simons and L. P. B. Katehi, "Coplanar Stripline Propagation Characteristics and Bandpass Filter", IEEE Microwave and Guided Wave Letters, Vol. 7, No. 8, August 1997.

[17] K. Goverdhanam, R. N. Simons and L. P. B. Katehi, "Coplanar Stripline Components for high frequency applications", IEEE Trans. Microwave Theory Tech., Vol. 45, No. 10, pp. 1725 - 1729, Oct. 1997.

[18] X. Zhang and K. K. Mei, "Time-Domain Finite Difference approach to the Calculation of the Frequency-Dependent Characteristics of Microstrip Discontinuities", IEEE Trans. Microwave Theory Tech., Vol. 36, No. 12, pp. 1775 - 1787, Dec. 1988.

[19] A. Bayliss and E. Turkel, "Radiation Boundary conditions for wave-like equations", Comm. Pure Appl. Math., Vol. 23, pp. 707-725, 1980.

[20] A. Bayliss, M. Gunzburger and E. Turkel, "Boundary Conditions for the numerical solutions of elliptic equations in exterior regions", SIAM J. Applied Math., Vol. 42, pp. 430 - 451, 1982.

[21] B. Engquist and A. Majda, "Absorbing Boundary Conditions for the numerical simulation of waves", Mathematics of Computations, Vol. 31, No. 139, pp. 629 - 651, 1977.

[22] G. Mur, "Absorbing Boundary conditions for the finite-difference approximation of the time domain electromagnetic field equations", IEEE Trans. Electromagnetic Compatibity, Vol. 23, No. 4, pp. 377 - 382, Nov. 1981.

[23] L. N. Trefethen and L. Halpern, "Well-posedness of one way wave equations and Absorbing Boundary Conditions", Mathematics of Computations, Vol. 47, pp. 421 - 435, 1986.

[24] R. L. Higdon, "Absorbing Boundary conditions for difference approximations to the multidimensional wave equation", Mathematics of Computations, Vol. 47, pp. 437 - 459, 1986.

[25] R. L. Higdon, "Numerical Absorbing Boundary conditions for the wave equation", Mathematics of Computations, Vol. 49, pp. 65 - 90, 1987.

[26] Z. P. Liao, H. L. Wong, B. P. Yang and Y. F. Yuan, "A transmitting Boundary for transient wave analyses", Scientia Sinica (series A), Vol. XXVII, pp. 1063 - 1076, 1984.

[27] K. K. Mei and J. Fang, "Superabsorption - A method to improve absorbing boundary conditions", IEEE Trans. Antennas and Propagat., Vol. 40, No. 9, pp. 1001 - 1010, Sep. 1992.

[28] A. Reineix and B. Jecko, "Analysis of Microstrip Patch Antennas using the Finite Difference Time Domain Method", IEEE Trans. Antennas and Propagat., Vol. 37, No. 11, pp. 1361 - 1369, Nov. 1989.

[29] W. D. Smith, "A nonreflecting plane boundary for wave propagation problems", J. Comp. Physics, Vol. 15, pp. 492 - 503, 1974.

[30] X. Zhang, J. Fang, K. K. Mei and Y. Liu, "Calculations of the dispersive characteristics of microstrips by the time-domain finite difference method", IEEE Trans. Microwave Theory Tech., Vol. 36, No. 2, pp. 263 - 267, Feb. 1988.

[31] E. L. Lindman, "Free Space Boundary Conditions for the time dependent wave equation", J. Computational Physics, Vol. 18, pp.66 - 78, 1975.

[32] J.-P. Berenger, "A Perfectly matched layer for the absorption of Electromagnetic Waves", J. Computational Physics, Vol. 114, pp. 185 - 200, 1994.

[33] K. R. Umashankar and A. Taflove, "A novel method to analyze electromagnetic scattering of complex objects", IEEE Trans. Electromagnetic Compatibility, Vol. 24, pp. 397 - 405, 1982.

[34] T. Shibata and H. Kimura, "Computer-Aided Engineering for Microwave and Millimeter-Wave Circuits using the FDTD Technique of Field Simulations", Inter. Jour. of Microwave and Millimeter-Wave Computer-Aided Engineering, Vol. 3, No. 3, pp. 238 - 250, May 1993.

[35] N. I. Dib, R. N. Simons and L. P. B. Katehi, "New Uniplanar Transitions for Circuit and Antenna Applications", IEEE Trans. Microwave Theory Tech., Vol. 43, No. 12, pp. 2868 - 2873, Dec. 1995

[36] T. Itoh (Ed.), "Numerical Techniques for Microwave and Millimeter Wave Passive Structures", John Wiley & sons, New York, 1989

[37] R. Sorrentino (Ed.), "Numerical Methods for Passive Microwave and Millimeter Structures", IEEE Press, New York, 1989

[38] E. Yamashita (Ed.), "Analysis Methods for Electromagnetic Wave Problems", Artech House, Boston, 1990

[39] R.F. Harrington, "Field Computation by Moment Methods", Macmillan, New York, 1968

[40] K. Hayata, M. Koshiba, M. Eguchi and M. Suzuki, "Vectorial finite-element method without any spurious solutions for dielectric waveguide problems using transverse magnetic field component", IEEE Trans. Microwave Theory Tech., Vol. 34, pp. 1120 - 1124, Nov. 1986.

[41] K. Bierwirth, N. Schulz and F. Arndt, "Finite-difference analysis of rectangular dielectric waveguide structures", IEEE Trans. Microwave Theory Tech., Vol. 34, pp. 1104 - 1113, Nov. 1986.

[42] P.B. Johns, "The solution of inhomogeneous waveguide problems using a Transmission line matrix", IEEE Trans. Microwave Theory Tech., Vol. 22, pp. 209 - 215, 1974

[43] K.S. Yee, "Numerical solution of initial boundary value problems involving Maxwell's equations in isotropic media", IEEE Trans. Antennas and Propagat., Vol. 14, pp. 302 - 307, May 1966

[44] P.H. Aoyagi, J.F. Lee, R.Mittra, "A hybrid Yee Algorithm/Scalar-Wave Equation Approach", IEEE Trans. Microwave Theory Tech., Vol. 41, No. 9, pp. 1593 - 1600, Sept. 1993.

[45] M. Mrozowski, "A hybrid PEE-FDTD Algorithm for Accelerated Time Domain Analysis of Electromagnetic Waves in Shielded Structures", IEEE Microwave and Guided Wave Letters, Vol. 4, No. 10, pp. 323 - 325

[46] L. Lapidus, G.F. Pinder, "Numerical Solution of Partial Differential Equations in Science and Engineering", John Wiley & sons, New York 1982, pp. 171 - 179.

[47] A. Taflove, "Computational Electrodynamics: The Finite Difference Time Domain Method", Artech House, 1995.

[48] S. Xiao, R. Vahldieck, "An improved 2D-FDTD Algorithm for Hybrid Mode Analysis of Quasi-planar transmission Lines", Digest of the 1993 IEEE Microwave Theory Tech. Symposium, pp. 421 - 424.

[49] D. M. Sheen, "Numerical Modeling of Microstrip Circuits and Antennas", Ph.D. dissertation, Massachusetts Institute of Technology, Cambridge, MA, June 1991.

[50] J. Fang, "Time Domain Finite Difference Computation for Maxwell's Equations", Ph.D. dissertation, University of California at Berkeley, 1989, pp. 138 - 158.

[51] R. Holland, L. Simpon, "Finite Difference Analysis of EMP coupling to thin struts and wires", IEEE Trans. Electromagn. Compat., Vol. 23, pp. 88 - 97, May 1981.

[52] S. S. Zivanovic, K. S. Yee, K.K.Mei, "A Subgridding Method for the Time-Domain Finite-Difference Method to Solve Maxwell's Equations", IEEE Trans. Microwave Theory Tech., Vol. 39, No. 3, pp. 471 - 479 March 1991.

[53] P. Monk and E. Suli, "A convergence analysis of Yee's scheme on non-uniform grids," SIAM J. Numerical Analysis, Vol 31, pp. 393 - 412, 1994.

[54] P. Monk, "Error estimates for Yee's method on non-uniform grids," IEEE Trans. Magnetics, Vol. 30, pp. 3200 - 3203, 1994.

[55] T. A. Manteuffel and J. A. White, "The numerical solution of second-order boundary value problems on nonuniform meshes," Mathematics of Computation, Vol. 47, pp. 511 - 535, 1986.

[56] H. Kreiss, T. Manteuffel, B. Schwartz, B. Wendroff and J. A. B. White, "Supraconvergent schemes on irregular meshes," Mathematics of Computation, Vol. 47, pp. 537 - 554, 1986.

[57] K. Sabetfakhri, "Novel Efficient Integral-Based Techniques for Characterization of Planar Microwave Structures", Ph.D. dissertation, The University of Michigan, Radiation Laboratory, 1995.

[58] E. M. Tentzeris, "Time Domain Numerical Techniques for the Analysis and Design of Microwave Circuits", Ph.D. dissertation, The University of Michigan, Radiation Laboratory, 1998.

[59] S.G. Mallat, "A theory for Multiresolution Signal Decomposition: The Wavelet Representation", IEEE Trans. Pattern Anal. Machine Intell., Vol. 11, pp. 674 - 693, July 1989.

[60] B. Jawerth, W. Sweldens, "An overview of wavelet based Multiresolution Analyses", SIAM Review, Vol. 36, No. 3, pp. 377 - 412, Sept. 1994.

[61] B.Z. Steinberg, Y. Leviatan, "On the use of wavelet expansions in the method of moments", IEEE Trans. Antennas and Propagat., Vol. 41, pp.610 - 619, May 1993.

[62] G. Wang, G.-W. Pan, "Full wave Analysis of microstrip floating line structures by wavelet expansion method", IEEE Trans. Microwave Theory Tech., Vol. 43, pp. 131 - 142, Jan. 1995.

[63] K. Sabetfakhri, L.P.B. Katehi, "An Integral Transform Technique for the analysis of planar dielectric structures", IEEE Trans. Microwave Theory Tech., Vol. 42, pp. 1052-1062, June 1994.

[64] M. Krumpholz, P. Russer, "On the Dispersion in TLM and FDTD", IEEE Trans. Microwave Theory Tech., Vol. 42, No. 7, pp. 1275 - 1279, July 1994.

[65] M.Krumpholz, L.P.B.Katehi, "New Prospects for Time Domain Analysis", IEEE Microwave and Guided Wave Letters, pp. 382 - 384, November 1995.

[66] M.Krumpholz, L.P.B.Katehi, "MRTD: New Time Domain Schemes Based on Multiresolution Analysis", IEEE Transactions on Microwave Theory and Techniques, pp. 385-391, April 1996.

[67] M.Krumpholz, C. Huber and P. Russer, "A field theoretical comparison of FDTD and TLM", IEEE Transactions on Microwave Theory and Techniques, Vol. 43, pp. 1935 - 1950, Aug. 1995.

[68] L. N. Trefethen, "Group Velocity in Finite Difference Schemes", SIAM Review, Vol. 24, No. 2, April 1982.

[69] D. R. Lynch, K. D. Paulsen, "Origin of Vector Parasitics in Numerical Maxwell Solution", IEEE Trans. Microwave Theory Tech., Vol. 39, No. 3, pp. 383 - 394, March. 1991.

[70] X. Zhang, K. K. Mei, "Time-Domain Finite Difference Approach for the Calculation of Microstrip Open-Circuit End Effect", Digest of the 1988 IEEE Microwave Theory Tech. Symposium, pp. 363 - 366.

[71] I. Wolff, "Finite Difference Time-Domain Simulation of Electromagnetic Fields and Microwave Circuits", International Journal of Numerical Modelling: Electronic Networks, Devices and Fields, Vol.5, pp. 163 - 182, 1992

[72] P. Alinikula, K. S. Kunz, "Analysis of Waveguide Aperture Coupling Using the Finite-Difference Time-Domain Method", IEEE Microwave and Guided Wave Letters, Vol. 1, No. 8, pp. 189 - 191, Aug. 1991.

[73] G-C. Liang, Y-W Liu, K. K. Mei, "Full-Wave Analysis of Coplanar Waveguide and Slotline Using the Time-Domain Finite-Difference Method", IEEE Trans. Microwave Theory Tech., Vol. 37, No. 12, pp. 1949 - 1957, Dec. 1989.

[74] I. Daubechies, "Orthonormal Bases of compactly supported wavelets", Comm. Pure Appl. Math., Vol. XLI, pp. 909 - 996, 1988.

[75] S. G. Mallat, "Multifrequency Channel Decompositions of images and wavelet models", IEEE Trans. Acoust., Speech, Signal Processing, Vol. ASSP-37, pp. 2091 - 2110, Dec. 1989.

[76] S. G. Mallat, "Multiresolution Approximation and wavelet orthonormal bases of L^2", Trans. Amer. Math. Soc., Vol. 3-15, pp. 69 - 87, Sept. 1989.

[77] A. E. Yagle, "Image reconstruction from projections under wavelet constraints", IEEE Trans. Signal Proc., Vol. 41, pp. 3579 - 3584, Dec. 1993.

[78] K. Goverdhanam, E. Tentzeris, M. Krumpholz and L.P.B. Katehi, "An FDTD Multigrid Based on Multiresolution Analysis," Proceedings of the 1996 IEEE International Symposium on Antennas and Propagation, Baltimore, MD, pp. 352 - 355, July 1996.

[79] E.Tentzeris, R.Robertson, M.Krumpholz and L.P.B. Katehi, "Application of the PML Absorber to the MRTD Technique", Proceedings of the 1996 IEEE Antennas and Propagat. International Symposium, pp. 634 - 637.

[80] K. Goverdhanam, A. Cangellaris and L. P.B. Katehi, "Applications of Multiresolution Based FDTD Multigrid," Proceedings of the 1997 IEEE International Symposium on Microwave Theory and Techniques, Denver, CO, June 1997.

[81] K. Goverdhanam, E. Tentzeris and L. P.B. Katehi, "Treatment of Boundaries in Multiresolution based FDTD Multigrid," 1998 ACES Conference Digest.

[82] R. F. Drayton and L. P. B. Katehi, "Development of Self-Packaged High Frequency Circuits Using Micromachining Techniques", IEEE Trans. Microwave Theory Tech., Vol. 43, No. 9, pp. 2073 - 2080, Sept. 1995.

[83] K. Goverdhanam, R.N. Simons and L.P.B. Katehi, "Micro-Coplanar Striplines - new transmission Media for Microwave Applications", Digest of 1998 IEEE MTT-S Inter. Microwave Symp., Baltimore, Maryland, pp. 1035 - 1038, 1998.

[84] K. Goverdhanam, R.N. Simons and L.P.B. Katehi, "Micro-Coplanar Striplines - New Transmission Line Media: Propagation Characteristics and Applications", to be submitted to IEEE Trans. Microwave Theory Tech.

[85] K. Goverdhanam, R.N. Simons and L.P.B. Katehi, "Novel Three-Dimensional Vertical Interconnect Technology for Microwave and RF Applications", submitted for review to the 1999 IEEE MTT-S Inter. Microwave Symp.